



# A Configurable Terasample-per-second Imaging System for Optical SETI

## Citation

Mead, Curtis Charles. 2013. A Configurable Terasample-per-second Imaging System for Optical SETI. Doctoral dissertation, Harvard University.

## Permanent link

<http://nrs.harvard.edu/urn-3:HUL.InstRepos:11158246>

## Terms of Use

This article was downloaded from Harvard University's DASH repository, and is made available under the terms and conditions applicable to Other Posted Material, as set forth at <http://nrs.harvard.edu/urn-3:HUL.InstRepos:dash.current.terms-of-use#LAA>

## Share Your Story

The Harvard community has made this article openly available.  
Please share how this access benefits you. [Submit a story](#).

[Accessibility](#)

# **A Configurable Terasample-per-second Imaging System for Optical SETI**

A dissertation presented  
by

Curtis Charles Mead

to

The School of Engineering and Applied Sciences  
in partial fulfillment of the requirements

for the degree of  
Doctor of Philosophy  
in the subject of

Applied Physics

Harvard University  
Cambridge, Massachusetts

April 2013



©2013 - Curtis Charles Mead

All rights reserved.

# A Configurable Terasample-per-second Imaging System for Optical SETI

## Abstract

A new instrument for conducting astronomical searches for nanosecond-scale optical pulses has been designed, built, and is now operating at Oak Ridge Observatory in Harvard, MA. The Advanced All-sky Camera, based on the previous generation ASIC-based design, is implemented using Xilinx Virtex-5 LX110 FPGAs to create a flexible and configurable system. Each FPGA has 32 1.5 Gbps analog-to-digital converters, implemented as 8-level flash ADCs using 256 of the Virtex-5's LVDS input pairs. Thirty-two FPGAs in the system total 1024 ADC channels, each with 8kB of sample memory, for triggering on and recording coincident pulse waveforms from an array of 1024 photomultiplier tube anodes.

The camera performs a transit-mode search of the Northern sky from  $-20^\circ < \delta < +70^\circ$  for nanosecond astronomical phenomena and pulsed laser beacon signals from extrasolar technological civilizations. The 1.8 m f/2.5 telescope images a  $1.6^\circ \times 0.2^\circ$  area of the sky onto the camera's beamsplit focal plane where coincident optical (300 nm–900 nm) pulses in matched PMT pixel pairs trigger the camera readout.

Initial observations with the Advanced All-sky Camera recorded 318 coincident pulse events, eighteen of which are identified as Čerenkov light from cosmic ray induced extensive air showers,  $\sim 30$  are traced to aircraft, and the rest are single-pixel, low-amplitude pulses caused by detector artifacts.

This thesis examines the plausibility of pulsed optical interstellar communications, describes briefly the original all-sky camera and its limitations, presents the design of the PulseNet-V FPGAs and the Advanced All-sky Camera, and concludes with tests and initial observations using the new system.

# Contents

Title Page . . . . .	i
Abstract . . . . .	iii
Table of Contents . . . . .	iv
List of Figures . . . . .	vii
List of Tables . . . . .	x
Acknowledgments . . . . .	xi
Dedication . . . . .	xii
<b>1 Background . . . . .</b>	<b>4</b>
1.1 “Is Anybody Out There?” . . . . .	4
1.1.1 Search Methods . . . . .	5
1.1.2 Galactic Census . . . . .	7
1.1.3 What are we looking for? . . . . .	12
1.1.4 The Spectrum . . . . .	13
1.1.5 Modulation . . . . .	16
1.2 Pulsed Optical SETI . . . . .	17
1.2.1 Scheme . . . . .	17
1.2.2 Example Systems . . . . .	27
1.2.3 Summary . . . . .	31
1.3 Optical SETI Backgrounds . . . . .	32
1.3.1 Astronomical . . . . .	32
1.3.2 Stellar Pileup . . . . .	33
1.3.3 Photomultiplier Issues . . . . .	35
1.3.4 Cosmic Ray Air Showers . . . . .	36
1.3.5 Muons . . . . .	39
1.3.6 Atmospheric and Anthropic . . . . .	43
<b>2 All-Sky Optical SETI . . . . .</b>	<b>44</b>
2.1 The All-sky System . . . . .	45
2.2 Observatory . . . . .	46
2.3 Telescope . . . . .	47
2.4 SETI Camera . . . . .	50

2.4.1	Optical Front End	50
2.4.2	Electronics Backend	54
2.5	Observatory Equipment	56
2.5.1	Test Instruments	56
2.5.2	Environmental Sensors	57
2.5.3	Networking	59
2.6	Observatory Control	60
2.6.1	User Interface	62
2.7	Limitations	64
2.7.1	Spectral Sensitivity	64
2.7.2	One Sample Buffer Per PulseNet	64
2.7.3	Sample Depth	65
2.7.4	Triggering	65
2.7.5	Sampling Rate	66
2.7.6	Communication Bandwidth	66
2.7.7	Astronomy Functionality	66
<b>3</b>	<b>PulseNet-V</b>	<b>68</b>
3.1	Design Overview	71
3.2	Pulsenet-V Architecture	73
3.2.1	Microblaze	75
3.2.2	Embedded System Peripherals	77
3.3	PulseNet Core	78
3.3.1	Design Structure	80
3.3.2	Digitization	84
3.3.3	Trigger Logic	86
3.3.4	Astronomy Counters	87
3.3.5	Configuration Registers	89
3.4	Software	92
3.4.1	Operating System	92
3.4.2	Drivers	93
3.4.3	Boot Script	95
3.4.4	Debug	96
3.4.5	Bootloaders	96
3.4.6	Daemon Programs	97
3.5	FPGA Configuration and Flash	100
3.6	Design Tools	101
<b>4</b>	<b>Advanced All-Sky Camera</b>	<b>103</b>
4.1	Advanced All-sky Optical SETI Camera	105
4.1.1	Photomultiplier Tubes	105
4.1.2	Daughterboards	106

4.1.3	Motherboard	116
4.1.4	Server	130
4.1.5	Other Camera Equipment	131
4.2	Camera Control	132
4.2.1	Web User Interface	133
4.2.2	Processing Application	134
4.3	Future Enhancements	135
<b>5</b>	<b>Advanced All-Sky – Testing and Observations</b>	<b>137</b>
5.1	Testing	137
5.1.1	Sampler Performance	137
5.1.2	PMT Voltage	142
5.1.3	Camera Trigger Sensitivity	146
5.2	SETI Observations	152
5.2.1	Observation Procedure	152
5.2.2	Observation Summary	153
5.2.3	Dark Current and Pileup	156
5.2.4	Airplanes	158
5.2.5	Cosmic Rays	164
5.3	Cosmic Ray Simulations	168
5.3.1	Corsika	168
5.3.2	Telescope Perspective	169
5.3.3	Energy Threshold	171
5.3.4	Cosmic Ray Trigger Rate	174
5.4	Pointing Calibration	176
5.5	Limits on the Prevalence of Transmitting Civilizations	179
5.6	Recommendations For Future Work	183

# List of Figures

1.1	EM Spectrum . . . . .	15
1.2	Range for 10 AU beam . . . . .	21
1.3	Extinction . . . . .	24
1.4	Galactic Visual Extinction . . . . .	25
1.5	Muon Ring Track . . . . .	39
1.6	Čerenkov from Muon Track . . . . .	41
1.7	Muon Ring Geometry . . . . .	42
1.8	Muon Beamsplitter Trigger Geometry . . . . .	43
2.1	Transit Survey . . . . .	46
2.2	Observatory Building . . . . .	47
2.3	Telescope and Camera . . . . .	49
2.4	PMT Rack Model . . . . .	52
2.5	Photomultiplier Tubes . . . . .	53
2.6	All-sky Circuit Boards . . . . .	55
2.7	Gelfand Flashers . . . . .	56
2.8	Rain Sensor . . . . .	58
2.9	PTZ Camera . . . . .	59
2.10	Server Connections . . . . .	61
2.11	User Interface . . . . .	63
3.1	PulseNet-V Overview . . . . .	69
3.2	PulseNet-V Block Diagram . . . . .	74
3.3	<code>pulsenet_core</code> Block Diagram . . . . .	79
3.4	Pulsenet VHDL Stucture . . . . .	83
3.5	Flash ADC Block Diagram . . . . .	85
3.6	Astronomy Counters . . . . .	88
3.7	PulseNet-V ADC Channel Pinout . . . . .	91
3.8	PulseNet-V Communication Protocol . . . . .	99
4.1	AdvCam Photomultiplier Tubes . . . . .	106
4.2	Daughterboard Front and Back . . . . .	107

4.3	Daughterboard Section Layout . . . . .	108
4.4	Daughterboard Layer Stackup . . . . .	109
4.5	Daughterboard PMT Signal Amplifier Schematic . . . . .	110
4.6	Daughterboard Ethernet Schematic . . . . .	111
4.7	Daughterboard DDR SDRAM Schematic . . . . .	112
4.8	Daughterboard FPGA Configuration Schematic . . . . .	113
4.9	Daughterboard DAC Schematic . . . . .	114
4.10	Daughterboard Power Regulators Schematic . . . . .	115
4.11	Motherboard . . . . .	117
4.12	Motherboard SDRAM and Ethernet Circuits . . . . .	118
4.13	Motherboard GPS and Clock Circuits . . . . .	119
4.14	Motherboard Config Circuits . . . . .	120
4.15	Motherboard Spartan-6 Banks (1 of 2) . . . . .	121
4.16	Motherboard Spartan-6 Banks (2 of 2) . . . . .	122
4.17	Motherboard Power Supplies . . . . .	123
4.18	Motherboard Communication Protocol . . . . .	128
4.19	JTAG Bus Connections to Daughterboards . . . . .	130
4.20	UI Telemetry Panel . . . . .	134
5.1	Full Scale Test Pulse . . . . .	139
5.2	Low Level Test Pulse . . . . .	141
5.3	PMT0 Setpoint . . . . .	144
5.4	PMT0 Astronomy Count Rates . . . . .	145
5.5	Camera Sensitivity: Unlinked. HV Off. . . . .	147
5.6	Camera Sensitivity: Linked. HV Off. . . . .	148
5.7	Camera Sensitivity: Unlinked. HV On. Shutter Closed. . . . .	149
5.8	Camera Sensitivity: Linked. HV On. Shutter Closed. . . . .	150
5.9	Camera Sensitivity: Linked. HV On. Shutter Open. . . . .	151
5.10	Advanced All-sky Observations . . . . .	154
5.11	Events By PulseNet-V Number . . . . .	155
5.12	Random Coincidence Event . . . . .	157
5.13	Airplane Trigger Waveforms . . . . .	160
5.14	Airplane Trigger Skycam . . . . .	161
5.15	Skycam: Photos Explained . . . . .	162
5.16	Airplane Trigger Times . . . . .	163
5.17	Typical Cosmic Ray Coincidence . . . . .	165
5.18	Cosmic Ray Waveform . . . . .	166
5.19	Cosmic Ray Coincidences . . . . .	167
5.20	Cosmic Ray Impact Parameter . . . . .	170
5.21	Cosmic Ray Differential Trigger Rates . . . . .	173
5.22	Cosmic Ray Trigger Rate . . . . .	175
5.23	Deneb Transiting PMT2 . . . . .	177

5.24 Declination Regression Line . . . . .	178
5.25 Pointing Calibration . . . . .	179
5.26 Technological Transmitting Civilization Limits . . . . .	182
5.27 VERITA FADC System . . . . .	185
5.28 Analog Memory System . . . . .	186
5.29 IACT OSETI Trigger . . . . .	189



# List of Tables

1.1	Drake Equation Estimates . . . . .	12
1.2	Electromagnetic Bands . . . . .	14
1.3	Example Systems . . . . .	30
3.1	PulseNet-V At-A-Glance . . . . .	70
3.2	Microblaze Options . . . . .	76
3.3	Pulsenet-V Address Table. . . . .	76
3.4	Pulsenet-V Peripherals. . . . .	78
3.5	PulseNet-V Core Configuration Registers . . . . .	89
3.6	Kernel Config Options . . . . .	93
4.1	Spartan-6 Peripherals. . . . .	124
4.2	mbrd_trig Configuration Registers . . . . .	125
4.3	Python Files . . . . .	132
5.1	Aircraft Minimum Light Intensities . . . . .	159
5.2	Pointing Calibration Stars . . . . .	178

# Acknowledgments

First and foremost, thanks to Paul Horowitz, my principle investigator, mentor, and friend, who has given his unwavering support and unrestrained encouragement throughout my graduate studies. The creative space, unrestricted access, and generosity Paul offered to me exceeded anything a graduate student could ever expect from his professor. Paul's infinite energy and enthusiasm inspire me continue pushing forward through uncertain, difficult, and daunting tasks.

Financially, this work has been faithfully supported by the Bosack-Kruger Foundation and The Planetary Society. The all-sky telescope and building are dedicated to The Planetary Society. I am forever grateful to the Bosack-Kruger Foundation for consistently providing for my graduate stipend, year after year, and for supporting the construction of the Advanced All-sky Camera.

I thank our friends at Xilinx and Vicor for their support of my project. Xilinx generously provided the Virtex-5 FPGAs for the Advanced All-sky Camera. Vicor donated the switching power supplies needed to power the camera.

Many thanks must go to Joe Zajac who keeps watch over our remote observatory and has saved the day more times than can be mentioned. Al Sliski and his sons, David and Aaron, also deserve a wealth of gratitude. Over the years they have enthusiastically spent spare evenings and weekends with us at the observatory, helping to keep this project running.

William Walker, a member of the School of Engineering and Applied Sciences staff, has been much more than an administrative resource since I met him in the electronics shop during my first year at Harvard. His compassion and friendly ear I will long remember as one of Harvard's greatest assets.

A special thanks goes to Andrew Huang who introduced me to the idea, through his blog, of using an FPGA as a flash ADC. This key idea had a substantial influence on the design of the Advanced All-sky Camera. Mr. Huang's other writings (<http://www.bunniestudios.com>) have also been a source of inspiration and enlightenment.

To Laura Tully, thank you for sharing in all my thoughts and aspirations, and filling each day with a special dose of awesome. Finally, thanks to my family, Audrey, Charles, April, and Clinton, for their financial and emotional support. Without them, I would be nowhere.

*For Laura.*

# Introduction

The subject of this dissertation is the design, construction, and operation of a one-of-a-kind instrument in pursuit of a bio-astronomical goal, the discovery of life on other worlds. Though the goal might at first seem unorthodox or far-out, it is in fact entirely conventional, and is a discovery hotly pursued by many professional planet-hunting astronomers and robotic spacecraft engineers, as will be explained shortly. A discovery of such significance does not come easily and will probably employ the efforts of many more generations of astronomers and engineers. My contribution to the effort, included in these pages, required solving substantial engineering challenges. As the thesis has been produced for partial fulfillment of the degree of doctor of philosophy in applied physics from the Harvard School of Engineering and Applied Sciences, much space has been devoted to a detailed technical description of the detection and processing system itself. The secondary focus is on one specific search for interstellar transmissions from technological civilizations within the Galaxy: a survey of the Northern sky for non-anthropogenic artificial optical pulses. The survey, conducted using the Harvard/Planetary Society's 1.8 m Optical SETI Telescope at Oak Ridge Observatory in Harvard, MA, has been on-going since April, 2004. The original camera for this system, the All-sky Camera (AsCam), uses 32 custom integrated circuits (called PulseNets) to record the waveforms of any strong coincident pulses received from 512 pairs of light detectors. In 1998, when the PulseNet design effort was conceived, a full custom integrated circuit seemed to be the only way to accomplish the high-speed data conversion and pulse processing task, for so many detectors, at reasonable cost, power, and density. After a few years of operating the survey, it was obvious that more capability was needed than PulseNet could provide. Eventually I developed a way in which a more advanced and flexible PulseNet could be built using commercially available electronics, i.e. without having

to go through a long and failure-prone custom integrated circuit design process. The end product of my re-design, PulseNet-V, was installed into the all-sky camera, now called the Advanced All-sky Camera (AdvCam), in August, 2012 and is currently in operation at Oak Ridge. The elegance of the PulseNet-V design is that the analog-to-digital conversion of the light detector signals and the processing of those signals can be handled by field programmable gate arrays (FPGAs), highly flexible integrated circuit, without the need for external analog-to-digital converters (ADCs). The differential input pairs of the FPGAs can be combined to create flash ADCs, allowing high-speed, low resolution conversion en-masse for an FPGA with many I/O pairs. The re-configurable digital logic resources on the FPGA provide unlimited possibilities for pulse processing, waveform acquisition, and triggering after the detector signals have entered the digital domain. Using PulseNet-V, the Advanced All-sky Camera is able to search for nanosecond pulsed optical sources more effectively than ever before. Its design, implementation, and performance is detailed herein.

## Outline

We begin with relevant background information including a discussion of the plausibility of the pulsed optical technique, the feasibility of transmitting and receiving in the optical band through the interstellar medium (ISM), and noise sources which must be considered. The all-sky survey and the drawbacks of its ASIC-based camera system are explained in [Chapter 2](#). [Chapter 3](#) introduces the PulseNet-V, its samplers, data acquisition and triggering circuitry, processor architecture, and software features. [Chapter 4](#) describes the operation of the All-sky observatory and the Advanced All-sky Camera. Test results and characterizations of PulseNet-V and the Advanced All-sky Camera are shown in [Chapter 5](#) along with the interpretation of the initial observations using the full Advanced All-sky System.

Chapter 1: Background

Chapter 2: All-Sky Optical SETI

Chapter 3: PulseNet-V

Chapter 4: Advanced All-Sky Camera

Chapter 5: Advanced All-Sky – Testing and Observations

# Chapter 1

## Background

### 1.1 “Is Anybody Out There?”

Are humans the only intelligent life in the cosmos? This is a fundamental question about the nature of our universe. As far as we know, humans are unique. But our constituents are not. Forged in the stellar furnaces of dying stars and broadcast throughout the galaxy, the atoms of our bodies are identical to the atoms we find in the interstellar medium. Humans, plants, animals, and most of everything we see, is all star stuff [55]. The same stellar material is found scattered through space forming basic organic molecules so common to terrestrial life. The Earth, the Sun, and even the Milky Way, we know, are not unique in the universe. The process by which we evolved is not predicated on the location in which it occurred, amidst the thin veneer on top of a blue marble, the third planet orbiting a middle aged yellow star in a rural dust lane of a common barred-spiral galaxy. The ingredients for life, the substrates, the processes, and the time needed to grow thinking beings exist throughout celestial space. What, then, is the reason to assume that life exists nowhere else but on Earth, and that humans are the only living thing able to look into a dark, seemingly empty abyss, and say “Hello”? The universe is unimaginably vast, and one has to accept the possible existence of other intelligent civilizations, capable of communication, evolving and inhabiting a planetary body just as humans have done. If we choose to answer the question “Is anybody out there?”, how should we search for intelligent civilizations given the incredible timescales and distances inherent to the universe? How can we attempt to

discover, from our terrestrial outpost, evidence of life?

### 1.1.1 Search Methods

Past generations have suggested ways to communicate with our possible celestial neighbors which sound quaint, even dubious, by today's standards. A proposal emerged in the 1820's to create a visual representation of the Pythagorean theorem in the Siberian forests large enough to be seen from the moon or Mars. Vast strips of pine trees were to be used to form the borders of a right triangle, and fields of wheat fill the interior of the triangle and exterior squares<sup>1</sup>. Austrian astronomer Joseph von Littrow (1781–1840) imagined a scheme to dig circular trenches in the Sahara, fill with water topped with kerosene, and set on fire when Mars was close to the Earth [30]. A mathematician, the German Carl Friedrich Gauss (1777–1855), had an interest in using a heliotrope, a surveying instrument of his invention, with one hundred 16ft<sup>2</sup> mirrors to signal the inhabitants of the moon, making “a discovery even greater than that of America” [19]. Contemporary scientists are still looking for ways to discover extraterrestrial life. The modern methods generally fall into one of three categories:

1. *Direct Sensing* Examining the surfaces of planets and other rocky bodies in the solar system for biological activity by receiving material in the form of meteorites or by sending robotic, and eventually human, spacecraft to explore the bodies;
2. *Planet Hunting* Identifying extra-solar planets that have environmental conditions known to produce biological lifeforms that can later be tested for bio-signatures indicative of life;
3. *Technological Search* Attempting the discovery of the technological indications of a civilization, usually in the form of intentionally or unintentionally sent electromagnetic communications.

Governmental aerospace organizations have the available resources to engage in the first type of search. The National Aeronautics and Space Administration (NASA) has been especially

---

<sup>1</sup>The attribution of the proposal is sometimes given to Gauss, but this has been called into question by Crowe [19].



active in use of the direct sensing method. In 1976, NASA landed two Viking space probes on Mars to take high resolution pictures of the surface, analyze the composition of the atmosphere, and specifically test for gaseous emissions from heated martian soil to detect the presence of microbes. New missions searching for life on Mars continue to this day with the Mars Curiosity rover seeking out environments on the surface where life exists or has existed in the past. Planetary material, that was ejected from the martian surface and landed on the Earth as meteorites, has been studied for signs of biogenic activity [45]. Numerous future missions are planned by NASA and others. For example, the European Space Agency (ESA) is planning an outer planet flagship mission to the Galilean satellites of Jupiter with two of the stated science goals being “Explore Europa to investigate its habitability” and “Characterize Ganymede as a planetary object including its potential habitability” [29]. Billions of dollars are spent on these missions. They present the most direct way to investigate nearby planets for evidence of microbial life.

Professional astronomers are advancing the techniques in method two. At least 837 extra-solar planets have been confirmed, most in the last decade. With each discovery, details of the planet are assessed. The most exciting discoveries are of “Earth-like” planets with mass, orbital distance from its host star, radii, and density similar to the Earth. These planets may be more likely to harbor life. To confirm whether one of the discovered planets hosts a biological ecosystem would require observation of some kind of indicator, or combination of indicators, that can only exist on living planets, a bio-signature. There is ample debate over what constitutes a bio-signature. Possibilities include the presence of combinations of atmospheric gases like methane and oxygen, light polarization from a planet’s surface due to molecular chirality [42], planetary features due to photosynthesis [57], or characteristic seasonal changes to global biomass. With some exceptions, details of exoplanets’ atmospheres and surfaces are currently beyond modern day capabilities<sup>2</sup> The idea of using bio-signatures to make an indirect discovery of life on an exoplanet may be workable in the future, but today it is still in the realm of speculation.

---

<sup>2</sup>Bowler et al. [7] was able to detect methane absorption and infer the very dusty nature of the atmosphere of HR8799b, a 4-7 Jupiter mass planet orbiting 68 AU from its host star, which is  $\sim 40$  pc away. The technique is only practical for large planets in distant orbits. Berta et al. [5] reports the flat atmospheric transmission spectrum of the super-Earth GJ1214b. The observation was made possible by the extremely small radius of the M dwarf stellar host ( $0.21 R_{\odot}$ ) and the closeness of the system (13 pc).

With space probes limited to our solar system and planetary searches for bio-signatures left to future astronomers, technological searches have the advantage that they can be accomplished using existing technology and are not limited to the solar system or very close planetary systems. Observing the second-order effects of microbial life on a small planet next to a bright star is a highly attenuated signal, making for a controversial indirect discovery. A technological civilization that is transmitting in the electromagnetic spectrum might provide a much stronger signal that represents direct, incontrovertible proof of extraterrestrial life.

### 1.1.2 Galactic Census

The galaxy is a vast expanse so large that it challenges our perception of time and space. The distances involved cannot be compared to anything we normally experience on Earth. To travel to even the nearest star, Proxima Centauri, would require some tens of thousands of years, much longer than a human lifetime, and perhaps longer than the lifetime of our entire modern civilization<sup>3</sup>. Even the light from Proxima Centauri takes 4.24 years to arrive at the Earth, meaning we are seeing it as it was four years past. This is often how distances in the galaxy are measured, in light-years (ly). The galaxy is composed of three main structures: the disk, the halo, and the central bulge. The disk is  $\sim 100,000$  ly across,  $\sim 1,000$  ly thick, and contains the galaxy's spiral arms, hydrogen and molecular clouds, and stars of similar metallicity to the Sun but with a wide range of ages and sizes. The spherical halo extends somewhat beyond the radius of the disk and contains metal-poor, high velocity, older stars. Globular clusters, spherical collections of hundreds to thousands of stars, very tightly bound by gravity, are a main feature of the halo. The central region of the galaxy, the bulge, is a roughly spherical region 10–20 kly in radius with  $1/6$  to  $1/3$  the mass of the disk. It is dense with mostly older, but metal rich stars. At the nucleus of the galaxy is a massive black hole surrounded by thousands of old, red stars, but there is also a disk of very young massive Wolf-Rayet stars. The galaxy is filled by a weak magnetic field that bends the path of cosmic rays – high energy charged particles that stream throughout the galaxy but whose

---

<sup>3</sup>Though we certainly hope not!

origin is unknown<sup>4</sup>. Another even more mysterious yet pervasive constituent of the galaxy is dark matter. Galactic rotation curves indicate the existence of this as-yet-unknown source of mass that has, so far, eluded discovery. The Sun lies in the disk on the inner rim of the Orion-Cygnus arm, in a diffuse interstellar cloud called the Local Bubble,  $\sim 27,000$  ly from the galactic center.

## The Drake Equation

Given the scale of the galaxy, does it even make sense to assume that contact with a neighbor is possible? Frank Drake proposed an equation to spur discussion of the problem. His equation attempts to estimate and place a bound on the average number of communicating civilizations in the galaxy, and therefore, the average distance between them. It collects the factors that we might need to know about in order to discover life in space.

$$N_{\text{civ}} = R^* \cdot f_p \cdot n_e \cdot f_l \cdot f_i \cdot f_c \cdot L \quad (\text{Drake Equation}) \quad (1.1)$$

Where,

$R^*$  = The rate of formation of stars suitable for the development of intelligent life,

$f_p$  = The fraction of those stars with planetary systems,

$n_e$  = The number of planets, per solar system, with an environment suitable for life,

$f_l$  = The fraction of suitable planets on which life actually appears,

$f_i$  = The fraction of life bearing planets on which intelligent life emerges,

$f_c$  = The fraction of civilizations that develop a technology that releases detectable signs of their existence into space, and

$L$  = The length of time such civilizations release detectable signals into space.

---

<sup>4</sup>Lower energy cosmic rays can originate in supernovae blast waves but higher energy cosmic ray origins are more speculative and include active galactic nuclei, quasars, gamma ray bursts, or new physics (dark matter annihilation [6], strongly-interacting neutrinos [24], topological defects in the universe [49]).

## Planetary Findings

When Frank Drake proposed his equation in 1961, the value of  $f_p$ , the term that represents the fraction of stars having planets, could only be guessed. Numerous methods for discovering extrasolar planets (exoplanets) have been developed since then. The three most productive techniques are stellar transits, Doppler spectroscopy, and gravitational microlensing.

In the transit method, a planet passing in front of its star causes a small decrease in the apparent brightness of the star that can be detected by very accurate photometric measurements. The size of the planet can be determined from the details of the light curve and, with many brightness measurements over time, periodicities in the apparent brightness will indicate the planet's orbital period. For this method to work, the planet's orbital plane must be oriented such that the planet occludes a piece of the star's disk. Large planets are more likely to be found using the transit method since more of the star will be occluded during a transit, resulting in a bigger dip in brightness. Planets with small orbital distance will also be preferentially observed since larger orbital inclination angle will still result in an occultation of the star's disk. Requirements for orbital distance and inclination means that many stars must be observed before one is found whose planet has the right parameters for detection. The Kepler mission is one such telescope using the transit method. Launched in March 2009, Kepler is a space-based telescope focused on a roughly  $11^\circ \times 11^\circ$  field in which brightness measurements are taken on  $\sim 150,000$  stars every 30 minutes, looking for planet transit events. As of 19 February, 2013, Kepler has 116 confirmed planet discoveries and 2,717 candidate planets waiting to be confirmed [\[47\]](#).

Doppler spectroscopy uses a star's spectral lines to measure the radial velocity of the star. An orbiting planet will exert a gravitational tug on the star, causing it to wobble back and forth. This indirect indication of the planet's effect on its parent star is often used to confirm planet candidates found using the transit method. From the radial velocity measurements, a minimum value of the planet's mass can be determined. The planet's true mass and density can be calculated with both doppler and transit measurements of a candidate planet's star. Spectrometers like HiRES on the W.M. Keck Observatory in Hawaii and ESO's HARPS at La Silla Observatory in Chile have confirmed about two-thirds of all identified exoplanets.

Howard et al. [40] report that extrapolation of radial velocity data obtained using the HiRES spectrometer predicts 14% of sun-like stars host Earth mass planets ( $1 M_{\oplus}$ – $3 M_{\oplus}$ ).

The gravitational microlensing method makes use of an effect whereby the gravitational field of a foreground star lenses the light from a distant background star. The lensing can be seen only when the background star, foreground star, and the Earth are very closely aligned. The effect will typically last weeks or days. If the foreground star has a planet, the planet’s gravitational field will affect lensing of the background star, allowing the existence of the planet to be detected. The probability of the precise alignment for a planet to be detected is very low, so detections are made by continuously monitoring many stars for lensing events. The center of the galaxy has the highest density of stars and is normally the target for microlensing observations. As of February 19, 2013, gravitational microlensing accounts for 17 confirmed exoplanet discoveries. A disadvantage of this planet finding method is that the lens stars are typically very far away (kiloparsecs) so follow-up observations using Doppler spectroscopy or stellar transits are normally not possible. On the other hand, gravitation microlensing can detect planets that are much farther away from their bound star than the other methods. Cassan et al. [11] issued a report on the abundance of planets in the galaxy using statistical analysis of microlensing data. For planets between 0.5 AU and 10 AU, they calculate that 17% of stars host Jupiter mass planets ( $0.3$ – $10 M_J$ , mass of Jupiter  $M_J = 318 M_{\oplus}$ ), 52% of stars host Neptune mass planets ( $10$ – $30 M_{\oplus}$ ), and 62% of stars host super-Earths ( $5$ – $10 M_{\oplus}$ ). Extrapolating to Earth mass planets seems to point to an even higher abundance. Cassan et al. [11] further conclude that planets *outnumber* stars in the galaxy.

Beyond advances in extrasolar planet discoveries, Strigari et al. [59] present an analysis claiming there may be up to  $10^5$  compact gravitationally unbound objects between  $10^{-8}$ – $10^{-2} M_{\odot}$  (mass of the Sun =  $M_{\odot}$ ) for every star in the galaxy. These objects are termed “nomads” as they are free to wander the galaxy. Though they don’t have a parent star to provide light and warmth, some may have thick atmospheres and enough internal heating to support a thriving microbial world [1]. With  $\sim 400$  billion stars in the galaxy, an average of more than one planet per star, and potentially  $4 \times 10^{16}$  other wandering compact objects, the available real estate for extraterrestrial life is vast.

## Communicating Civilization Estimates

In addition to the estimates of  $f_p$ , the fraction of stars with planetary systems, values of  $R^*$  have a fair amount of quantitative backing. Recent investigations of star forming regions using the Spitzer Space Telescope, a space-based infrared observatory, find that the total star formation rate in the galactic plane is  $0.68\text{--}1.45 M_\odot\cdot\text{yr}^{-1}$  [54]. Diehl et al. [20] report that measurements of gamma rays from radioactive  $^{26}\text{Al}$ , which provide a “snapshot” of nucleosynthesis in the Galaxy, indicate a star formation rate of  $4.0 M_\odot\cdot\text{yr}^{-1}$  and corresponding stellar production rate of  $\sim 7.5$  stars per year. The terms of the Drake equation having to do with the abundance and development of life,  $f_l$ ,  $f_i$ , and  $f_c$ , are somewhat more speculative. The analysis by Glade et al. [27] in 2012 uses 0.5, 0.2, and 0.2 respectively. By combining all but the final terms into  $R_{\text{com}}$ , the rate that communicative civilizations arise, we can write a simpler equation  $N = R_{\text{com}}L$ . Estimates for the number of civilizations have a wide spread because the result is based on two very uncertain numbers. The average lifetime of civilizations is an important number, not only because of its existential implications, but because if civilizations are long lived, then the nearest one might be close by, within communicative range. If civilizations are short lived, or do not arise often, then the nearest communicative civilization may be very far away, and there may not be any temporal overlap with our human civilization [8].

One last point to keep in mind is that the number of communicating civilizations predicted by the Drake equation is only an estimate of the average. For the last few terms, accurate values can really only be acquired by sampling habitable planets in many galaxies and averaging how often life arose, evolved, and produced an intelligent communicating species. If that were even possible, it spoils the game as finding even one intelligent species *is the whole purpose*. Having an exact expected value for the number of intelligent communicating civilizations in our galaxy is somewhat beside the point. We want to know, specifically, if there are *any* communicative civilizations in our galaxy. An average of all galaxies would not provide that answer. The only way to find the answer is through exploration of our galaxy through space missions, astronomical observations, or conducting SETI surveys.

Table 1.1: Drake Equation Estimates

Scenario	$R_{\text{com}}(\text{yr}^{-1})$	L (yr)	$N_{\text{civ}}$	Distance (ly)
Optimist	1	$10^8$	$10^8$	$\approx 100$
...	1	$10^4$	$10^4$	$\approx 2,500$
...	$10^{-2}$	$10^4$	$10^2$	$\approx 10,000$
...	$10^{-2}$	$10^6$	$10^4$	$\approx 2,500$
...	$10^{-4}$	$10^6$	$10^2$	$\approx 10,000$
Pessimist	$10^{-4}$	$10^4$	$10^{-2}$	$\approx 10^7$

Note: Table adapted from Ekers [23].

### 1.1.3 What are we looking for?

Short of an alien landing a spaceship and announcing its presence, what type of evidence do we need to constitute discovery of extraterrestrial intelligence? Intelligence is not directly detectable, per se, only the consequences of the intelligence can be observed. The effects of an intelligent civilizations actions or its technologies' effects are observables that can be quantified and understood as evidence. The night lights of a metropolis, fouling of the planet's atmosphere with an industrial chemical, or by-products of spacecrafts' propulsion engines are examples of technological indicators.

How can the evidence of technology be acquired? Obtaining a physical artifact from the civilization would suffice. This might involve the artifact being captured by the Earth's gravity and falling to the surface, or being captured by an orbiting spacecraft, or being discovered buried on the surface of Earth, the moon, or even Mars. While the possibility of discovering an artifact exists and we should be open to it, the majority of what we know about the universe comes to us in the form of electromagnetic radiation. An intentional or unintentional signal or communication that constitutes evidence of technology and intelligence could take the form of any elementary particle, known or unknown. While we think of photons as being the most efficient particle for communication, others may exist. An ideal particle for signaling should have the following properties [48]:

1. The energy per quantum should be minimized, other things being equal,
2. The velocity should be as high as possible,
3. The particles should be easy to generate, launch, and capture, and

4. The particles should not be appreciably absorbed or deflected by the interstellar medium.

For a signal to be detected and to be recognized as artificial:

5. The number of particles received must significantly exceed the background, and
6. The signal must exhibit some non-natural property.

Charged particles, like protons and electrons, interact and are absorbed by other matter in the interstellar medium and are deflected by magnetic fields unless they are of very high energy, in opposition with property 1. Uncharged particles, if they have mass, neutrons being one example, are less desirable compared to photons as they will have a lower velocity (photons always travel at the maximum, the speed of light), or if they are created with a very high kinetic energy, the energy per quantum will be large, violating property 1 again. Neutrinos are neutral, have a very small mass, and can be formed in beams, but detection is difficult due to their extremely low interaction probability. Gravitons violate property 3 for being difficult to generate, detect, and direct. Our experience with photons, by contrast, is that they are easy to transmit and detect, they carry much of the information that we know about the universe, and humans have developed many tools and resources for detecting electromagnetic waves. We conclude that the photon is the best of the known fundamental particle that satisfies the above requirements for interstellar signaling and efforts for detecting intelligent life should concentrate on the electromagnetic spectrum.

#### **1.1.4 The Spectrum**

Detectable photons in the electromagnetic spectrum span 24+ orders of magnitude in energy, from the extreme low frequency (ELF) radio waves to the highest energy gamma rays of  $10^{12}$  eV or more. Within certain energy ranges, photons seem to interact with matter in similar ways, so the spectrum is separated into bands.

Observational astronomy is occurring in all these bands so any one of them could be conceivably used for a potential search for interstellar communications. Historically, the radio band has been favored. Cocconi and Morrison are regarded as being the first to analyze



Table 1.2: Electromagnetic Bands

Band	wavelength	frequency	energy
Radio waves	33 km–1000 $\mu\text{m}$	9 kHz–300 GHz	40 neV–10 meV
Microwave radiation	10,000 $\mu\text{m}$ –1000 $\mu\text{m}$	30 GHz–300 GHz	0.01 meV–1 meV
Terahertz radiation	1000 $\mu\text{m}$ –100 $\mu\text{m}$	300 GHz–3 THz	1 meV–10 meV
Infrared radiation	1000 $\mu\text{m}$ –0.74 $\mu\text{m}$	300 GHz–0.4 PHz	1 meV–1.7 eV
Visible radiation	740 nm–350 nm	0.4 PHz–0.86 PHz	1.7 eV–3.5 eV
Ultraviolet radiation	350 nm–10 nm	0.4 PHz–30 PHz	1.7 eV–100 eV
X-ray radiation	10 nm–0.01 nm	30 PHz–30 EHz	100 eV–100 keV
Gamma radiation	<0.01 nm	>30 EHz	>100 keV

objectively the choice of optimum wavelengths, and to propose a search for these interstellar communications [14] in 1959. They suggested the neutral hydrogen radio emission line (1,420 Mc./s) was a frequency every technological civilization in the galaxy must know. Since then, many more astronomical radio emission lines have been discovered, reducing the appeal of a special frequency. Later studies by Cordes and Lazio [17] showed that interstellar scintillation can confuse detection of microwave carriers and hamper decoding of any information contained within it. Cocconi and Morrison considered the possibility of using optical or gamma ray wavelengths, but dismissed them as requiring complicated techniques and requiring too much power. Only two years after Cocconi and Morrison’s paper, Schwartz and Townes [56] recognized the potential of the laser, suggesting that it was only an accident of history that caused its development to come 30 years late, and perhaps another civilization reversed our history, becoming much more advanced in laser technology before advancing short-wave radio techniques. Even with this historical disadvantage, on Earth at least, the laser has transformed terrestrial telecommunications, enabling the high-speed digital fiber-optic networks which form the backbone of our communications infrastructure. Laser development has seen exponential growth in recent decades. There are now continuous wave megawatt lasers<sup>5</sup> [3], lasers that can nearly achieve inertial confinement fusion with nanosecond megajoule pulses [46], and lasers able to explore atomic timescales with attosecond pulses [28]. These developments call into question the early dismissal of the optical band.

In order to decide which band is “best”, radio or optical, Townes<sup>6</sup> [61] questioned what

---

<sup>5</sup>Used for, of course, shooting down satellites in orbit [58].

<sup>6</sup>Charles Hard Townes, of Nobel prize winning, maser and laser inventing, and sturdy middle-name-having fame.

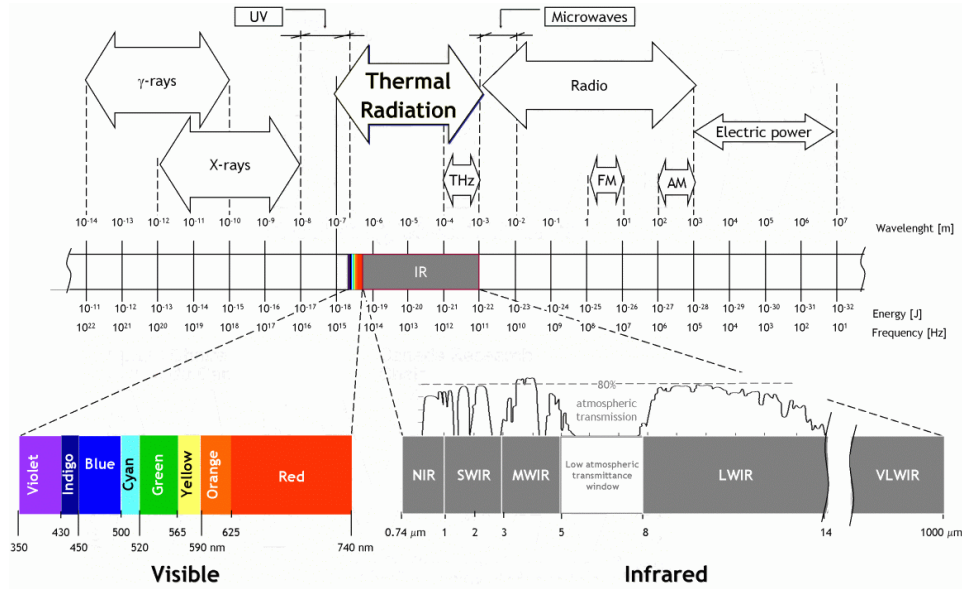


Figure 1.1: Electromagnetic Spectrum [41]

should be the metric for comparison. How are we to know what factors are important? Is it most important for the signal to be easy to recognize or exceptionally simple to receive? Total broadcast power or energy consumed by the transmitter could provide a cost function to be minimized, but can a long-lived civilization be expected to consider power a limited resource? A scarcity of a particularly important resource could certainly restrict the options, but resource availability may be very different on other planets and in other parts of the galaxy. A complex system might be limited by costs associated with building materials, construction, and design. The size of the transmitter or receiver might need to be minimized for space flight. To perform in extreme weather conditions, such as wind, rain, sand, or ice storms, a system may need to be as rugged as possible. While atmospheric transmission is an issue for terrestrial systems, it is completely bypassed for operation in space or on a small moon.

If information is to be relayed in a signal, a critical parameter for a communication system that cannot be ignored is the delivered signal-to-noise ratio. On the sole basis of signal-to-noise for equal broadcast power, Townes [61] concludes that, using reasonable assumptions, optical/infrared systems using photon detection can be as good as, and possibly much better than, microwave systems using linear detection. The directionality achievable at shorter

wavelengths with optical telescopes tends to make up for the additional energy needed to create the photons.

The take-home message is that both the radio/microwave and optical/infrared regions of the spectrum are viable spaces for interstellar communication, and an incidental consideration could cause one or the other to be seen as more favorable. Since explorations of the radio bands have been underway for over fifty years without success, let's consider the type of signal which might reasonably be expected in the optical band.

### 1.1.5 Modulation

Should we be looking for short pulses of light or some kind of spectral lines? Howard, Horowitz, et al. [39] answered this question best and most succinctly. Operating with very narrow linewidths is part-and-parcel of radio frequency techniques. For radio frequency (RF) oscillators, bandwidths are routinely made pure to a part in  $10^9$ , and detection of such a pure frequency can be accomplished with a simple power-in-band estimate without assuming anything about the modulation of the waveform. Out-of-band RF noise can be filtered with a range of high quality filters. Coherent detection is routine; signals can easily be mixed with a local oscillator down to baseband to give quadrature output. Nature also seems to be amenable to pure RF tones. Narrow linewidth signals are barely affected by the interstellar medium. For most lines of sight through the galaxy within 100 kpc, frequencies around 1 GHz are broadened  $<1$  mHz [17]. In contrast, as seen in observations of pulsars, short RF pulses in time get stretched significantly by travel through the galaxy. Due to the dispersion, a pulsed RF communication link would have a limited bandwidth, so broadband RF pulses would be less useful for interstellar communication.

Recovery of a narrow frequency in the optical range, however, must use complicated optical heterodyning techniques to mix down to a microwave intermediate frequency (IF). Coherent detection, though common at radio frequencies, is subject to a quantum limit precisely because it simultaneously measures amplitude and phase. The added noise is normally not significant compared to  $k_B T$  for RF. At optical frequencies, where  $h\nu \gg k_B T$ , the Bose-Einstein distribution dictates that the electromagnetic modes are mostly empty. Photon arrivals in different modes are statistically independent, so individual photons can

be counted [43]. Detection at optical frequencies using photon counters is not subject to the  $h\nu$  of quantum noise because the counting process only measures the number of photons in a wave, but not the phase of that wave. The noise associated with detection then is proportional to the square root of the number of counted photons. Whereas a carrier wave is ripe for detection at radio frequencies, short pulses of photons are efficiently detected at optical frequencies. Doppler broadening of an optical carrier due to the Earth’s rotation (0.5 km/s) is of the order 1 GHz whereas the broadening is only  $\sim 2$  kHz for a 1 GHz RF carrier. This is simply due to the optical frequencies being so much higher than radio frequencies. Not only that, the galaxy has changed her mind too, allowing nanosecond optical pulses to pass with very little dispersion in the interstellar medium [23]. Very short pulses are easy to produce with lasers (several techniques are available: Q-switching, pulse pumping, and mode-locking) and achievable even with megajoule output power [46].

A *pulsed* communication system or beacon, then, seems more favorable than a modulated carrier for optical interstellar signaling. Still, the fact that coherent optical systems are so widely used for terrestrial high-bandwidth fiber-optic telecommunications networks should leave open the possibility of searching for CW narrow-band optical features. Whenever possible, astronomical optical spectroscopic observations should be on the look-out for artificial laser lines, as in the study by Reines and Marcy [52].

## 1.2 Pulsed Optical SETI

To determine if a pulsed optical communication system is feasible, we shall explore some of the relevant issues in more detail. Let’s consider how transmission and reception might work, the communication range that can be reasonably expected, and the role the interstellar medium plays.

### 1.2.1 Scheme

From the transmitter’s perspective, an efficient scheme would be to observe and select nearby stars for targets with a high likelihood of harboring life. Powerful broadcasts could then be sent to the resultant list of candidate stars. Presumably an advanced technologi-

cal civilization would have commissioned a detailed study of the galaxy before attempting interplanetary communication and would have knowledge of planets in their stellar neighborhood, and further, which of those planets are in habitable zones. With fast steering optics, a beacon pulse could be transmitted sequentially to each of a list of target stars. For example, with a target list of 1000 nearby stars with habitable zone planets, a transmitter which can slew and achieve acceptable pointing accuracy in 100 ms can send a beacon pulse to each star every  $\sim 100$  seconds. The galaxy is a kinetic landscape with radial and proper motions unique to every star so care must be taken when aiming in order to accurately hit a moving target from light years away. A long list of targets reduces the pulse repetition rate for each star, and potentially the chances of reception by any one target. However, an abundance of good targets would be an opportune complication as more habitable planets means a higher probability that at least one of them will play host to an intelligent civilization (see § 1.1.2 for details of galactic planetary abundance). The beacon message could be one or more short pulses from a high powered laser mated to a large optical telescope.

At the reception end, complicated pointing procedures are unnecessary. A telescope pointing directly at the apparent position of the transmitter's host star would receive the transmission. The photons from the laser pulse that are unscattered by the ISM arrive at the receiver with the same pulse width as when they were transmitted. In order for the received laser pulse to be noticed, its intensity must exceed the stellar background during the pulse period. As a practical matter, the minimum number of photons collected from the pulse must be a few dozen to account for reflection losses and quantum efficiency of the detectors. With these minimums met, if a casual observer could perceive the incoming pulse at short timescales, he/she would see many photons arrive all at once as opposed to the steady but random arrival of single stellar and night sky background photons, i.e. the star would appear orders of magnitude brighter during the pulse arrival window. A pair of photomultiplier tubes and a threshold circuit are all that is needed to detect the pulse. Filters are unnecessary and undesirable when searching for a signal as the transmission wavelengths is unknown; broadband detectors are sensitive to a pulse of any wavelength within their passband.

How feasible is it to send a laser pulse over interstellar distances? In terms of technological constraints, we can draw conclusions based on what we know is possible given the current

state of telescope and laser development. Ground based optical telescopes have attained apertures of 10 m (Keck and Gran Telescopio Canarias) and 40 m class telescopes are being planned [26]. With sufficient effort and resources, we see no reason why this could not be scaled to at least 100 m apertures. Space-based telescopes diameters are less than an order of magnitude smaller (JWST planned for  $\sim 6.6$  m [25]) but are not constrained by ultraviolet and infrared atmospheric absorption, so very long and short optical wavelengths should be considered. For an idea of the scale of possible high power lasers, the National Ignition Facility has achieved 2 MJ, 4 ns (500 TW) pulses at 1053 nm (converted to 527 nm and 351 nm) [46]. The construction is parallelizable and the efficiency of the NIF is low (using 10% efficient flash lamps) so future lasers could conceivably reach 100 MJ or more. Engineering a ground-based telescope to control mirror heating and to account for air turbulences while maintaining a diffraction limited focus with such high energy density pulses is no doubt a major challenge, but adaptive optics provides hope that this complication could be overcome.

The possibility of beaming a pulse to another star through the interstellar medium will now be considered. We will show, assuming only current levels of technology, that pulsed optical communication over many parsecs (pc) (1 pc=3.26 ly) is feasible.

## Telescope Beamwidth and Directivity

To make an interstellar communication link efficient, the energy radiated by the transmitter should be tightly focused at the target rather than wasted by being lost into space. Telescopes are able to create very tight beams using precision optics. The beam divergence is physically limited by diffraction, but practically limited by the optical and mechanical precision of the telescope, and by atmospheric turbulence. For a uniformly illuminated circular aperture, the far-field beam intensity at angle  $\theta$  is given by the Airy disk diffraction pattern. For small angles, the full width at half power beam size is approximately

$$\theta_{\text{FWHP}} \approx 1.05 \frac{\lambda}{D_t}. \quad (1.2)$$

A small amount of power is lost to the sidelobes for a uniformly illuminated aperture. The fraction contained within the beam is given by

$$f(\theta) = 1 - J_0^2\left(\frac{\pi D_t}{\lambda} \sin \theta\right) - J_1^2\left(\frac{\pi D_t}{\lambda} \sin \theta\right) \quad (1.3)$$

where  $J_0$  and  $J_1$  are the Bessel functions. For the FWHP beam, the fraction contained  $f_{\text{FWHP}}$  is 82.9%. The solid angle for the beam is

$$\Omega = \frac{\pi}{4} \theta_{\text{FWHP}}^2 \quad (1.4)$$

and the directivity  $G$  compared to an isotropic radiator is the ratio of the isotropic solid angle  $\Omega_{\text{iso}}$  to the transmitter's solid angle  $\Omega_{\text{t}}$ .

$$G = \frac{\Omega_{\text{iso}}}{\Omega_{\text{t}}} = \frac{16}{\theta_{\text{FWHP}}^2} \approx \frac{16D_{\text{t}}^2}{\lambda^2} \quad (1.5)$$

### Inverse-square Loss

The power radiated from an isotropic transmitter becomes diluted as the spherical wave spreads out as it travels away from its source. At range  $R$  from the transmitter, the area covered by radiation is  $4\pi R^2$  and the intensity is  $\frac{P_{\text{isotropic}}}{4\pi R^2}$ . The same inverse-square falloff holds for a directed radiator of power  $P_{\text{t}}$ , directivity  $G$ , and width  $\theta_{\text{b}}$ ; the beam power spreads  $\propto R^{-2}$  and the beam diameter spreads to  $D_{\text{b}} = R\theta_{\text{b}}$ . A receiving antenna (telescope) at range  $R$  of diameter  $D_{\text{r}}$  collects a power equal to

$$P_{\text{r}}(R) = \frac{GP_{\text{t}}\pi D_{\text{r}}^2}{4\pi R^2} \quad (1.6)$$

if it is within the beam diameter  $D_{\text{b}}$ . It is advantageous to confine the beam to as small a diameter as possible, as long as there is sufficient pointing precision and the illuminated area at the target star includes the habitable zone. A transmitting civilization would presumably have undertaken a galactic census to find nearby habitable planets or star systems before embarking on a transmitting campaign, so target coordinates may be known to better than 1 AU. We will only assume knowledge of general habitable zones such that the beam diameter at the target should be  $>2$  AU. To get a sense of scale, based on the diffraction limit, a 10 m (Keck-size) telescope could maintain a 10 AU beam diameter out to 1 kpc for wavelengths  $\leq 500$  nm.

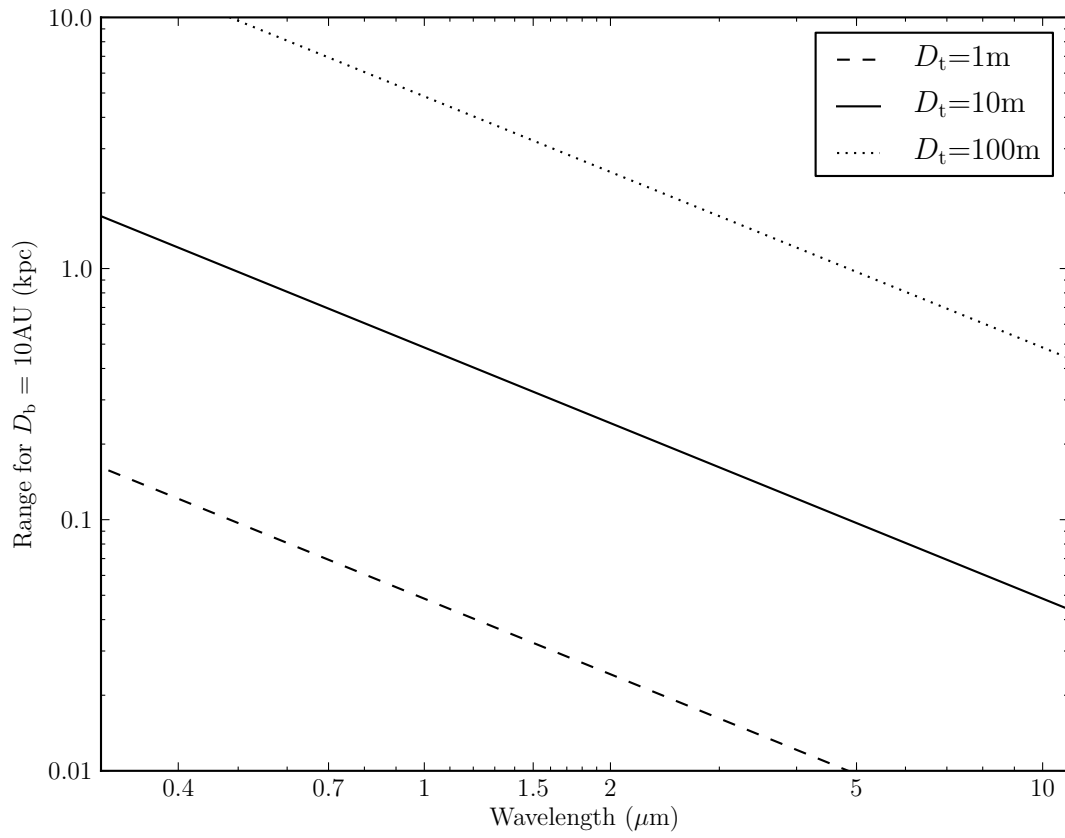


Figure 1.2: The range for which a diffraction limited telescope illuminates a 10 AU spot size. The beam diameter at the target depends on the range and telescope diameter.



## Pointing

Narrow beam forming is an advantage in terms of reducing the amount of wasted energy that gets broadcast into space, but it requires high precision for the beam steering mechanics. From a transmitter's perspective, it is not enough to simply point at a target star. Following the analysis by Howard, Horowitz, et al. [39], to illuminate a star (literally a moving target), the transmitter must point to where the star will be once the signal arrives. This requires knowledge of the target star's position ( $\theta_0$ ), range ( $R$ ), proper motion ( $\mu$ ), and radial velocity ( $\nu_r$ ). The transmitter must aim at the sky position:

$$\theta = \theta_0 + \mu \frac{2R}{c - \nu_r}. \quad (1.7)$$

The positional, proper motion, and range precision required are

$$\theta_0 \pm \tan^{-1}(D_b/2R), \quad (1.8a)$$

$$\mu \pm \frac{\tan^{-1}(D_b/2R)}{R/(c - \nu_r)}, \quad \text{and} \quad (1.8b)$$

$$R \pm \frac{D_b}{4} \cdot \frac{c - \nu_r}{\nu_t}. \quad (1.8c)$$

where  $\nu_t$  is the star's transverse velocity. Let's put some values into the equation to get a sense of the magnitude of the precision needed for the range, proper motion, and radial velocity. For a star at a range of 1000 ly, to aim a beam within 10 AU of the star requires a positional accuracy of 33 mas and a proper motion precision of  $33 \mu\text{as}\cdot\text{yr}^{-1}$ . The range accuracy depends on a star's transverse velocity and desired beam accuracy. Velocities of  $<30 \text{ km}\cdot\text{s}^{-1}$  are common for nearby stars. For a transverse velocity of  $30 \text{ km}\cdot\text{s}^{-1}$  and 10 AU beam accuracy, the range must be known to better than 0.5 ly, or 0.5% at 1000 ly. The required accuracies aren't technically unreasonable. The Hipparcos mission, run by the European Space Agency (ESA) from 1989 to 1993, cataloged over 100,000 stars to an accuracy of  $\sim 1$  mas. Its successor, Gaia, planned for 2013 to 2018, will measure the positions of over 1 billion stars ( $\sim 1\%$  of the galaxy!) at an accuracy of  $7\mu\text{as}$ - $300\mu\text{as}$  (depending on star brightness) and distances to within 1% [44, pp. 321]. Knowledge of the required targeting information is feasible with current Earth technology. A much older civilization would likely have even more advanced capabilities.

## ISM Effects

Visible and infrared light is affected by nanometer to micron-sized dust grains in the interstellar medium. For optical pulses, these grains cause light to be scattered and absorbed. The distribution of dust grains is not uniform so the magnitude of the effect depends heavily on the line of sight between two objects. Extinction is normally measured in magnitudes, calculated as

$$A(\lambda) = 2.5 \log \frac{F_0(\lambda)}{F(\lambda)} \quad (1.9)$$

where  $A(\lambda)$  is the magnitude of extinction at wavelength  $\lambda$ ,  $F_0(\lambda)$  is the flux before extinction, and  $F(\lambda)$  is the observed flux. The remaining fraction, given the total extinction  $A(\lambda)$  is

$$f_{\text{ext}}(\lambda) = 10^{-\frac{2}{5}A(\lambda)}. \quad (1.10)$$

Fluxes are measured using standardized sets of filters, called the “photometric system”, with well-defined passbands. The specific filter used for a flux or extinction measurement is designated by the letter subscript, e.g.,  $A_B$  for the magnitude of extinction in the B-band centered at 442 nm or  $A_V$  for the magnitude of extinction in the V-band centered at 540 nm. Extinction in the galactic plane is highly variable and values range from 0–2 mag·kpc<sup>−1</sup> with a reasonable “average” being  $\sim 0.7$ – $1.5$  mag·kpc<sup>−1</sup> [13]. At high galactic latitudes ( $>50^\circ$ ), extinction can be much lower, with total extinction out to 1 kpc in the range of 0.0–0.3 mag·kpc<sup>−1</sup> [32]. Shorter wavelengths generally have higher absorption than longer wavelengths, due to the size and composition of the dust grains. There are strong peak in absorption at 217 nm (graphite pi-valence orbital?), 9.7  $\mu\text{m}$  (silicate absorption MgSiO<sub>3</sub>, FeSiO<sub>3</sub>, Si-O bond stretch), and 18  $\mu\text{m}$  (O-Si-O bending mode) [21]. The amount of preferential extinction for shorter wavelengths is sometimes characterized by a single parameter  $R_V$ , the ratio of the visual band extinction and the difference between the B and V band extinction:

$$R_V \equiv \frac{A_V}{A_B - A_V}. \quad (1.11)$$

If the extinction is not wavelength dependent (gray), such as would be the case for large interstellar dust grains, then  $R_V \rightarrow \infty$ . Rayleigh scattering ( $\sim \lambda^{-4}$ ), which gives the sky its blue color, would give an  $R_V \approx 1.2$  [21]. Typical values of  $R_V$  range from  $<2$  for some high galactic latitude sightlines to 5 or 6 for dense nebulae. Cardelli et al. [10] provides the

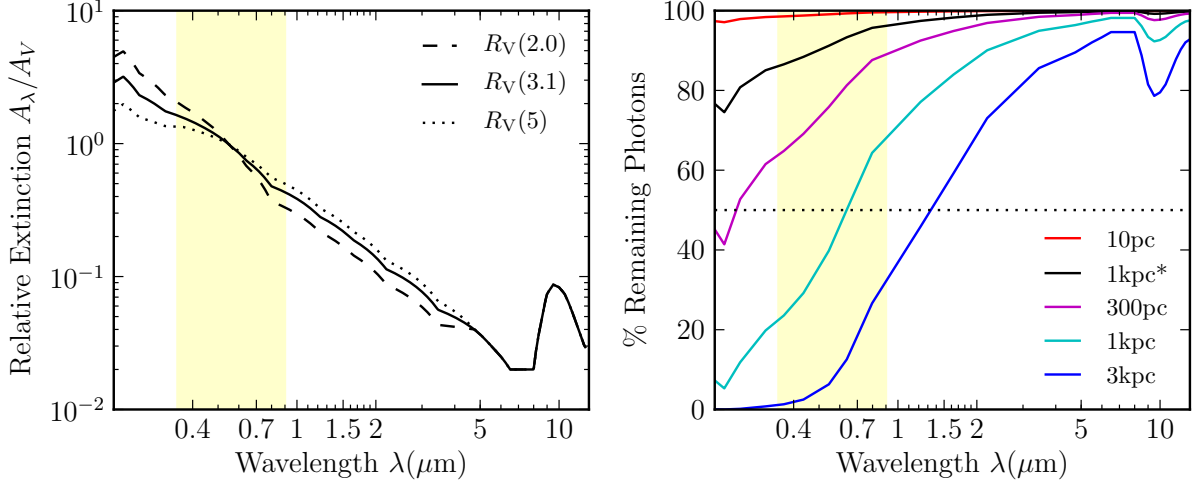


Figure 1.3: Left: The “extinction law”, relative extinction curves for  $R_V=2.0$ , 3.1, and 5. Right: Fraction remaining after traversing 10 pc, 300 pc, 1 kpc, and 3 kpc in the galactic plane. The black line (1 kpc\*) is representative of a line of sight out of the galactic plane (visual extinction of  $0.1 \text{ mag}\cdot\text{kpc}^{-1}$ ). Data from Cardelli et al. [10] and Rieke and Lebofsky [53]. Plot adapted from Howard [38].

empirically derived average “galactic extinction law”, parameterized by  $R_V$ . Figure 1.3, on the left, shows the relative extinction for three values of  $R_V$ . For the diffuse ISM, the average  $R_V$  value is considered to be 3.1. On the right side of Figure 1.3,  $R_V=3.1$  has been used to plot the extinction from 200 nm to  $12 \mu\text{m}$  at various ranges, using an average visual extinction of  $1 \text{ mag}\cdot\text{kpc}^{-1}$  to represent a sightline in the galactic plane. The starred trace (\*) indicates a visual extinction value of  $0.1 \text{ mag}\cdot\text{kpc}^{-1}$ , more indicative of an out-of-plane sightline. Out of the galactic plane, extinction can be low, even to intergalactic distances. More detailed directional extinction values are modeled by Chen et al. [13] and plotted in Figure 1.4. In-plane extinction out to 1000 pc is shown in the top of Figure 1.4 and total visual extinction at 1 kpc is plotted on the bottom.

Assuming that 50% loss would be an acceptable limit, the expected range in the optical region is about  $\sim 1 \text{ kpc}$  in the galactic plane. There seems to be a minimum around  $8 \mu\text{m}$  where the extinction is low enough to signal half way across the galaxy. If we are not restricted to the galactic disk, extinction is much lower and optical frequencies would suffice

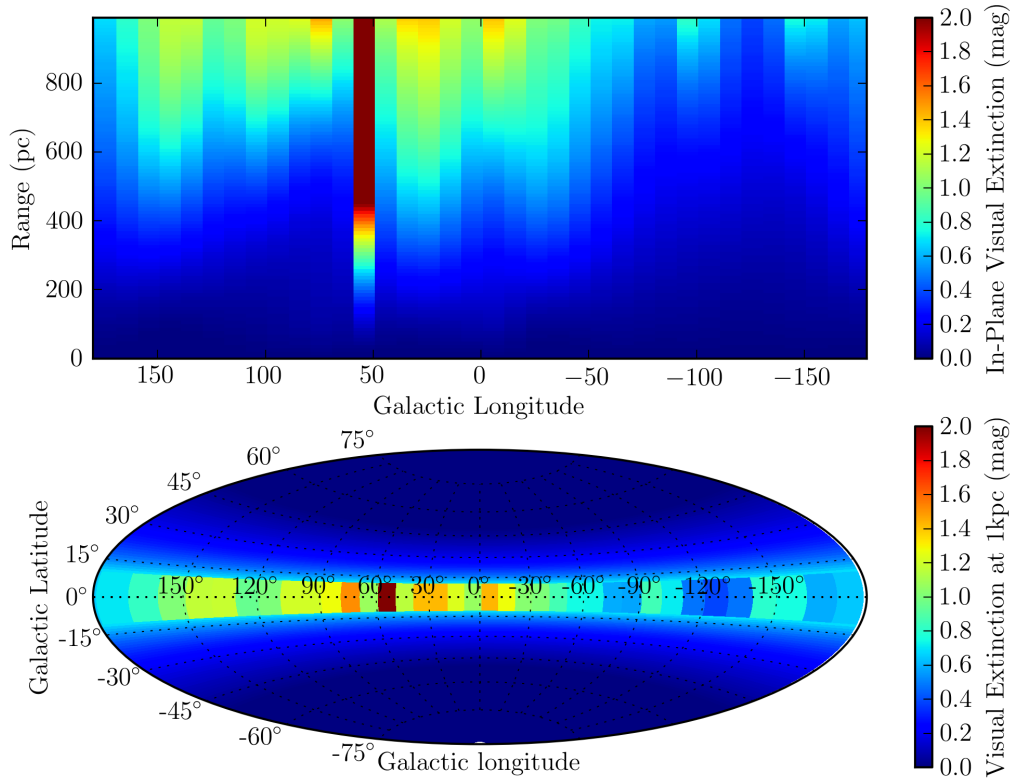


Figure 1.4: Total visual extinction varies with galactic latitude  $b$  and longitude  $l$ . The model shown here is from Chen et al. [13] and uses an analytic polynomial expression to compute the extinction within 1000 pc in 36 cells of  $\Delta l = 10^\circ$ . Top: In-plane extinction magnitude from 0 to 1 kpc for galactic longitude  $180^\circ$  to  $-180^\circ$ . Bottom: Total visual extinction at  $R=1$  kpc.

for galactic latitudes  $>10^\circ$ . Given that the majority of stars in the galaxy reside in the thin,  $\sim 300$  pc galactic disk, out-of-plane range may be less important. In that case, if the distances between civilizations are great, a longer wavelength would be more efficient (2–9  $\mu\text{m}$ ) as less light is lost due to extinction. Photon energy in the infrared is lower, also leading to a more efficient system. The benefits to going to longer wavelengths are eventually limited by decreased telescope directivity which is  $\propto \lambda^{-2}$  (see § 1.2.2).

The last effect to consider is pulse dispersion. Dispersion of pulses can reduce the bandwidth of a communication system by causing inter-symbol interference. In appendix M of SETI:2020, Cordes explains the effect of the ISM on nanosecond optical pulses [23]. His calculations show that the scattering of optical photons by dust grains causes delayed light to arrive on two timescales. There is a close-in tail caused by forward scattering which arrives seconds after the prompt pulse and a long tail from diffuse scattering that arrives much later. The prompt pulse arrives unscattered (“ballistic”) hence it is not broadened in time. Therefore, dispersion is not an issue at optical wavelengths as long as the pulse height is not reduced below a receiver’s sensitivity threshold. The remaining fraction in the prompt pulse is given by  $e^{-\tau}$  where  $\tau$  is the total optical scattering depth.

## Received Photons

The strength of the signal depends upon the number of photons received by the detector. After traversing the distance  $R$ , the photons in the laser pulse  $N_{\text{sent}}$  are spread out over an area  $R^2\Omega$ . The receiving telescope will collect the photons within the telescope aperture  $\pi(D_r/2)^2$ . Some fraction of photons are lost from beam diffraction  $f_{\text{FWHM}}$  and to extinction  $f_{\text{ext}}$  in the ISM. Also, the number of photons collected by the receiving telescope will be reduced by the detector quantum efficiency and telescope mirror efficiency ( $Q_d Q_m = Q$ ). The number of photons produced at the transmitter is

$$N_{\text{sent}} = \frac{E_{\text{pulse}}}{hc/\lambda} \quad (1.12)$$

and the number of received photons is then

$$N_{\text{rec}} = N_{\text{sent}} \cdot \frac{1}{R^2\Omega} \cdot \pi(D_r/2)^2 \cdot Q \cdot f_{\text{FWHM}} \cdot 10^{-\frac{2}{5}A(\lambda)} \quad (1.13)$$

$$= \frac{E_{\text{pulse}} D_t^2 D_r^2 Q f_{\text{FWHM}}}{hc\lambda R^2} 10^{-\frac{2}{5}A(\lambda)} \quad (1.14)$$

The host star of the transmitter will also contribute to the number of photons detected by the receiver. The number of stellar photons counted by the detector during the pulse on-time  $\tau_{\text{pulse}}$  is

$$N_* = \frac{P_* \tau_{\text{pulse}}}{hc/\lambda} \cdot \frac{\pi(D_r/2)^2}{4\pi R^2} \cdot Q \cdot 10^{-\frac{2}{5}A(\lambda)} \quad (1.15)$$

The power radiated by a star  $P_*$  of temperature  $T$  in a band from  $\lambda_{\min}$  to  $\lambda_{\max}$  can be found by integrating the blackbody radiation (Planck's Law) over the surface area of the star:

$$B_\lambda(T) = \frac{2hc^2}{\lambda^5} \frac{1}{e^{hc/(\lambda k_B T)} - 1} \quad (\text{Planck's Law}) \quad (1.16)$$

$$P_* = 4\pi R_*^2 \int_{\lambda_{\min}}^{\lambda_{\max}} d\lambda \int_0^{2\pi} d\phi \int_0^{\pi/2} d\theta B_\lambda(T) \cos(\theta) \sin(\theta) \quad (1.17)$$

For simplicity, we assume that the power emitted in the band produces photons of the transmitted wavelength  $\lambda$ . In the following example systems, a sun-like star will be assumed ( $L_\odot = 4 \times 10^{26}$  W,  $T = 5780$  K) and the band will be 300 nm and 800 nm for wavelengths within that range and  $\lambda \pm 500$  nm otherwise. As an example, the power emitted between 300 nm and 800 nm (sensitivity range of the photomultipliers used in the Advanced All-sky Camera) is  $\sim 2 \times 10^{26}$  W. Ignoring extinction and detector loss, at a distance of 100 pc, the number of photons arriving in a 10 ns window is 0.04 photons·m<sup>-2</sup>. For purposes of the example systems, the signal-to-background (SBR) will be calculated as

$$\begin{aligned} \text{SBR} &= 10 \log \left( \frac{N_{\text{rec}}}{N_*} \right) \\ &= 10 \log \left( 16 f_{\text{FWHM}} \cdot \frac{E_{\text{pulse}}}{P_{\text{star}} \tau_{\text{pulse}}} \cdot \frac{D_t^2}{\lambda^2} \right). \end{aligned} \quad (1.18)$$

## 1.2.2 Example Systems

Now that we have the equations to determine the number of photons received, we can present a number of example systems. The systems start with a modest telescope size and laser pulse energy (1 m and 50 kJ) of the scale that a small group of determined private individuals might build, and increases to scales that are beyond what has been built today but that we expect is possible with a concerted effort given national government-scale resources. The modest sizes are fully compatible with current technological capabilities. The larger sizes (100 m telescope, 500 MJ laser pulse) could be built in a few decades so they

should be viewed as achievable by any sufficiently advanced civilization. For the largest sizes, diffraction limited optics create very small beam widths which could be artificially degraded if the required pointing precision cannot be achieved. The first sequence, systems 1–4, are categorized by the sophistication needed to construct them. Their performance ( $N_{\text{rec}}$ ) and range  $R$  scale accordingly. At low ranges ( $<100$  pc), a small, high-quality transmitter telescope can be used with a large, low-quality (cheaper) receiving telescope. This is because the beam diameter at the target  $D_b$  should be about the size of the habitable zone ( $\sim 2$  AU) and at low ranges, where there is little extinction and short wavelengths can be used, a small diffraction-limited transmitter is sufficient. At longer ranges ( $>100$  pc), larger transmitters are needed to increase directivity because of the additional beam widening at range and because longer wavelengths are needed to avoid interstellar extinction. In the second sequence, systems 5–10, the wavelength has been varied to explore the effects of in-plane extinction at 1 kpc. The transmitter and receiver are 10 m, Keck-sized telescopes and the pulse energy is NIF-sized at 2 MJ. All of the systems produce detectable numbers of photons (5–21) but a wavelength of 800 nm gives the best compromise between directivity and extinction. Systems 11–16 show the relative sizing necessary for symmetrical systems at 1  $\mu\text{m}$  for ranges of 100 pc, 1 kpc, and 10 kpc, both for sightlines in the galactic plane and toward the galactic poles. Telescope sizes are adjusted to keep the number of received photons constant. At 1  $\mu\text{m}$ , extinction is low for distances up to 1 kpc so the size difference between in-plane and galactic pole systems is small. The extinction difference between directions is much higher at 10 kpc, allowing for telescope diameters of half the size for the galactic pole sightline. The systems 17–26 are “All-sky”-like in that the receiving telescope collector area and detector quantum efficiency are on par with that of all-sky survey (see [Chapter 4](#)). Transmitter size and pulse energy have been adjusted to give a sense of the scale needed for in-plane and out-of-plane signaling for 100 pc, 500 pc, 1 kpc, 2.5 kpc, and 5 kpc.

From the example systems, it’s clear that even short range systems require more than just an amateur level of expertise on the transmitter side. At only 10 pc, a diffraction-limited primary mirror of 1 m is needed to achieve reasonable small pulse energies ( $\sim 50$  kJ). The beam width, in this case, would be 86 mas, which would require a very precise pointing system, hardly in the amateur realm, such as adaptive optics or using a space-based system. Larger pulse energies could be used, but this again pulls even a short-range system out of

the amateur range. With enough resources to develop a Keck-sized transmitter and receiver telescope mated to a NIF-sized pulse laser, respectable ranges can be reached. A transmission distance of 1 kpc looks reasonable for those systems over the range of optical wavelengths. Symmetrical systems of 30 m telescope diameter and 100 MJ pulse energy could communicate half-way across the galaxy, especially if infrared wavelengths are used for in-plane signaling to reduce extinction.

For our all-sky system of  $\sim 2 \text{ m}^2$  collecting area, a disproportionate effort is required of the transmitting civilization. We expect, however, that any communicating civilization will be much older and likely to have more advanced technology. The technological capability required for reasonable ranges (a few 100 pc), though, is not beyond that which already exists on Earth. Example systems 17 and 18 (100 pc range) assume transmitting telescopes of 4 m diameter and 1 MJ pulse energy, well within human technological capabilities. For 500–1000 pc at mid-optical wavelengths, the additional extinction in the galactic plane forces the pulse energy to increase to an order of magnitude larger than currently exists but this should not be seen as an upper limit. For the all-sky system to receive an in-plane transmission from a few kiloparsecs, however would require substantially larger transmitting telescope (50–100 m) and pulsed lasers (100–500 MJ).



Table 1.3: Example Systems

Sys	Transmitter				Sightline				Receiver					Type
#	$\lambda$	$E_{\text{pulse}}$	$D_t$	$\theta_{\text{FWHP}}$	$D_b$	$R$	$l$	$b$	$f_{\text{ext}}$	$D_r$	Q	SBR	$N_{\text{rec}}$	
1	.4 $\mu\text{m}$	50 kJ	1 m	86 mas	.9 AU	10 pc	0°	0°	.99	4 m	.3	4	35	Amateur
2	.5 $\mu\text{m}$	100 kJ	4 m	27 mas	3 AU	100 pc	0°	0°	.90	10 m	.3	13	38	Pro-Am
3	1 $\mu\text{m}$	4 MJ	10 m	21 mas	21 AU	1 kpc	0°	0°	.70	15 m	.3	26	82	Pro
4	8 $\mu\text{m}$	100 MJ	30 m	57 mas	577 AU	10 kpc	0°	0°	.83	30 m	.3	28	110	Super Pro
5	.4 $\mu\text{m}$	2 MJ	10 m	9 mas	9 AU	1 kpc	0°	0°	0.26	10 m	.3	28	17.0	Keck
6	.6 $\mu\text{m}$	2 MJ	10 m	13 mas	13 AU	1 kpc	0°	0°	0.46	10 m	.3	24	20	+
7	.8 $\mu\text{m}$	2 MJ	10 m	17 mas	17 AU	1 kpc	0°	0°	0.64	10 m	.3	21	21	NIF
8	1 $\mu\text{m}$	2 MJ	10 m	22 mas	21 AU	1 kpc	0°	0°	0.7	10 m	.3	19	18	
9	2 $\mu\text{m}$	2 MJ	10 m	43 mas	43 AU	1 kpc	0°	0°	0.88	10 m	.3	22	11	
10	5 $\mu\text{m}$	2 MJ	10 m	108 mas	108 AU	1 kpc	0°	0°	0.97	10 m	.3	29	5	↓
11	1 $\mu\text{m}$	1 MJ	4.2 m	51 mas	5 AU	100 pc	0°	0°	0.97	4.2 m	.3	9	39	Symmetric
12	1 $\mu\text{m}$	1 MJ	4.2 m	51 mas	5 AU	100 pc	0°	90°	0.99	4.2 m	.3	9	40	
13	1 $\mu\text{m}$	10 MJ	8.1 m	27 mas	27 AU	1 kpc	0°	0°	0.7	8.1 m	.3	25	39	
14	1 $\mu\text{m}$	10 MJ	7.5 m	29 mas	29 AU	1 kpc	0°	90°	0.96	7.5 m	.3	24	40	
15	1 $\mu\text{m}$	100 MJ	30 m	7 mas	72 AU	10 kpc	0°	0°	0.04	30 m	.3	46	42	
16	1 $\mu\text{m}$	100 MJ	15 m	14 mas	144 AU	10 kpc	0°	90°	0.7	15 m	.3	40	46	↓
17	.5 $\mu\text{m}$	1 MJ	4 m	27 mas	3 AU	100 pc	0°	0°	0.9	1 m	.2	13	25	All-sky
18	.5 $\mu\text{m}$	1 MJ	4 m	27 mas	3 AU	100 pc	0°	90°	0.98	1 m	.2	13	27	type
19	.5 $\mu\text{m}$	20 MJ	14 m	7 mas	4 AU	500 pc	0°	0°	0.59	1 m	.2	16	16	
20	.5 $\mu\text{m}$	20 MJ	14 m	7 mas	4 AU	500 pc	0°	90°	0.94	1 m	.2	16	25	
21	.5 $\mu\text{m}$	40 MJ	20 m	5 mas	5 AU	1 kpc	0°	0°	0.35	1 m	.2	19	10	
22	.5 $\mu\text{m}$	40 MJ	20 m	5 mas	5 AU	1 kpc	0°	90°	0.9	1 m	.2	19	25	
23	.5 $\mu\text{m}$	100 MJ	70 m	1 mas	4 AU	2.5 kpc	0°	0°	0.08	1 m	.2	23	11	
24	.5 $\mu\text{m}$	100 MJ	70 m	1 mas	4 AU	2.5 kpc	0°	90°	0.77	1 m	.2	23	105	
25	.5 $\mu\text{m}$	500 MJ	100 m	1 mas	5 AU	5 kpc	0°	0°	0.00674	1 m	.2	30	2	
26	.5 $\mu\text{m}$	500 MJ	100 m	1 mas	5 AU	5 kpc	0°	90°	0.59	1 m	.2	30	206	↓

### 1.2.3 Summary

To sum up, a pulsed optical communication system has the following characteristics and advantages:

**No Astrophysical Background** No natural astrophysical emitters of nanosecond optical pulses are known to exist.

**Low Dispersion** Optical pulses are not significantly broadened in time by the interstellar medium, even for nanosecond pulses.

**High Directionality** Large optical telescopes can achieve very small diffraction limited beamwidths because of the much smaller wavelengths in the optical band (compared to radio). This makes optical systems more efficient for a given telescope size because the broadcast energy can be focused on a target star rather than being lost into space.

**Low Computational Requirements** Radio systems require many calculations to search through the band looking for spikes in the frequency domain. Signals can be drifting in frequency as the radial velocity between transmitter and receiver changes due to planet rotation and orbit. Fast Fourier transforms must be calculated at many different Doppler accelerations. Optical pulse detection needs very relatively little processing power<sup>7</sup>.

**No Optical Filtering** Since optical detectors operate over an entire band, and pulses are detected by counting photons in the band within a short time window, optical filtering is not necessary. While filters may increase the signal-to-noise ratio when the transmit wavelength is known, searching for a beacon whose wavelength is not known a priori may render filtering undesirable, at least until a signal has been detected.

**Simple Receiver Strategy** Two fast photodetectors and a coincidence logic circuit can be combined with large area, low resolution optics to make a simple optical pulse receiver.

---

<sup>7</sup>One radio SETI effort, SETI@HOME was recognized by the Guinness Book of World Records in 2001 as being the largest computation ever performed with  $890 \times 10^{18}$  floating point operations ( $10^{22}$  as of Feb, 2013) [31].

**Availability of High Power Lasers** Lasers have experienced exponential growth in maximum output power since they were invented in the '60s. At that time microwave transmitters were available at high powers whereas lasers were not, leading to a consensus of microwaves being preferred for interstellar signaling. The advance of lasers to extraordinary powers demonstrates that lasers powerful enough to transmit over interstellar distances could be constructed by a civilization with modest effort.

**Radio Searches Unsuccessful** Despite 50 years of searching the radio spectrum for signal from extraterrestrial civilizations, no detections have yet been made. This may be the strongest argument for searching in other bands. As shown by Townes [61], the optical region may be just as promising as radio, based primarily on delivered energy efficiency. Other consideration may tip the scale in favor of an optical or radio system. Therefore, this justifies ETI searches at optical wavelengths.

## 1.3 Optical SETI Backgrounds

In a search for nanosecond astronomical pulses, any background sources of light and even the detectors themselves can produce pulses that could be confused with a distant laser source. These background sources need to be categorized and understood in order to design a proper detection strategy that minimizes the effects of the background noise.

### 1.3.1 Astronomical

The allure of searching for a nanosecond pulsed beacon is in part because no natural emitters of such short pulses are known to exist. This gives the signal an artificial quality that makes it a technological indicator. A natural astronomical nanosecond emission would need to be the result of a process confined to a region less than a foot in diameter but with enough intensity to be seen light years away, or it would need to be coherent. Dravins et al. [22] offer a number of possibilities for high-speed astrophysics including *a*) atmospheric intensity scintillation of stars on the shortest timescales, *b*) plasma instabilities and the fine structure in accretion flows onto white dwarfs and neutron stars, *c*) small-scale [magneto-] hydrodynamic instabilities in accretion disks around compact objects, *d*) radial oscillations

in white dwarfs ( $\simeq 100 - 1000$  ms), and non-radial oscillations in neutron stars ( $\leq 100$   $\mu$ s), *e*) optical emission from millisecond pulsars ( $\simeq 1 - 10$  ms), *f*) fine structure in the emission (‘photon showers’) from pulsars and other compact objects, *g*) photo-hydrodynamic turbulence (‘photon bubbles’) in extremely luminous stars, *h*) stimulated emission, e.g., synchrotron radiation, from magnetic objects (‘cosmic free-electron laser’), *i*) non-equilibrium photon statistics (i.e. non-Bose-Einstein distributions) from certain sources, and *j*) VLBOI intensity interferometry over  $1 - 100$  km to search for fine structure (granulation) on stellar surfaces. None of these phenomena are expected to produce nanosecond optical flashes, however. An additional possibility for a nanosecond scale astrophysics comes from the discovery by Hankins et al. [34] of “giant” radio bursts with 1–3 ns time structure emanating from the Crab nebula, 2 kpc away. They theorize that plasma turbulence from the relativistic flow are causing the explosive collapse of wave packets to produce coherent radio emission from source regions 60 cm in diameter. Though nanosecond radio pulses have been seen, optical pulses of an astrophysical nature at that timescale are still unknown. Therefore, astronomical nanosecond optical pulses should not be a background source. In fact, a side benefit of searching for pulsed optical laser transmitters is the possibility of discovery of an astrophysical phenomenon that has not been theoretically predicted.

### 1.3.2 Stellar Pileup

From a receivers perspective, the light from a pulsed laser’s host star would be a strong contributor of background photons delivered to an optical detector. The steady stream of photons from the star arrive at a rate dependent upon the star’s brightness. Let’s consider, as an example, the photons that would be received by a  $1 \text{ m}^2$  telescope using a 20% quantum efficiency photodetector when pointed at a sun-like star (visual magnitude  $m_V = 12$ ) 1000 ly away. The star delivers  $\sim 2 \times 10^6$  V-band photons  $\text{s}^{-1}\text{m}^2$  [50]. Not every photon is detected however. Inefficiencies of the telescope optics and the detector quantum efficiency reduce the number of photons that can be counted. Fast photodetectors, such as photomultiplier tubes, register these detected photons, or “photo-electrons”, as individual pulses lasting a few nanoseconds. The  $m_V = 12$  star would cause our photodetector with 20% quantum efficiency to produce on average one photo-electron every 2500 nanoseconds. At such a

low rate, the pulses from two photo-electrons would rarely, just by chance, overlap in time. However, a star of visual magnitude  $m_v = 5$ , visible to the naked eye, is bright enough to produce about one photo-electron every 4 nanoseconds. Especially with brighter stars, the random arrival of photons could result in multiple photo-electrons being produced in the detector at nearly the same instant, conspiring to appear as a short burst of light.

Poisson statistics helps quantify the situation. Assuming a Poisson arrival rate  $r$ , the probability rate of  $n$  photons arriving within the time interval  $\tau$  is

$$R = \frac{r\tau^{n-1}}{(n-1)!}e^{-r\tau} \quad (1.19)$$

Often one wants to know the probability rate of  $n$  or more photons arriving within a time interval. The above equation simplifies to

$$R = \frac{r^n\tau^{n-1}}{(n-1)!} \quad (1.20)$$

for  $n$  or more photons when  $r\tau \ll 1$ . The rise time of the detectors and electronics determine the value of  $\tau$ . The all-sky systems use photomultiplier tubes with rise times of 1–2 ns. Assuming  $\tau$  is 2 ns and the photo-electron arrival rate is 100 kHz (from the above example), on average two or more photo-electrons will arrive within 2 ns at a rate of 20 Hz. An arrival of three photons or more occur once every 500 seconds and every 89 days for four or more photons.

How many photo-electrons are required within the detection time period in order to be considered a possible pulsed laser source detection? The multiple photo-electron arrival rates are an important factor to consider. If the threshold for detection in a single detector system is placed too low, at say two photo-electrons, the system will issue a possible detection notice 20 times per second whenever a magnitude 12 star comes into view. To decrease the number of false alarms, the threshold would need to be raised to the point that a possible detection from stellar photons is a rare event. Of course, this reduces the system's sensitivity to any actual laser pulses that are below the threshold.

Using multiple detectors in coincidence is an alternative to increasing the threshold. This technique is used in imaging atmospheric Čerenkov telescopes (IACTs) where the cameras are usually a close packing of cylindrical photomultiplier tubes. As an example, in the Whipple Telescope, three or more adjacent tubes must detect an amount of light over a

set threshold to cause a readout of the tubes' output by the systems' electronics (a system "trigger"). In the all-sky cameras, a two detector coincidence is needed to cause a system trigger however, unlike IACTs, the sky image entering the all-sky camera's entrance window is divided onto two image planes using a beamsplitter. Photomultiplier tubes from each image plane, aligned to view the same area of sky, form "coincident pairs". The Advanced All-sky Camera has an adjustable "coincidence window"  $\tau_c$  during which over-threshold pulses from both photomultiplier tubes in a pair must be received in order to trigger the system. A trigger from the coincident pair is called a "coincidence". The joint probability of two independent events  $P_1$  and  $P_2$  both occurring is  $P_1P_2$ . So the probability of a photo-electron arriving in the coincidence window  $\tau_c$  in each of two independent detectors with rates  $r_1$  and  $r_2$  is

$$P_c = r_1\tau_cr_2\tau_c \quad (1.21)$$

The coincidence probability rate per unit time is

$$r_c = r_1r_2\tau_c. \quad (1.22)$$

Continuing the above example (a sun-like star at 1000 ly) and assuming two detectors in coincidence, the photo-electron arrival rate to each detector is cut in half to 50 kHz due to the beamsplitter. The 2+ photon pileup rate for one detector becomes 5 Hz and the coincidence rate for 2+ photon pileup in two detectors with coincidence window  $\tau_c=2.5$  ns is  $(5 \text{ Hz})^2 \times 2.5 \text{ ns}$  or twice a year.

By using two detectors in coincidence, the two or more photon pileup rate went from 50 kHz for a single detector to 62 *nano*-Hz. It should be clear from the rate calculations that using a pair of photo-detectors in coincidence is a useful strategy for reducing the false alarms from stellar photon pileup. It is equally important for reducing false alarms due to detector noise, as is seen in the next section.

### 1.3.3 Photomultiplier Issues

Ideally, photomultiplier tubes produce output pulses at a rate proportional to the intensity of light entering the entrance window. Even in a completely dark state, there will still be some amount of output from the photomultiplier tubes. This output, called dark current,

can be produced by secondary breakdown, thermionic emission from the cathode or dynodes, ion feedback, and environmental ionizing radiation including muons and radioisotopes.

Most dark current comes from thermionic emission from the photocathode. The dynodes, as well as the photocathode, have very low work functions so they emit electrons even at room temperature. These emitted electrons will be accelerated and multiplied just like any other photo-electron that results from a photon striking the photocathode. Extended-red and infrared sensitive photomultipliers have especially high dark currents. They can be cooled to reduce the dark current to an acceptable level for photon counting. Ion feedback is another common source of dark currents. There is a residual amount of gas in the phototube after it is evacuated. This gas can be ionized by collisions with electrons. Ionized atom will accelerate towards the photocathode or first dynode stage, creating many secondary electrons when the ion lands. These secondary electrons will be multiplied and cause a large output pulse. A large input pulse of light can often cause ion feedback, causing an afterpulse to occur. Other sources of dark current can come from glass scintillations that occur when electrons deviate from their normal paths and hit the photomultiplier's glass envelope. Field emission dark current may result from a photomultiplier tube being operated near its maximum voltage. This can be damaging to the tube if the supplied voltage becomes too high.

Corona discharge can cause dark current and electromagnetic interference (EMI) for detectors that use very high negative cathode voltages. Breakdown of the electric field (caused by sharp points, dust, etc. that ionize gas between the points) produces bursts of light by visible corona. The light and EMI can couple into independent detectors causing correlated output pulses. Corona breakdown was particularly high during the humid summer month for an experiment using hybrid-avalanche photodiodes (HAPDs) operating with 7.5 kV negative cathodes [38]. The effect can be mitigated by dessicating the atmosphere around the detectors and using “bake-out heaters” to remove absorbed moisture.

### 1.3.4 Cosmic Ray Air Showers

When very energetic particle in space reach the Earth and collide with atoms of the atmosphere, they initiate cascades of particles called extensive air showers (EAS). The most common initiators (called the “primary”) are protons and atomic nuclei, but electrons and

gamma rays also take part. The cosmic ray flux is highly isotropic as most of the primaries are charged particles that respond to, and get mixed by, galactic, stellar, and planetary magnetic fields. The EAS cascades propagate through the atmosphere, creating particles (electrons, muons, pions, gamma rays, etc.) as they go, until the energy of the initiator is exhausted. The first interaction occurs high in the atmosphere. The cascade develops until it reaches a maximum number of particles ( $\sim 7\text{-}8$  km for a 1 TeV proton or gamma ray) and then peters out as remaining particles have less energy to induce further reactions. The number of particles at shower maximum is proportional to the initial energy of the primary and the depth at maximum is related to the log of the energy [37]. Photon initiated EAS begin when the gamma ray passes close to an atmospheric nuclei, producing an electron-positron pair from the gamma ray ( $\gamma \rightarrow e^- e^+$ ). The relativistic electron-positron pair travel until they interact with nuclei in the bremsstrahlung process, creating another gamma ray photon. That photon undergoes pair production and bremsstrahlung, multiplying the number of photons and electron-positrons as the cascade progresses. Pions, which decay to muons, are also produced, instead of an electron-positron pair, but the pion production probability is much lower. Beyond shower maximum, the cascade rapidly ceases as the electrons lose more energy to ionization, rather than radiation, and are quickly absorbed. Hadron initiated EAS (protons and heavier nuclei) begin by the primary colliding with an atmospheric nuclei, producing pions, kaons, and nucleons that have various decay chains. A large component of the hadron cascades are charged pions, which decay into muons and neutrinos, and neutral pions which decay into gamma rays. The gamma rays from the neutral pions cause electromagnetic cascades, as previously described. The muons created by the charged pions penetrate to ground level because they effectively have an increased lifetime in the atmosphere than in their rest frame due to their relativistic velocity. During the charged pion's lifetime, they interact with atmospheric nuclei causing hadron sub-showers of more pions and nucleons. The hadronic particles multiply until the average particle energy is less than the pion production threshold. The electromagnetic cascades from the remaining neutral pions continue until their energy is expended.

Relativistic charged particles (electrons, positrons, muons, pions) in the EAS induce radiation at optical wavelengths as they travel at velocities comparable to the phase velocity of light in the atmosphere. The molecules in the atmosphere are polarized as the charged



particle passes and emit photons in coherent wave-fronts as the molecules along the charged particle's path relax back to their resting state. This is called Čerenkov radiation [62]. Extensive air showers produce large amounts of Čerenkov radiation due to the many relativistic charged particles in the electromagnetic and hadron cascades. The minimum energy that a particle must have to induce Čerenkov radiation is

$$E_{\min} = \frac{m_0 c^2}{\sqrt{1 - 1/n^2}} \quad (1.23)$$

where  $m_0$  is the rest mass of the particle and  $n$  is the index of refraction of the material in which the particle is traveling. The emission angle of Čerenkov radiation is given by

$$\cos \theta_C = \frac{1}{\beta n} \quad (1.24)$$

where  $\beta = v/c$ , the ratio of the particle speed to the speed of light. At relativistic velocities,  $v \simeq c$  and the emission angle only depends on the index of refraction. In the atmosphere, the emission angle is  $\sim 1.3^\circ$  at sea level,  $\sim 1.0^\circ$  at 8 km, and decreasingly smaller at higher altitudes. The number of photons radiated per unit length can be calculated using the Frank-Tamm equation:

$$\frac{dN}{dx d\lambda} = 2\pi\alpha z^2 \frac{1}{\lambda^2} \left( 1 - \frac{1}{\beta^2 n(\lambda)^2} \right) \quad (1.25)$$

$$= 2\pi\alpha z^2 \frac{1}{\lambda^2} \sin^2 \theta_C \quad (1.26)$$

where  $\alpha$  is the fine structure constant ( $\approx 1/137$ ), and  $z$  is the particle charge number.

At sea level, an electron yields  $\sim 30$  photons $\cdot\text{m}^{-1}$  between 350 and 500 nm [63]. The radiation is proportional to  $\lambda^{-2}$  but the intensity peaks in the ultraviolet-blue, beyond which the index of refraction is reduced and the atmosphere becomes more absorptive. There is significant power in the blue to red part of the spectrum; this Čerenkov radiation reaches to the ground and can be detected by imaging telescopes. The amount of Čerenkov light is proportional to the number of particles in the cascade, which is proportional to the energy of the primary, so the Čerenkov light provides a good measure of the primary energy. The Čerenkov radiation from a cosmic ray EAS is spread over a  $20^\circ$ , but the bulk is produced by the particle dense core of the cascade near the shower maximum. A second Čerenkov component comes from particles that initiate electromagnetic cascades at low altitudes, in

the shower tail, depositing Čerenkov light close to the ground near the impact point of the shower core. A third and final component, particles that actually reach to the ground, can cause Čerenkov rings to appear in telescopes that can image the Čerenkov light.

The Čerenkov emission angle is small and the particles receive relatively little lateral momentum compared to the longitudinal momentum of the shower, so the Čerenkov light is strongly beamed in the shower direction. The angular width of the image of the Čerenkov light is  $\sim 1\text{--}2^\circ$ . Hadron initiated EAS tend to have a broader structure due to the momentum transferred to pions in strong reactions [37]. Most of the light lands on a 125 m radius ground footprint for 1 TeV gamma ray showers and a somewhat larger radius for a 1 TeV hadron showers. The density of Čerenkov photons on the ground for these energies is  $\sim 50 \text{ photons}\cdot\text{m}^{-1}$  [63]. Since the particles producing the Čerenkov radiation, and the light itself, are both traveling near the speed of light, Čerenkov light production from all levels of the EAS travels in a thin pancake  $\sim 2$  m wide and arrives at the ground in a flash lasting a few nanoseconds. These Čerenkov flashes have the short timespan of the order that we expect from a laser transmitter. However, the Čerenkov radiation is spread over  $1\text{--}2^\circ$ , so they can be distinguished from a laser pulse that would create an image given by the telescope's point spread function. Cosmic ray rates from the all-sky survey and simulations of EAS are discussed further in § 5.2.5 and 5.3.

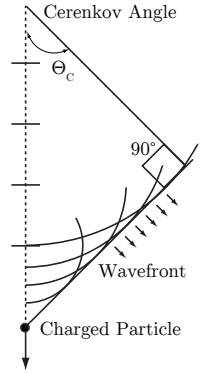


Figure 1.5

### 1.3.5 Muons

Muons are a common component of hadronic cosmic ray extensive air showers. Similar to an electron but  $>200$  times more massive, muons have a lifetime of  $2.2\mu\text{s}$  before decaying into an electron or positron and a pair of neutrinos. They are produced in air showers mainly by the decay of charged pions. Electrons are also produced in air showers by pion decays, but muons do not strongly interact with matter so they survive down to the lowest altitudes. Muons can potentially cause false triggers in three ways:

- a) by passing through the glass envelopes of a matched coincident PMTs pair and generating Čerenkov radiation;

- b) by producing Čerenkov radiation directly on axis and in close range ( $<40$  m) to the telescope;
- c) by producing Čerenkov radiation when passing through the beamsplitter or entrance window.

The first type could occur if the muon is on a trajectory to encounter both PMTs in a coincident pair. Passing through the glass envelope of the photomultiplier tube creates a burst of Čerenkov radiation, much more than in the atmosphere owing to the higher index of refraction of glass ( $\sim 1.5$ ). From Equation (1.25), a muon produces  $0.08 \text{ photons}\cdot\text{mm}^{-1}$  in the atmosphere at sea level ( $\nu=1.0003$ ) whereas in glass it produces  $74 \text{ photons}\cdot\text{mm}^{-1}$  (250 nm to 900 nm). For a relativistic muon, the distance  $d_{\text{PMT}}$  between the two PMTs cannot be more than

$$d_{\text{PMT}} \approx c\tau_c \quad (1.27)$$

where  $c$  is the speed of light and  $\tau_c$  is the coincidence detection time window. Otherwise, the two pulses from the muon encountering both PMTs will not be counted as a coincidence. For the closest pair of PMTs in the all-sky array (separation  $\sim 80$  mm), the acceptance solid angle is  $\Omega_{\text{PMT}} \simeq 10^{-4} \text{ sr}$  and the cross section for two PMTs is  $\sigma_{\text{PMTs}} \simeq 0.5 \text{ cm}^2$ . The energy threshold for muons to produce Čerenkov radiation in glass (index of refraction  $\sim 1.5$ ) is  $\sim 160 \text{ MeV}$ . At sea level, muons  $>200 \text{ MeV}$  [4] arrive with a vertical flux  $J_\mu \simeq 10^{-2} \text{ cm}^{-2} \cdot \text{sr}^{-1} \text{s}^{-1}$ . Using the approximated values above the muon coincidence rate  $r_{\mu c}$  would be

$$\begin{aligned} r_{\mu c} &= J_\mu \cdot \sigma_{\text{PMTs}} \cdot \Omega_{\text{PMTs}} \\ &\simeq 16 \text{ yr}^{-1} \end{aligned} \quad (1.28)$$

In the all-sky system, there are three other PMT pairs that have wider separations. They would exhibit lower coincidence rates due to their increased separation. These coincidences would occur whether the shutter of the camera is open or closed. Experiments with the all-sky system show that with the shutter closed, coincidences at the 3–4 photo-electron level occur less than once per 8 hours. Theoretically and experimentally, muons passing through two PMTs, then, are not a significant source of triggers for the all-sky system.

The second type of possible false triggers caused by muons are “muon rings” (Figure 1.6) created by the Čerenkov radiation of energetic cosmic ray muons at close range to the

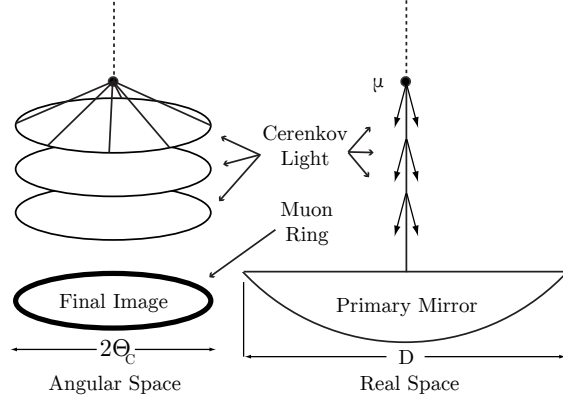


Figure 1.6: The Čerenkov radiation from muons produce rings in the image plane. Adapted from Horan [37].

telescope. If the muon paths are parallel to the telescope axis and moving toward the telescope with energy above the Čerenkov threshold, the Čerenkov radiation will be focused by the telescope into a ring on the imaging plane, the angular diameter of the ring being equal to the Čerenkov radiation angle. The total amount of Čerenkov light collected from a muon ring is limited by the track length over which its light is accepted into the telescope aperture. For the Čerenkov light to be captured by the telescope primary mirror, the muon must be within  $L = \frac{D}{2 \tan \theta_C}$  of the telescope (Figure 1.7).

A relativistic muon produces

$$N_\gamma = 2\pi z^2 \alpha \sin^2 \theta_C \frac{D}{2 \tan \theta_C} \int_{\lambda_1}^{\lambda_2} \frac{d\lambda}{\lambda^2} \quad (1.29)$$

photons over track length  $L$  which get focused into a ring on the image plane. The ring has an angular diameter  $2\theta_C$  so the density of photons per unit angle is

$$\rho_\gamma = \frac{N_\gamma}{2\pi\theta_C}. \quad (1.30)$$

The light produced over the track length may be incompletely collected by the primary mirror if the impact parameter or angle of incidence is too great. In that case, a partial ring would be seen on the image plane. We want to determine the maximum light density from muon rings so we will consider a muon with a impact parameter of 0 m and  $0^\circ$  angle of incidence. Assuming a constant atmospheric index of refraction, the ring would be infinitely

thin (a line) on the image plane. The index of refraction does, however, vary with altitude and wavelength which leads to a broadening of the ring. Multiple scattering of the muon, telescope aberrations, and ionization losses also work to broaden the ring. We additionally assume the broadening of the muon ring is less than the width of a camera pixel such that all the light from a segment of the muon ring is captured by one pixel.

The number of photons per track length is given by Equation (1.25) and is  $\sim 105 \text{ photons}\cdot\text{m}^{-1}$  for a muon at sea level (250 nm to 900 nm). For the all-sky camera pixel size of 1.5 arcmin and telescope diameter of 1.8 m, a muon deposits  $\sim 0.25$  photon per camera pixel. This should not be enough to cause a false trigger in the all-sky camera as the trigger threshold is normally set to three or four photo-electrons. Therefore muon rings can reasonably be neglected as a trigger source.

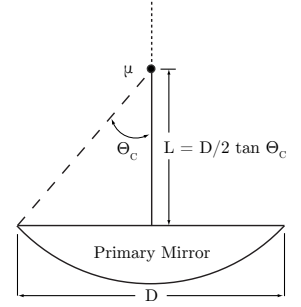


Figure 1.7

Lastly, Čerenkov production by muons passing through the beam-splitter or shutter entrance window should be considered. Since the Čerenkov angle in glass is about  $48^\circ$ , the geometry of the entrance window and photomultiplier tubes precludes muon rings from the entrance window being imaged onto the tubes' photocathodes. A muon traveling in the plane of the beamsplitter could produce Čerenkov radiation that arrives in a matched pair of photomultiplier tubes, however, the rate at which this occurs should be very low. The beamsplitter is mounted with its axis horizontal. The integral horizontal muon flux is about three orders of magnitude less than the vertical flux [12]. Additionally, the acceptance angle for a muon whose Čerenkov radiation reaches matched PMT pixels is small,  $\theta_{\text{pixel}} \times \theta_{\text{pmt}} \simeq 10 \times 10^{-3} \text{ sr}$ . Together with a cross-section of  $\sim 8 \text{ cm}^2$ , we calculate a muon striking the beamsplitter enters at an angle that couples into a matched pixel pair every  $\sim 200$  hours of observations. The photon density is highest for the inner-most PMT pair ( $D_{\text{sep}}=80 \text{ mm}$ ). The PMTs, angled at  $45^\circ$  to the beamsplitter, only accept the Čerenkov radiation from a track length of  $w_{\text{pixel}} \sin 45^\circ$  or 1.4 mm. We previously calculated the Čerenkov photon production in glass to be  $\sim 74 \text{ ph}\cdot\text{mm}^{-1}$ . This results in 1.2 photons in one photomultiplier tube pixel in a coincident pair and 0.4 photons in the other due to reflection off of the beamsplitter's silvered surface. This is below the normal trigger threshold, therefore muons hitting the beamsplitter should not be a significant source of false triggers.

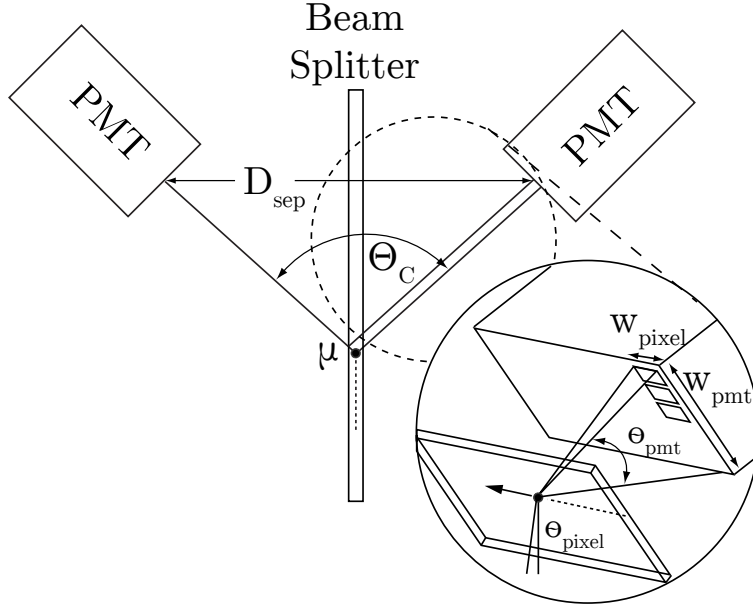


Figure 1.8

### 1.3.6 Atmospheric and Anthropogenic

Any bright object in the atmosphere can cause false triggering. Suspects include airplanes, helicopters, satellites, meteors, and even car headlights. Experience shows that airplanes are the most problematic as they have strobe lights which create very intense flashes. Strobe light flashes are typically long compared to photomultiplier tube rise times and produce a signal consisting of many photo-electrons over a few microseconds. This is much longer than what is expected from a far-off pulsed laser transmitter. A wide-field night sky camera provides a way to identify when airplanes are in the field of view. See § 5.2.4 for more details on airplane triggered coincidence events.

Far away lightning strikes are not considered to be an issue as they would appear on the horizon at an elevation that All-sky does not observe. Additionally, observations are rarely conducted when a storm is anywhere in the vicinity.

## Chapter 2

# All-Sky Optical SETI

In order to search for the pulsed optical signals described in [Chapter 1](#), in 2003, the original all-sky optical SETI system was built. It was designed as a complement to a previous targeted survey. The targeted survey ran for five years and observed 6,176 main sequence A to M class stars within 100 pc. Although this is a significant number of stars to vet, it is only a small fraction of the  $\sim 10^5$  stars within the 100 pc range, and even smaller if one considers larger distances. The total sky area observed in the targeted survey was also very small. Given the revelations of potentially  $10^5$  “nomadic” objects for every star roaming the galaxy [\[59\]](#), the space between the stars may present an opportunity to receive a signal. An attempt was made to choose target stars that have a higher likelihood of being able to support life. Since life has not been discovered in other star systems, however, our assumptions of what makes a good target type may be anthropically skewed. For these reasons, the all-sky survey was developed to observe large areas of the sky without making *a priori* assumptions about target habitability. Its telescope views a wide-field so that over the course of a year, it can observe the entire night-sky, hence the all-sky moniker. A detailed description of the legacy all-sky system has been presented in detail in Andrew Howard’s PhD thesis [\[38\]](#). The description of the observatory and its equipment below follows his lead and adds updated information where changes have been made. This chapter is included to give a general understanding the *original* all-sky system. The description of the *advanced* all-sky system follows this chapter in [Chapters 3](#) and [4](#). Targeted survey implementation details can be found in Chip Coldwell’s thesis [\[15\]](#) and an analysis of the targeted survey

results are in Howard et al. [39].

## 2.1 The All-sky System

The all-sky system consists of an observatory building with a roll-off roof, a telescope and control room housed by the building, the all-sky camera (AsCam), instruments to provide short test flashes, environmental sensors to monitor the weather, and a server computer that provides a web interface so the system can be controlled remotely. On clear nights, an operator engages the automated observation routines which open the roof, calibrate the telescope, choose an observation declination, begin half-hour observations that repeat throughout the night, and park the telescope and close the roof before dawn twilight. When observing, the 1.8 m quasi-newtonian telescope focuses the night sky onto the AsCam’s beamsplit detector array comprised of 16 pixelated photomultiplier tubes (8 tube pairs, 512 anode pairs total) arranged on two  $1.6^\circ \times 0.2^\circ$  image planes. Paired photomultipliers view the same area of the sky and the AsCam’s electronics wait for coincident pulses, which represent short flashes of light, from the photomultiplier tube anode pairs. When a pulse is received in both detectors at the same time, the AsCam electronics convert the analog pulse waveform to a 3-bit digital representation at 600 Megasamples-per-second and then notify the server that a “coincidence” has occurred. The server collects all coincidences in a database along with other state information of the instrument and observatory’s operations. The transit-mode telescope is only driven in elevation, so on subsequent nights different declination stripes on the sky are observed. Over the course of a night, stars in the AsCam’s field of view transit across the photomultiplier tubes with a minimum dwell time of  $\sim 48$  seconds at the celestial equator. Throughout the year,  $\sim 200$  clear nights are needed to observe all right ascensions between  $-20^\circ$  to  $+60^\circ$  declination.



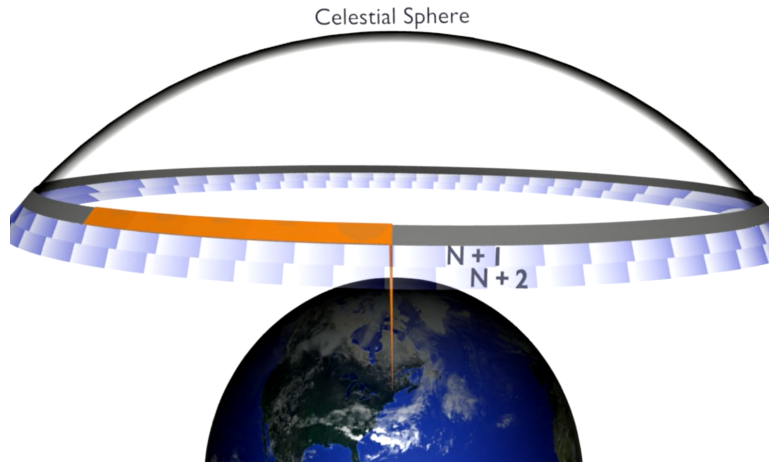


Figure 2.1: In this transit survey, the sky drifts past the telescope’s field of view as the Earth rotates. On successive nights, the telescope is moved to a new declination.

## 2.2 Observatory

The observatory building is located at Oak Ridge Observatory in Harvard, MA, in a rural wooded area 30 miles West of Boston. The building was built specifically for the all-sky survey to house the 1.8 m all-sky telescope. It is a wood-facade, steel-truss structure containing the telescope bay on the South end of the building and a control room on the North side. The roof-supporting frame and the control room are built on a foundation that is a separate concrete pour from the telescope’s mounting pier. On the mounting pier in the telescope bay, the telescope has the freedom to move in altitude from  $30^\circ$  to  $120^\circ$ . Observations of low altitudes are made possible by a set of barn doors that are opened using electric linear actuators. The observatory’s 3.5 ton roof is hung by 120 heavy duty rollers that move within steel box track channels. The roof rolls North along an extended steel structure to expose the telescope to the sky. A custom motor controller engages a 3/4 HP motor to pull the roof open and closed using a steel cable wound around a thick stainless steel worm gear. The control room is fully enclosed, insulated, and temperature controlled with electric heaters in the winter and a wall mounted A/C unit in the summer. The observatory’s electronics are stationed in the control room, protected from the elements. Remote observations are enable by a cable-internet connected server PC that communicates and controls many observatory sub-systems. A server-connected power relay switch-box



Figure 2.2: The wood-facade, steel truss observatory building has a roof that moves onto a steel support structure to the North along enclosed box tracks to expose the all-sky telescope. Barn doors open to the south for observations at low declinations. The Harvard clad object within is the author. Photo Credit: Paul Horowitz.

controls power delivery to the telescope, camera, lights and other equipment. The control room also houses three uninterruptible power supplies so that the server may close the roof and shut down gracefully in the event of a power failure.

## 2.3 Telescope

The telescope is a  $f/2.5$  quasi-newtonian design with a 1.8 m primary mirror and a  $22.5^\circ$  offset 0.9 m flat secondary. The primary is held in a frame constructed of 2" square steel

tubing and the secondary is suspended in front of the primary with a welded spider structure. The camera is mounted outside the frame on the Eastern side midway between the primary and secondary mirrors. The telescope pointed towards the Southern meridian, moving freely on horizontal shafts along the East-West axis. Bearings welded in the frame allow the telescope to rotate on horizontal shafts mounted to tubular steel risers atop the concrete telescope pier. The telescope axis is about three feet off the ground and the interior of the telescope pier is a pit that allows the primary end of the telescope to rotate below ground level. A six foot diameter, laser-cut stainless steel ring is mounted to the telescope and driven by a stepper motor in spring-loaded pressure contact to actuate telescope rotation. Weights are added to the frame, behind the primary mirror, to balance the telescope.

The primary mirror is spherical and figured to a point spread function of 1–2 arcminutes, comparable to the spherical aberration of the  $f/2.5$  mirror. Higher quality optics are not required because the size of the photomultiplier pixels are 2 mm, or about 2 arcminutes in angular extent at the focal plane. While a parabolic mirror would have much less optical aberration on-axis, the all-sky system needs a field-of-view of nearly  $2^\circ$ . For an  $f/2.5$  parabolic mirror, at  $1^\circ$  off-axis the aberration from coma almost 2 arcmin, similar to the aberration of a spherical mirror. Using a spherical mirror, as opposed to parabolic, simplifies the polishing operation, thereby reducing its ultimate cost. The spherical mirror was the optimum choice as it provided the same performance at a lower price.

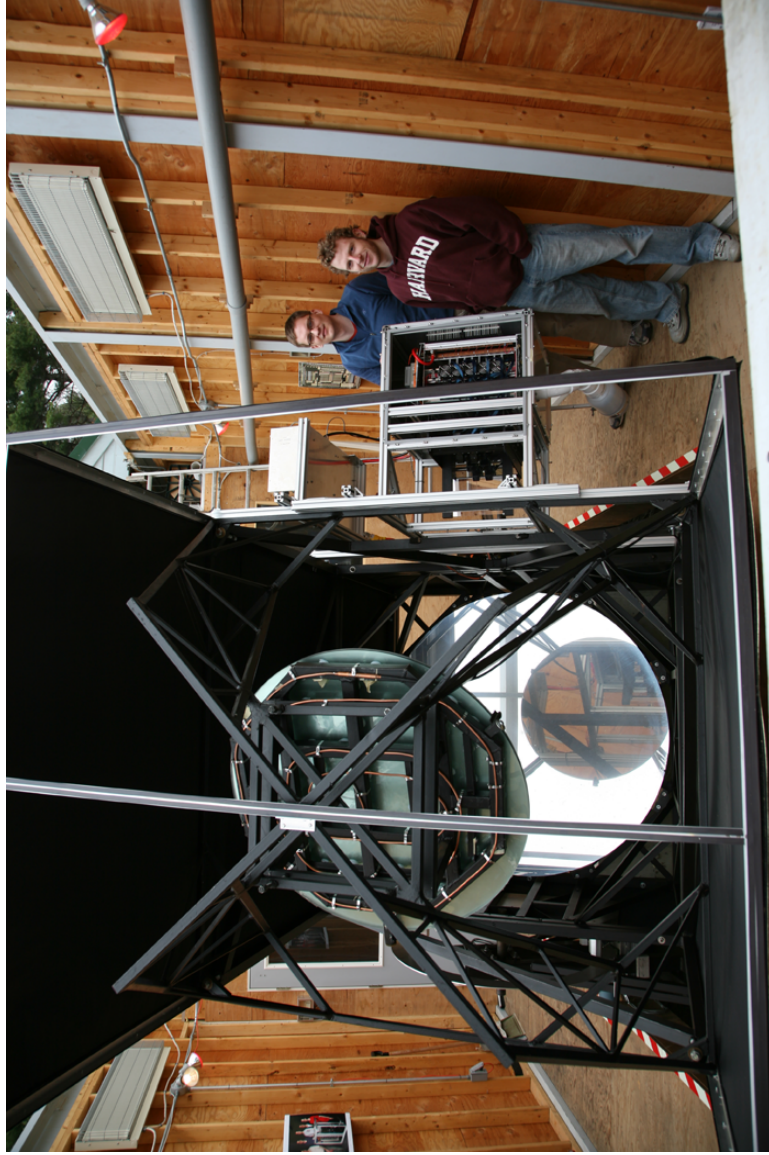


Figure 2.3: The telescope's black welded frame is seen here with the 1.8 m spherical primary mirror in the background and the back of the 36'' secondary in the foreground. To the right, Andrew Howard (background) and the author (foreground) are standing next to the SETI camera. Photo Credit: Paul Horowitz.



## 2.4 SETI Camera

The camera is composed of an optical front end – the shutter, beamsplitter, and photomultiplier tubes – and an electronics back-end that receives signals from the photomultipliers over short cables. The electronics digitize the signals, filter the digital waveforms for coincident pulses, and send acquired waveforms to a host computer for long-term storage. The camera frame is 36" deep with a 27"  $\times$  24" cross-section and is constructed of 1.5" square Rexroth aluminum extrusions. It is skinned with 1/16" aluminum plates that have gasketing material where the plates join the camera to seal against dust and moisture. Internally there are two compartments, one for the photomultiplier tube cage and one for the circuit board rack. The circuit board rack has 10 blower fans and 10 exhaust fans to carry the heat from the circuit boards to the walls. As the camera is sealed, heat is dissipated through large heat sinks that are mounted on the internally and externally surfaces of the back and right-hand side skin plates. To keep the internal camera air dry, a bottle filled with silica gel desiccant is attached to the bottom skin plate of the camera through a 3" PVC pipe and light baffle<sup>1</sup>. Power and communication enter and exit the camera through connections on the top rear plate. An additional 5" square window port on the front right-side skin plate allows visual access to the image plane without obstructing the entrance window.

### 2.4.1 Optical Front End

The light from the telescope enters the camera through an entrance window that keeps the camera sealed. The light passes through a 60/40 beamsplitter angled at 45° to the light path. Roughly half the light is transmitted through the beamsplitter onto a staggered array of 8 photomultiplier tubes and half is reflected onto an identically arranged set of 8 photomultipliers in the PMT cage. The photomultiplier tubes are from Hamamatsu Photonics, model H7546B-01 and are sensitive from 250 nm to 800 nm with a peak quantum efficiency of 20% at  $\sim$ 350 nm. Each photomultiplier has an 18.1 mm square glass envelope with an 8  $\times$  8 pixelated array of anodes which covers a total of about 0.2°  $\times$  0.2° of the sky. They are not directly abutable so they are spread out laterally (Right Ascension) and then offset

---

<sup>1</sup>a.k.a petahertz field annihilator

vertically (Declination) on the image plane. The photomultipliers are mounted on two rows, four across on a  $0.6^\circ$  pitch in right ascension and a  $0.2^\circ$  pitch in declination. This creates a  $1.6^\circ \times 0.2^\circ$  declination stripe of active photomultiplier area across a  $2^\circ \times 0.8^\circ$  field-of-view due to the separation of the PMTs. The two sets of PMTs are aligned to view the same areas of the sky. PMTs are mounted into female sockets on PMT circuit boards that are held by Elma enclosure hardware within a custom machined aluminum, black-anodized PMT cage.

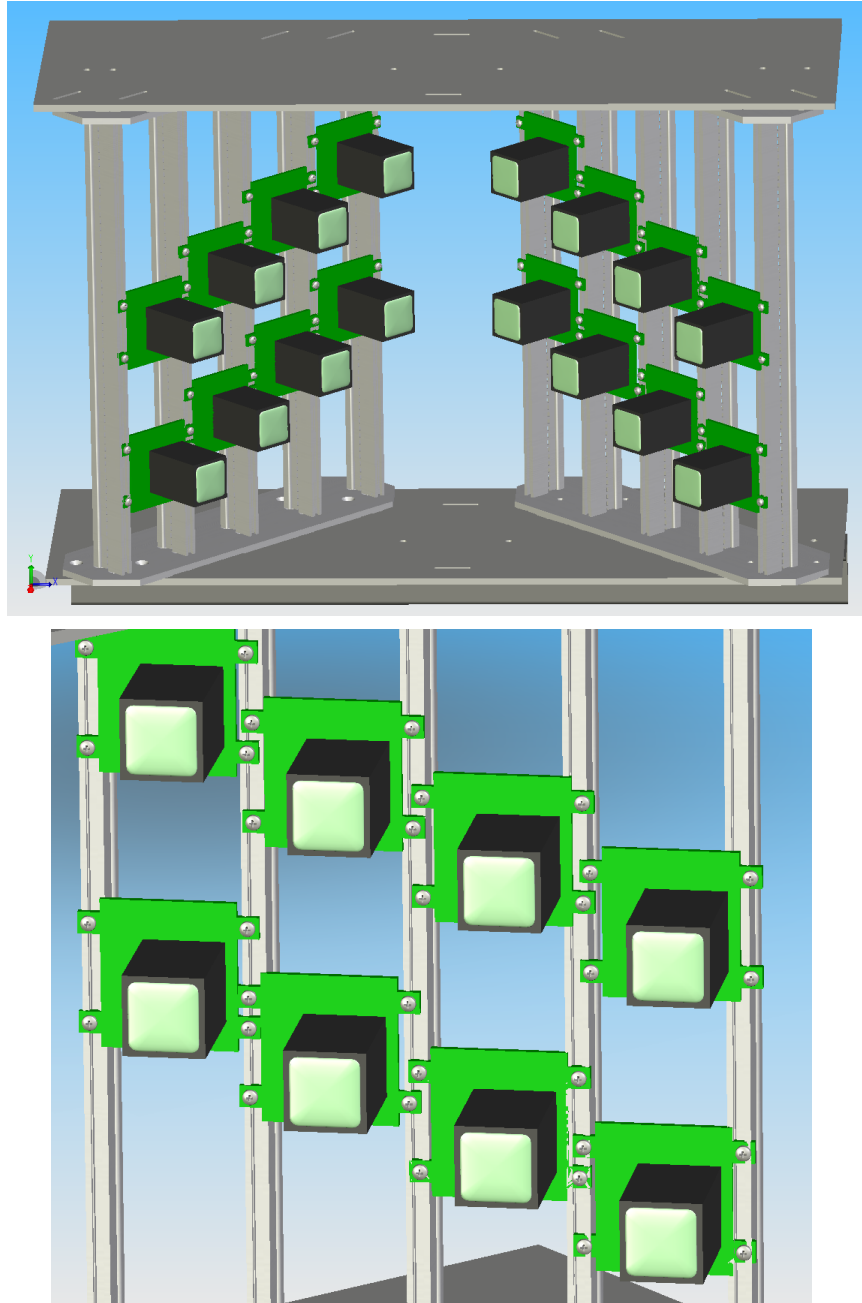


Figure 2.4: These 3D models show the photomultipliers (black) mounted onto the PMT circuit boards (green) mounted to Elma rail hardware with the custom machined PMT cage. The beamsplitter, which is mounted in a machinable plastic base along the line of symmetry between the  $90^\circ$  PMT image planes, is not shown here.

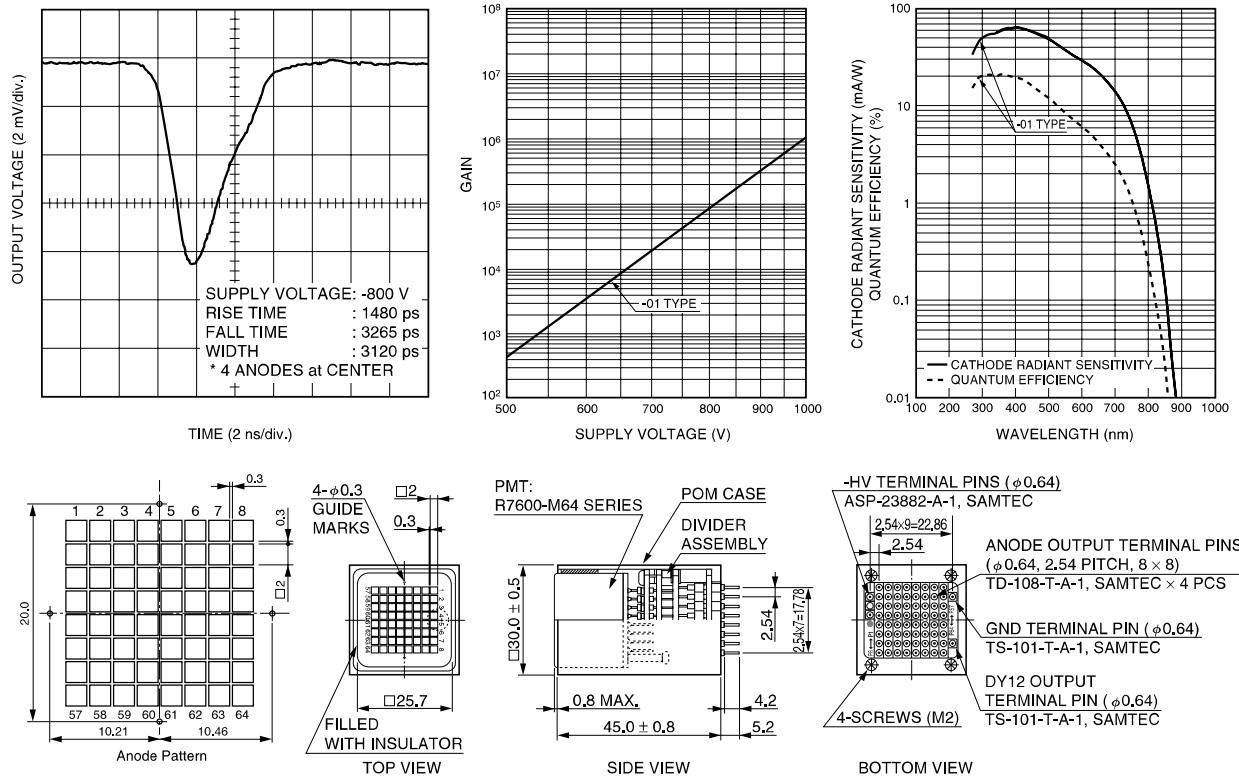


Figure 2.5: The Hamamatsu H7546B photomultiplier assemblies use the R7600-M64 tubes with an  $8 \times 8$  anode array. They are available with numerous different cathode chemistries; the original all-sky system used the -01 multialkalai model [33].



### 2.4.2 Electronics Backend

The camera electronics are split onto 8 daughterboards that plug into a main motherboard. The daughterboards handle amplification, digitization, and waveform capture of the photomultiplier tube (PMT) signals. The motherboard provides global signals like clocks, analog reference voltage, GPS signals and power to the daughterboards. The photomultiplier tubes plug into sockets on individual PMT circuit boards that also contain an adjustable 600 V to 900 V potted DC-DC power converter. Two flat ribbon cables, each containing 40 individual coaxial lines, connect the 64 photomultiplier tube anode signals, +15 V power, and a high voltage sense line from a PMT circuit board to the daughterboards. The daughterboards have four PMT cable connectors to provide connections to two PMTs, a beamsplitter transmission-side PMT and a reflection-side PMT. The low voltage PMT signals are amplified by NEC 2710TB MMIC amplifiers with a fixed 30 dB gain and 1.5 GHz of bandwidth. After amplification, the signals are fed into PulseNet, a full-custom integrated circuit (ASIC) developed by Andrew Howard [38] specifically for the original optical SETI. PulseNet performs 3-bit flash conversion at up to 1 Gigasample-per-second on 16 analog input signals pairs. Each daughterboard has four PulseNets in order to handle 64 PMT anode pairs. When a coincident pulse arrives on an input pair, PulseNet directs the data stream from that pair into a 512 sample deep buffer for temporary storage. PulseNet activates an output pin that notifies a Silabs C8051 microcontroller on the motherboard that a “coincidence” has occurred and the microcontroller serially shifts the data from the buffer out of PulseNet. The microcontroller places the data in a dual-ported RAM that can also be accessed on its other port over a legacy PC104 (ISA-like) bus. The PC104 bus spans the motherboard and is controlled by a Diamond Systems PC104 single-board computer (SBC). The SBC communicates with the 8 dual-ported RAM chips on the motherboard to acquire the coincidence data and forwards it over ethernet to a database computer. PulseNet also provides an “astronomy mode” where a counter is incremented for every sample that is over one of the seven reference voltages. This astronomy mode is meant to count single photoelectron pulses and be able to observe stars transiting across the PMTs. Only one input pair and one reference voltage can be used in astronomy mode at a time. In addition to the microcontroller and PC104 bus for data readout, the motherboard provides a mooring

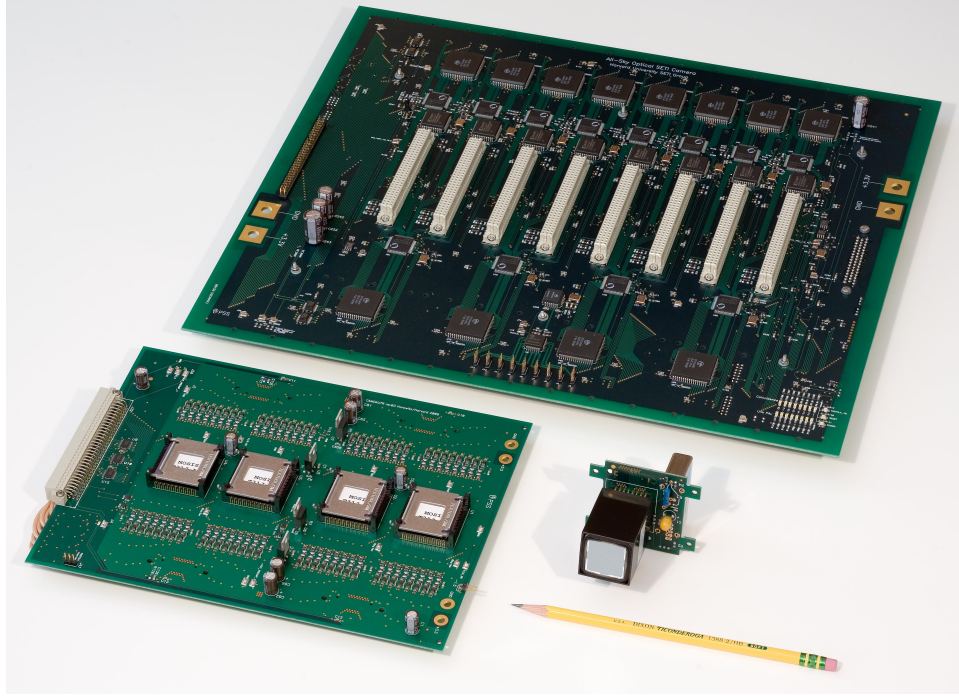


Figure 2.6: The original AsCam motherboard (top) connects eight daughterboards (bottom left) to sixteen photomultiplier tubes (bottom right). Board schematics by Chris R. Laumann and layout by Pratheev Sreetharan. Photo Credit: Paul Horowitz.

for daughterboards and some global signals. A clock distribution chip on the motherboard provides a 300 MHz LVPECL clock signal to each daughterboard. GPS signals, a 10 MHz clock and a one-pulse-per-second clock, are distributed to the PulseNets via the motherboard connector. PulseNet has a GPS counter that uses these signals to attach a GPS timestamp to every coincidence data message that gets read out by the microcontroller along with the 512 ADC samples. Reference voltages that set the flash ADC levels are produced by a DAC on the motherboard and distributed to all daughterboards. The motherboard also provides microcontroller readout of a humidity and temperature sensor.



Figure 2.7: Gelfand Flashers I and II. Photo credit: Paul Horowitz.

## 2.5 Observatory Equipment

### 2.5.1 Test Instruments

Two test instruments are installed at the observatory to verify that short light pulses will successfully be captured by the all-sky system. These are the Gelfand Flasher I (GFI) and the Gelfand Flasher II (GFII). An end-to-end test with one of these instruments provides assurance that the photomultiplier tubes are powered, the camera electronics are correctly programmed, and coincidence events are being stored in the experiment database. The GFI is located inside the AsCam, within view of all photomultiplier tubes. It uses a small blue LED to present a  $\sim 100$  ns pulse bright enough to bring the PulseNet ADC output to the maximum level. Normally, one pulse from the GFI will trigger all 32 PulseNets. A test flash is performed at the start of every half-hour observation, using the GFI, so that subsystem failures or programming errors are recognized before an observation begins. Because the GFI is inside AsCam, tests can be performed at night, or even in the daytime with the shutter closed. In contrast, the GFII is external to the AsCam, located just in front of the center of the primary mirror. A lens system and steerable mirror on the GFII allow a light pulse from an LED to be projected onto any pixel in the AsCam's PMT array. The GFII, then, is able to selectively test individual pixel pairs, rather than the entire array, as with the GFI. The GFII's pulse is of much lower intensity than the GFI's, so it can also be used to compare the sensitivity variations of different photomultiplier tube pixels.

## 2.5.2 Environmental Sensors

Remote and semi-automated operation of the all-sky telescope requires accurate knowledge of the environment. The observatory employs multiple sensors keep the observer and control software informed of the state of the observatory. Some of the sensor subsystems have hardware enforced interlocks to prevent the observatory or equipment from being damaged.

### Daylight Sensor

Daylight poses two dangers to the all-sky survey. First, were the roof to remain open during the daytime, the sun could reflect off the telescope primary mirror and be focused onto an inner wall of the observatory building, a potential fire hazard. Second, as the photomultiplier tubes can be damaged by exposure to sunlight, observations should not be started during daylight hours. For these reasons, a light sensor connected to the roof controller provides the system with a binary indication of day or night. The sensor consists of a wavelength-shifting fiber, positioned on the North wall of the observatory building, and a photodiode connected to the end of the fiber. The photodiode is read by the roof controller. Sensitivity can be adjusted via a trimmable comparator setpoint. The roof controller will not allow the roof to open and will force closure of the roof after a timeout period of one minute when daytime is sensed.

### PMT HV Lockout Sensor

Too much light can be damaging to the photomultiplier tubes, especially when powered, so a photodiode is placed near the photomultipliers to measure the average light level. If the light level exceeds an adjustable threshold, the power relay to the PMT +15 V supply is de-energized, preventing PMT damage.

### Rain Sensor

Rain, sleet, and snow are common threats to buildings with removable roofs and sensitive electronics inside. The observatory has two rain sensors to detect falling moisture. The rain sensors consist of two inter-digitated copper strips to which a low voltage is applied across. Moisture on the surface of the sensor allows current to flow between the copper strips. The

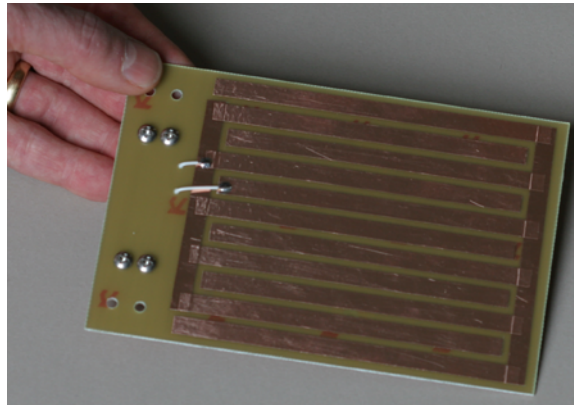


Figure 2.8: The observatory has two rain sensors, one of which will force roof closure if rain is detected. Photo Credit: Paul Horowitz.

current change is sensed by the roof controller. One rain sensor is located outside on the West wall of the observatory, and the other is within the telescope dome, only exposed to the elements when the roof is opened. The roof controller will force the roof to close after a timeout period if moisture is sensed from the dome rain sensor. The outside rain sensor is not wired to force roof closure as snow often falls onto the sensor when the roof is opening in the winter.

## **Weatherstation**

A Davis weatherstation collects traditional weather facts such as outside and inside temperature, wind speed and direction, barometric pressure, and rain volume. These environmental data are periodically read and stored in the all-sky experiment database. The weatherstation consists of a base unit with LCD display, mounted in the control room, that connects serially to Costas (server PC) and the wireless, solar-powered unit that is mounted outside on a pole at the end of the building's South-East roof rail.

## **PTZ and Web Cameras**

Web cameras are strategically mounted around the observatory building for visual indication of the observatory state. The four web cameras have views of the control room, the telescope from behind, the telescope from the front, and the area outside the entrance to the



Figure 2.9: A wintery scene of the observatory from the pan-tilt-zoom IP security camera.

building. Camera images are acquired and stored on Costas using a four-input video-capture card.

A pan-tilt-zoom (PTZ) IP security camera is located in a separate building  $\sim 200$  ft from the all-sky building. The PTZ camera looks through a window with view of the all-sky building and the surrounding area. It provides a live image from the observatory at about one frame-per-second.

## GPS

A Symmetricom GPS receiver provides a time reference to Costas (the observatory's server computer) and to the AsCam so that events can be timestamped with a high quality time reference. The GPS receiver is connected serially to Costas and sends timestamps in a coded text stream. The GPS timing reference 10 MHz and 1 PPS clocks signals are distributed to the AsCam using custom copper-to-fiber-optic transmitter at the GPS receiver and a matching fiber-optic-to-copper receiver at the AsCam. The GPS receiver antenna is mounted atop the pole to which the outdoor wireless weatherstation unit is mounted.

### 2.5.3 Networking

The network at Oak Ridge Observatory consists of a Charter cable internet connection, a VPN that connects to the Harvard internal network, a Cisco 851 router to isolate the all-sky

building from the rest of the Oak Ridge network, an Axis 214 PTZ IP security camera, and a number of ethernet enabled seismographs. Inside the all-sky building, Costas connects to the all-sky camera through one ethernet port and to the Cisco 851 through its other ethernet port. The camera connection is run through 10 Mbit/s ethernet-to-fiber converters. Three uninterruptible power supplies (UPSs), which support the roof controller, Costas, telescope drive, and other critical systems during a power outage. One UPS is connected serially to Costas to enable automated shutdown in the event of a loss of mains power.

## 2.6 Observatory Control

A PC running Ubuntu Linux is used to enable web control of the AsCam, telescope, and other observatory equipment. Named after Costas Papaliolios (1931-2002), this PC located in the observatory control room acts as web and database server. To perform observatory control operations, Costas must be running the `oseti.py` python application, which serves up the all-sky web interface (Firefox and Chrome compatible). The python application and web interface was developed by Jason Gallicchio, Andrew Howard, Steve Howard, and the author.

From the web interface, the roof can be opened, the telescope can be positioned, and the AsCam can be programmed. Most observatory infrastructure can also be controlled from Costas using its array of serial ports, USB ports, and ethernet connection. [Figure 2.10](#) shows the interconnections between the server and observatory equipment.

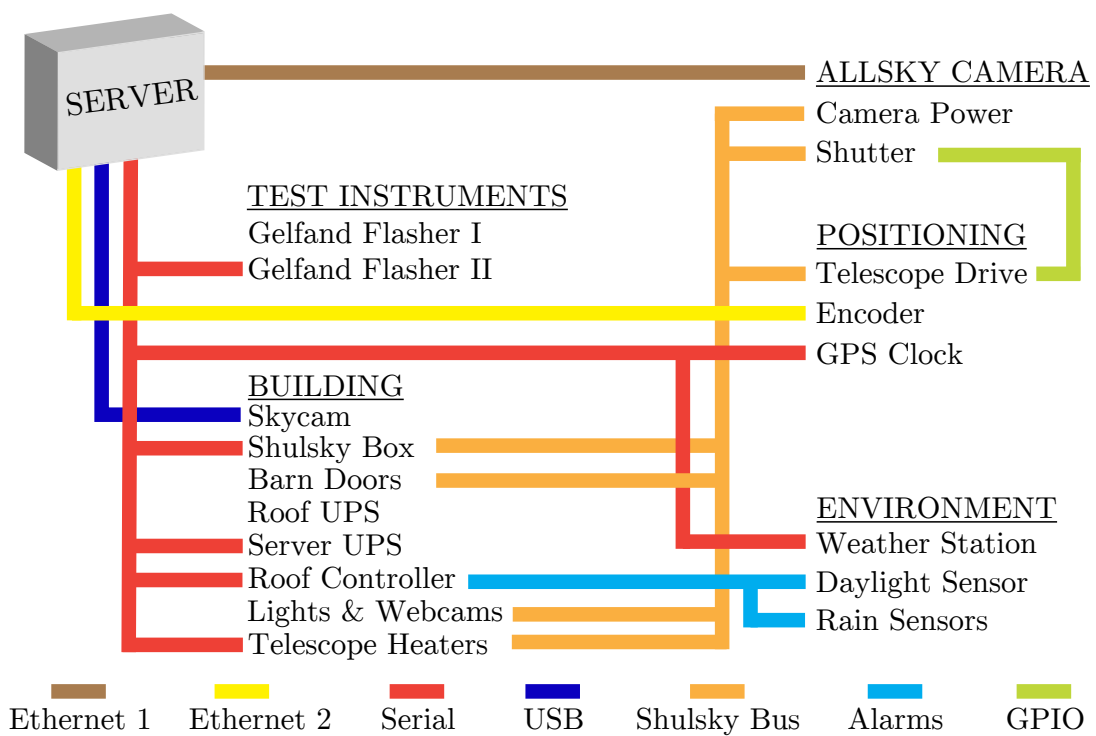


Figure 2.10: Costas connects to many instruments in the observatory to enable completely remote observations.



### 2.6.1 User Interface

Observations are controlled through a web interface which is provided by Costas through the `oseti.py` application. The interface consists of a viewer frame and many subpanels (Figure 2.11). The frame provides a snapshot of commonly needed information such as the sidereal time, temperature, humidity, and telescope and roof positions at the top of the frame. A sidepanel on the left allows the user to open different subpanels. Subpanels are listed by category; for example, the roof and telescope subpanel in the observatory category has buttons and input forms for opening and closing the roof and moving the telescope to the desired elevation. A weather forecast panel, for convenience, provides a moving radar and satellite image from Accuweather.com. The most often used panels are for DAC, PMT, and PulseNet programming.

An important feature of the user interface is for viewing the results of a night's observations. This is accomplished through the use of the “event view” panel. During observations, the state of the camera, telescope, observatory and accompanying hardware is recorded in a database whenever an “event” occurs. Many different types of events are defined. Examples of events include a change to the programming state of the camera, receiving a position update from the telescope encoder, or the stoppage of an observation. All of these events may be inspected by using the event view panel. The “Coincidence” events are recorded every time the camera is triggered and these are the events of most interest after an observing run. The Coincidence events, which consist of sampled data from a pair of PMT pixels, will be displayed textually upon the click of a mouse and also graphically in the “Event Display” panel.

Nightly observations can be automated from the user interface. The “Automation” subpanel offers input controls for setting an observation schedule, scheduling downtime, and viewing scheduled observations. When placed into “automatic observation” mode, a state machine is enabled which goes through a checklist for opening up the observatory, readying all electronics, and determining the next observation declinations if none are already set, and closing the roof and telescope before dawn twilight. To aid in planning observations, completed, scheduled, and current observations can be explored on an interactive skymap in the “Stars” subpanel.

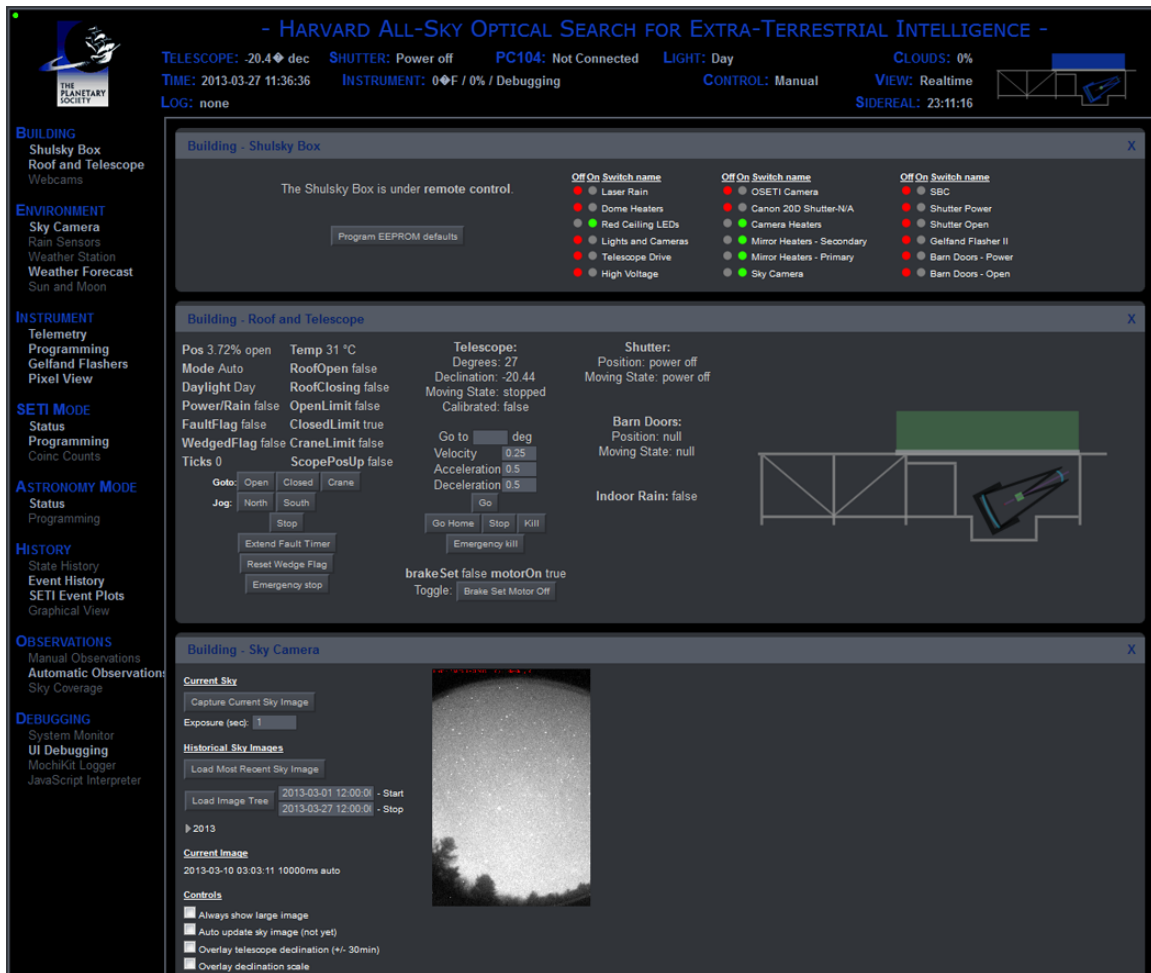


Figure 2.11: From the user interface web page, the experiment can be controlled remotely. We see in this image a quick view of observing information along the top, links to panels on the left, and three open panels—the power control panel, the roof and telescope panel, and the skycam panel.

## 2.7 Limitations

The all-sky system is a novel design but, being the first of its kind, it has a number of drawbacks. Some of the drawbacks were intentional trade-offs made to reduce costs, some are related to design errors, and others became apparent only after observing operations began. This section lists the issues with the all-sky system that could be improved.

### 2.7.1 Spectral Sensitivity

Longer optical wavelengths are more appealing for interstellar signals if the distance between civilizations is great. This is because there is three to four times less extinction, on average, at  $1\ \mu\text{m}$  than there is at  $550\ \text{nm}$ . The mid-infrared is even more advantageous with  $\sim 50$  times less extinction at  $8\ \mu\text{m}$ . For ground based observations, we are limited by the atmospheric absorption in the infrared. As a practical matter, we are also limited by detector performance, cost, and convenience. For the all-sky survey, a large active area is desirable, but the pixel size must be limited to reduce the night sky background and cosmic ray sensitivity. A fast rise time ( $< 2\ \text{ns}$ ) is important for the same reasons. The sweet spot for price and performance at the commencement of the all-sky survey were the H7546B-01 multipixelated photomultiplier tubes from Hamamatsu. These PMTs do not need to be cooled to reduce dark count (as contrasted with IR-sensitive detectors), adding to their convenience factor, but they only offer quantum efficiency above 5% between  $300\ \text{nm}$  to  $600\ \text{nm}$ . Since the original all-sky camera (AsCam) was built, Hamamatsu's manufacturing process has improved and the H7546 PMTs are available with extended red sensitivity (up to  $900\ \text{nm}$ ) and 5% quantum efficiency out to  $850\ \text{nm}$ . Improved sensitivity at longer wavelengths would make the all-sky survey a novel experiment again and extend the range and number of stars surveyed, especially in the galactic plane where extinction is higher.

### 2.7.2 One Sample Buffer Per PulseNet

Owing to the available silicon, the PulseNet ASICs were designed so that when one of its 16 flash ADC channel pairs received a coincident pulse, only that one channel pair was switched into a sample buffer to store the trigger waveform. Hence, only the waveform from

that channel pair is recorded and the information in the other 15 pairs is lost. A situation where this information could be important is with a cosmic ray Čerenkov flash. The Čerenkov flashes from cosmic ray induced extensive air showers (EAS) generally subtend  $1\text{--}2^\circ$ . This imaging information is traditionally used in very high energy gamma ray astronomy to distinguish gamma rays induced EAS from hadron induced EAS but it can also act as an anti-coincidence for pulsed optical SETI. A system with full buffer capture for every pixel pair would enable some cosmic rays to be distinguished from distant laser pulses.

### 2.7.3 Sample Depth

The sample buffer for PulseNet is 512 samples deep, enough room to capture 853 ns at the normal operating sampling speed of 600 Megasamples-per-second (MSPS). This is more than enough samples storage for a  $1\text{--}10$  ns pulsed laser beacon waveform of the type proposed in [Chapter 1](#). A solitary pulse is not a convincing pulsed laser signature, however. Many different noise sources (see [§ 1.3](#)) can create nanosecond pulses in fast photodetectors. Multiple pulses would need to be received to make a positive detection. Therefore, a long sample buffer is needed to record for as long as possible after a triggering pulse in order to capture any subsequent pulses. Additionally, some noise sources, airplane strobe lights for example, create flashes of light microseconds long and bright enough to trigger the camera. These noise sources could more easily be identified and characterized if the entire microsecond flash can be captured.

### 2.7.4 Triggering

The PulseNet ASICs can only be triggered by an over-threshold coincident pulse on paired flash ADC inputs. There is no accommodation made for an external trigger. This independence is limiting in that if a flash of light is bright enough to trigger only one pixel, the waveform is only available from that pixel and no others. The adjacent pixels may carry information about the brightness or shape of the image which can be used to distinguish noise sources. For example, a cosmic ray Čerenkov flash that is just bright enough to trigger one pixel will appear to be consistent with a distant laser pulse. The extended  $1\text{--}2^\circ$  structure of the Čerenkov light will go unnoticed. If a system-wide trigger was implemented, where

a single pixel coincidence would trigger waveform readout for all pixels in the array, weak Čerenkov flashes could be distinguished from possible pulsed laser sources.

### **2.7.5 Sampling Rate**

The rise time of the photomultipliers used in the all-sky survey is 1-2 ns so the sampling rate for PulseNet was targeted for 1-2 gigasamples-per-second (Gsps). While some production PulseNets can sample at 1 Gsps with increased power supply voltage, the all-sky system is conservatively operated at a sample rate of 600 Msps for all PulseNets. A higher sampling rate is desirable in order to match the bandwidth of the detectors. At 600 Msps, some single photo-electron pulses can be missed. In addition, faster sampling offers better time resolution and possibly the ability to compare the time structure of multi-pixel triggers.

### **2.7.6 Communication Bandwidth**

In the original all-sky camera, readout of coincidence data was accomplished using a microcontroller to serially shift the data samples out of the PulseNet sample buffer. The microcontrollers sent the data to dual-ported RAM which was addressable on a legacy ISA-bus using PALs for address decoding. A single-board computer (SBC) connected to the ISA-bus of the camera’s motherboard, read the data, and sent it over ethernet to a database computer. The total trigger dead-time from this low bandwidth connection was on the order of hundreds of microseconds. The dead-time could have been lowered by increasing the bandwidth to the camera. This would be especially important if a system-wide trigger were implemented and the sample depth was increased since a coincidence event would contain much more data.

### **2.7.7 Astronomy Functionality**

Counters were added to PulseNet so that the arrival rate of single photo-electrons could be counted, giving an indication of the average night sky background light level. The hope was that the telescope pointing could be calibrated by using these counters in an “astronomy mode” to register the stars transiting the photomultiplier tubes. The astronomy functions

were fairly limited however. Only one out of the sixteen PulseNet channel pairs could be used in astronomy mode at any one time. The acquisition a one second integration for every pixel in the camera takes a minimum of sixteen seconds. At least two cycles are needed in order to calculate a difference between pixel counts, and for the all-sky system, the minimum transit time of a star crossing a photomultiplier tube is 48 seconds. The precise timing needed to capture a star transit made the task very difficult. The astronomy counters increment for every sample that exceeds the selected reference voltage, so it is not strictly counting photo-electron pulses. Additionally, the threshold bias offsets across PulseNets can be up to 50 mV or more, making counting of pulses below 50 mV impossible for some channels and inconsistent for others.

To address these shortcomings of the original all-sky system (AsCam), we designed and built a second-generation pulsed optical all-sky SETI system, described beginning in the next chapter. The new system implements the PulseNet ASICs in FPGA hardware. The FPGA design of the new implementation, called PulseNet-V, is detailed in [Chapter 3](#) and the full second-generation camera implementation, the Advanced All-sky Camera (AdvCam) is described in the following chapter, [Chapter 4](#).

# Chapter 3

## PulseNet-V

The main engineering challenge of the all-sky survey is to digitize and record 1024 analog voltages, the photomultiplier tube anode outputs, at gigasample per second speeds. The most straightforward solution to that end, using commercially available analog-to-digital converters, at a price of  $\sim$ \\$200 and consuming 2 watts each, would result in an overly large, power hungry, and expensive system. When the all-sky survey was first conceived circa 1999, the most promising solution was to build a custom integrated circuit (IC) to perform the analog-to-digital conversion and recording task. The result was PulseNet, an IC able to convert 32 channels (16 pairs) at up to 1 gigasample per second and hold 512 samples of any one channel pair when triggered [38]. This was enough to get the survey started, but after years of use, its limitations became more clear. A commercial part was eventually found which could be programmed to meet the specifications of the original PulseNet. PulseNet-V, built on a Xilinx Virtex-5 field programmable gate array (FPGA), is the next generation digitizer and signal processor for the all-sky survey. A unique feature is the use of groups of LVDS input pairs to form low resolution, high-speed flash ADCs. A single FPGA can accommodate 32 such ADCs, with demonstrated simultaneous conversion rates up to 1.5 gigasamples-samples-per-second. PulseNet-V has many more programming options compared to the previous PulseNet ASIC. For example, the ADC channel pairs can be unlinked to disable the coincidence requirement in the trigger hardware, and the number of post-trigger samples can be changed from 0 to 65,534 (however the number of total samples per channel is always 8,192). Because the Virtex-5 is a commercial part, it was available

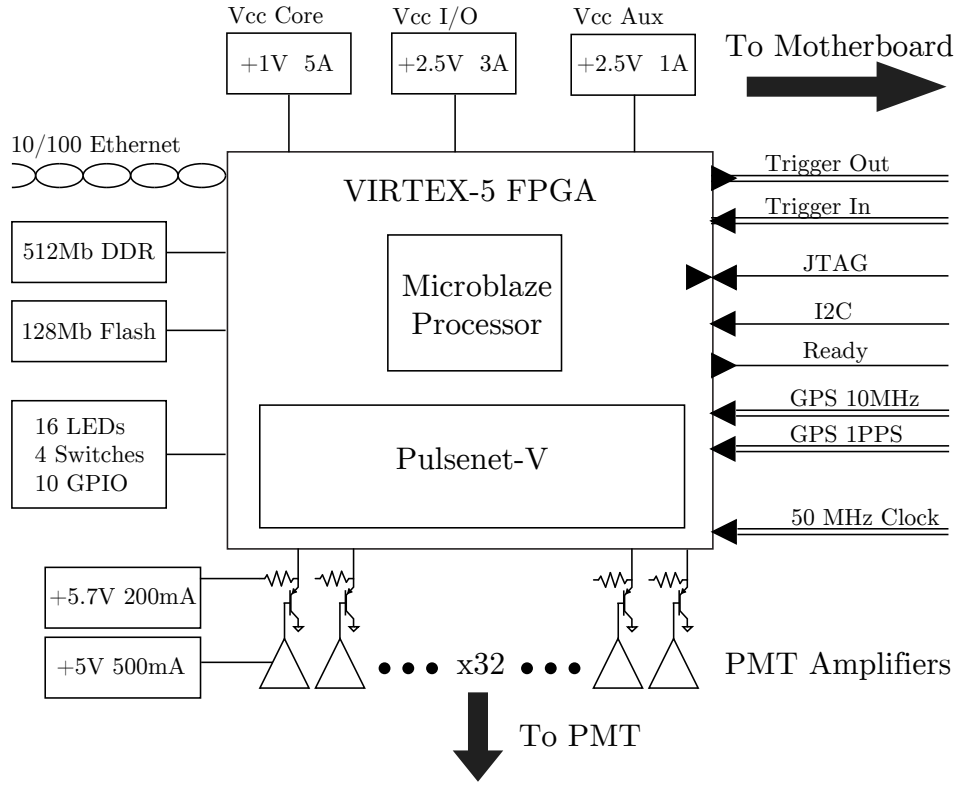


Figure 3.1

immediately and did not require a long IC design effort by us. Most importantly, as the Virtex-5 is an FPGA, it is inherently re-programmable allowing design changes which can be applied incrementally. The operation of the PulseNet-V can be frequently changed as needed from our Cambridge laboratory to allow new modes of operation to be explored.



Table 3.1: PulseNet-V At-A-Glance

---

**Description**

The Pulsenet-V is an FPGA design for pulsed optical SETI. It combines 256 LVDS inputs into thirty-two, 8-level flash ADCs. Samples are stored in 8k block RAM circular buffers. Coincident pulses on channel pairs cause the digitized waveform in block RAM to be uploaded to a host computer over ethernet.

**Capabilities**

32 flash ADC channels  
 Sampling up to 1.5 Gsps, 8 level, 3-bit resolution  
 8192 sample depth per channel  
 2 pulse counters per channel

**Triggering**

Channels can be independent or linked for coincidence triggering  
 Adjustable coincidence window  
 Adjustable number of post-trigger samples (0–65,534)  
 External trigger input and output for system-wide triggering

**FPGA Design**

Microblaze processor with PLB peripherals  
 PulseNet core peripheral with 68 config registers

**Hardware**

Xilinx Virtex-5 FPGA  
 1153-pin BGA package, 1 mm pitch  
 800 single ended I/O or 400 differential  
 17k logic-blocks, 4.6 Mbits block RAM

**Communication**

10/100 Mbit Ethernet MAC  
 I<sup>2</sup>C bus  
 RS-232 serial

**Configuration**

FPGA configured over JTAG or with parallel flash at power-up  
 FPGA configuration and bootloader stored in parallel Flash  
 Flash programmed indirectly over JTAG or by FPGA within Linux or U-boot

**Software**

OS is a Linux kernel running on Microblaze  
 SETI daemon responds to control messages over ethernet  
 Astronomy daemon continuously sends pulse counts over UDP  
 Telnet interface for command-line access

**Power**

2.8 A @ 1.0 V  
 2.4 A @ 2.5 V

### 3.1 Design Overview

PulseNet-V's main function is to digitize 16 analog signal pairs, filter the digital streams for coincident pulses, store the coincident pulse waveforms, and transmit the waveforms along with a timestamp to a waiting database server. A flash analog-to-digital conversion topology is used for digitization of each analog input at speeds of up to 1.5 Gigasamples-per-second. For each channel, eight LVDS input pairs combine to form an 8-level flash converter. The positive pin pair is the analog input and the negative pin is one of eight reference voltages  $V_{\text{REF}}(7:0)$ . The digitized output from the flash converters are sent to both a triggering circuit and a block RAM circular memory buffer (8192 samples deep) for storage. The triggering circuit monitors a pair of flash ADC channels and waits for the pair to exhibit outputs levels greater than or equal to a pre-selected  $V_{\text{REF}}$  level within an adjustable time window of two to ten clocks. A valid trigger starts a state machine which allows digitization to continue for an adjustable period of time to fill the circular buffer with post-trigger digital samples. The state machine then stops conversion for all input pairs and notifies a processor via an interrupt signal. The processor runs an interrupt service routine that bundles together the conversion data held in the circular buffers from all 16 input pairs and transmits that data over Ethernet to a database server. Most of this activity occurs within the pulsenet core, which is a peripheral of the Microblaze processor. The pulsenet core communicates with the processor over the processor local bus (PLB). Configuration registers that control the pulsenet core's adjustable settings such as post-trigger samples and coincidence window are available as memory mapped registers on the processor local bus.

A second function of PulseNet-V is to use counters to keep track of the rate at which pulses are arriving on each of its 32 analog inputs (16 pairs). The pulses represent photons arriving at the photomultiplier tubes. Since the pulse rate is proportional to photon arrival rates, the pulse counts measure the intensity of light hitting the PMTs. The level of night sky background and starlight can be acquired for each photomultiplier tube anode, thus forming a crude astronomical sky image. The counters represent the "astronomy mode" feature of PulseNet-V. The pulse counting block consists of a 24-bit counter that is incremented for every clock sample that is above one of the eight selectable  $V_{\text{REF}}$ 's. Alternatively, the counter can be configured to increment for every positive or negative edge. A timer counter causes

the 32 pulse counter values (one per channel) to be transferred a set of processor readable registers every 0.75, 2, 4, or 10 seconds. A program running on the processor reads the pulse counter values periodically and transmits them over Ethernet to a database server.

Proprietary modules of the PulseNet-V design are coded in VHDL (VHSIC Hardware Description Language) and are targeted for the Xilinx Virtex-5 1153-pin LX110 FPGA (field programmable gate array). FPGAs are reprogrammable integrated circuits that contain many general purpose logic gates (configurable logic blocks), RAM blocks, PLLs, I/O blocks, and other digital elements but the interconnections between elements is left to the designer. Depending on the connections, anything from a simple AND logic circuit to a complete processor with floating point instructions and a memory management unit could be constructed out of the available on-chip digital elements. The Virtex-5 used here (part#:XC5VLX110FF1153-3) has 17,280 configurable logic blocks (CLBs), 4,608 kbits of available RAM blocks, 6 clock management tiles (CMTs) each containing a PLL, and 800 single-ended I/Os. Its selection was mainly based on needing a minimum of 256 differential I/O pairs so that thirty-two 8-level flash ADC converters can be formed. Having thirty-two channels allows the PulseNet-V to fit the same motherboard/daughterboard form factor of the original all-sky system. Secondary considerations required that there be enough logic space available for a Microblaze soft-core processor and at least 64 block RAMs for the flash converter sample memory. These secondary considerations were more than accommodated by choosing the smallest LX device in the 1153 ball-grid package size. The processor and pulsenet core, which includes the flash conversion, triggering, and pulse rate counters as describe briefly above, are constituted from these digital elements (via VHDL code), but the pulsenet core is just one of many peripherals attached to the processor's bus. Additional peripherals include the Ethernet MAC, external flash memory controller, synchronous DRAM controller, interrupt controller, I<sup>2</sup>C controller, system timer, and others. A custom Linux kernel, with a specialized driver module for the pulsenet core, coordinates the processor and its peripherals while two user code applications, one for interacting with a database server and one for transmitting pulse counts, run on top of the Linux kernel during normal operation.

This chapter describes many different hardware and software elements of the PulseNet-V design. Hardware signal names (VHDL and PCB layout) will use a **sans serif** font, as in `ram_counter` and `VREF`. Signal widths are specified in parenthesis after the signal name with an

intervening colon, e.g. `ram_counter(12:0)`, and the  $n^{th}$  bit of signal `ram_counter` is referred to as `ram_counter(n)`. The signal names of registers with multiple outputs are given `_q` designations followed by the output number. This only occurs for the input dual-edge registers that have output 1 corresponding to the positive-edge sampled input (`ddr_int.q1`) and output 2 corresponding to the negative-edge sampled input (`ddr_int.q2`). Finally, filenames, VHDL module names, and hexadecimal and binary values will appear in a typewriter font, as in `pnet_ram.vhd`, `0x9000000C`, and `1001b`.

## 3.2 Pulsenet-V Architecture

Pulsenet-V is a microprocessor based design, consisting of a single-core parameterized soft-core processor, a memory bus for processor instructions, a memory bus for processor data, and numerous peripherals connected to the processor local bus (PLB). Many PLB peripherals are provided by Xilinx for users as part of the Xilinx Platform Studio (XPS), the software program used for development of designs utilizing Microblaze, a soft-core processor developed by Xilinx for use in FPGAs. The Microblaze processor and various PLB peripherals are used in the Pulsenet-V design. Microblaze and all the PLB peripherals of Pulsenet-V are stock Xilinx modules with the exception of the `pulsenet` core. The custom logic needed for the flash ADCs and pulse rate counting is packaged into the `pulsenet` core.

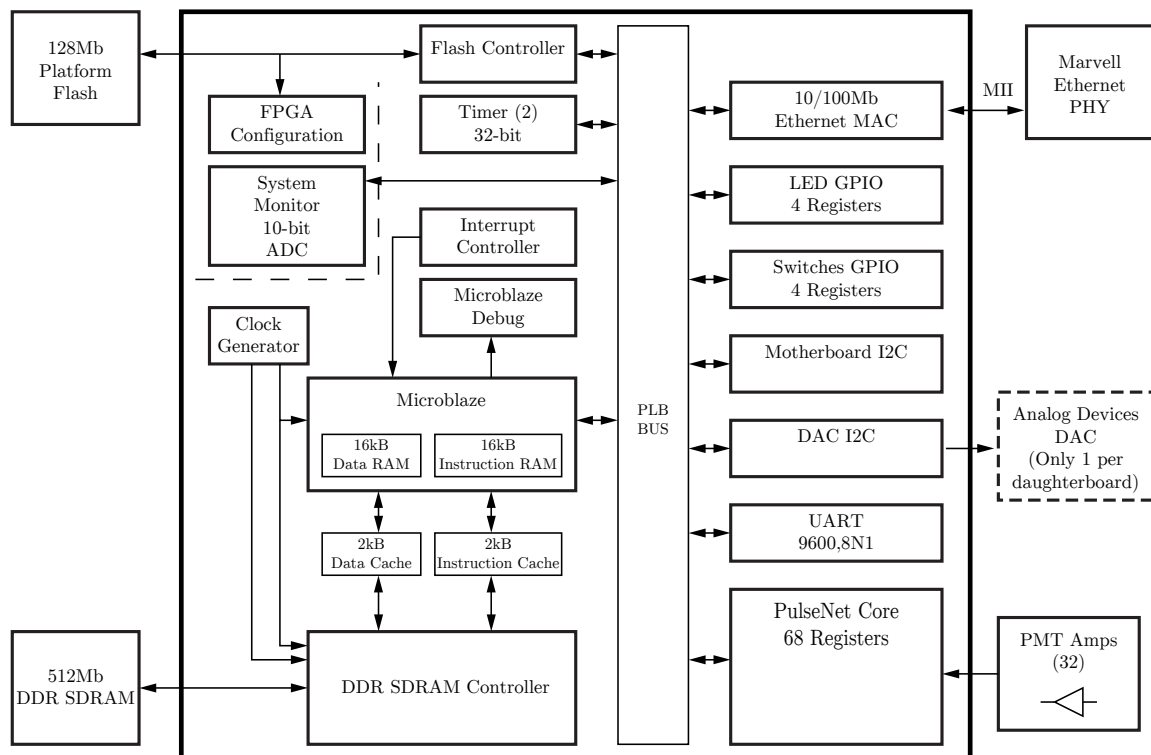


Figure 3.2: The block diagram of PulseNet-V includes the Microblaze processor, the `pulsenet_core` VHDL module, ethernet MAC, DDR SDRAM controller, and various other modules.

### 3.2.1 Microblaze

Pulsenet-V is based around the Xilinx provided Microblaze soft-core processor. The Microblaze processor can be customized to employ a range of functionality including integer multiplication and division, single or double-precision floating point units, a barrel-shifter, math and bus hardware exceptions, instruction and data caches, and various levels of memory management. A more complex processor utilizes more FPGA resources and will have a lower maximum operating frequency. For this design, higher speeds are desired but a minimum amount of functionality is required to support the Linux kernel. As such, a full virtual memory management unit is included in the Microblaze design. Instruction and data caches (2kB, 4-line) are enabled for all DDR SDRAM accesses. Other options selected include a barrel shifter, integer multiplier and division units, and debug module interface, but no exception handling is included. Exception handling was found to significantly decrease the maximum attainable clock frequency. See [Table 3.2](#) for further detail. Microblaze is a Harvard architecture and requires dedicated connections to data and instruction memory spaces. Separate local memory busses for these connections are routed to two ports of the Multi-Port Memory Controller (MPMC). Peripherals communicate with the Microblaze processor over the Processor Local Bus. The PLB has a 32-bit wide address bus and 32-bit wide data bus.

Table 3.2: Microblaze Options

Microblaze					
The Microblaze is a paramaterizable soft-core processor. The following options were used for the PulseNet-V design:					
<b>Cache</b>		<b>Instructions</b>		<b>Exceptions</b>	
Instruction	2kB, 4-line	Barrel Shifter	Yes	Floating Point	No
Data	2kB, 4-line	Floating Point Unit	Basic	Integer Divide	No
I-Cache Writes	Enabled	Integer Multiplier	32-Bit	Data-side PLB	No
D-Cache Writes	Enabled	Integer Divider	Yes	Instruction-side PLB	No
		Machine Status Register	Yes	Illegal Instruction	No
		Pattern Comparator	Yes	Unaligned Data	No
<b>Memory Management</b>		<b>Optimizations</b>		<b>Misc</b>	
Type	Virtual	Area Optimized	No	Processor Ver. Reg	None
D Look-Aside Buf	4	Branch Target Cache	No	BRAM Usage	5
I Look-Aside Buf	2			DSP48E Usage	5
MMU Reg Access	Enabled			Hardware Ver.	7.30.b
Protection Zones	2				

Table 3.3: Pulsenet-V Address Table.

Peripheral	Base	High	Size	Bus
Microblaze Data RAM	0x00000000	0x00007FFF	32kB	LMB
Microblaze Instruction RAM	0x00000000	0x00007FFF	32kB	LMB
pulsenet_bram_0	0x00010000	0x00013FFF	16kB	PLB
pulsenet_bram_1	0x00014000	0x00017FFF	16kB	PLB
pulsenet_bram_2	0x00018000	0x0001BFFF	16kB	PLB
pulsenet_bram_3	0x0001C000	0x0001FFFF	16kB	PLB
pulsenet_bram_4	0x00020000	0x00023FFF	16kB	PLB
pulsenet_bram_5	0x00024000	0x00027FFF	16kB	PLB
pulsenet_bram_6	0x00028000	0x0002CFFF	16kB	PLB
pulsenet_bram_7	0x0002C000	0x0002FFFF	16kB	PLB
pulsenet_bram_8	0x00030000	0x00033FFF	16kB	PLB
pulsenet_bram_9	0x00034000	0x00037FFF	16kB	PLB
pulsenet_bram_10	0x00038000	0x0003BFFF	16kB	PLB
pulsenet_bram_11	0x0003C000	0x0003FFFF	16kB	PLB
pulsenet_bram_12	0x00040000	0x00043FFF	16kB	PLB
pulsenet_bram_13	0x00044000	0x00047FFF	16kB	PLB
pulsenet_bram_14	0x00048000	0x0004BFFF	16kB	PLB
pulsenet_bram_15	0x0004C000	0x0004FFFF	16kB	PLB
ddr_sdram	0x50000000	0x53FFFFFF	64MB	PLB
flash	0x60000000	0x60FFFFFF	16MB	PLB
Ethernet_MAC	0x81000000	0x8100FFFF	64kB	PLB
leds	0x81420000	0x8142FFFF	64kB	PLB
switches	0x81440000	0x8144FFFF	64kB	PLB
dac_iic	0x81600000	0x8160FFFF	64kB	PLB
intc	0x81800000	0x81800000	64kB	PLB
mbrd_iic	0x82000000	0x8200FFFF	64kB	PLB
sysmon	0x83800000	0x8380FFFF	64kB	PLB
systimer	0x83C00000	0x83C0FFFF	64kB	PLB
rs232_uart	0x84000000	0x8400FFFF	64kB	PLB
mdm_debug	0x84400000	0x8440FFFF	64kB	PLB
pulsenet_single	0xC7E00000	0xC7E00000	64kB	PLB
pulsenet_core	0xCD400000	0xCD400000	64kB	PLB

### 3.2.2 Embedded System Peripherals

In the PulseNet-V Microblaze design, system peripherals can be independent, or they can be associated with one or more busses. The PulseNet-V system has three busses, two are Local Memory Bus (LMB) for memory access and one is the Processor Local Bus. The Microblaze processor uses the two LMBs for high-speed data and instruction local memory. Peripherals that need to communicate with the processor attach to the PLB. Some peripherals do not need the complexity of the PLB and are independently connected to the processor or to other peripherals. Of the 61 peripherals, one is the actual PLB bus itself, 2 are the LMBs, 44 are connected to the Processor Local Bus and 11 are not affiliated with any bus. All the peripherals are Xilinx XPS modules except two, `pulsenet_core` and `pnet_single`, which are custom modules coded specifically for PulseNet-V. The purpose of the Xilinx modules are described in the subsections below. A description of the PulseNet-V specific module, `pulsenet_core`, follows in its own dedicated section. The `pnet_single` module is simply a `pulsenet_core` with only one flash channel. This superfluous channel was included as an added feature for future use.



Table 3.4: Pulsenet-V Peripherals.

Name	Desc	IP	Bus
flash	Flash memory controller	xps_mch_emc v3.01.a	PLB
ddr_sdram	Double data rate SDRAM controller	mpmc v5.04.a	XCL0:XCL1
mdm_debug	In-circuit debugging for Microblaze	mdm v1.00.g	PLB
intc	Interrupt coalescing and control	xps_intc v2.01.a	PLB
Ethernet_MAC	Ethernet Media Access Controller	xps_ethernetlite v3.01.a	PLB
leds	GPIO controller for 16 LEDS	xps_gpio v2.00.a	PLB
switches	GPIO controller for 4 switches	xps_gpio v2.00.a	PLB
mbrd_iic	I <sup>2</sup> C controller for motherboard I <sup>2</sup> C bus	xps_iic v2.03.a	PLB
pv_bus	IIC controller for DAC	xps_iic v2.03.a	PLB
sysmon	Virtex on-board temp monitor	xps_sysmon_adc v2.00.a	PLB
systimer	Dual system timer	xps_timer v1.02.a	PLB
rs232_uart	Serial port	xps_uartlite v1.02.a	PLB
clock_gen	Clock generator	clock_generator v3.02.a	None
gps10M_ds_buf	Differential buffer for GPS 10MHz clock	util_ds_buf v1.01.a	None
gps1pps_ds_buf	Differential buffer for GPS 1PPS clock	util_ds_buf v1.01.a	None
sys_clk_ds_buf	Differential buffer for main system clock	util_ds_buf v1.01.a	None
trig_in_n_ds_buf	Differential buffer for external coincidence trigger	util_ds_buf v1.01.a	None
trig_out_n_ds_buf	Differential buffer for coincidence trigger output	util_ds_buf v1.01.a	None
trig_in_mux	Multiplexer for input trigger and serial port input	util_io_mux v1.00.a	None
trig_out_mux	Multiplexer for trigger output and serial port output	util_io_mux v1.00.a	None
sys_reset	System reset controller	proc_sys_reset v2.00.a	None

### 3.3 PulseNet Core

The pulsenet core is the PulseNet-V proprietary VHDL module that contains the design for the flash converters, coincidence triggers, astronomy pulse counters, GPS timestamp counters, and configuration registers. It communicates with the Microblaze processor over the processor local bus and has numerous non-PLB and external pin connections. The core is controlled by reading and setting its 68 configuration registers.

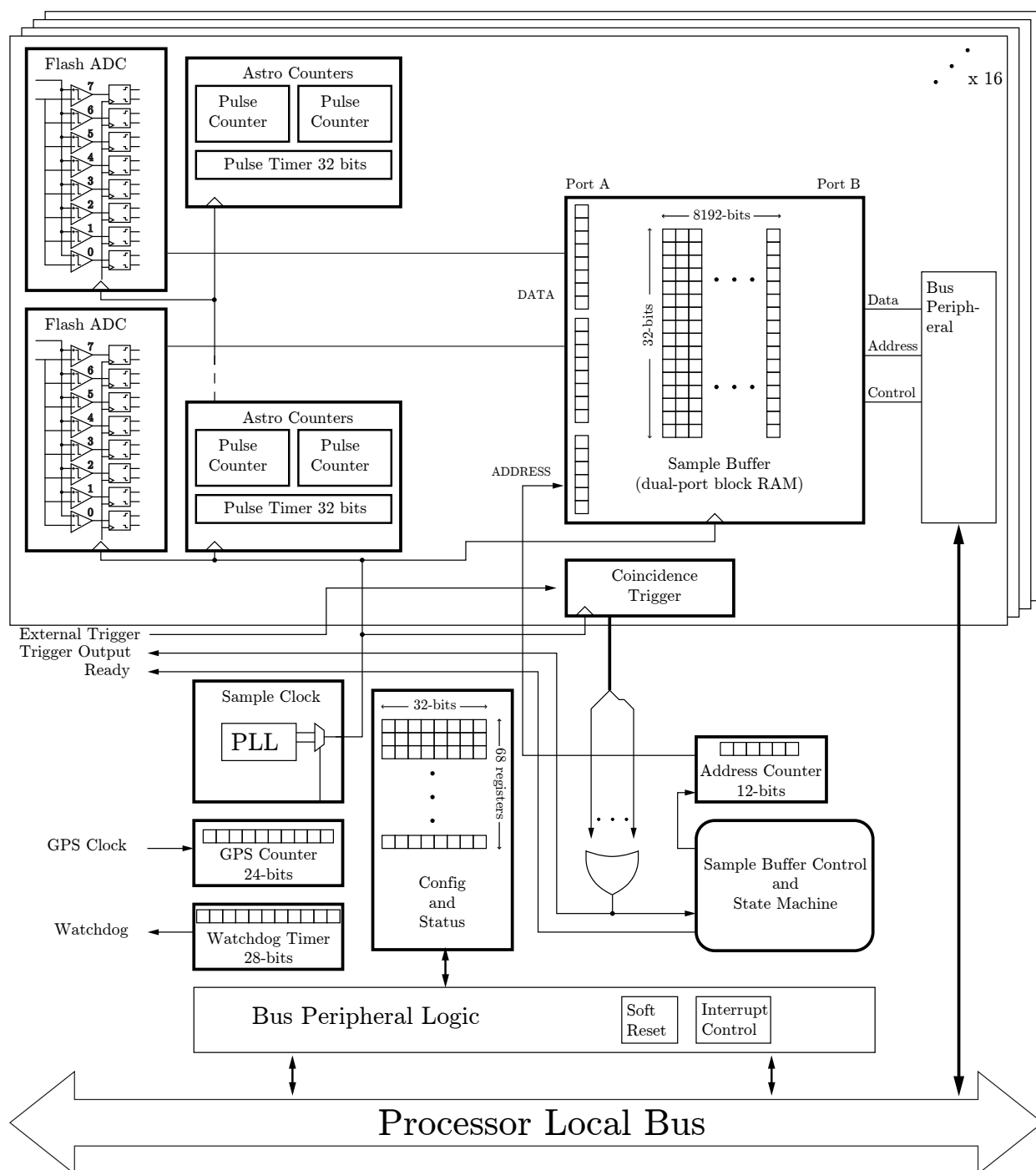


Figure 3.3: `pulsenet_core` contains configuration registers and 16 paired 3-bit, 800 Msps (1.5 Gsps capable) flash ADC converters.

### 3.3.1 Design Structure

The overall structure is shown in figure [Figure 3.3](#). At the top level, the pulsenet core is a PLB peripheral with sixty-eight 32-bit registers, interrupt logic, and soft reset capability. The code structure splits the pulsenet core into four files, `pulsenet_top.vhd`, `userlogic.vhd`, `pnet_control.vhd`, and `pnet_ram.vhd`. `pulsenet_top.vhd` and `userlogic.vhd` are auto-generated files that contain the PLB bus connection structures. They have been heavily modified to create additional bus connections to block RAM and other microblaze bus peripherals. The triggering control logic is contained within the component `pnet_control` which contains 32 instances of `pnet_ram`. The triggering control state machine, address counters, GPS counters, and other features common to the 32 flash converters are included within `pnet_control`. Flash converters, astronomy pulse counters, coincidence triggers, and all other logic operating on the sampler clock is contained within `pnet_ram.vhd`.

#### `pulsenet_top`

The top module of the pulsenet core hierarchy is `pulsenet_top` where the Xilinx library components and `user_logic` is instantiated. A PLB slave component, `plbv47_slave_single_v1_01_a`, is needed to provide access to bus signals to `user_logic`. The interrupt component, `interrupt_control_v2_01_a`, coalesces registered, level, and edge triggered interrupts into a single interrupt signal for the pulsenet core. The interrupt address space has registers for configuring and monitoring individual interrupts. Only one registered-level interrupt is utilized for the `data_ready` signal. A soft reset module (`proc_common_v3_00_a.soft_reset`) is instantiated to provide a software reset for the pulsenet core. Sixteen bus connections are made by `pulsenet_top` in order to connect the sampled data lines (`ddr_int_q`), address counter lines, and sample clock to block RAM. The sample memory block RAM are bus peripherals that are instantiated elsewhere.

External connections to pins are made at the top level by `pulsenet_top` in order to pass the signals down to lower pulsenet core levels. These connections are not associated with any bus and include the 256 LVDS pins pairs (`data_0(7:0)` to `data_31(7:0)`) for data sampling, the 50 MHz pre-PLL-multiplied sample clock (`sys_clk`), the trigger lines (`trig_in_n` and `trig_out_n`), the GPS clocks (`gps10M` and `gps1pps`), the pnet ready output (`pnet_ready`), a

board-level resistor coded ID number (`pulsenet_id`), and the serial/trigger multiplexer control output (`serial_debug_disable`).

#### `user_logic`

The `user_logic` module instantiates `pnet_control`, a clock manager to generate the sample clock, and 68 registers that are accessed from the PLB bus. The registers are used for both configuring how the pulsenet core operates and for providing status information from the core. For example, register 7 sets which of the 8  $V_{REF}$ 's will be used as the trigger threshold and register 0 indicates whether a trigger has occurred. [Table 3.5](#) shows the purpose of each register. `User_logic` also synthesizes a digital clock manager (DCM) module, two PLL's, and a global clock buffer multiplexer to provide two speed options for the sample clock, 400 MHz and 300 MHz. Lastly, `user_logic` feeds through many external signals, such as the LVDS pin inputs, to `pnet_control` and `pnet_ram`.

#### `pnet_control`

The trigger state machine and 32 `pnet_ram` instantiations constitute the bulk of `pnet_control`. The state machine reacts to triggers from any of the 32 flash ADC's (or 16 pairs if linked for coincidence) by continuing to sample data for a configurable number of clocks to obtain post-trigger data before stopping the samplers and copying GPS timestamp and trigger registers into the `user_logic` configuration register space. A GPS counter is created by this module; by default it increments for every edge of the 10 MHz clock and resets at the 1 pulse-per-second positive clock edge. The edge polarity is selectable through the `user_logic` configuration registers. The trigger interrupt signal is generated by logic in `pnet_control`. External triggers are handled in `pnet_control`, as well as the circuitry for coincidence linking of the flash ADC channels of `pnet_ram`. Special care is taken for the coincidence linking, reset, and block ram address counter code. Signals in these sub-circuits span the entire Virtex-5 FPGA. Timing closure could not be achieved for large fanout signals like reset and the block ram address counters so register duplication was enabled to reduce the fanout in stages. This register duplication also pipelines the signals. Pipelining is especially important for signals that must travel from one side of the chip to the other. This is not possible in

one sample clock cycle so the signal pipelining is required.

#### `pnet_ram`

`Pnet_ram`'s main job is to build a flash ADC out of 16 I/O pins. Trigger logic for each flash ADC channel, two astronomy pulse counters, and astronomy counter multiplexers are also part of the `pnet_ram` module. Because all the logic in `pnet_ram` runs at the sample clock speed, the design has very few levels of logic and some signals have multiple pipeline stages.

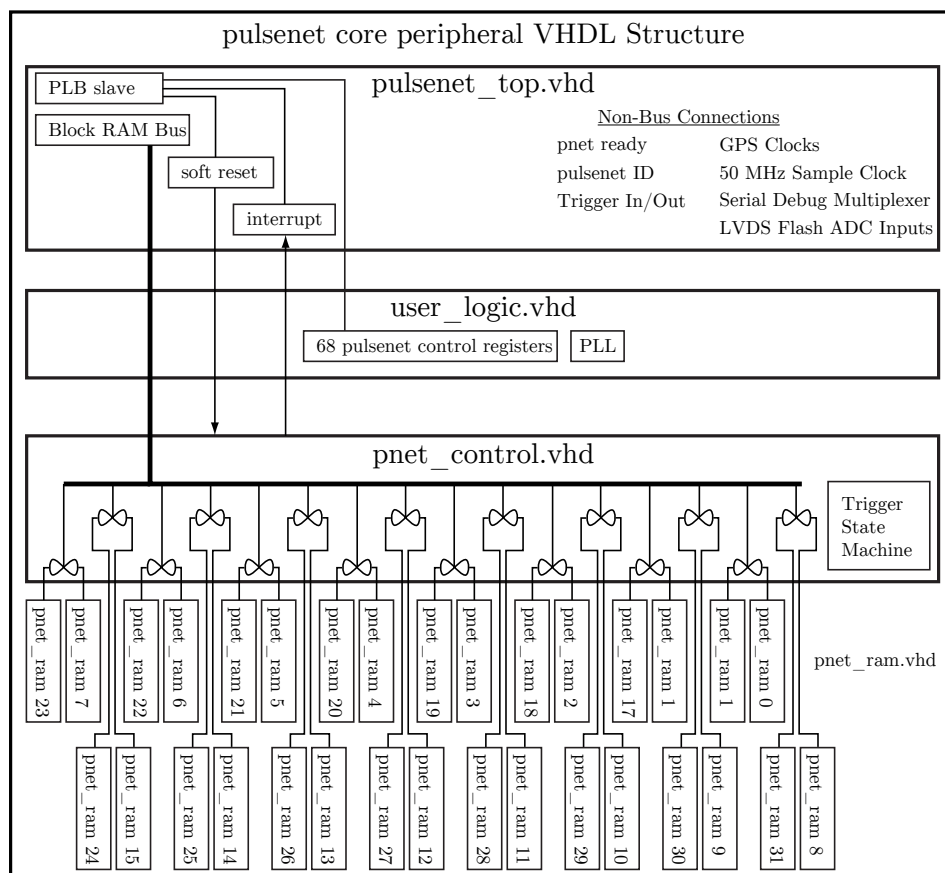


Figure 3.4

### 3.3.2 Digitization

For every differential input pair, there is a differential amplifier (IBUFDS) that acts as a comparator for the two inputs. Dual-edge flip-flops (IDDR) follow in the signal path directly after the differential amplifiers (Figure 3.5). The dual-edge flip flops are clocked by a 300 MHz or 400 MHz PLL-multiplied clock derived from the 50 MHz master clock `sys_clk`. The IDDR outputs are pipelined so that both the positive-edge and negative-edge samples appear at the output on the positive-edge clock cycle. This aligns both samples to the positive clock edge so they can be processed and stored using logic that is clocked by the same positive clock edge. The IDDR outputs are sent through two D-flops before being written to a block RAM (the sample memory). The two D-flops are used as buffers. IDDR outputs may be routed to a block RAM that is too far away to meet signal timing margins in one clock period. Extra D-flops in between the IDDR and block RAM allow for additional delay. Block RAM is not instantiated in `pnet_ram`, rather it exists as a peripheral (`pulsenet_ram_[0:15]`) on the Processor Local Bus; `pnet_ram` provides the data and address lines that are connected to the block RAM peripheral.

The above digitization configuration allows sample rates up to 800 Msps. Use of an ISERDES input stage rather than the IDDR dual-edge flip-flop can achieve sampling at 1.5 Gsps. The ISERDES accepts an input clock up to  $\sim 750$  MHz and can sample the LVDS differential amplifiers on both clock edges. The output rate divisor is set to 4 and so that 4 samples are written to the block RAM at a rate of 375 MHz. This high-speed configuration is not used by the Advanced All-sky Camera during normal observations, but it has been tested and validated (pulse tests are shown in Chapter 5).

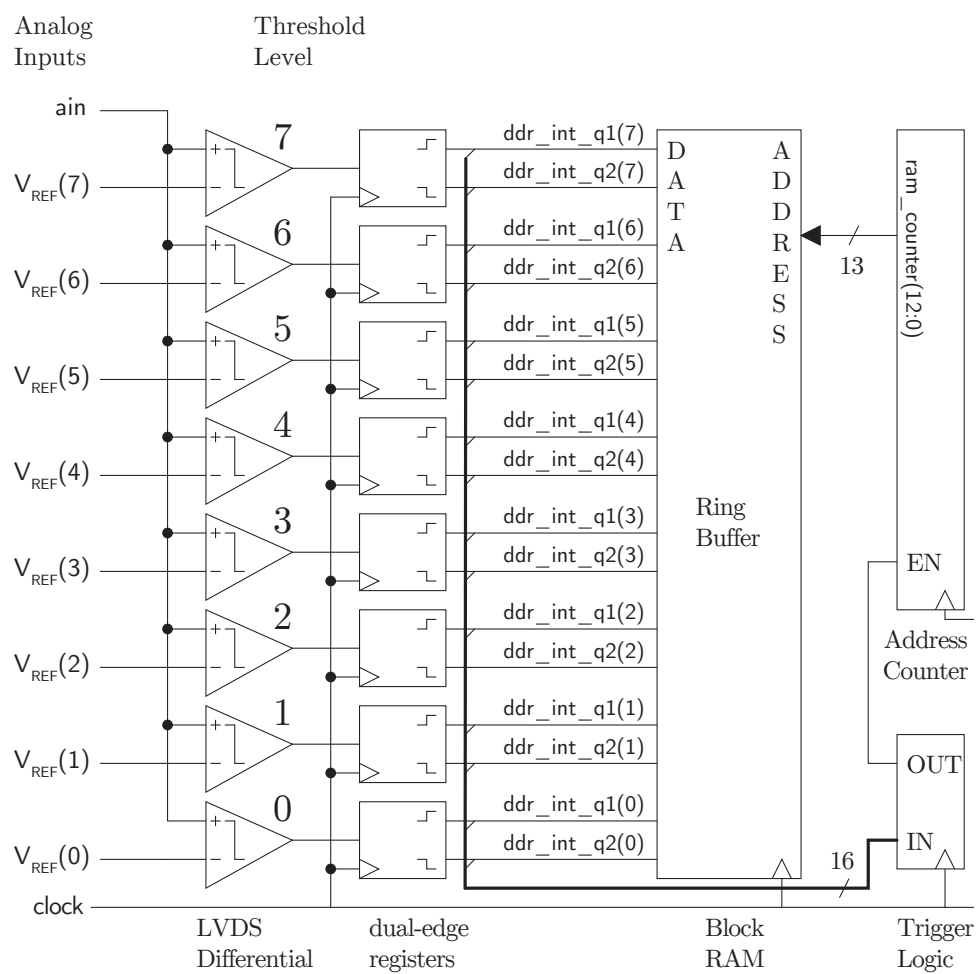


Figure 3.5



### 3.3.3 Trigger Logic

Recognizing and capturing coincidence pulses is a critical feature of the pulsenet core. It must react to coincident pulses on 16 ADC channel pairs at the full sample clock rate and coordinate the gathering of sample data by the processor when a coincident pulse is received. When the “trigger logic” detects a coincident pulse, it activates the “trigger” signal. Within the PulseNet-V’s pulsenet core, the trigger starts a chain of events called the “trigger sequence”:

1. The current state of the GPS timestamp counter is stored in `gps_addr`;
2. Individual channel trigger outputs are stored in `triggers_lock`;
3. Post-trigger samples are recorded for a number of clocks according to `dataout_count` ;
4. The Microblaze processor is notified through an interrupt that a trigger occurred and the ADC sampler data is ready to be handled;
5. Samples from all 32 ADC channels are transferred from block RAM into DDR SDRAM by the processor as directed in the interrupt service routine (ISR);
6. The processor retrieves the stored GPS timestamp from the time of the trigger;
7. The pulsenet core is notified by the processor when all of the data transfers are completed before exiting the ISR;
8. The pulsenet core samplers and trigger/control logic are reset;
9. The trigger logic becomes active again, waiting for a new set of coincident pulses on any analog input pair;

The `threshold`, `trig_width_select`, `dataout_count`, `trigger_invert`, and `link` configuration options can affect how the trigger sequence proceeds. The `threshold` option sets which  $V_{REF}$  comparator from each pulsenet core channel is routed to the trigger logic. Comparators from channel pairs are AND’ed together (constituting the “coincidence” requirement), and then the sixteen pairs are OR’ed to create the `master_trigger` signal. The channel pair AND circuit

can be extended to include delayed versions of the  $V_{\text{REF}}$  comparator outputs. This creates a “coincidence window” where the trigger will fire if the  $V_{\text{REF}}$  comparator of input pairs are active ( $V_{\text{REF}}$  comparators operate active-low in the actual design) within `trig_width_select`+1 sample periods. Valid options for `trig_width_select` are 0 to 4 indicating a coincidence window of 1 to 5 sample clocks. PulseNet-V is normally operated with a 400 MHz sample clock (two samples per clock) using the smallest coincidence window, but the window is selectable between 2.5 ns, 5 ns, 7.5 ns, 10 ns, and 12.5 ns. The number of post-trigger samples is configured through the `dataout_count` option. The trigger logic state machine waits

$$\frac{2 \times \text{dataout\_count} \times \text{sampleClockFreq}}{125\text{MHz}} \quad (3.1)$$

before stopping the sample memory address counter. Normal operation uses a value of 900 for `dataout_count` (2432 samples or 3.04  $\mu\text{s}$  of pre-trigger). The lowest  $V_{\text{REF}}$  level is normally set above (in voltage) the bias level so the `ddr_int.q(0)` outputs of the  $V_{\text{REF}}(0)$  LVDS amplifiers are almost always active. If `threshold` was set to  $V_{\text{REF}}(0)$ , the pulsenet core would be continuously triggered. The option `trigger_invert` is needed to flip the sense of the trigger activation to prevent this behavior. It is a rarely used option, and then only for debugging purposes. Another useful debugging feature is the `link` option. With `link` enabled, coincidences between channel pairs are required for the trigger logic to fire. However, disabling `link` removes the coincidence requirement from the trigger logic; a signal level  $\geq V_{\text{REF}}$  in any pulsenet core ADC channel will cause the system to trigger.

In addition to coincidences from the analog input pairs, triggers can be caused by an external trigger input `trig_in`. The `trig_in` line is controlled by a Spartan-6 FPGA on the Advanced All-sky Camera’s motherboard. The Spartan-6 receives a trigger output (`trig_out`) from each of the camera’s 32 PulseNet-V’s. The `trig_out` of a PulseNet-V is active-low when any channel pair of the pulsenet core is triggered. The Spartan-6 essentially acts as a 32-input OR gate; it distributes the `trig_out` from any PulseNet-V to the remaining 31 PulseNet-V’s in the camera via their `trig_in` input.

### 3.3.4 Astronomy Counters

Two 25-bit astronomy counters are available for each flash ADC channel. The circuit for one counter of channel 0 shown in [Figure 3.6](#). The astronomy counter inputs are connected

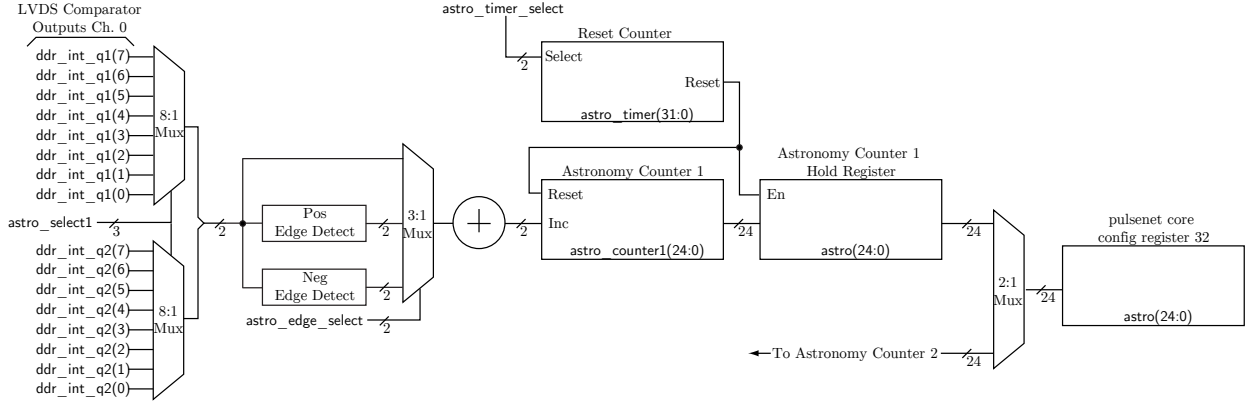


Figure 3.6: Astronomy Counter Circuit Diagram

to the IDDR sampled data outputs through a multiplexer. The configuration register **astro\_select1** chooses which LVDS comparator output ( $V_{REF}$ ) is counted. There are two samples per clock from the dual-edge register (**\_q1** and **\_q2**) that are added to increment the counter either directly or after edge-detection has been performed. The configuration register **astro\_edge\_select** chooses whether positive levels, positive edges, or negative edges increment the counter **astro\_counter1**. The **astro\_timer** resets periodically, according to **astro\_timer\_select**, and causes **astro\_counter1** to be loaded into the **astro** register. The width of the **astro\_timer** counter is also selectable; the overflow period can be 0.75, 2.1, 4.7, or 10 seconds. The counter that appears in the **user\_logic** configuration register **astro\_reg** is selected by **astro\_reg\_select**. Channel 0 is mapped to the pulsenet core configuration register 32. The astronomy counters for channel 1 are mapped to register 33, and so on, up to register 63 for channel 31.

### 3.3.5 Configuration Registers

Table 3.5: PulseNet-V Core Configuration Registers

Register	Num	Bits	Name	Dir	Description
Status 1	0	24	data_ready	R	Indicates sampler data from trigger event can be read
	0	23	trig_in_lock	R	Indicates external trigger from motherboard
	0	5:0	PulseNet ID	R	PulseNet ID set by resistors on daughterboard
Status 2	2	11:0	trig_addr	R	Sampler address counter value when triggered.
Status 3	3	31:0	trig_lock	R	Indicates which channels were triggered. Ch 31–0
GPS Status 1	4	23:0	GPS trig'd count	R	Triggered GPS counter
Trig Debug	5	31	trig_in	R	External trigger from motherboard
	5	30	trig_in_pending	R	trig_in trig_in_enabled
	5	29	trig_int_only	R	OR of all channels' Trigger excluding external trigger
	5	28	trig_out_i	R	Internal trigger out signal
	5	27	trig_simple_lock	R	Internal signal to trigger system
	5	26	Trig In Disable	RW	Disables external triggers from motherboard
Reset	6	31	pll_en	RW	PLL is enabled when pll_en=1
	6	0	pnet_dis	RW	Hold samplers in reset when pnet_dis=1
Threshold	7	31	trig_inv	RW	Triggers on $V_{input} < V_{REF}$ if trig_inv=1
	7	2:0	threshold	RW	Threshold $V_{REF}$ setting [0–7]
Dataout Cnt	8	12:0	dataout_cnt_stop	RW	Sets post-trigger samples= $dataout\_cnt\_stop \times 125/400$
Link	9	0	link	RW	Requires coincidence for trigger when link=1
GPS Cfg	10	1	gps10MhzInvert	RW	Set for active low 10 MHz GPS clock
	10	0	gps1PPSInvert	RW	Set for active low 1 PPS GPS clock
GPS Counter	11	23:0	gps_count	R	Direct read access to the GPS counter
Triggers	12	31:0	triggers	R	Direct read access to channel trigger output
Ready Ack	13	0	data_ready_ack	W	Write to allow the pulsenet core to reset
Serial Cfg	14	0	serial_debug_disable	RW	Clear to direct serial debug terminal of Microblaze onto trigger lines
Watchdog Cfg	15	31	watchdog_timer_reset	W	Set to kick watchdog
	15	30	watchdog_alarm	RW	Set if watchdog times out
	15	29	dcm_rst	R	Reset status bit of sampler clock module
	15	28	init_ready	R	pulsenet core control state machine initialized status bit
	15	27:0	watchdog_timer	R	Direct read access to the watchdog timer
Pnet Status	16	0	pnet_ready_i	R	External signal to motherboard that the pulsenet core and <b>pulsenetvcd</b> are active – <b>!watchdog_alarm &amp; !dcm_rst &amp; init_ready</b>
DCM Cfg	17	31:28	DCMDO	R	Output bits of pulsenet core clock module skew adjust
	17	3	PSDONE	W	Done signal for pulsenet core clock module skew adjust
	17	2	PSINCDEC	W	$\overline{\text{Inc/Dec}}$ signal for pulsenet core clock module skew adjust
	17	1	PSEN	W	Enable signal for pulsenet core clock module skew adjust
	17	0	PSCLK	W	Clock signal for pulsenet core clock module skew adjust
Astro Cfg 1	18	31	astro_reg_select	RW	Select which <b>astro_select1</b> is routed to registers 32–63
	18	17:16	astro_select1	RW	Select which $V_{REF}$ is routed to <b>astro_counter1</b>
	18	1:0	astro_select2	RW	Select which $V_{REF}$ is routed to <b>astro_counter2</b>
Clock Sel	19	0	clock_select	RW	Clear for 400MHz, set for 300MHz
Trig Width	20	2:0	trig_width_select	RW	Coincidence window is $2 \times trig\_width\_select + 1$ clocks
State Mach	21	31:28	state_readout	R	State machine encoding
	21	22	data_ready	R	Is set if trig'd data is available in block RAM
	21	21	self_reset	R	Is set after <b>data_ready_ack</b> goes high

Continued on next page

Table 3.5 (Continued)

Register	Reg#	Bit	Name	Dir	Description
	21	17	dataout_counter_reset	R	Status of dataout counter reset line
	21	16	dataout_counter_enable	R	Status of dataout counter enable line
	21	13:0	dataout_counter	R	Direct read access to dataout counter
RSVD	22	31:0	None	RW	Reserved for future use
RSVD	23	31:0	None	RW	Reserved for future use
RSVD	24	31:0	None	RW	Reserved for future use
RSVD	25	31:0	None	RW	Reserved for future use
RSVD	26	31:0	None	RW	Reserved for future use
RSVD	27	31:0	None	RW	Reserved for future use
Astro Cfg 2	28	5:4	astro_edge_select	RW	Astronomy pulse count type selector; high(00b), positive edge(01b), negative edge(11b)
	28	1:0	astro_timer_select	RW	Astronomy pulse counter period selector; 0.75 sec(00b), 2.1 sec(01b), 4.8 sec(10b), or 10.1 sec(11b)
Astro Cfg 3	29	24:0	astro_addr	RW	Select the channel that is routed to <b>astro_reg1</b>
Astro Stat 1	30	24:0	astro_ref1	R	Read access to the astronomy pulse counter <b>astro_counter1</b> selected by <b>astro_addr</b>
Astro Stat 2	31	24:0	astro_ref1	R	Read access to the astronomy pulse counter <b>astro_counter2</b> selected by <b>astro_addr</b>
Astro Cntr	32-63	24:0	astro_reg[0-31]	R	Astronomy counter for channel 0 to 31
RSVD	64	31:0	None	RW	Reserved for future use
RSVD	65	31:0	None	RW	Reserved for future use
RSVD	66	31:0	None	RW	Reserved for future use
RSVD	67	31:0	None	RW	Reserved for future use

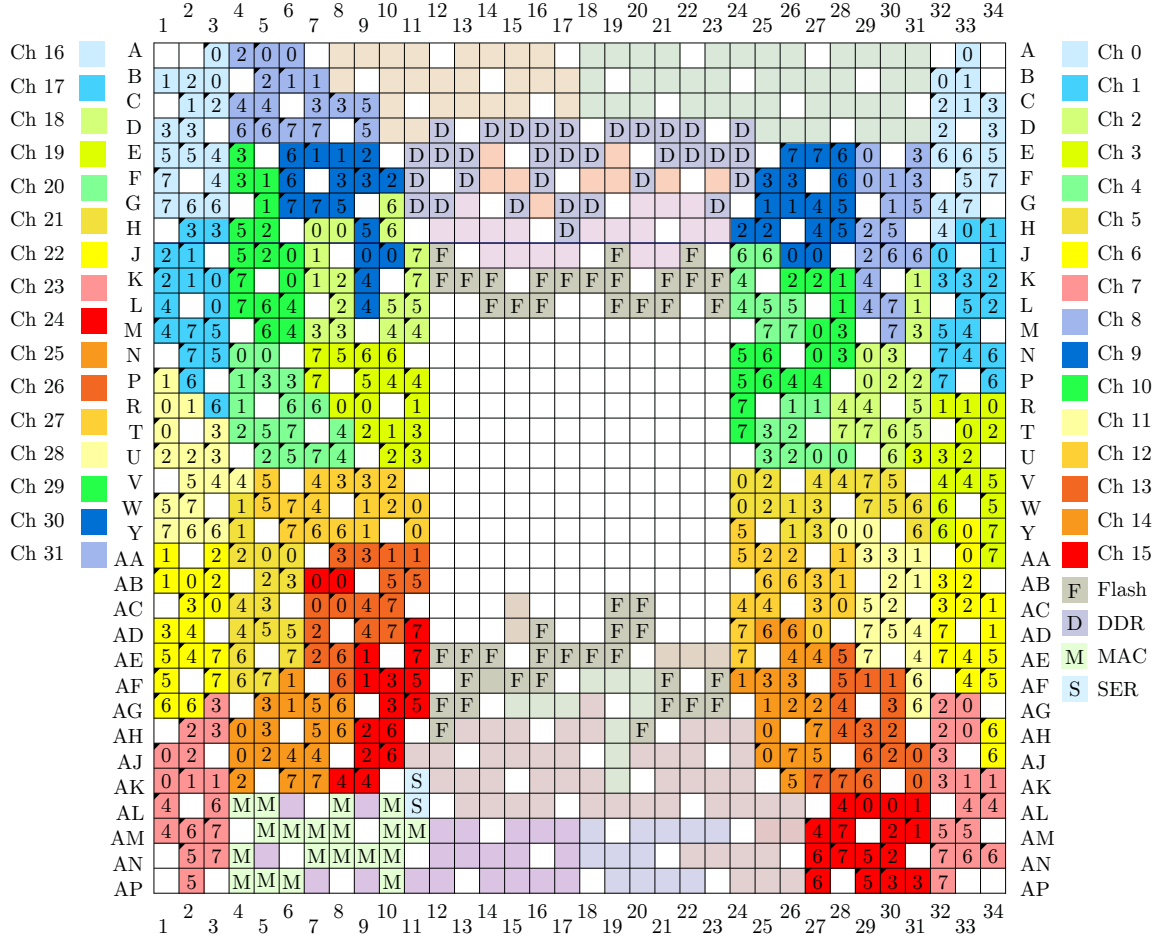


Figure 3.7: Virtex-5 FF1153 package pinout for PulseNet-V ADC channels (a.k.a Virtex-5 Sudoku). Each channel consists of 8 differential pair (16 pins) labeled 0-7. The number represents the pin's  $V_{REF}$ . A triangle to the top left indicates the signal or p-pin of the pair. Pin assignments for flash memory, DDR SDRAM, 10/100 MAC PHY, and serial are also shown. White boxes are the power and ground pins and other lightly colored boxes are mainly unused GPIO.

## 3.4 Software

The PulseNet-V design exploits numerous levels of software. At the lowest firmware level, the PulseNet-V VHDL code is itself software. The VHDL and FPGA design has been described in the section above. This section deals with the operating system, drivers for the FPGA hardware, interrupt service routines, compiled software libraries, bootloader code, configuration scripts, and daemon programs.

### 3.4.1 Operating System

The PulseNet-V uses a custom compiled Linux kernel as the operating system for the Microblaze processor. Linux is a widely used open-source operating system that has a massive base of programs, drivers, and tools written for it. PulseNet-V makes use of the open-source tools to compile its daemon programs and even the kernel itself. The linux kernel source, GNU libraries, and compilers were obtained from Xilinx (<http://wiki.xilinx.com/microblaze-linux>). Since Microblaze is a soft-core processor, it can be configured to have a hardware integer divider, a 32-bit or 64-bit integer multiplier, a floating point unit, a barrel shifter, a pattern comparator, a machine status register, instruction and data cache, exception handling, and many other options. These options must be passed to the kernel so that the correctly optimized functions and assembly instructions are used by the compiler. **Table 3.6** lists a selection of the config option used to compile the kernel.

The compiler needs to know about other devices in the system besides the processor. This information is conveyed by a device tree file (`.dts`). A device tree for the PulseNet-V design was generated using Xilinx's device tree generator (<http://xilinx.wikidot.com/device-tree-generator>). The device tree and kernel config were used to produce a kernel with the matching configuration options to be compatible with the soft-core Microblaze processor and the rest of the PulseNet-V hardware. The big-endian linux kernel was used in order to support the processor local bus (a little-endian kernel is also available for the AXI bus).

Table 3.6: Microblaze Kernel Config Options

Option
CONFIG_MICROBLAZE=y
CONFIG_KERNEL_BASE_ADDR=0x50000000
CONFIG_XILINX_MICROBLAZE0_FAMILY="virtex5"
CONFIG_XILINX_MICROBLAZE0_USE_MSR_INSTR=1
CONFIG_XILINX_MICROBLAZE0_USE_PCOMP_INSTR=1
CONFIG_XILINX_MICROBLAZE0_USE_BARREL=1
CONFIG_XILINX_MICROBLAZE0_USE_DIV=1
CONFIG_XILINX_MICROBLAZE0_USE_HW_MUL=1
CONFIG_XILINX_MICROBLAZE0_USE_FPU=1
CONFIG_XILINX_MICROBLAZE0_HW_VER="7.30.b"
CONFIG_XILINX_DRIVERS=y
CONFIG_NEED_XILINX_LLDMA=y
CONFIG_XILINX_EMACLite=y
CONFIG_SERIAL_UARTLite=y
CONFIG_SERIAL_UARTLite_CONSOLE=y

### 3.4.2 Drivers

Drivers for most of the Xilinx embedded system modules, such as the UARTLite serial port and EMACLite ethernet MAC exist in the mainline Linux source code. The EMACLite driver was slightly modified to accept a MAC address parameter from the U-boot bootloader. Each PulseNet-V needs a unique MAC address for networking purposes. This unique address is stored in the XCF128XL Platform Flash along with the FPGA configuration and bootloader code. The address is passed to the Linux kernel as a boot string and then is passed to the EMACLite driver.

A device driver (`\dev\pnet`) for the pulsenet core was written to handle the interrupt requests that occur when a coincidence pulse triggers the system. The full interrupt handler code is derived in part from the `short.c` example by Alessandro Rubini and also from the PC104 interrupt driver written for the original all-sky camera by Chip Coldwell. A valid interrupt forces the kernel to execute the function shown in [Listing 3.1](#).



Listing 3.1: The `pnet_interrupt` function is executed when an interrupt is emitted from the pulsenet core.

```

irqreturn_t pnet_interrupt( int irq, void *dev_id ) {
    struct timeval tv;
    int written;
    int reg;
    //takes 48us to get here
    /* Copy all coinc samples from BRAM to kernel space.
     * Then copy all pnet registers to kernel also. */
    memcpy_fromio( (unsigned long*)coinc_buffer_area, (unsigned long*)
        bram_base, bram_size);
    memcpy_fromio( (unsigned long*)(coinc_buffer_area+(bram_size/4)),
        (unsigned long*)pnet_base, PNET_SIZE/4);

    //acknowledge the copying of block ram
    iowrite32( 0xa0, pnet_base+13*4 );
    iowrite32( 0xa1, pnet_base+13*4 );
    iowrite32( 0xa0, pnet_base+13*4 );

    //takes 2.325ms to get here
    /* Record the time.
     * Write a 16 byte record.
     * Assume PAGE_SIZE is a multiple of 16 */
    do_gettimeofday(&tv);
    written = sprintf((char *)pnet_head, "%08u.%06u\n",
        (int)(tv.tv_sec % 1000000000), (int)(tv.tv_usec));
    BUG_ON(written != 16);
    pnet_incr_bp(&pnet_head, written);

    /* awake any reading process */
    wake_up_interruptible(&pnet_queue);
    reg = ioread32(pnet_base);
    printk(KERN_INFO "Trig! 0x%x\n", reg)
    return IRQ_HANDLED;
}

```

The `pnet_interrupt` function is executed about 48  $\mu$ s after the interrupt is received. The full 256kB of sample data from all 32 PulseNet-V flash ADC channels is first copied into a kernel buffer (`coinc_buffer_area`). The 68 pulsenet core configuration registers are then appended to the end of the sample data kernel buffer. An acknowledgement of the interrupt is written to the pulsenet core in register 13. This causes the pulsenet core to be reset and reprogrammed so that it is immediately available to collect additional coincidence pulses. The pulsenet core is acknowledged about 2.33 ms after the first interrupt is received. Next, the `pnet_interrupt` function writes the system time into the `pnet_head` buffer. This buffer is read by accessing the device at `\dev\pnet` in the Linux filesystem. Finally, the text “Trig!” is printed to the console and the interrupt exits, giving execution back to the kernel. The daemon program, `pulsenetvd` (§ 3.4.6), becomes active when data is put into the `\dev\pnet` device and will read and transmit the sample data in the kernel buffer to a host computer over a transmission control protocol (TCP) connection. The `pnet` interrupt module is not compiled into the kernel. It is inserted into the kernel at boot time by the boot script to allow changes to the driver without recompiling the kernel.

### 3.4.3 Boot Script

After Linux finishes its own boot process, it runs the `rcS` script before giving up execution to the console shell terminal. The script starts by mounting the `proc`, `sys`, and `tmp` filesystems. A writeable directory is mounted using NFS over TCP at the filesystem node `\var` and a default network gateway route is added to the host. System log, kernel log, and the network time protocol NTP daemons are started and the system date gets set. A telnet daemon is started to allow remote command-line access. The `\dev\pnet` driver module is inserted before starting the `pulsenetvd` daemon. Finally, the `astro_udp` daemon (`\dev\pnet`) is started and a log of the boot script is written to `\var\bootscriptlog`.

Important default pulsenet core configuration settings are initialized by the `rcS` script. The GPS clock lines are inverted for some PulseNet-V's. The script reads the pulsenet ID in register 0 of the pulsenet core and calculates the inversion, if any, of the 10 MHz and 1 PPS clocks. The coincidence window is set to the smallest value (0b) to specify a 2.5 ns window.

The astronomy pulse counters are set to count negative pulse edges. Last, the phase of the main system clock is delayed an amount dependent on the length of the daughterboard clock trace to the PulseNet-V.

### 3.4.4 Debug

With a high-level operating system like Linux, boot messages can be critical to debugging software and start-up issues. The PulseNet-V contains a special feature to allow serial port access to Linux during boot and even to the bootloader before Linux has booted. At reset and at power-on, the pulsenet core routes its default serial console through the trigger in and trigger out lines. In the Advanced All-sky Camera, the trigger lines for all PulseNet-V's are routed to a Spartan-6 FPGA. The Spartan-6, then, has access to the serial console of each PulseNet-V, as they boot, through the trigger lines. When PulseNet-V completes its boot script, a configuration bit is set in the pulsenet core to return the trigger lines to their normal behavior. The serial console is then routed to a header on the daughterboard. The serial console can be remotely accessed by the Spartan-6 at any time, however, by resetting the `serial_debug_enable` bit of the desired PulseNet-V. The serial console communicates at 9600 baud using 8 data bits, no parity, and one stop bit

### 3.4.5 Bootloaders

PulseNet-V implements a two-stage bootloader for booting the Linux kernel. Stage-1 initializes the flash memory which contains the stage-2 bootloader and transfers the second stage bootloader code from the flash memory into RAM. Execution then transfers to the beginning of the stage-2 bootloader code in RAM. U-boot, the stage-2 bootloader, grabs the compressed Linux kernel from a server over ethernet, uncompresses the kernel, and executes from the base of the uncompressed kernel.

The two-stage bootloader process is necessary because the size of the initial code that can be executed by the FPGA at power-up is very small. At power-on, the FPGA automatically loads its configuration from a flash memory. The first instructions executed by Microblaze are whatever exists in the instruction RAM after configuration. Therefore, the minimal stage-1 bootloader is placed in this small instruction RAM space. The instruction RAM for

PulseNet-V is 32kB, so the stage-1 bootloader, which is written into the FPGA configuration, must fit within that space.

The stage-2 bootloader is a version of U-boot, an open source bootloader meant to be small, fast, and configurable. U-boot is closely related to Linux and has special features for booting Linux images. Additionally it offers a command-line interface prior to booting the target application, the ability to read and write to flash, and a user datagram protocol (UDP) stack for loading files using the trivial file transfer protocol (TFTP). The setup for U-boot is not trivial and numerous settings have to be applied to ensure proper compilation for a custom configuration. U-boot has its own environment settings which must be stored in a block of flash memory that can be separately erased and written.

The U-boot executables and default environments are initially written to the Virtex-5 over JTAG using Xilinx's Impact programming software and Platform Cable USB programming pod. The default U-boot environments must be customized, in the case of the Virtex-5 FPGAs, with a static IP address, MAC address, location of root filesystem (normally located in a common folder on Costas and mounted over NFS), and other linux kernel boot arguments.

At boot time, U-boot follows a script of commands. U-boot starts by downloading the file `linux.uimg` from Costas using TFTP. This is a U-boot specific file which contains a small header that describes the size, CRC, and compression scheme of the payload, an executable image file. The `.uimg` file is initially placed at a high address in RAM. The payload is decompressed if necessary and then copied to the start of RAM at address `0x0`. The location of the *bootargs* string is loaded into the Microblaze register R5 and execution is passed to the Linux kernel.

### 3.4.6 Daemon Programs

PulseNet-V must provide a mechanism for the outside world to command and control its operation. A linux daemon program named `pulsenetvd` provides this mechanism by exposing the PulseNet-V's services over ethernet. The daemon accepts and processes pulsenet core programming commands and data requests. An additional daemon, `astro_udp`, continuously reads the astronomy pulse counters and sends the count values to a specified

IP address.

### `pulsenetvd`

This program is executed at the end of the Linux boot script and must be running to be able to control PulseNet-V. It first opens a socket and listens for connections by default on port 8001. Once connected, commands from a host are received, executed, and a response is returned. The main function of `pulsenetvd` contains a select function that allows the program to sleep until the socket receives a command. Commands have three parts, a tag, a length, and the value. Tags are one-byte positive numbers for commands coming to the PulseNet-V and negative for replies from PulseNet-V. The length is a two-byte word specifying the number of bytes in the value part of the command. The value contains data according to the tag of the command. Commands are ASCII encoded with newline terminators and spaces separating the tag, length, and value. A typical command set from `oseti.py` would be to reset the pulsenet core, set programming options, and enable the ADC samplers. [Figure 3.8](#) lists the available commands and their formatting.

A Linux supervisor keeps watch over `pulsenetvd` and will restart the program if it ever crashes. In addition, PulseNet-V provides a watchdog timer that is periodically reset by `pulsenetvd`. If `pulsenetvd` is not active, the watchdog timer will overflow and set the `watchdog_alarm` signal. A hardware pin output, `pnet_ready` will be deactivated if `watchdog_alarm` is set. This hardware signal is read by the Spartan-6 FPGA on the motherboard so that it can reset the system or a specific PulseNet-V if `pulsenetvd` is inactive.

PulseNet-V Communication Protocol				
T	<input type="text"/>	Tag - 1 byte	Tags are positive number when sent from host to PulseNet-V. PulseNet-V replies with negative numbered tags.	
L	<input type="text"/> <input type="text"/>	Length - 2 bytes	All multiple byte values are sent MSB first.	
V	<input type="text"/> . . . <input type="text"/>	Value - L bytes	<input type="text"/> ContentsName : NumBytes	
Command	T	L	V	
reset	1	1	<input type="text"/> PN# 0...31	
echo reset	-1	1		
program	2	6	<input type="text"/> PN# <input type="text"/> Threshold <input type="text"/> Veto <input type="text"/> Pattern <input type="text"/> Counts:2	
echo program	-2	6		
autoreprogram	3	2	<input type="text"/> PN# <input type="text"/> ReprogNum	
echo autoreprogram	-3	2		
telemetry	4	0		
telemetry reply	-4	25	<input type="text"/> PN# <input type="text"/> VccInt:2 <input type="text"/> VccAux:2 <input type="text"/> Vrefp:2 <input type="text"/> Temp:2 <input type="text"/> Vref[0]:2 <input type="text"/> Vref[1]:2 <input type="text"/> Vref[2]:2 <input type="text"/> Vref[3]:2 <input type="text"/> Vref[4]:2 <input type="text"/> Vref[5]:2 <input type="text"/> Vref[6]:2 <input type="text"/> Vref[7]:2	
coincidence data	-5	variable	<input type="text"/> Sample Data 8192 bytes x 32 channels <input type="text"/> zlib compressed, base64 encoded <input type="text"/> 0x4F <input type="text"/> TrigInFlag <input type="text"/> TrigReg:4 <input type="text"/> LockAddr:2 <input type="text"/> GPS:3 <input type="text"/> TrigReg:4 <input type="text"/> LockAddr:2 <input type="text"/> Threshold <input type="text"/> Veto <input type="text"/> Pattern <input type="text"/> Counts:2	
program DAC	12	18	<input type="text"/> PN# <input type="text"/> 0x00 <input type="text"/> ValCh[0]:2 . . . <input type="text"/> ValCh[15]:2	
echo program DAC	-12	18		
fastclk enable	13	1	<input type="text"/> PN#	
echo fastclk enable	-13	1		
fastclk disable	14	1	<input type="text"/> PN#	
echo fastclk disable	-14	1		
set register	15	5	<input type="text"/> RegNum <input type="text"/> Value:4	
echo set register	-15	5		
read register	16	1	<input type="text"/> RegNum	
read register reply	-16	4	<input type="text"/> Value:4	
core enable	17	1	<input type="text"/> PN#	
echo core enable	-17	1		
core disable	18	1	<input type="text"/> PN#	
echo core disable	-18	1		
read astro counters	25	0		
read astro counter reply	-25	128	<input type="text"/> CountsCh[0]:4 . . . <input type="text"/> CountsCh[31]:4	

Figure 3.8: Messages are sent to PulseNet-V over ethernet and are handled by `pulsenetvd`. The communication protocol is shown in the table above. Messages are encoded in ASCII before transmission.

## `astro_udp`

**Astro\_udp** is the PulseNet-V's linux user-space program for disseminating astronomy counts. Its task is to read the count values from the 32 **astro\_counter1** registers and forward the data to a host. **Astro\_udp** will emit a UDP packet containing all of the counts at the count update rate, which is configurable between 0.75, 2, 4, or 10 seconds. The count rates are perishable information so using the UDP protocol allows packets to be dropped during periods of high network traffic. Since the only intervening network between the server and the camera are dedicated switches, packet loss is rare.

## 3.5 FPGA Configuration and Flash

The programming of the Virtex-5 FPGA with the PulseNet-V design can be effected in multiple ways. During development and testing, the FPGA is normally configured using a Xilinx USB programming cable plugged into a header on the PulseNet-V's circuit board. For boot time configuration, the Advanced All-sky Camera's daughterboards provide a Xilinx Platform Flash XL XCF128X 128 Mbit parallel NOR flash memory chip for each PulseNet-V. The Platform Flash XL has 16 data lines for fast loading of the configuration data; PulseNet-V bit files specify a 2 MHz config clock (CCLK) so that the configuration loads in about one second. The FPGA configuration as well as the stage-2 bootloader are held in the Platform Flash. The Virtex-5 configuration bitfile consumes the bottom 29,124,608 bits of the Platform Flash XL and the U-boot bootloader resides in the top 512kB starting at address 0xF80000.

Initial programming of the Platform Flash uses the “indirect method” provided by the Xilinx EDK. The flash programming MCS file is generated to contain the bitswapped versions of the PulseNet-V FPGA configuration and the U-boot bootloader. Then the indirect programming core is loaded over JTAG onto the Virtex-5. The programming core contains a flash memory controller able to write to the Platform Flash XL. The flash programming data is sent to the indirect programming core serially within JTAG commands. This process is slow, taking about 15 minutes to completely erase and program the 128 Mbit flash chip. Faster programming of the XL can be performed from within a Linux environment running

on the PulseNet-V using the Memory Technology Device (MTD) software libraries. The PulseNet-V's Microblaze processor controls the address, data, and control lines of the XL using an external memory controller core (`xps_mch_emc` v.3.01a). At power-on, the stage-1 bootloader sets a configuration register of the XL to enable asynchronous read mode operation before reading from the XL. From that point, the XL address space is mapped to the start of the `xps_mch_emc` memory controllers address space. The Microblaze processor can directly access the XL flash memory simply by performing a read on the PLB using the `xps_mch_emc` address offset as the start of the flash memory address space. The MTD software libraries are then able to read, write and erase the XL flash memory. Rewriting the PulseNet-V FPGA configuration using the MTD libraries takes about two minutes. A third option for rewriting the Platform Flash is from the U-boot command-line. The U-boot environment is able to be accessed for the first few seconds after power up. If a key press is sent to the PulseNet-V's serial console, the U-boot command-line will prevent booting into Linux and allow further commands to be entered. U-boot is essentially a stripped down Linux environment but it also has the ability to read and write flash memories. Flash programming MCS files can be downloaded from a TFTP server, stored in DDR SDRAM, and then programmed to the Platform Flash XL.

## 3.6 Design Tools

The PulseNet-V encompasses multiple layers of software which must be designed, compiled, and debugged. In FPGAs, even the hardware level is coded using software. For the FPGA design, Xilinx provided the toolchain called ISE Design Suite. As PulseNet-V features a Microblaze processor, much of the design work centered around configuration of the processor and peripherals using Xilinx Platform Studio (XPS) in ISE's Embedded Development Kit (EDK). XPS synthesizes VHDL and Verilog peripheral libraries provided by Xilinx and by the user into netlists, merges the netlists and constraints into a design file, maps the design to resources on the target FPGA, places and routes the design, analyzes the design timing, and generates a programming file. Initial development of the pulsenet core module was done with ISE Project Navigator for synthesis, RTL browsing, and simulation using the ISim Simulator. Xilinx PlanAhead and `fpga_editor` software was useful for final system design



file inspection and timing constraint verification. The Xilinx Software Development Studio was used for code development of Microblaze executables such as the first stage bootloader and various test programs. Software development of the PulseNet-V Linux kernel, Linux executables, and U-Boot (second stage bootloader) utilized the Microblaze-linux GCC cross-compiler running under a virtualized Ubuntu 11.02 distribution for compilation.

## Chapter 4

# Advanced All-Sky Camera

The Advanced All-sky Camera (AdvCam), together with the existing all-sky optical SETI infrastructure, the observatory, telescope, and control software, complete the Advanced All-sky Optical SETI System. The AdvCam was designed to address the limitations of the first generation All-sky Camera (AsCam). The AsCam and its limitations were described in [Chapter 2](#). These limitations include single pixel triggering, short sample memory record length, low-refresh rate astronomy functions, limited threshold level adjustment, and lack of extended-red photomultiplier tube spectral sensitivity. Advances in modern FPGA's allowed these limitations to be overcome while offering higher data link bandwidth, flexible on-board processing, and the ability for hardware functions to be upgraded through FPGA design revisions and firmware changes. The following are the most important new features of the Advanced All-sky Camera:

**Triggering** The triggering system of the AdvCam can be linked so that a coincident pulse in one pixel pair will cause waveform readout of every pixel in the camera. The purpose of this trigger mode is to discriminate between cosmic ray induced Čerenkov flashes which are an isotropic source of background events. The digitized waveforms of the pixels surrounding the triggered pixel provide imaging information that can recognize Čerenkov flashes so that they are not mistaken for distant laser pulse transmission. The trigger system works by collecting trigger output signals from the PulseNet-V's at a central Spartan-6 FPGA on the motherboard. The Spartan-6 immediately relays the trigger output of any PulseNet-V to the external trigger inputs of all other PulseNet-V's

in the system.

**Astronomy Mode** The AdvCam has the potential to run in an “astronomy mode” by counting the single photo-electron pulses from each photomultiplier tube anode in the detector array and displaying this information in an image format. The AsCam could operate in this astronomy mode, however counts could only be acquired from 32 out of the 512 available pixels at any one time. While a crude image of the sky could be made, the readout time severely limited the usefulness of this mode for telescope pointing calibration. The AdvCam enables a much more robust astronomy mode. Pulse counts can be retrieved from the camera for every pixel once a second, frequent enough to easily recognize stars transiting the PMTs and use the star transits to calibrate the pointing position of the telescope.

**Sample Memory** A major advantage of the Advanced All-sky Camera over its predecessor is its larger sample memory. A total of 8k samples at 800 megasamples-per-second give the camera 10.25  $\mu$ s of record time per trigger versus the 512 samples at 600 megasamples-per-second of the AsCam. Laser pulses with repeat times longer than 850 nanoseconds but shorter than a few seconds would not be acquired by the previous camera. The Advanced All-sky System increases the record time by twelve-fold.

**Threshold Levels** The AsCam was hampered by clock noise coupling on its daughterboards into certain flash ADC channels. This caused excessive coincidence triggering on those channels at much higher threshold voltages than other channels with little clock noise coupling. Care has been taken to route high-speed digital lines away from the analog inputs and reference voltages on the AdvCam daughterboards. Additionally, each daughterboard has its own reference voltage DAC and noise filters on the reference voltage lines. This has allowed the threshold voltage of the AdvCam to be lowered, increasing the system’s sensitivity.

**PMT Spectral Sensitivity** New photomultiplier tubes are used in the Advanced All-sky Camera to extend the spectral range of the all-sky survey and increase the red and near-infrared sensitivity. This is expected to increase the range and number of stars

observed by the AdvCam, especially in the galactic plane where there is more extinction of shorter wavelengths.

## 4.1 Advanced All-sky Optical SETI Camera

The main purpose of the Advanced All-sky Camera is to monitor photomultiplier tubes for flashes of light over a certain intensity threshold, record the waveforms of light flash events, and send that information to a database server which serves as a repository for all events. Auxiliary functions include recording the timing of events, measuring environmental temperature and humidity, measuring telescope inclination angle, setting photomultiplier tube supply voltage, and sensing ambient light levels.

The camera consists of a front compartment containing a shutter, entrance window, beamsplitter, and photomultiplier array. A rear compartment contains the electronics necessary to digitize and record the signals coming from the photomultiplier array. Save for the new PMTs used in the AdvCam, the camera's front end optics have already been described in § 2.4.1. The electronics are split onto nine boards: a single motherboard that links the operations of eight daughterboards. The motherboard carries power rails, a 50 MHz master clock signal, Global Positioning System (GPS) clocks (10 MHz and 1 pulse-per-second), trigger signals, an I<sup>2</sup>C bus, and JTAG programming lines to the daughterboards. Each daughterboard connects to a matched pairs of photomultipliers; the PulseNet-V's perform flash conversion and coincidence triggering on photomultiplier tube anodes pairs.

### 4.1.1 Photomultiplier Tubes

The AdvCam's photomultipliers are Hamamatsu H7546B-20's which use extended red multi-alkalai photocathodes. Their spectral sensitivity extends from 250–900 nm with a peak quantum efficiency of 20% (Figure 4.1). They have a gain of about  $10^5$  at  $-900$  V and a single photo-electron pulse width of  $\sim 3$  ns. The tubes are divided into an  $8 \times 8$  array of anodes with an active cathode area of  $2 \text{ mm} \times 2 \text{ mm}$  per anode. Cross-talk between anodes is low ( $\sim 1\%$ ) but uniformity between anodes is poor, typically 1:3. The central four pixels generally have the best time response, gain, and sensitivity. These photomultiplier tubes

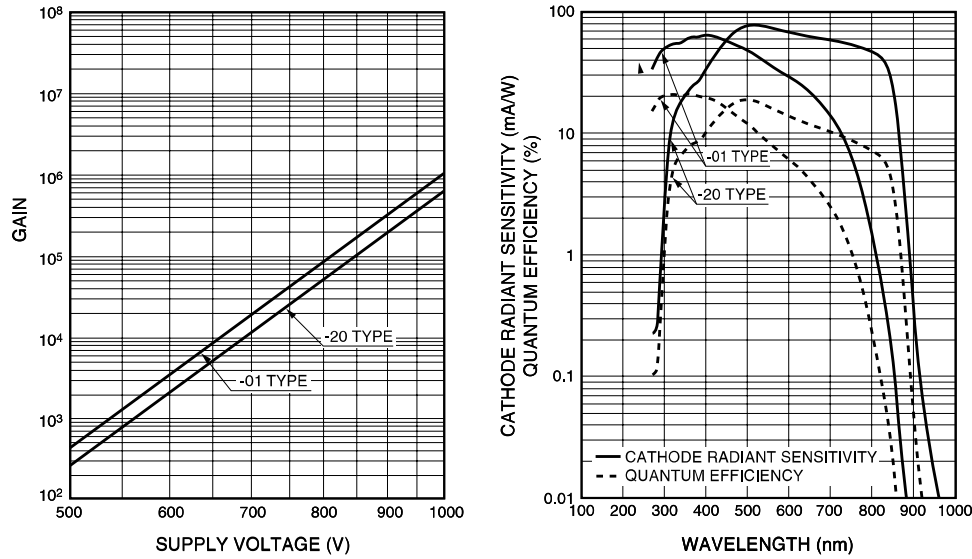


Figure 4.1: The Advanced All-sky Camera uses the Hamamatsu H7564B-20 extended red multi-alkalai photomultiplier tube, extending the spectral range of the original all-sky camera (H7546B-01) and enhancing red sensitivity [33].

were chosen so as to be pin compatible with the circuit boards and power supplies of the previous all-sky camera. This important feature was necessary because the AdvCam circuit boards were retrofitted into the frame of the existing all-sky camera, reusing the PMT rack, mounting hardware, and PMT circuit boards.

### 4.1.2 Daughterboards

Each daughterboard hosts four PulseNet-V's – the FPGA design for all-sky optical SETI that handles the digitization and coincidence triggering of photomultiplier tube pixel pairs (see [Chapter 3](#) for details of PulseNet-V). The PulseNet-V sections are identical except for the routing of global signals from the motherboard such as the system clock, GPS clocks, JTAG lines, and trigger signals. Each section includes the PulseNet-V's Virtex-5 FPGA, a Micron 64MB DDR RAM chip, a Marvell 88E3015 10/100 Ethernet PHY with RJ-45 connector, a Xilinx Platform Flash XL 128-Mbit parallel NOR flash EEPROM for FPGA configuration and bootloader storage, 32 NEC UPC2710TB amplifiers to boost the photomultiplier signals, and a myriad of linear regulators for voltage regulation of each sub-circuit. Additionally,

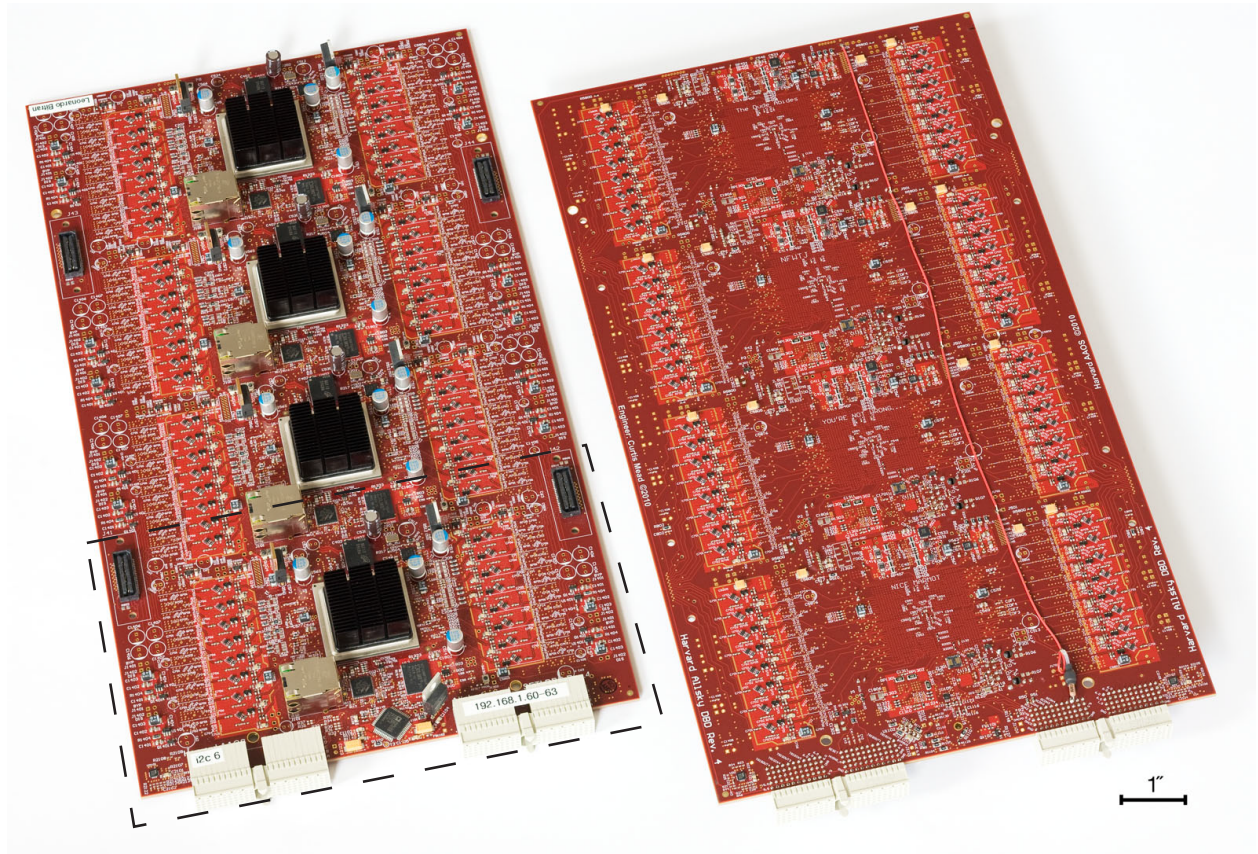


Figure 4.2: Each crimson daughterboard sports four PulseNet-V's. Section contents are shown in [Figure 4.3](#). Photo Credit: Paul Horowitz.

each board has one 16-channel Analog Devices AD5390 DAC that is used for setting the flash ADC reference voltages ( $V_{REF}$ 's) for all four PulseNet-V's on the daughterboard.

The daughterboards are 7.4" wide and 13.1" long. They are built on twelve layers: six signal layers, four ground plane layers, and two split power plane layers ([Figure 4.4](#)). All signal layers are impedance controlled. This is necessary for the DDR SDRAM data and clock lines (200 MHz) and for system clock and GPS clock differential pair routing.

The top and bottom layers are used for photomultiplier tube analog lines and low speed digital routing. Mid-layers 1–4 are high speed digital routing layers. Plane layers 1, 3, 4, and 6 are solid ground planes (except 3) that are stitched together with vias throughout the board. Plane layer 3 has an isolated ground island under each Virtex-5 that is used as an analog ground reference for the Virtex-5's on-board 10-bit ADC. Plane layers 2 and 5 are

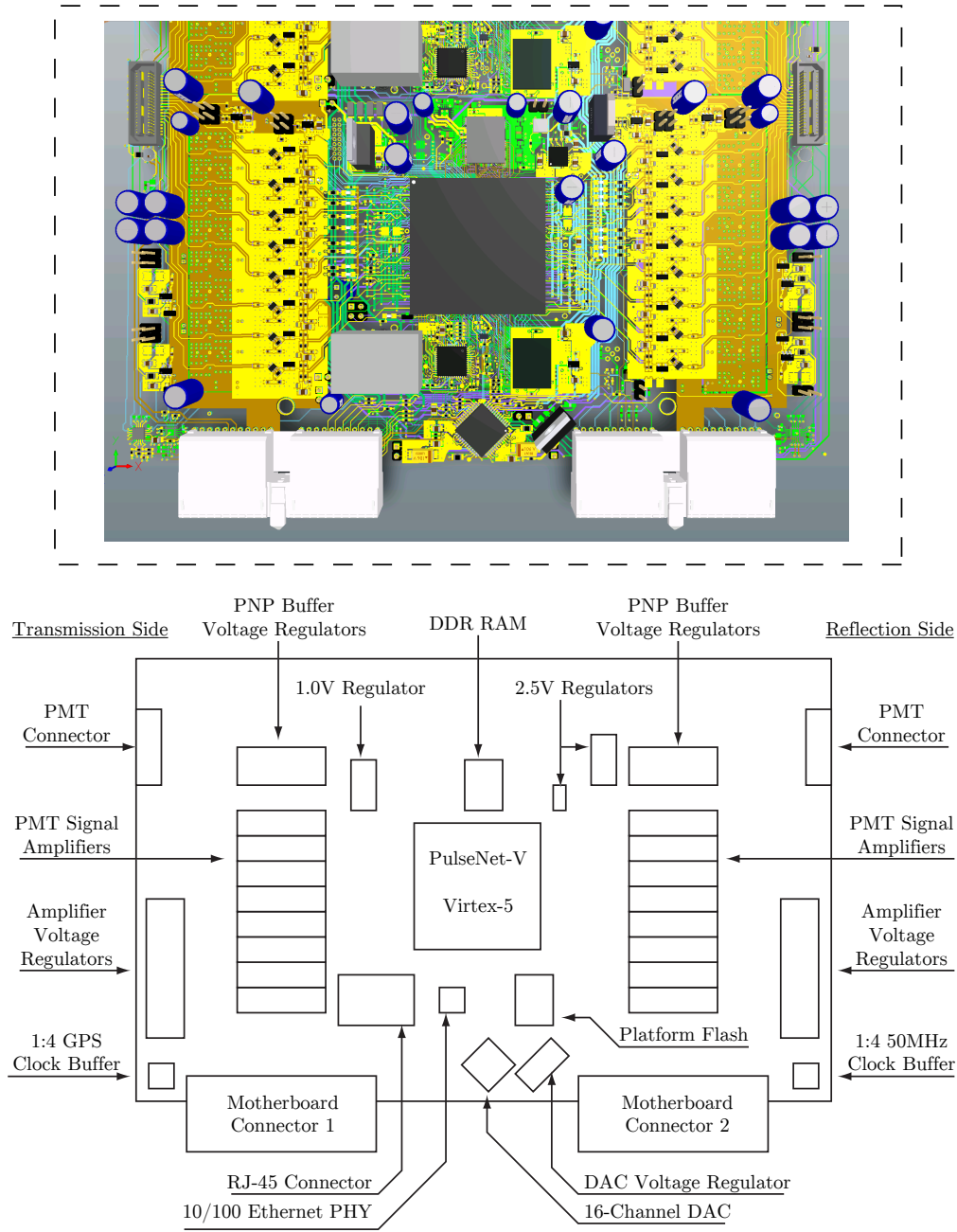


Figure 4.3: Top: This false color layout shows one of the four similar PulseNet-V sections of the daughterboard, the “Duderino” area. The six signal layers from the top to the bottom are yellow, purple, aqua, mint, and green, respectively. Bottom: A schematic showing the area’s contents.



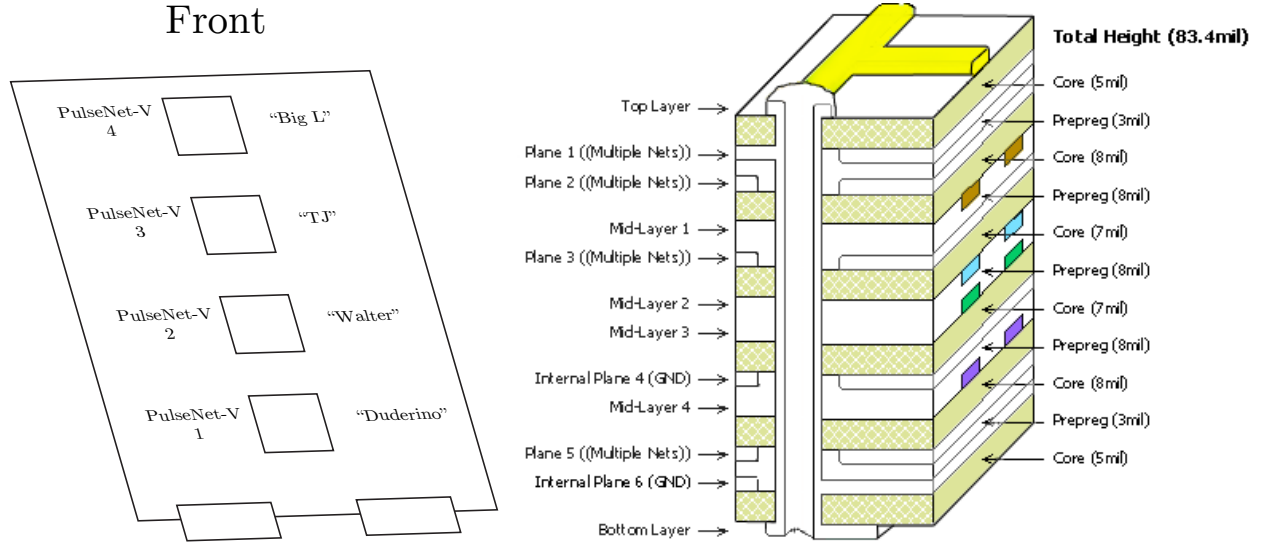
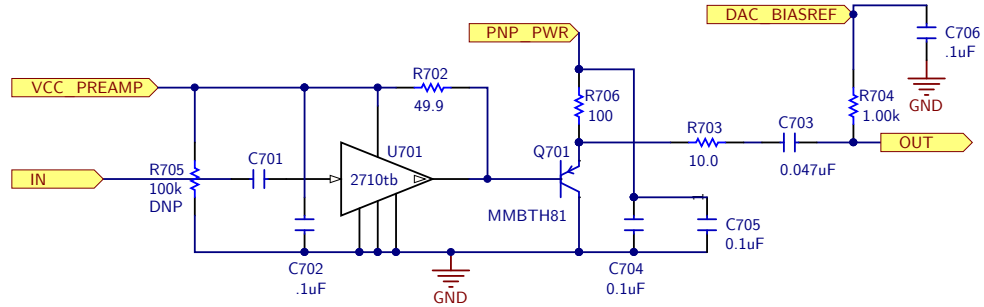


Figure 4.4: Left: The area naming scheme for the daughterboard's PulseNet-V locations. Right: Daughterboard layer stackup.

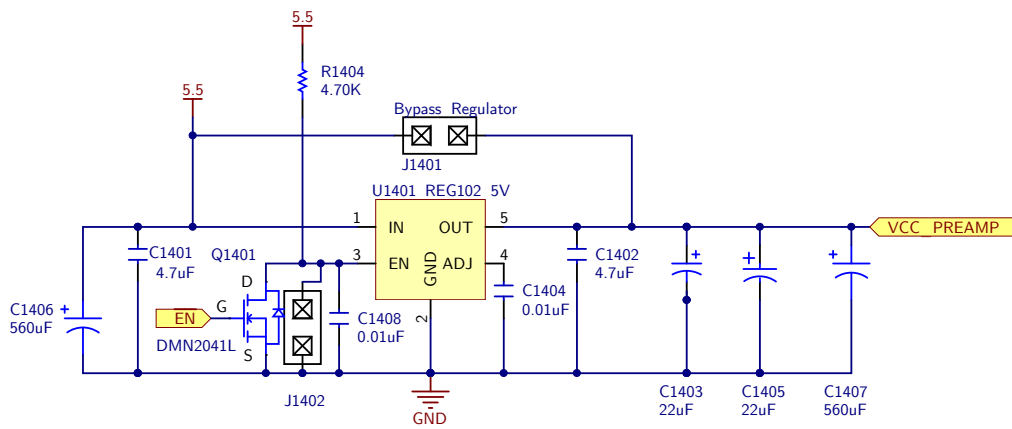
highly split power planes that bring the many different bus voltages to each section of the board. Care was taken to have ground planes adjacent to the top and bottom layers where the PMT signal amplifiers are located. Previous daughterboards had exhibited coupled high-frequency oscillations between signal amplifiers. The close-in ground plane reduces stray inductances that help to prevent the amplifier oscillation. The power plane of each bank of eight amplifiers was isolated and given individual linear power regulators to further increase isolation between the amplifiers.



## PMT Signal Amplifier



## 5 V Power Regulator



## 5.7 V Power Regulator

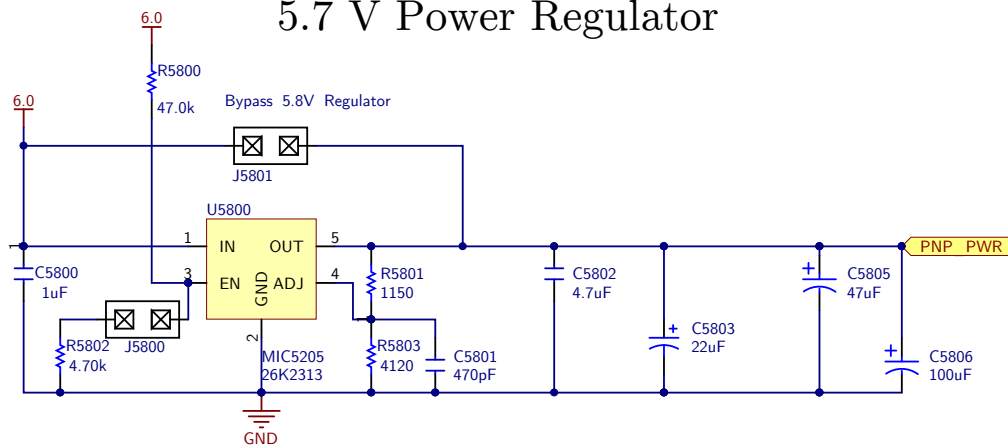


Figure 4.5: PMT Signal Amplifier Schematic.



# Micron DDR SDRAM



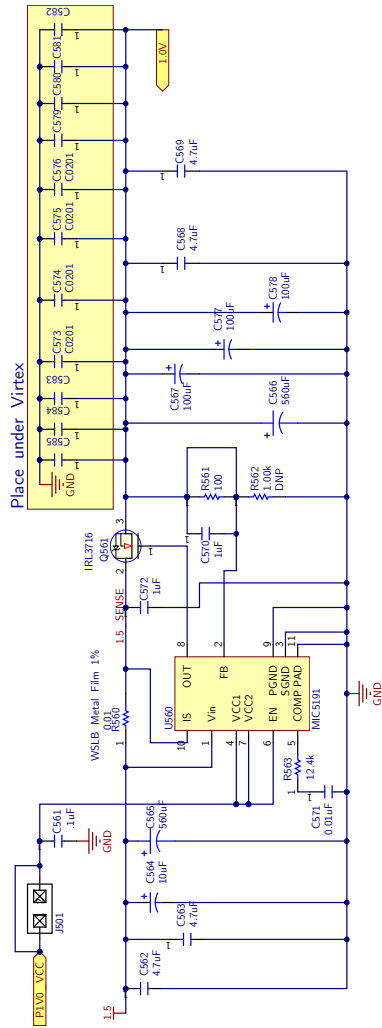
112



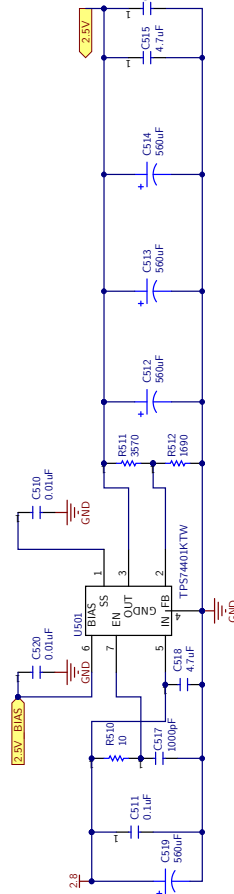
[illegible]

Figure 4.9: Daughterboard DAC Schematic.

## 1.0 V FPGA Core Supply



## 2.5 V Main Supply



## 2.5 V Auxiliary Supply

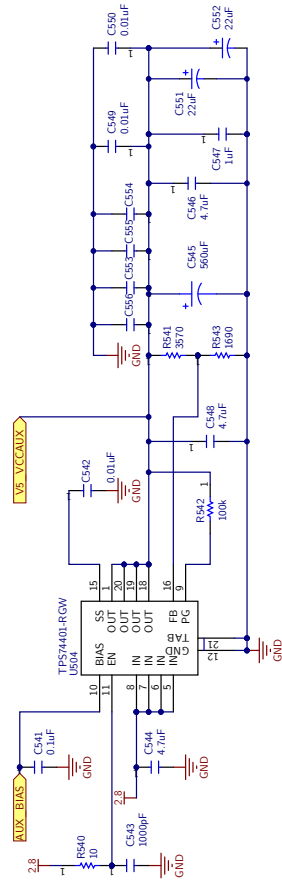


Figure 4.10: Daughterboard Power Regulators Schematic.

### 4.1.3 Motherboard

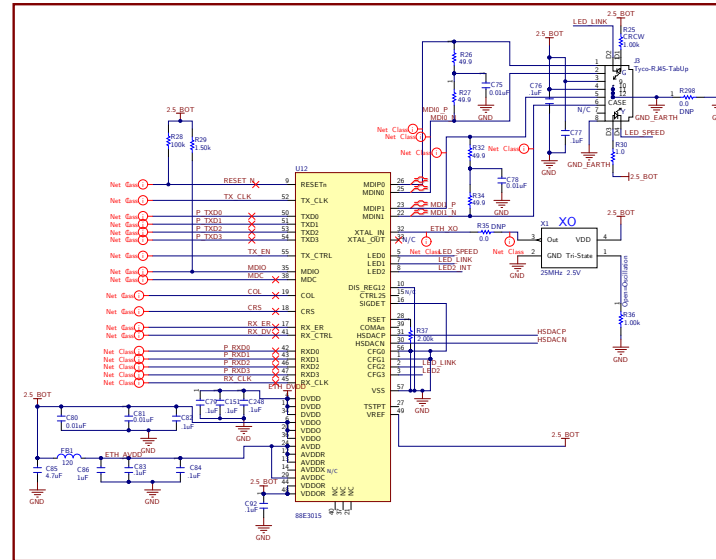
The motherboard distributes common signals and power to the daughterboards and mechanically supports them at the connector end. It has a Xilinx Spartan-6 LX45 FPGA for coalescing trigger outputs from the 32 PulseNet-V's, and for collecting humidity, temperature, and inclination angle from on-board sensors. The Spartan-6 is connected to 512 Mb of 16-bit wide DDR SDRAM, a micro-SD connector, two serial transceivers, a USB serial transceiver, a Xilinx X32P serial Flash PROM for FPGA configuration memory, a Marvell 88E3015 10/100 ethernet PHY, a Xilinx CoolRunner-II CPLD for daughterboard JTAG programming distribution, a 1:8 LVDS clock buffer to distribute a master clock to the daughterboards, two 1:8 LVDS clock buffers to distribute GPS clocks, a Xilinx Spartan-3 AN50 FPGA, and a Silabs C8051 microcontroller. The daughterboards are provided with five supply voltages, 1.4 V, 2.8 V, 5.5 V, 6.0 V, and 12 V. The 1.4 V, 2.8 V, 5.5 V, and 6.0 V supplies are brought on to the motherboard with Phoenix Contact terminal blocks and passed through to the daughterboards on 2 mm hard metric backplane connectors. The 12 V rail is regulated down from 15 V on the motherboard with a linear voltage regulator before making its way onto the daughterboard to power the 1.0 V regulator controller. Other signals distributed to the daughterboards include the GPS 10 MHz and 1 PPS clocks, a 50 MHz system clock, an I<sup>2</sup>C bus, JTAG lines, and trigger in/out signals. The GPS signals arrive at the motherboard from a fiber translator in the camera that receives the GPS signals over multimode fiber cables from a Symmetricom GPS clock located in the observatory control room. The 50 MHz daughterboard system clock is generated by an ECS surface mount clock oscillator on the motherboard and passed through the Spartan-6. The clock is then sent through a 1:8 buffer and the eight outputs are distributed to the daughterboard connectors.



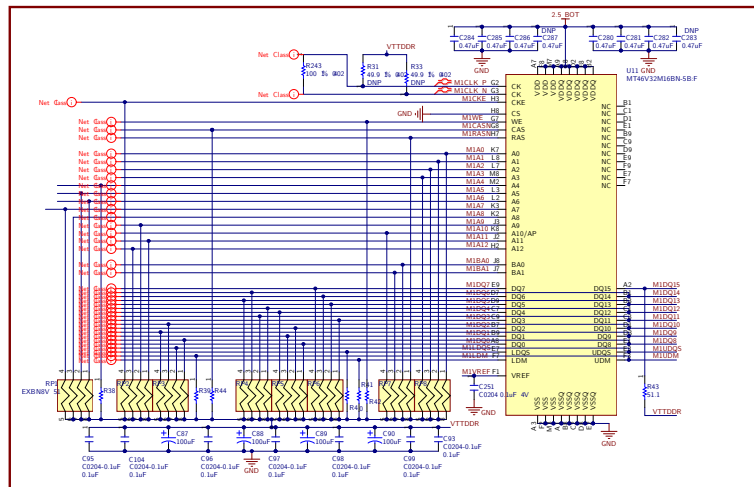
Figure 4.11: The motherboard distributes power and global signals to the daughterboards. A Spartan-6 on the board functions as the system-wide trigger for the 32 PulseNets-V's. Photo Credit: Paul Horowitz.



## Ethernet



## DDR SDRAM



### Termination Voltage Controller

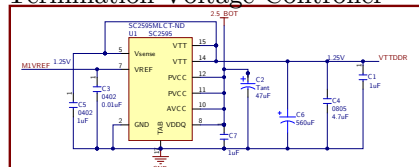
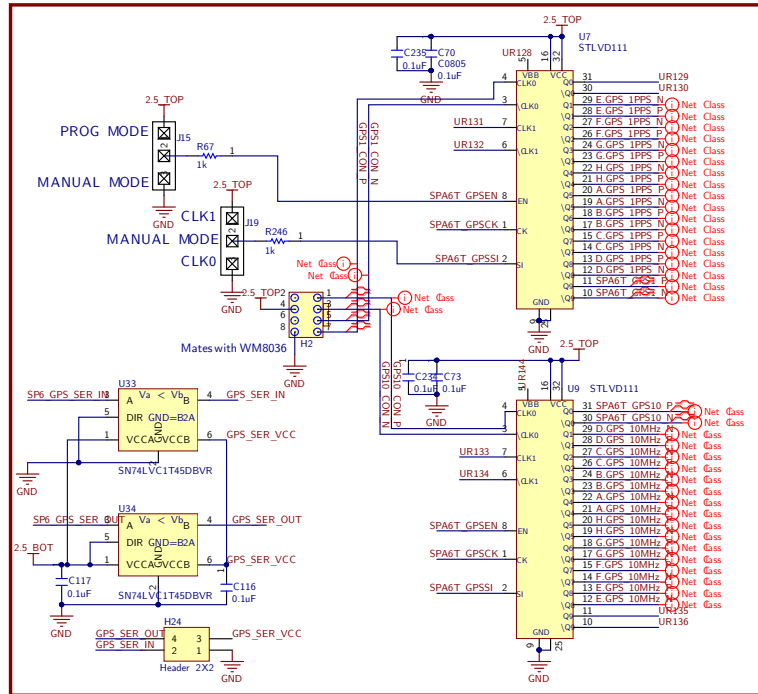


Figure 4.12: Motherboard SDRAM and Ethernet Circuits

## GPS and GPS Distribution



## Clock and Clock Distribution

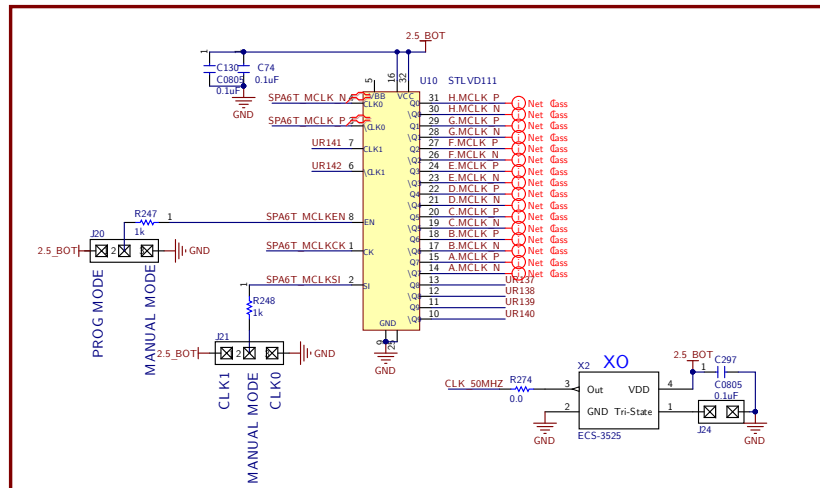
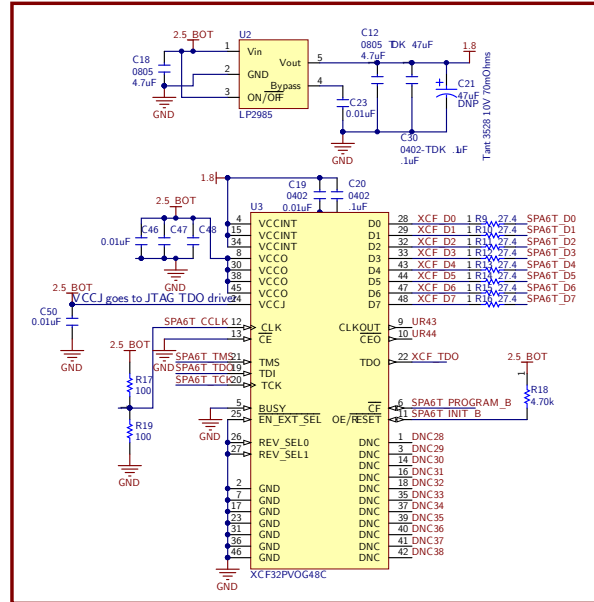


Figure 4.13: Motherboard GPS and Clock Circuits

## Platform Flash



## JTAG and Config

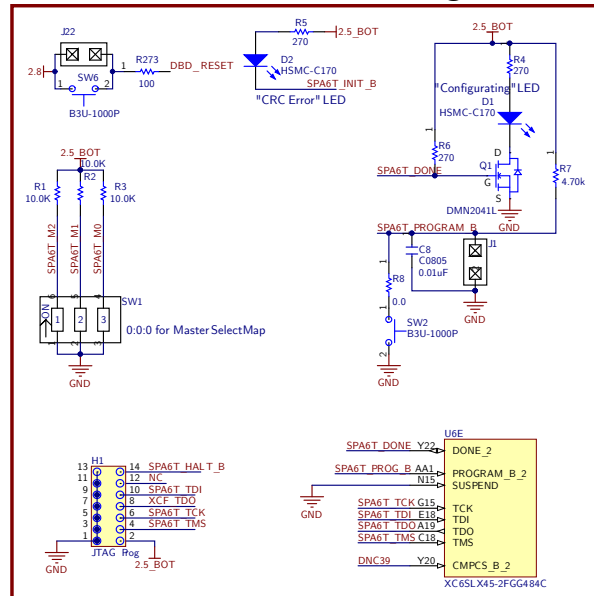


Figure 4.14: Motherboard Config Circuits







Table 4.1: Spartan-6 Peripherals.

Name	Desc	IP	Bus
microblaze	Microblaze processor	microblaze v8.20.a	AXI
axi4	AXI bus 100 MHz	axi_interconnect v1.03.a	AXI
axi4lite	AXI-Lite bus 50 MHz	axi_interconnect v1.03.a	AXI-Lite
microblaze_dlmb	Data mem bus	lmb_v10 v2.00.b	DLMB
microblaze_ilmb	Instruction mem bus	lmb_v10 v2.00.b	ILMB
MCB_DDR	Double data rate SDRAM controller	axi_s6_ddrx v1.03.a	AXI
microblaze_bram_block	16k Bram Block	bram_block v1.00.a	DLMB:ILMB
microblaze_d_ctrl	8k Local Data Mem	lmb_bram_if_cntlr v3.00.b	DLMB
microblaze_i_ctrl	8k Local Instruction Mem	lmb_bram_if_cntlr v3.00.b	ILMB
debug	In-circuit debugging for Microblaze	mdm v2.00.b	AXI-Lite
microblaze_intc	Interrupt coalescing and control	axi_intc v1.01.a	AXI-Lite
axi_ethernetlite	Ethernet Media Access Controller	axi_ethernetlite v1.00.a	AXI-Lite
gpio_pf	GPIO controller for Flash	axi_gpio v1.01.a	AXI-Lite
jtag_dbrd	GPIO controller for DBD JTAG	axi_gpio v1.01.a	AXI-Lite
dbd_iic	I <sup>2</sup> C controller for daughterboard I <sup>2</sup> C bus	axi_iic v1.01.a	AXI-Lite
inclinometer_spi	SPI controller for Inclinator	axi_spi v1.01.a	AXI-Lite
microsd	SPI controller for SD card	axi_spi v1.01.a	AXI-Lite
axi_timer	Dual system timer	axi_timer v1.02.a	AXI-Lite
rs232_uart_1	Serial port 1	axi_uartlite v1.02.a	AXI-Lite
rs232_uart_2	Serial port 2	axi_uartlite v1.02.a	AXI-Lite
jtag_master	JTAG bus master	jtag_master v1.00.a	AXI-Lite
mbrd_trig	Trigger module	mbrd_trig v3.08.a	AXI-Lite
clock_gen	Clock generator	clock_generator v4.02.a	None
proc_sys_reset	System reset controller	proc_sys_reset v3.00.a	None
gps10M_buf	Differential buffer for GPS 10MHz clock	util_ds_buf v1.01.a	None
gps1pps_buf	Differential buffer for GPS 1PPS clock	util_ds_buf v1.01.a	None
eth_xo_ff	Ethernet 25 MHz clock	util_flipflop v1.10.a	None

The Spartan-6 FPGA design contains a Microblaze embedded processor, DDR SDRAM memory controller, 10/100 ethernet MAC, an I<sup>2</sup>C bus master, two serial ports, and the motherboard trigger distribution module called `mbrd.trig`. The Microblaze system design is similar to the PulseNet-V design, mostly comprised of Xilinx library modules. The bus that connects internal peripherals to the Microblaze processor is an AXI bus as opposed to the PLB bus used in PulseNet-V. The AXI bus is a more recent bus standard and is used for new Microblaze embedded system designs. The SDRAM memory controller of the Spartan-6 is a hard silicon feature and is less flexible than the Multi-port Memory Controller (MPMC) of the PulseNet-V Virtex-5 design. The data, address, control, and clock line pin locations of Spartan-6 SDRAM controller are not adjustable. The full list of peripherals used in the Spartan-6 design is shown in [Table 4.1](#). The `mbrd.trig` module is the only all-sky proprietary module. It is described in the next section.

Table 4.2: `mbrd_trig` Configuration Registers

Register	Num	Bits	Name	Dir	Description
Trig In	0	31:0	<code>ins_reg</code>	R	State of the 32 trigger input lines from PulseNet-V's
Trig Out	1	31:0	<code>outs_reg</code>	R	State of the 32 trigger outputs lines to PulseNet-V's
Ext Trig	2	0	<code>ext_trig_in_n</code>	R	State of the motherboard's external trigger input
Trig Mask	3	7:0	<code>_trig_in_n</code>	RW	Daughterboard mask for mbrd triggers
Trig Status	4	2	<code>count_done</code>	R	Indicates the end of the $2\mu\text{s}$ trigger timeout
	4	1	<code>trig_or</code>	R	An OR of the 32 trigger input lines and the external trigger
	4	0	<code>trig_in_only</code>	R	An OR of only the 32 trigger inputs lines
Dbd Reset	5	0	<code>dbd_reset</code>	RW	Resets all daughterboards
Trig Reset	6	0	<code>soft_reset</code>	RW	Resets the mbrd trigger state-machine
PN Ser Sel	7	5:0	<code>ser_sel</code>	RW	Selects a PulseNet-V for serial debug
Ready Status	8	2	<code>ready_override</code>	RW	Debug override of <code>pnet_ready</code>
	8	0	<code>pnets_ready</code>	R	Indicates all PulseNet-V's active
Trig In 2	9	31:0	<code>ins_mailbox</code>	R	State of PulseNet-V inputs during the last mbrd trigger
Trig Flags	10	1	<code>ins_mailbox_flag</code>	R	Indicates if <code>ins_mailbox</code> has been read
	10	0	<code>gps_mailbox_flag</code>	R	Indicates if <code>gps_mailbox</code> has been read
GPS Timestamp	11	23:0	<code>gps_mailbox</code>	R	State of GPS counter during the last mbrd trigger
GPS counter	12	23:0	<code>gps_counter</code>	R	Direct read access to the GPS counter
GF1	13	0	<code>gf1_flash_nedge</code>	RW	Neg edge activates the GF1
RSVD	14	31:0	N/A	RW	Reserved for future use
GPS Level	15	0	<code>gps_level</code>	RW	Invert the GPS 1PPS clock signal

## Spartan-6 Trigger Module

The `mbrd_trig` module's main function is as the AdvCam's system-wide trigger logic. All trigger in and trigger out lines from the AdvCam's 32 PulseNet-V's are routed into the module from the Spartan-6 pins. A state machine waits for one of the PulseNet-V trigger lines to activate. When activated, the state machine will enter a state that holds all Spartan-6 trigger output lines active-low for  $2\mu\text{s}$ . The PulseNet-V's receive this Spartan-6 trigger signal and follow a trigger sequence. When the PulseNet-V's trigger sequence has completed, it releases its trigger output. The `mbrd_trig` state machine keeps its trigger outputs active-low until all trigger signals from the PulseNet-V's become inactive indicating they are ready to be triggered again. The `mbrd_trig` state machine then resets and reverts the trigger outputs back to the initial inactive state.

The module contains a special feature that aids in debugging the PulseNet-V's. During boot, the PulseNet-V's connect their default serial console to their trigger in and trigger out lines. The `mbrd_trig` module has access to these lines and can connect any pair to a serial module in the Spartan-6 by setting a `mbrd_trig` configuration register. A user connected



to a Linux shell console of the the Spartan-6 (over telnet or hardware serial connection) can watch the boot process of any PulseNet-V in the system using a simple Linux terminal emulator.

A GPS counter for timestamping trigger events is also included in the module. This is similar to the counter used in the PulseNet-V designs. Test flashes from the Gelfand Flasher I are triggered by an output controlled by `mbrd_trig`. This output is set by bit 0 of `mbrd_trig` control register 13. The daughterboard’s 50 MHz master clock is generated by logic `mbrd_trig`. While it is currently a simple division by 2 from the Spartan-6 100 MHz master clock, a PLL could be used to make the daughterboard clock frequency adjustable.

The `mbrd_trig` is an AXI bus peripheral. The triggering options and status of the AdvCam’s system-wide trigger are controlled through `mbrd_trig`’s 16 configuration registers. The registers are listed in [Table 4.2](#). Register 0 and 1 are, respectively, the 32 trigger input lines from the PulseNet-V’s and the 32 trigger output lines from the Spartan-6 to the PulseNet-V’s. These registers are memory mapped I/O and are ephemeral. When a trigger occurs, the state of the trigger inputs (register 0) are loaded into register 9. Register 4 has additional trigger status information. The GPS counter also has a direct access register (12) and a register that is loaded with the GPS counter value when a trigger occurs (register 11). Flags that indicate whether the triggered GPS and trigger input registers have been read are located in register 10. Triggering can be prevented on a by-daughterboard basis using the trigger mask (register 3). This is useful during prototyping and debugging when only certain daughterboard positions in the motherboard are populated. Also useful for debugging, the motherboard has an external trigger switch that forces a system-wide trigger. The state of this switch is shown in bit 0 of register 2. A hardware reset for all PulseNet-V’s is provided in register 5. The PulseNet-V serial debug select line is in register 7; a `0x0` written to the register selects PulseNet-V 0 (“Duderino” on daughterboard 7) and `0x1F` selects PulseNet-V 31 (“Big L” on daughterboard 0). The ready status register (8) shows the status of the `pnets_ready` signal in bit 0. Each PulseNet-V has a `pnet_ready` output that is OR’d by the Spartan-3AN FPGA. The single OR’d output is sent to Spartan-6 and is the signal shown in the ready status register. This signal, if not active-high, will prevent the `mbrd_trig` module state machine triggering so an override is available in bit 2 of register 8 for debugging purposes. Finally, the GPS 1PPS clock signal can be inverted using register 15.

## Other Firmware

In addition to the Spartan-6, the Spartan-3AN and CoolRunner-II on the motherboard require firmware to perform their functions. They use very simple VHDL designs and were developed in Xilinx's ISE design tool. The CoolRunner-II essentially acts as a JTAG switch. A JTAG bus from the Spartan-6 is routed to the CoolRunner-II along with four address lines. The CoolRunner-II design connects the JTAG bus from the Spartan-6 to one of the eight daughterboard's JTAG busses based on the state of three of the address lines. The fourth address lines causes the JTAG bus input to come from a header on the motherboard, not from the Spartan-6. The Spartan-3AN design is even simpler. The four address lines pass through the Spartan-3AN before going to the CoolRunner-II; the Spartan-3AN acts as a simple buffer. The reason for this complexity is to allow for the flexibility to use the lines that are routed between the Spartan-6, Spartan-3AN, and CoolRunner-II in other ways if a future need arises. The Spartan-3AN has an additional job that it must perform. One single-ended GPIO pin from each PulseNet-V is routed to the Spartan-3AN. This line is used as the `pnet_ready` PulseNet-V output line. `Pnet_ready` indicates that the PulseNet-V is programmed, its `pulsenetvd` software is running, and it is ready to receive a coincidence trigger. The Spartan-3AN AND's these lines together. The output, `pnets_ready`, is sent to the Spartan-6. The Spartan-3AN also connects 10 I/O pins to a Silabs C8051 microcontroller on the motherboard but the microcontroller is unused and is included in the design as a general purpose resource.

## Software

The Spartan-6 uses a custom Linux kernel as its operating system. The compiler and kernel source were obtained from Xilinx. The Spartan-6 Microblaze processor uses an AXI bus which requires that the little-endian Linux kernel be used. The process for compiling the kernel was similar to the process for the PulseNet-V kernel (§ 3.4.1). A device tree from the Spartan-6 FPGA design and a kernel config file with the necessary options were produced and used during the kernel compile process. The Spartan-6 has one daemon program running on top of the kernel, `mbrdd`. The daemon program listens for connections on a TCP socket and responds to messages that are sent from the host. The commands and protocols are

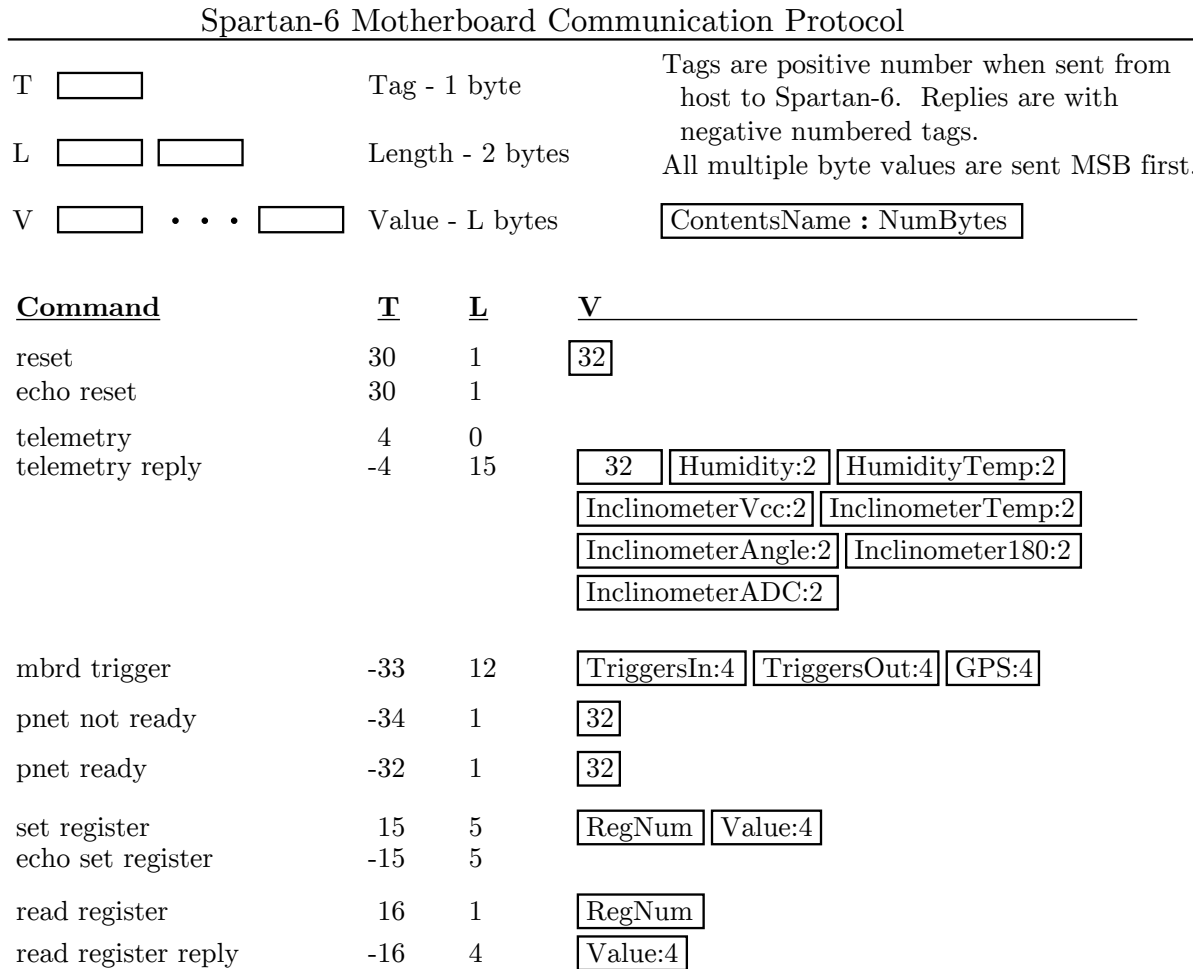


Figure 4.18: Spartan-6 Motherboard Communication Protocol

shown in **Figure 4.18**. In addition to responding to host messages, **mbrdd** will send a message to the host when a PulseNet-V trigger is received and if the **pnets\_ready** signal changes. A driver for the **mbrd.trig** module handles trigger and **pnets\_ready** interrupts by writing trigger data to a kernel buffer and then writing the trigger time to the `\dev\mbrd` device. Similar to **pulsenetvd**, **mbrdd** polls the `\dev\mbrd` device waiting for data from the kernel driver. When the poll returns the trigger time, the **mbrdd** program reads the kernel buffer and sends the trigger data to the connected host.

## Spartan-6 FPGA Config

The Spartan-6 configuration flash memory is a 32Mbit serial flash, the Xilinx XCF32P. The XCF32P has a JTAG port and can be programmed directly by the Xilinx USB Programming Cable. Spartan-6 designs bitfiles are turned into MCS flash programming files with the U-boot bootloader appended to the end of the file, following the FPGA configuration. The MCS file can then be programmed to the XCF32P. The Spartan-6 is initialized with a stage-1 bootloader that resets the XCF32P and locates the stage-2 bootloader within the serial flash. The XCF32P is specifically designed as FPGA configuration memory, and as such can only be accessed serially. The Spartan-6, after configuration, connects to the serial flash clock, reset, and data lines through a general purpose I/O core (`axi_gpio v1.01a`). Initialization of the serial flash involves resetting the flash and toggling the clock line, which increments the read address, until the bootloader code appears on the data lines. The stage-2 bootloader code for the Spartan-6 exists in the XCF32P directly after the FPGA configuration data. It is copied into a high DDR SDRAM address (`0x53000000`) and then executed. U-boot downloads the Spartan-6 motherboard kernel from a TFTP server (Costas), uncompresses it, copies it into place in DDR SDRAM, and then starts execution at the beginning of the kernel address space.

## PulseNet-V JTAG Config

Testing and debugging requires fast and reliable FPGA reconfiguration, both during the camera prototyping phase and in production. Consequently, JTAG access to each PulseNet-V, which is used to hot-load a new FPGA configuration, is an important feature of the Advanced All-Sky Camera. The motherboard Spartan-6 handles JTAG communication for each of the 32 in system PulseNet-V's. A JTAG bus connects the Spartan-6 to a Xilinx CoolRunner-II CPLD which acts as a multiplexer for the JTAG bus. A separate address bus controls which daughterboard (0-7) the CPLD targets. Once a daughterboard is selected, the Spartan-6 is directly connected to the JTAG chain for that daughterboard and can access any of the 4 PulseNet-V's on the daughterboard. The Spartan-6 uses a general purpose I/O controller to toggle the JTAG bus pins. A user-space program called `xsfttool-mbrd` takes as parameters the daughterboard number and SVF file to program. An external JTAG

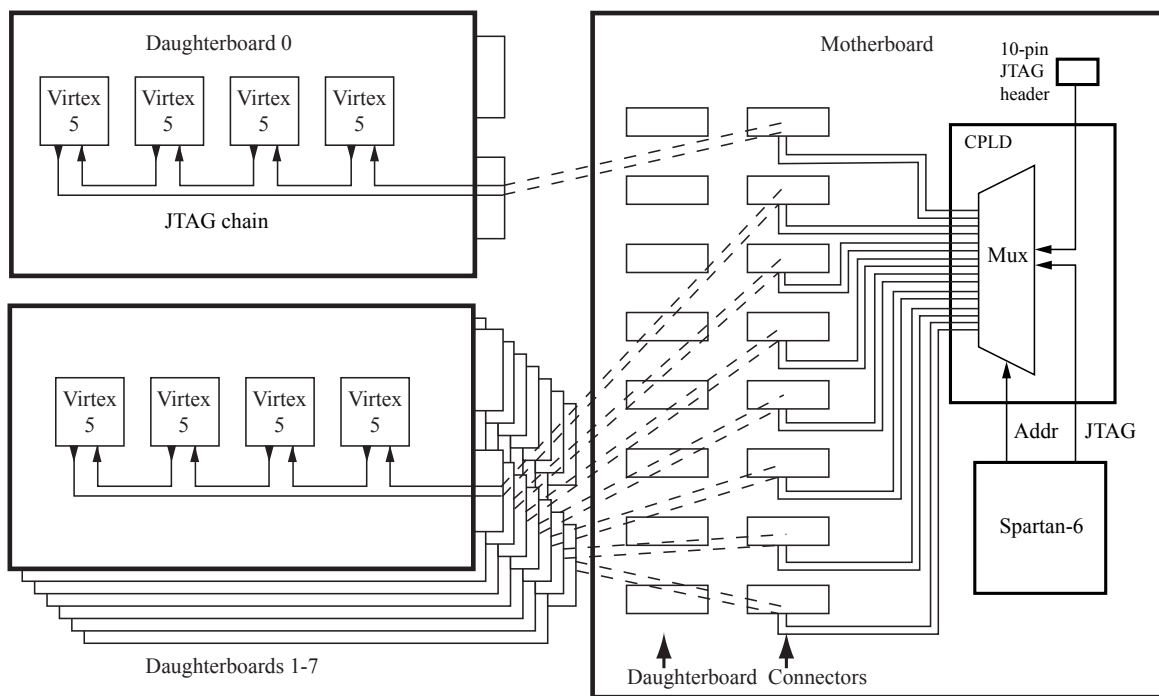


Figure 4.19: The motherboard Spartan-6 is used to reconfigure the Virtex-5 FPGAs using the JTAG bus. A CoolRunner-II CPLD multiplexes the Spartan-6 JTAG to one of the eight daughterboard JTAG chains.

programmer can also be used to reconfigure the PulseNet-V's. In this case, the CoolRunner-II CPLD is set to accept a JTAG bus from a pin header to forward to a specific daughterboard. The daughterboard address must still be set using the Spartan-6.

#### 4.1.4 Server

The camera electronics are very closely integrated with a server computer called Costas. Costas is a custom built PC with a quad-core Intel processor with two mirrored RAID arrays, one for the operating system and one for the database. Costas provides the Linux kernels that the Microblaze processor boots when the camera is powered on. Each PulseNet-V first loads the U-boot bootloader. U-boot knows the IP address of Costas and requests the Linux kernel using the TFTP protocol. When the kernel file is downloaded from Costas, U-boot uncompresses it, loads it into memory, and directs the processor to begin

execution of the kernel out of DDR SDRAM. During the boot process, Linux must mount a filesystem. This filesystem is located on the Costas operating system RAID array in the directory `\srv\common`. The booting Linux kernel of every PulseNet-V mounts this read-only directory as the filesystem root using the Network File System (NFS) protocol. The final stage of booting is the execution of the `rcS` script. This script mounts a writeable directory `\var\pn[0--31]`, again using NFS, so that each PulseNet-V has a private location to store system logs, temporary files, and the NTP drift file.

#### 4.1.5 Other Camera Equipment

The completed camera includes a number of other pieces of electronic equipment. To receive the GPS signals from a Symmetricom GPS clock unit in the observatory control room, a fiber-translator transmitter/receiver pair are used. The transmitter is located in the control room next to the GPS clock and transmits the electrical clock signals into two multi-mode fiber cables. The fibers are run from the control room into the telescope bay and enter the camera at a fiber-to-fiber coupling. The fiber receiver sits atop the circuit board rack and converts the optical signal back to an electrical signal that is connected to a header on the motherboard. An AxiomTech Pico820 single-board-computer also sits on top of the circuit board rack. This single-board-computer (SBC) has an Intel Z510 processor with a 8GB solid-state disk that is configured to boot an Ubuntu Linux distribution. It also mounts a writeable NFS folder on Costas for extra storage space. The SBC is connected to the USB serial transceiver on the motherboard and also to a Xilinx USB Programming Cable II. The programming cable's socket is plugged into the motherboard's Spartan-6 JTAG header. The purpose of the SBC is for reprogramming the motherboard's Spartan-6 configuration flash memory if it becomes corrupted or needs to be updated. Through the USB serial connection, it also has dedicated hardware access to the Spartan-6's serial port. Ethernet connections are provided for the 32 PulseNet-V's, the Spartan-6, and the SBC by three 16-port 10/100/1000 Netgear switches mounted to the camera frame between the photomultiplier and circuit board compartments. Startech.com MCMGBSC055 gigabit multi-mode fiber media converters make the connection between Costas and the upload port of one of the Netgear switches.

Table 4.3: The main control application `oseti.py` contains numerous additional files for controlling each of the observatory subsystems.

Filename	Purpose
<code>oseti.py</code>	Main application
<code>astronomy.py</code>	Calculates sunrise, sunset, moon position, etc.
<code>automation.py</code>	State machine for automated observational control
<code>barndoors.py</code>	Retrieves status of barn doors
<code>fits2jpg.py</code>	Converts skycam FITS files to jpg
<code>FitsFile.py</code>	Library for importing FITS files
<code>gf2.py</code>	Controls movement of Gelfand Flasher 2
<code>json.py</code>	Library for producing json from python objects
<code>observations.py</code>	High level observing control functions
<code>oseticameras.py</code>	Grabs images from 4 observatory cameras
<code>osetiencoder.py</code>	Retrieves index and count from telescope encoder
<code>osetievent.py</code>	Event definitions for postgres database
<code>osetiexptctrl.py</code>	Advanced All-sky Camera control
<code>osetipower.py</code>	Interface to Shulsky box for power control
<code>osetiroof.py</code>	Interface to Roof Controller
<code>osetiserial</code>	Generic class for serial port interfaces
<code>osetistate.py</code>	Postgres database table definitions
<code>osetitelescope.py</code>	Telescope control interface
<code>osetitwitter</code>	Uploads coincidence events to Twitter
<code>osetiutil.py</code>	Various utility methods
<code>osetiweather.py</code>	Retrieves weather data from web
<code>skyCamera.py</code>	Interface to wide-field night sky camera
<code>Sopen.py</code>	Library for opening system files
<code>systemMonitor.py</code>	Captures system usage statistics
<code>telescopeCalibration.py</code>	Calculates star positions and telescope pointing
<code>weatherstation.py</code>	Retrieves data from observatory weather station

## 4.2 Camera Control

The main application which controls the Advanced All-sky Camera, roof, and telescope and automates observations is written in the python programming language. This application is split into the main file `oseti.py` and more than 25 other python files each representing a different subsystem. For example, `osetiroof.py` contains the `RoofDriveSubsystem` class and functions for sending commands to the roof controller via the PC's serial port. The `osetiexptctrl.py` file contains the class `ExperimentControlSubsystem` and functions for opening ethernet sockets to the PulseNet-V and Spartan-6 FPGAs, functions for sending commands to the FPGAs, and functions for interpreting the responses. Table 4.3 lists all the python files included in the `oseti.py` application and their purpose. A primary function of `oseti.py` is to start a web service that accepts and responds to HTTP Get and Post commands on a web socket. Web addresses are translated by `oseti.py` into either requests for data (often a web page or template) that is sent back to the client web browser or

commands that are executed. Apache2 is used as the front end web server and python's CherryPy module converts the web addresses passed from Apache2 into python function calls to be executed. For example, `https://costas_ip_address/gotoOpen` corresponds to a function call that will fully open the roof and `https://costas_ip_address/doFixedFlash` sends a test flash of light to the camera. The state of the observatory and camera, such as the angle of the telescope and temperature inside the allsky camera, are stored in a PostgreSQL database running on Costas using the python Sqlobject library. Any data recorded by the camera is saved in the same database. The database and operating system are stored on separate physical magnetic hard disk drives and they are RAID mirrored to protect against data loss in case of drive failure.

Much of the oseti application was written for the original all-sky system and is carried over for use with the Advanced All-sky Camera. Extensive changes were made to `osetiexptctrl.py` to support 33 socket connections to the 32 PulseNet-V's and the motherboard Spartan-6. Notably, the coincidence event data is much larger, 262,144 bytes vs 384 bytes, and is sent in a zlib compressed form. Additionally, all Virtex-5 FPGAs send coincidence data when any one PulseNet-V is triggered, resulting in a deluge of data arriving at Costas via ethernet in a short period of time. The coincidence data is interpreted and saved in the database using functions that are called by 40 available worker threads. This is so the work can be done in parallel by Costas' quad-core Intel processor. The camera is controlled by messages that are sent over ethernet to each of the PulseNet-V's and the Spartan-6. The message protocols were shown previously in [Figures 3.8 and 4.18](#). During observations, the generation of all control messages is automated by the new code that has been added to `osetiexptctrl.py`.

### 4.2.1 Web User Interface

The user interface (UI) for the original all-sky system has been described in [§ 2.6.1](#). The AdvCam required changes, however, to the UI to accomodate the extra telemetry information that is produced by the camera. The AsCam relayed the voltages of two 2.5 V rails, two 5 V rails, a 3.3 V supply, a 15 V supply, and the eight system-wide DAC reference voltages. The AdvCam reports many more voltages. For each of the 32 PulseNet-V's, the



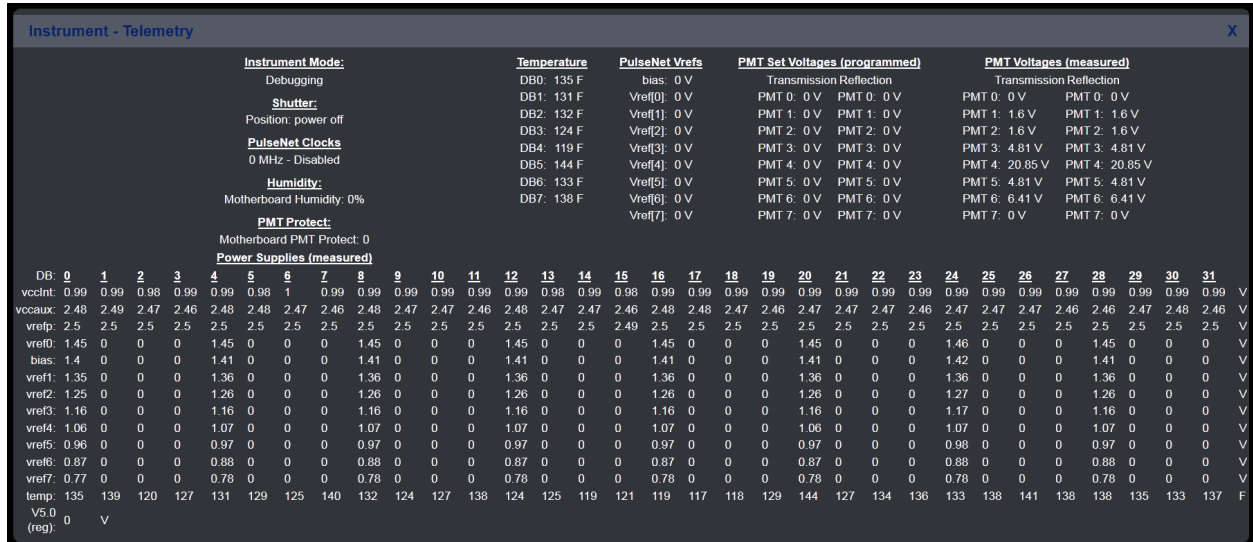


Figure 4.20: User interface telemetry panel

FPGA core voltage, I/O voltages, and auxiliary voltages are telemetered. In addition, every daughterboard has its own DAC reference voltages so 64 reference voltages are read by the system. A display of the UI telemetry panel is shown in [Figure 4.20](#).

## 4.2.2 Processing Application

The activity of the all-sky system is visualized through the web interface using a web browser. An independent application for visualizing the astronomy counters was warranted, however, because the update rate of the web interface is a few times a minute. The astronomy counts can be generated as fast as once a second. In order to make use of these fast update rates, an application using the Processing programming language was written. Processing is a java-based language that makes visual applications easy to program. A scalable vector graphic (SVG) of the photomultiplier tube array from the web user interface is imported into the Processing sketchbook and the astronomy counts are painted onto the photomultiplier pixel areas according to a blue-to-red colormap. The Processing sketchbook called `astro_count` receives the counts via UDP packets that are sent from each PulseNet-V to Costas by the `astro_udp` daemon. A remote user can use a network program like `socat` to have Costas forward the UDP packets to the user's computer. An example `astro_count` image is

shown in [Figure 5.23](#).

## 4.3 Future Enhancements

One drawback of the Advanced All-sky Camera is its trigger dead-time. This could be reduced to zero (assuming the average rate is low enough) by using only half of the sample memory for the first trigger. A second trigger could be handled immediately by using the other half of the sample memory while the first half is copied into main memory. Another area that could be enhanced are the trigger threshold settings. Currently, one threshold  $V_{\text{REF}}$  level is common to every pixel pair in the system. As noted in [§ 2.4.1](#), the Hamamatsu H7546B-20 photomultiplier tubes are multi-pixelated. A major difficulty with these detectors is their gain variation between pixels. It can vary by at least 1:3. Pixels with higher gain are more likely to trigger the system at any given threshold than lower gain pixels. Sensitivity suffers since the low gain pixel require more light to trigger. Lowering the trigger threshold would cause a surfeit of trigger events from the high gain pixels. One potential solution would be to use two separate  $V_{\text{REF}}$ 's as thresholds. The trigger hardware would be set to use the higher threshold  $V_{\text{REF}}$  for high gain pixels and the lower threshold  $V_{\text{REF}}$  for low gain pixels. This could of course be extended to have as many thresholds as there are  $V_{\text{REF}}$ 's in the system (8), however more than two or three thresholds likely wouldn't provide much benefit.

Looking further into the future, the price and power usage of high-speed ADCs may eventually come down to a point where it feasible to use a dedicated ADC for every channel. A new camera featuring 8-bit, 1 Gsps ADCs and the latest FPGAs could then be constructed, greatly enhancing the quality of the PMT signal data. Due to the demanding data rates of the gigasample-per-second sampled data, the coincidence triggering is currently an entirely localized process where each ADC channel pair has its own trigger circuitry. A pattern trigger that operates on the full complement of pixels as an image could be a useful addition to the trigger system especially if the all-sky system were to be scaled to a much larger telescope. With a large collecting area, Čerenkov flashes would more often cause coincidence triggers. A pattern trigger might be able to recognize the image pattern of the cosmic ray induced Čerenkov flashes and prevent the system from triggering. The implementation of this type

of system at the 3-bit, 1 Gbps data rates of the Advanced All-sky Camera would require a central pattern trigger FPGA with an input bandwidth of least 3 Tbits/s. The latest FPGA's can almost achieve these rates. Xilinx's Virtex-7 FPGAs have a maximum serial bandwidth of 2.7 Tbit/s. Data stream compression could be used if the available raw bandwidth is not sufficient or to make the system more energy efficient. In the pattern trigger system, high-speed serial links (10 Gbps) would transport the compressed data streams from 64 Virtex-7 FPGAs to a central trigger FPGA that would reconstruct the compressed streams and construct a trigger using any combination of pixel data. A trigger would cause the Virtex-7 FPGAs to record sampled data in block RAM, just as the AdvCam functions. Arbitrary trigger patterns could be set if all data streams are available at a single "trigger" FPGA. Signal quality, sampling speed, sample record length, and triggering capability would all be enhanced but more power would undoubtedly be required, especially if external ADCs are used. In order to save power, a switched capacitor array (SCA) could be used as an analog delay line, along with a simple discriminator, to power down the ADC if the signal is below an adjustable threshold.

# Chapter 5

## Advanced All-Sky – Testing and Observations

### 5.1 Testing

The Advanced All-sky SETI camera is a complex instrument with numerous levels of hardware and software that needed to be tested for proper function. While a large part of the feature tests were performed on an on-going basis during development, a few final tests were conducted to verify full functionality and to characterize its performance. This section describes the testing of the samplers and their ability to trigger on pulses. Once the camera was fully functional, the PMT voltage settings were explored and the astronomy count rates across the range of threshold voltage settings were characterized.

#### 5.1.1 Sampler Performance

To test sampler performance, test pulses were sent to PulseNet-V using an HP8082A Pulse Generator through a test signal breakout board. Pulses were captured with a Tektronix MSO4104 oscilloscope using P6243 1 GHz FET probes ( $<1$  pF). The probes were placed at the pulse generator output, after the photomultiplier signal amplifier, and at the Virtex-5 input via. For these pulse tests, the samplers were run at 1.5 gigasamples-per-second to evaluate the maximum speed and performance of the LVDS flash converters. The threshold

voltages are changed to accommodate the different two test cases. The first is a 20 ns full scale double pulse ([Figure 5.1](#)) and the second is a low-level, 4 ns 40 mV double pulse ([Figure 5.2](#)).

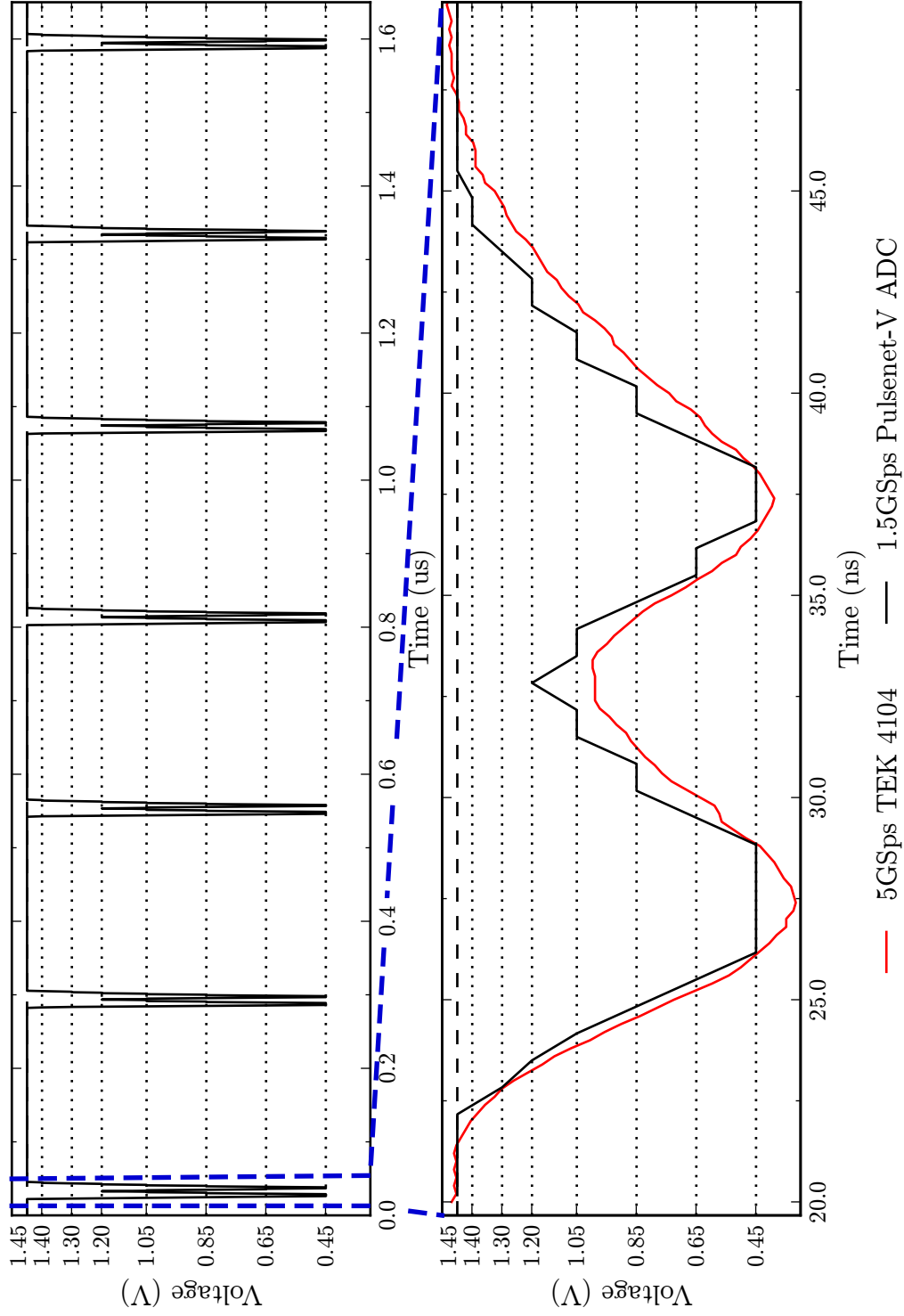


Figure 5.1: Full-scale double-pulse test waveform showing 7 sampled pulses over  $1.6 \mu s$  (dashed lines are  $V_{REF}$  levels) (top), and PulseNet-V 8-level reconstruction of a single pulse pair overlaid with oscilloscope “ground truth” capture (bottom).

From the pulse waveforms, we can see that for full-scale and small-scale pulses, the samplers track the input signal fairly well. This is also a verification that the trigger circuits can trigger on both large and small pulses. The input pulses from the pulse generator had  $<1$  ns rise time; it is clear that the input capacitance of the Virtex-5 pins slow the signal rise times. Since the rise-time from the test pulses is 3–5 ns, the total signal bandwidth into the PulseNet-V samplers is roughly around 100 MHz.

The threshold offsets and noise floor of the system were tested by varying the astronomy counter reference voltage with no signal connected to the sampler inputs (photomultiplier high-voltage power supplies turned off). As the reference voltage gets close to the bias level, the astronomy counts increase markedly; the noise floor causes the input signal to cross the counting reference voltage level. The results of this test on the full camera show that a reference level of 25 mV below bias is above the noise floor for all of the system's 1024 flash ADC channels. The threshold offsets for the PulseNet-V are therefore less than  $\sim 25$  mV.

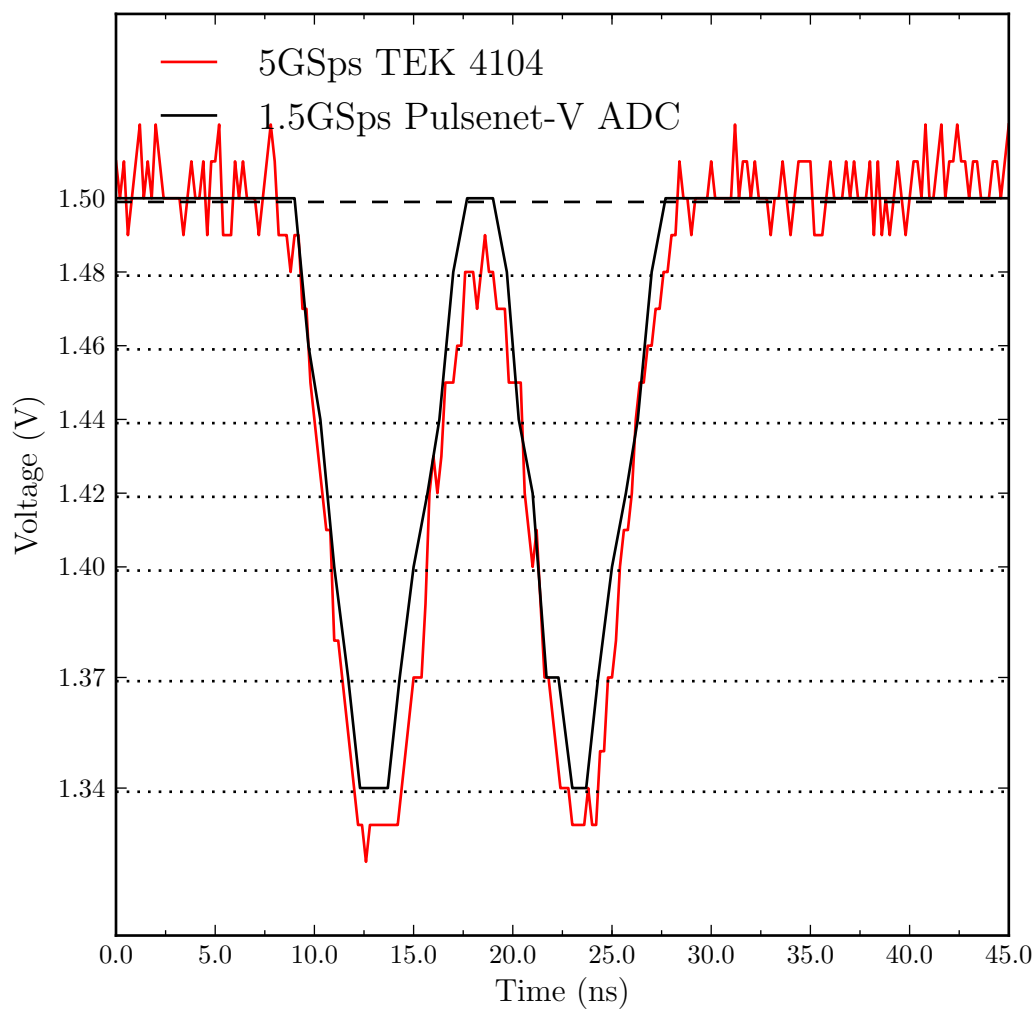


Figure 5.2: A low-level pulse sampled at 1.5 gigasamples per second. The input signal, measured at a Virtex-5 input pin using a Tektronix 4104 Oscilloscope with FET probe, is shown in red, and the black trace represents the sampled version of the input signal.



### 5.1.2 PMT Voltage

The Advanced All-sky Camera sees the sky with its photomultiplier tubes, so their performance is of utmost import. The PMTs degrade in relation to the amount of time they are used and the light intensity level at which they are used. To maintain a reasonably long life for the tubes, they should only be operated on dark nights and at a proper power supply voltage. The ideal supply voltage to ensure safety and long life while achieving maximum light sensitivity is a compromise between lifetime and sensitivity. In a photon counting mode, the supply voltage must be high enough for single photons to be counted by the electronics. Increasing the supply voltage can increase the single electron pulses above the noise floor but too much voltage can cause increased dark count rates. Application of too high a supply voltage may result in secondary emission, overheating of dynodes, loss of vacuum in the PMT glass envelope, loss of gain, and permanently increased dark count rates.

The Hamamatsu H7546B-20 photomultiplier tubes are multi-anode devices with a spread of pixel gains. The gain of each pixel cannot be individually adjusted because all anodes operate from the same high voltage supply. Therefore each pixel has a different gain, count rate, and pulse distribution. Because each PMT has so many individual anodes, setting the high voltage supply to achieve maximum camera sensitivity and safety in all pixels is not trivial. To understand the relationship between count rates, pulse distribution, and high voltage supply, the PMTs were characterized using the AdvCam's upgraded astronomy counter features. The two measurements shown in [Figures 5.3](#) and [5.4](#) are count rates vs. supply voltage and count rates vs. threshold voltage, respectively. Plotting count rates vs. supply voltage helps to determine how to set the supply voltage consistently across all 16 photomultiplier tubes. The count rate vs. threshold plot series indicates the pulse height distribution of each pixel at a given supply voltage.

The PMT supply voltage setpoints are chosen by measuring photo-electron count rates while sweeping the supply voltage from 600 V to 900 V. For each pixel, the supply voltage at which the counters detect  $\sim 1000$  counts $\cdot$ sec $^{-1}$  *while the shutter is closed* is displayed next to the plot ([Figure 5.3](#)). The red plots show the reflection side photomultiplier pixels and the blue plots show the transmission side photomultiplier pixels. A consistent gain

across the various PMTs is achieved by setting the supply voltage so that the PMT pixels have a dark count of  $\sim 1000$  counts $\cdot$ sec $^{-1}$ . This setting cannot be satisfied for all pixels at the same time so an average of the PMT's 64 pixels is used. This 1000 counts $\cdot$ sec $^{-1}$  level corresponds roughly to the point where the count rates vs. supply voltage plot starts to level off. Generally, photomultiplier tubes' supply voltage is set to the point of minimum slope, however this would present a danger of tube damage at higher light levels. [Figure 5.3](#) shows the count rates for PMT pair 0, the plots of the other 7 PMT pairs were measured and plotted but are not shown here.

After setting the supply voltage, an additional test of the astronomy counters was performed to get an indication of the count rate variation in different pixels. In [Figure 5.4](#), the astronomy counts for each pixel in PMT pair 0 are plotted as the astronomy  $V_{\text{REF}}$  is varied from from 25 mV to 100 mV. For this test, the telescope is pointed at zenith on a dark night. At 25 mV, the gain variation across pixels causes the central PMT pixels to provide count rates of  $10^5$  s $^{-1}$  while the edge pixels have count rates 2–3 orders of magnitude lower. The matching of paired pixels (red and blue) is not perfect either, though the count rate difference between matched pixels of different PMTs tends to be much less than the difference between center and edge pixels within a PMT.

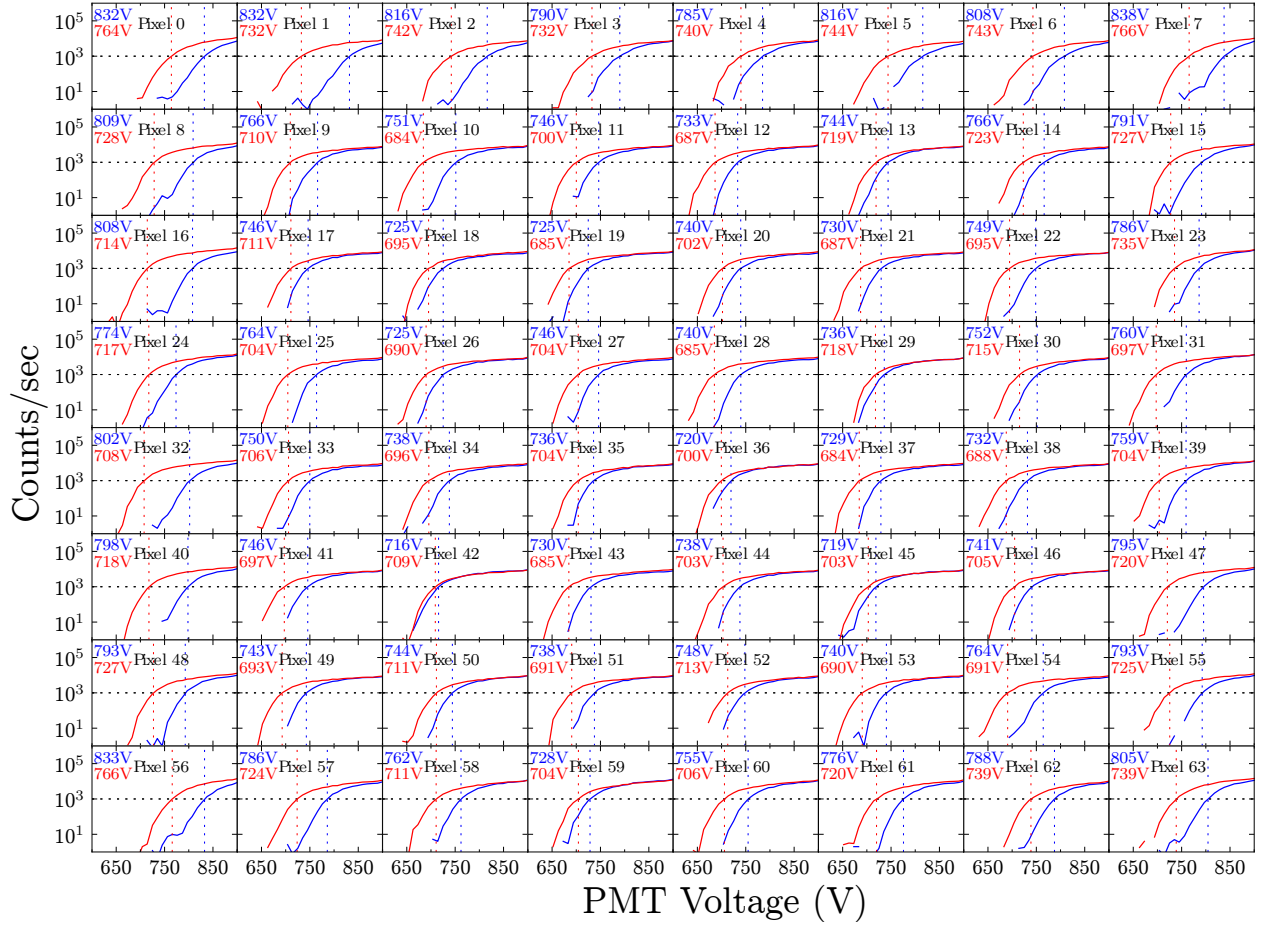


Figure 5.3: This figure shows the astronomy count rates ( $V_{\text{REF}} - V_{\text{BIAS}} = 25$  mV) of PMT pair 0 with the shutter closed at PMT supply voltages between 600 V and 900 V. The supply voltage set point is chosen for a count rate of  $1000 \text{ counts} \cdot \text{sec}^{-1}$  with the camera's shutter closed.

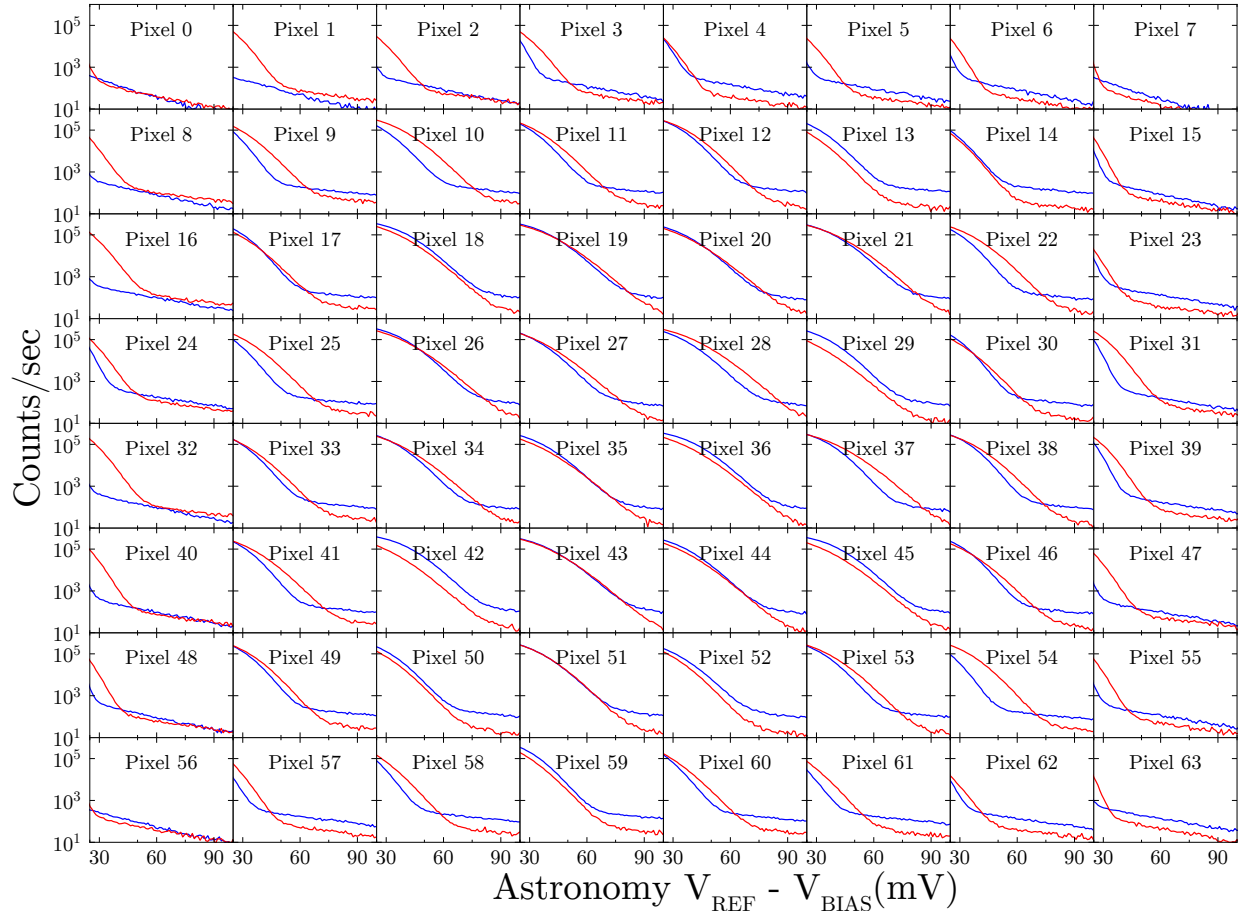


Figure 5.4: The astronomy count rates of PMT pair 0 are plotted as the astronomy counter reference voltage ( $V_{\text{REF}}$ ) is varied from 25 mV to 100 mV below the bias voltage.

### 5.1.3 Camera Trigger Sensitivity

To characterize the trigger rate at low threshold voltages, the number of pixels triggered in a one minute interval was recorded while varying the threshold voltage. This test was performed in five conditions:

1. High voltage off, shutter closed, pixel pairs unlinked (no coincidence requirement).
2. High voltage off, shutter closed, pixel pairs linked (coincidence required to trigger).
3. High voltage on, shutter closed, pixel pairs unlinked.
4. High voltage on, shutter closed, pixel pairs linked.
5. High voltage on, shutter open, telescope pointed at zenith on a dark night, pixel pairs linked.

Results can be seen in [Figures 5.5, 5.6, 5.8 and 5.9](#). The test show that with the channels linked, the threshold can be set much lower than 150 mV, which is a significant improvement over the original all-sky camera. The AdvCam could be operated with a threshold voltage as low as 60 mV and trigger less than once per minute. Operation at lower thresholds, down to  $\sim 25$  mV, is limited by the night sky background photon arrival rate and photomultiplier dark currents, not by on-board digital noise sources such as clock coupling or power-supply switching noise.

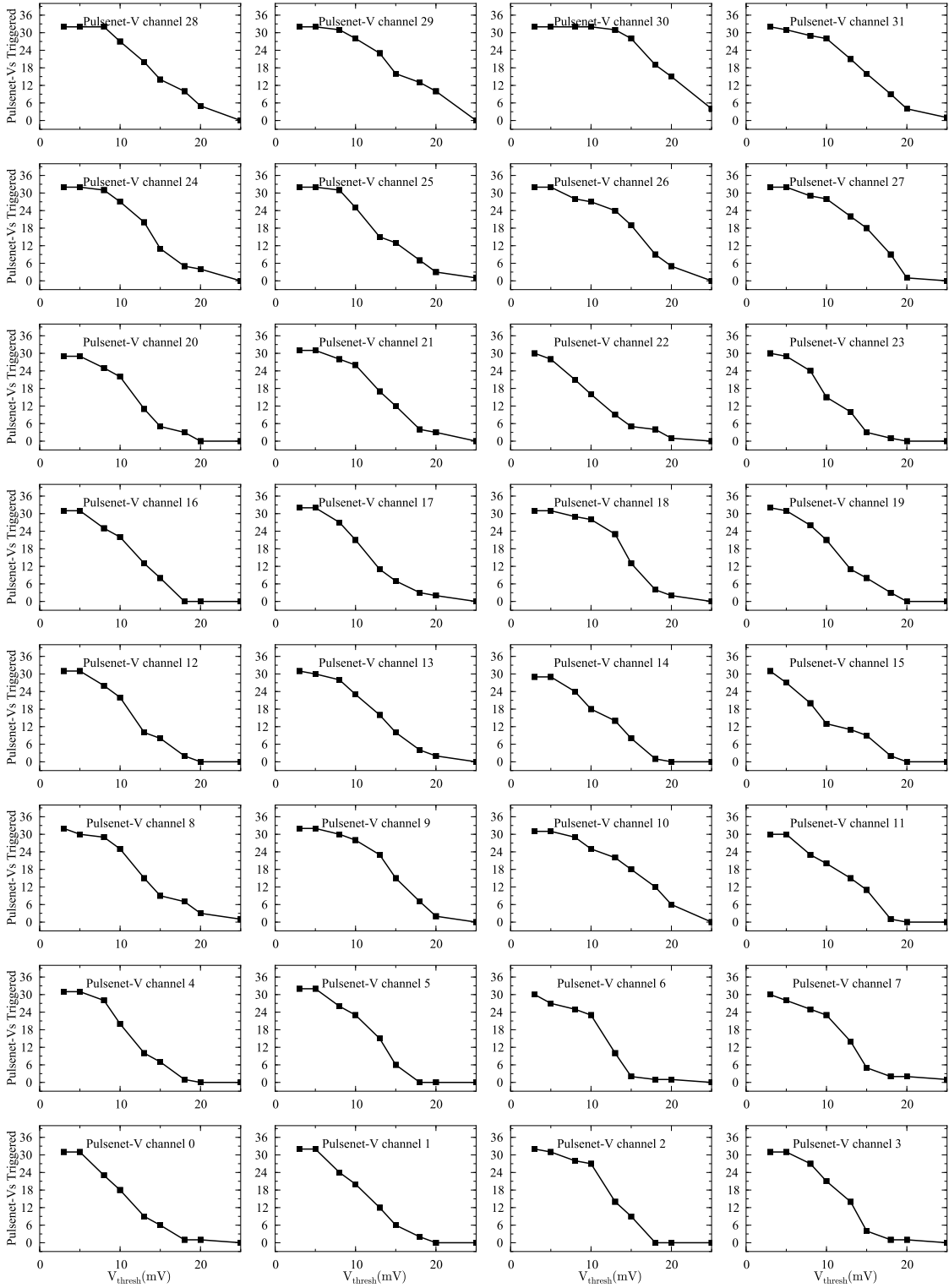


Figure 5.5: Sensitivity of the AdvCam by Pulsenet-V channel number. Conditions: One minute. Channels not linked. High voltage off.

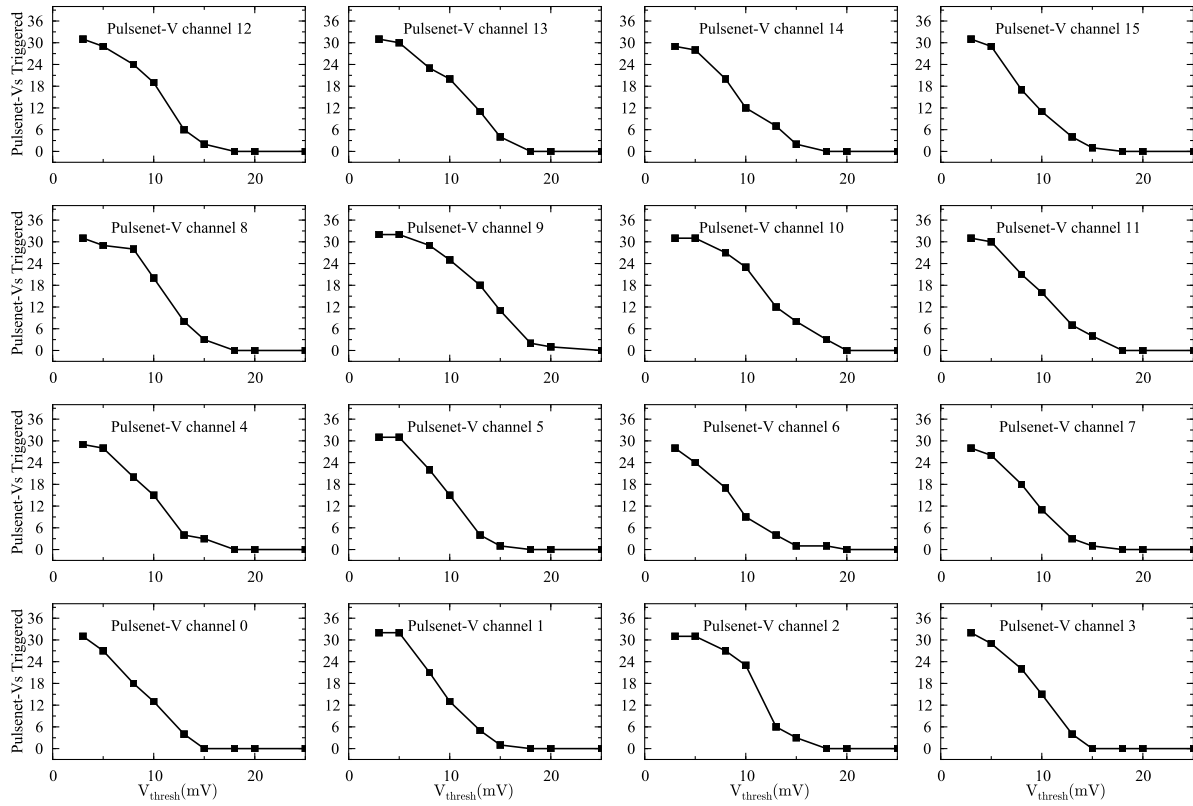


Figure 5.6: Sensitivity of the AdvCam by Pulsenet-V channel number. Conditions: One minute. Channels linked. High voltage off.

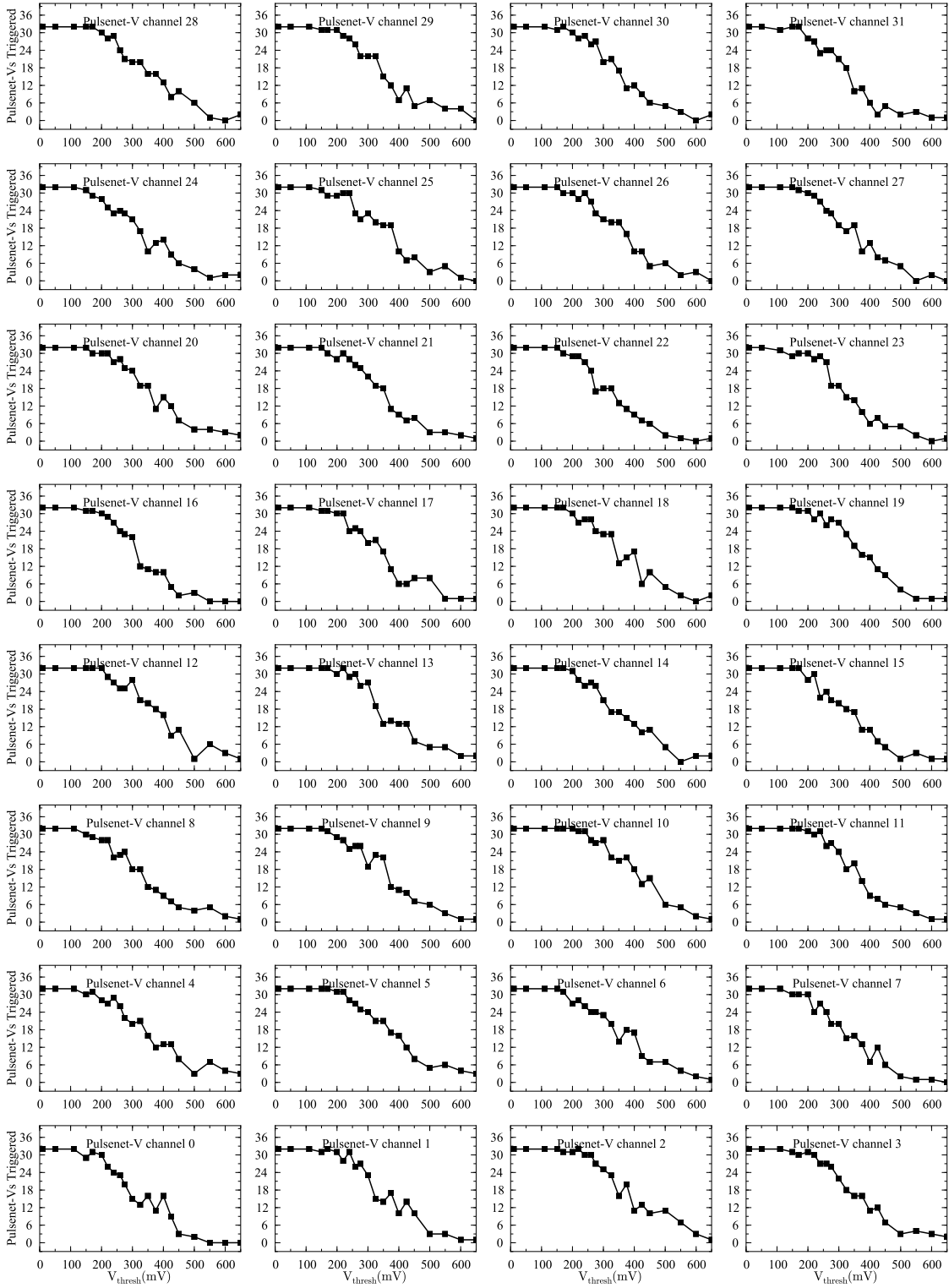


Figure 5.7: Sensitivity of the AdvCam by Pulsenet-V channel number. Conditions: One minute. Channels not linked. High voltage on. Shutter closed.



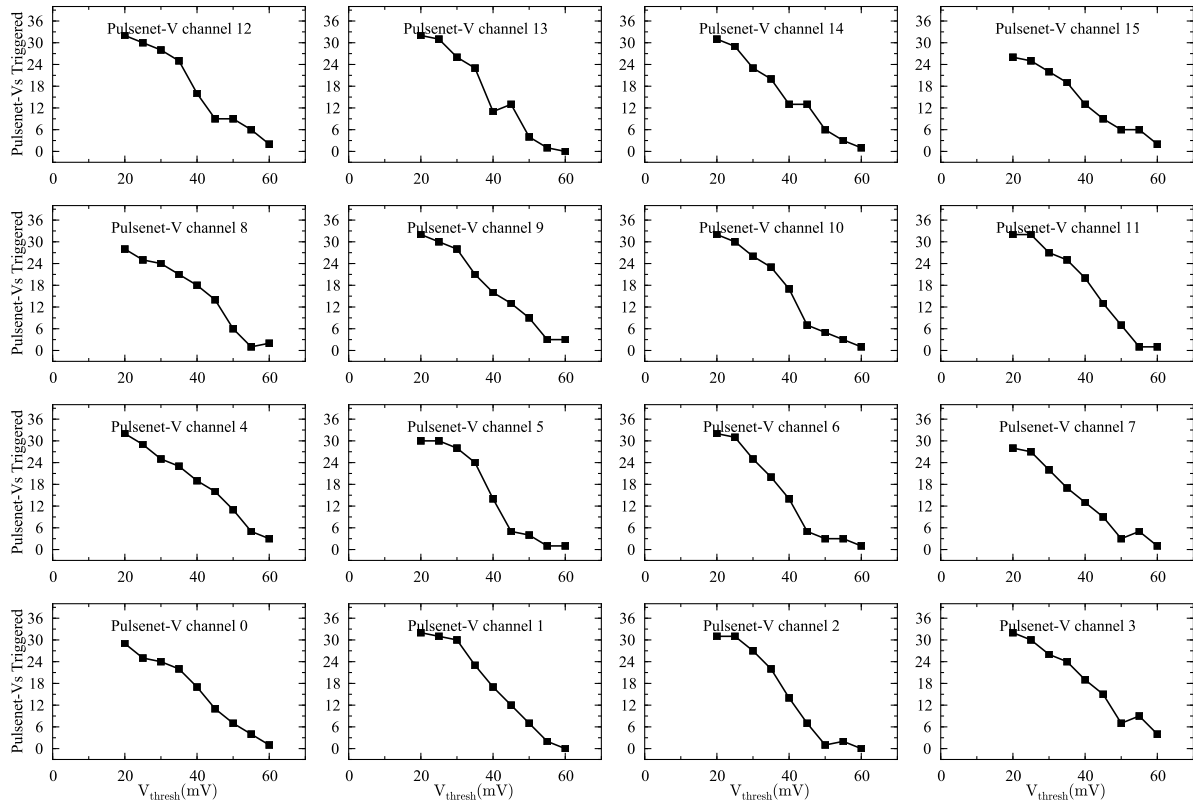


Figure 5.8: Sensitivity of the AdvCam by Pulsenet-V channel number. Conditions: One minute. Channels linked. High voltage on. Shutter closed.

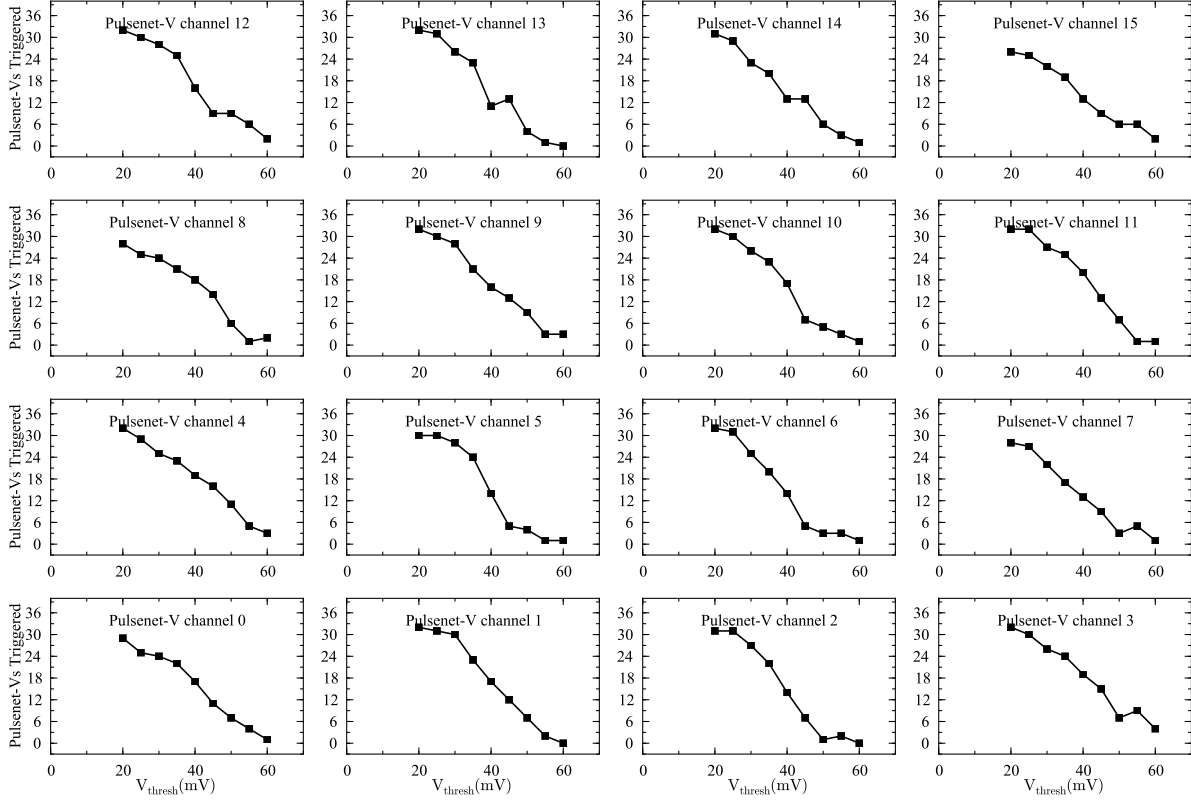


Figure 5.9: Sensitivity of the AdvCam camera by Pulsenet-V channel number. Conditions: One minute. Channels linked. High voltage on. Shutter open. Telescope pointed at zenith on a dark night.

## 5.2 SETI Observations

### 5.2.1 Observation Procedure

Observations are performed on a semi-automated basis. At the beginning of a night of observations, an operator logs into the observatory’s web interface and enables the “Automated Observation” mode. The observatory then operates under software control. The control software runs through a state machine that runs continuously until the operator disables automated observations or shuts down the system. The automated observation state machine starts by checking for “good observing” conditions, i.e the weather conditions, time of day, and equipment status. The system clock is checked to verify that time is between evening and morning twilight. A daylight sensor must indicate that it is dark, and the rain sensors must not detect rain. Additionally, the core temperature of all PulseNet-V’s must read  $<180^{\circ}\text{F}$  and there must not be any downtime currently scheduled for the good observing condition function to return `true`. If all these conditions are satisfied, the state machine will continue readying the building for observations. The building is readied by opening the roof, opening the shutter, and powering on the telescope drive. When the roof has fully opened, the state machine starts the telescope calibration procedure. The state machine waits for the telescope to finish calibration and then turns on the AdvCam and the PMT high-voltage supply. When the camera is ready, the state machine enters the observing loop. In the observing loop, if an observation is not in progress, a new observation is chosen as the current observation. The observation that is chosen can be one that has been scheduled previously or, if there are none scheduled for the current time, the parameters of an automated observation will be calculated. Automated observations are always scheduled for thirty minutes but manually scheduled observations can be any reasonable length. The state machine next moves the telescope to the declination of the chosen observation. At the beginning of the observation, the PulseNet-V’s are programmed and armed to trigger. A test flash is sent from the Gelfand Flasher and the number of trigger channels is counted to make sure that all pixels were triggered and, hence, functioning properly. The PulseNet-V’s are re-armed and then the observing mode is set to “Observing”. The state machine will allow the observation to proceed until the scheduled observing duration has passed (normally 30

minutes). At that point, there is no current observation and the state machine begins the observing loop again. This process continues until the observing conditions are no longer favorable. If any one of the “good observing” conditions is false, the telescope will be lowered if it is raised, the roof will be closed if it is open, and the observatory electronics will be powered down.

## 5.2.2 Observation Summary

The first observations with the Advanced All-sky Camera were performed on September 11th, 2012. As of March 31st, 2013, 174.4 hours of observations have been completed, covering 3,602 square degrees. [Figure 5.10](#) shows an equatorial sky map of the observation locations. Within these 174 hours, 318 coincidence events were recorded. Of these events, 306 were triggered by single pixels and 12 events had multiple pixels triggered. The coincidences are not distributed evenly across PulseNet-V’s and photomultiplier tubes. This can be seen in [Figure 5.11](#). PulseNet-V numbers 0–3 and 8–11 have at least 18–25 events each and PulseNet-V number 8 has nearly 40 events while numbers 4–7 and 12–19 have only a few each. This is most likely an effect of the photomultiplier tubes. Photomultiplier numbers 7 and 5 are handled by the PulseNet-V’s with the most events. It is possible the high-voltage applied to these photomultipliers is set higher relative to the other photomultipliers in the system. It is also possible that these photomultipliers experience greater large-amplitude noise pulse events leading to more random coincidence events.

In general the coincidence events can be split into three broad categories: single pulses of a few nanoseconds that trigger multiple pixels, single pulses of a few nanoseconds that trigger single pixels, and events of microsecond duration consisting of many single photo-electron pulse. We believe these correspond, respectively, to cosmic rays, photomultiplier tube dark currents and photon pileup, and airplanes. The coincidence types are described in the next sections.

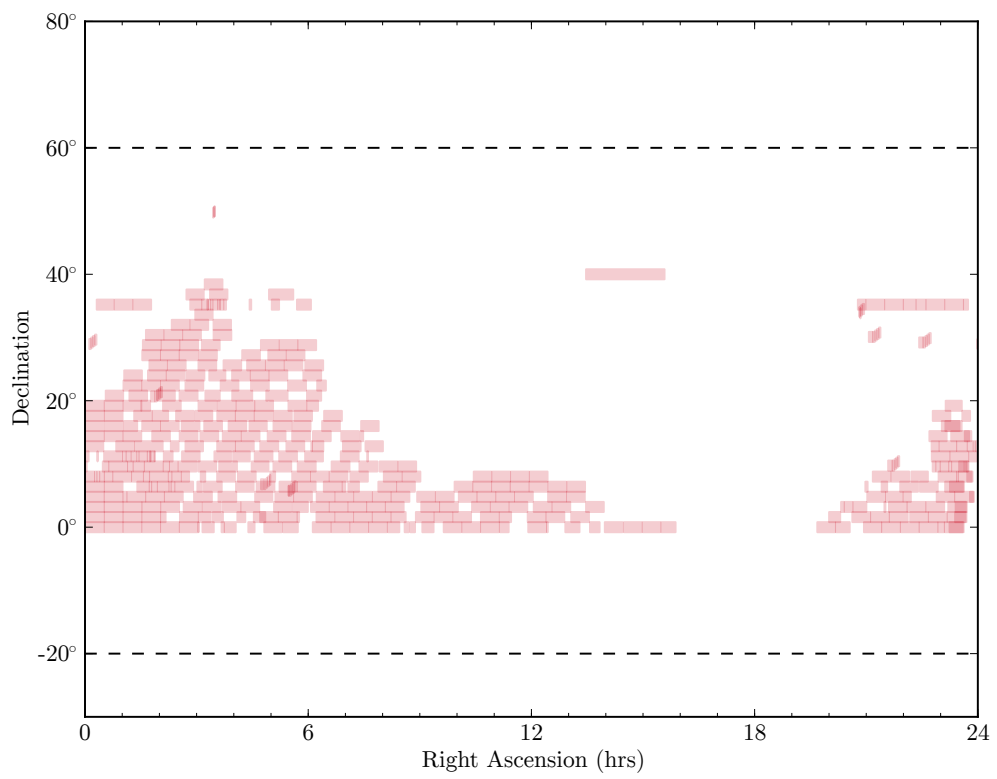


Figure 5.10: The Advanced All-sky System has observed for 174.4 hours and covered 3,602 square degrees.

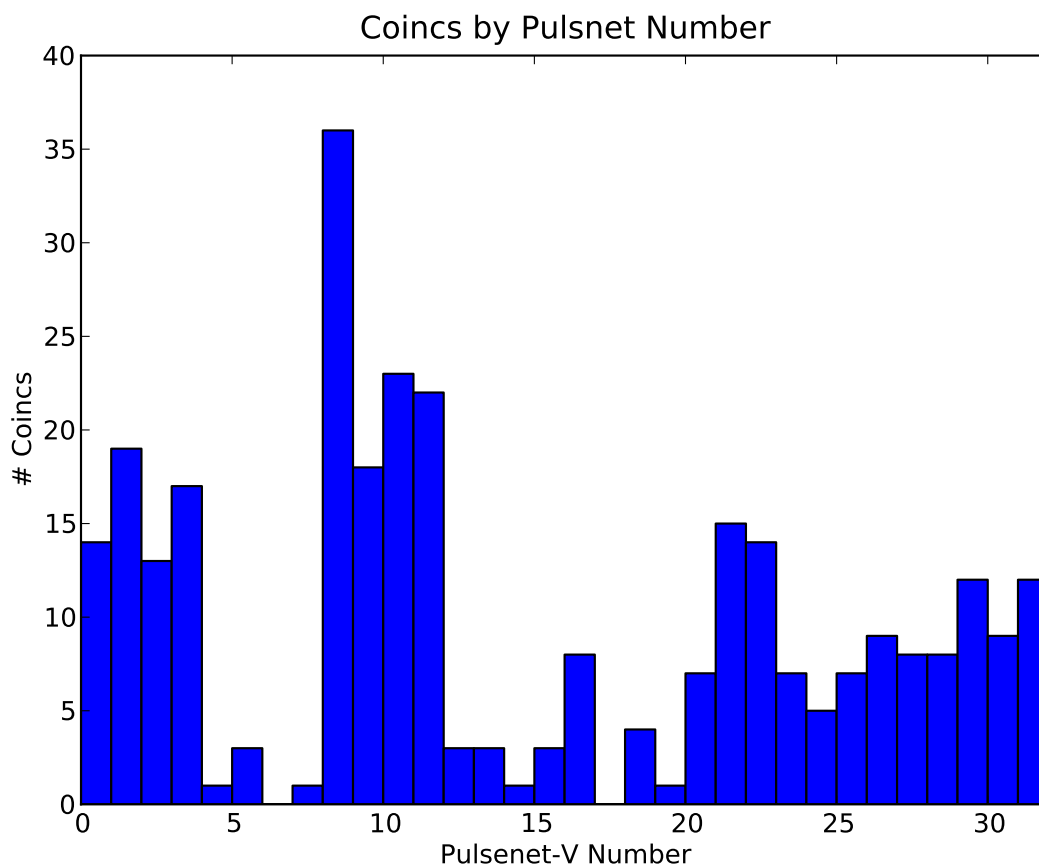


Figure 5.11: The distribution of events across PulseNet-V is not uniform. PulseNet-V's numbered 0–3 and 8–11 contribute to a much greater number of coincidence events. This could be due to the photomultiplier tubes serviced by these PulseNet-V's having higher gain, the supply voltage may be set too high, or the tubes having more frequent large-amplitude pulse events due to ion-feedback.

### 5.2.3 Dark Current and Pileup

The majority of coincidence events are single-pixel triggers that only reach the trigger threshold level or one level higher in amplitude. A typical example of the array image and the pixel waveform is shown in [Figure 5.12](#). In the photomultiplier array image (top of [Figure 5.12](#)), the pixels are colored with a blue to red color mapping according to the charge accumulated over a 22.5 ns window centered around the trigger sample. Blue pixels indicate zero charge accumulated and the pixel with the most charge accumulated is colored red. In [Figure 5.12](#), only the triggered pixel pair show any charge accumulation which means that the other photomultiplier pixels in the array showed very little activity at the time of the trigger. Another indication that this is a coincidence due to a random independent large-amplitude pulse in the pixel pair is the dissimilar shape of the waveforms on the transmission (left) and reflection (right) sides. The reflected side pulse is about 5 ns wide whereas the transmitted side pulse is about 2 ns wide. These are the hallmarks of a random coincidence as a result of night sky background light or dark current from the photomultipliers. About 85% of the coincidence events fit the random pulse description, i.e. a single pixel, single pulse event.

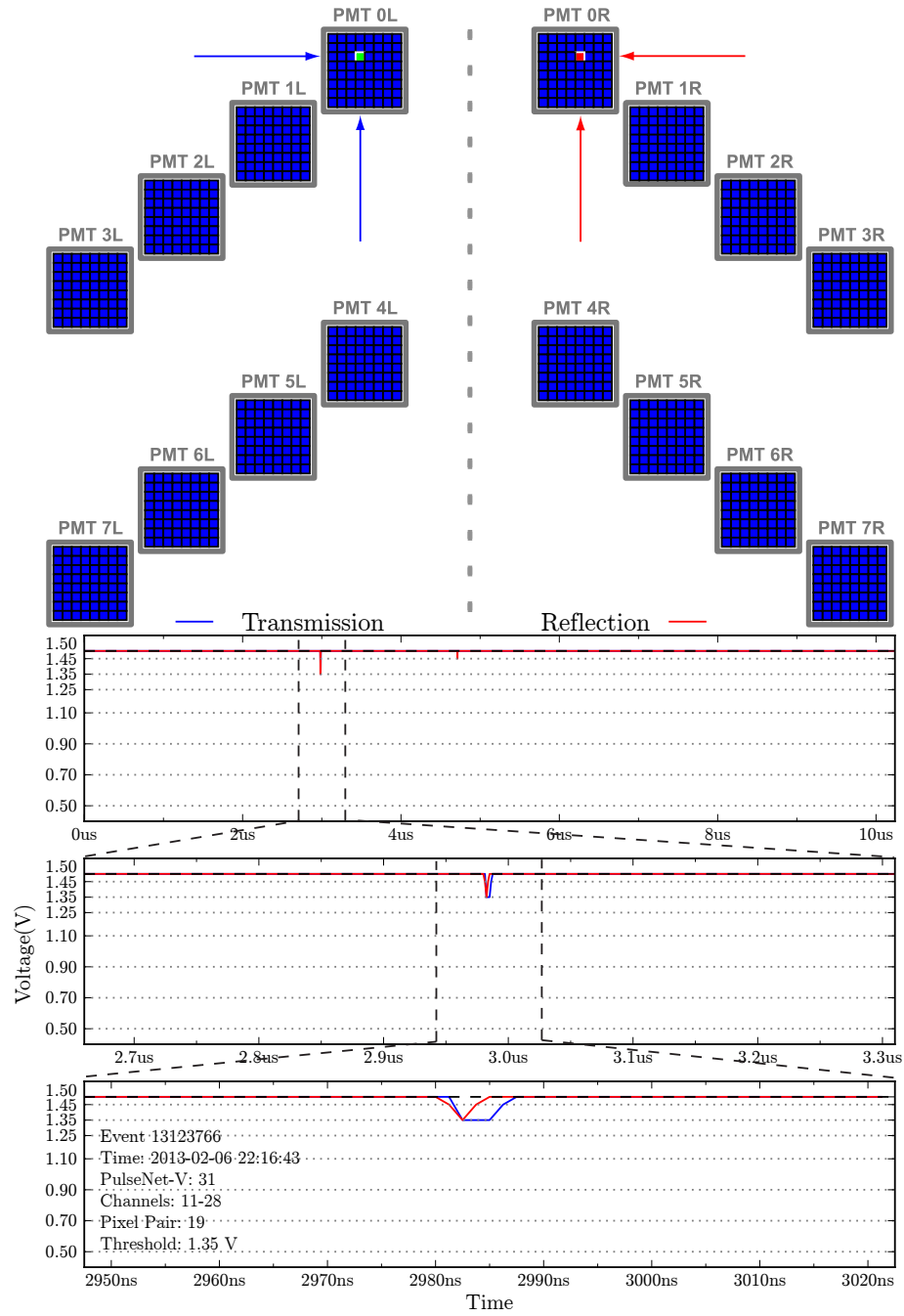


Figure 5.12: An example of a common single-pixel, single-pulse coincidence event is shown here. No other pixels show activity at the time of the trigger and the pulse event itself is of low amplitude and non-repeating.



### 5.2.4 Airplanes

Another category of common triggers are evidently caused by overhead airplanes. The FAA requires all aircraft to have anti-collision and position lighting systems for night operation. Lighting position, color, and intensity is specified by Special Federal Aviation Regulation No. 23, parts 1381-1401. In short, most aircraft have aviation white or red position lights on the tail and fuselage, red and green positional lights on the port and starboard wingtips, as well as strobe lights on the tail and wingtips. The strobe lights must have a frequency of 40 to 100 cycles per minute. These aircraft lights, particularly the strobe lights, can cause a false trigger in the camera. The typical strobe width is much longer than the  $\sim 2\text{-}5\text{ ns}$  single photo-electron pulse width of the photomultiplier tubes, and the strobe light is much brighter than any star in the sky. If the strobe is bright enough it will cause multiple photo-electron pileup, exceeding the trigger threshold. The signature of an airplane induced trigger can be seen by viewing full  $10\text{ }\mu\text{s}$  sample record of Coincident Event #964311 (Figure 5.13). This airplane induced trigger is composed of many single photo-electron pulses of small amplitude ( $\sim 125\text{ mV}$ ). In the brightest portion of the strobe pulse, the photo-electron pulses overlap, reaching the threshold level ( $V_{\text{thresh}}=1.22\text{ V}$  or  $280\text{ mV}$  below the bias level) in both pixel pairs at the same time. The smoking gun attributing this coincidence event to an airplane is seen when viewing the skycam image just a few seconds before the time of the trigger. A bright streak in the photograph points directly into the telescope's field of view (Figure 5.14). The bright lines here are the light of an airplane. The skycam photograph of Figure 5.15 provides a better illustration of the skycam images.

The All-sky Observatory's meteor sky camera (skycam) provides a secondary way to verify the identity of any camera triggers. The skycam is directed to take a  $90^\circ \times 120^\circ$ , ten second exposure every ninety seconds and whenever a trigger occurs. The southern horizon and nearby trees are seen at the bottom of skycam images. In the skycam image of Figure 5.15, a long streak can be seen with bright spots along its length. The constant brightness streak is from an airplane's positional lighting system while the bright spots are from the anti-collision strobe lights. The airplane's contrail is also visible against the darker night sky. Since the skycam has no shutter, the intense airplane lights accumulate in the CCD pixels as they are being read from the sensor and appear in the image as a horizontal

Table 5.1: Aircraft minimum effective intensities for anti-collision lights.

Angle Above and Below Horizontal Plane	Effective Intensity (candles)
0° to 5°	400
5° to 10°	240
10° to 20°	80
20° to 30°	40
30° to 75°	20

streak.

Airplanes are not an insignificant portion of the total observational triggers (5-10%) but are recognizable by examining the skycam images and the event record. The digitized waveforms of the airplane trigger events contain many single photo-electron pulses reaching the first  $V_{\text{REF}}$  level and some multiple photo-electron pulses reaching the second or even the third  $V_{\text{REF}}$  level. If the number of pulses above the first  $V_{\text{REF}}$  (single photo-electron level) are counted, the sum can give an indication of whether the waveform was caused by a very bright and long flash, indicative of an airplane strobe. Plotting the number of pulses versus the time of night for every trigger event shows when airplanes are most likely to cause camera triggers ([Figure 5.16](#)). The hours between midnight and 4 A.M. are, as expected, the best for avoiding airplanes.

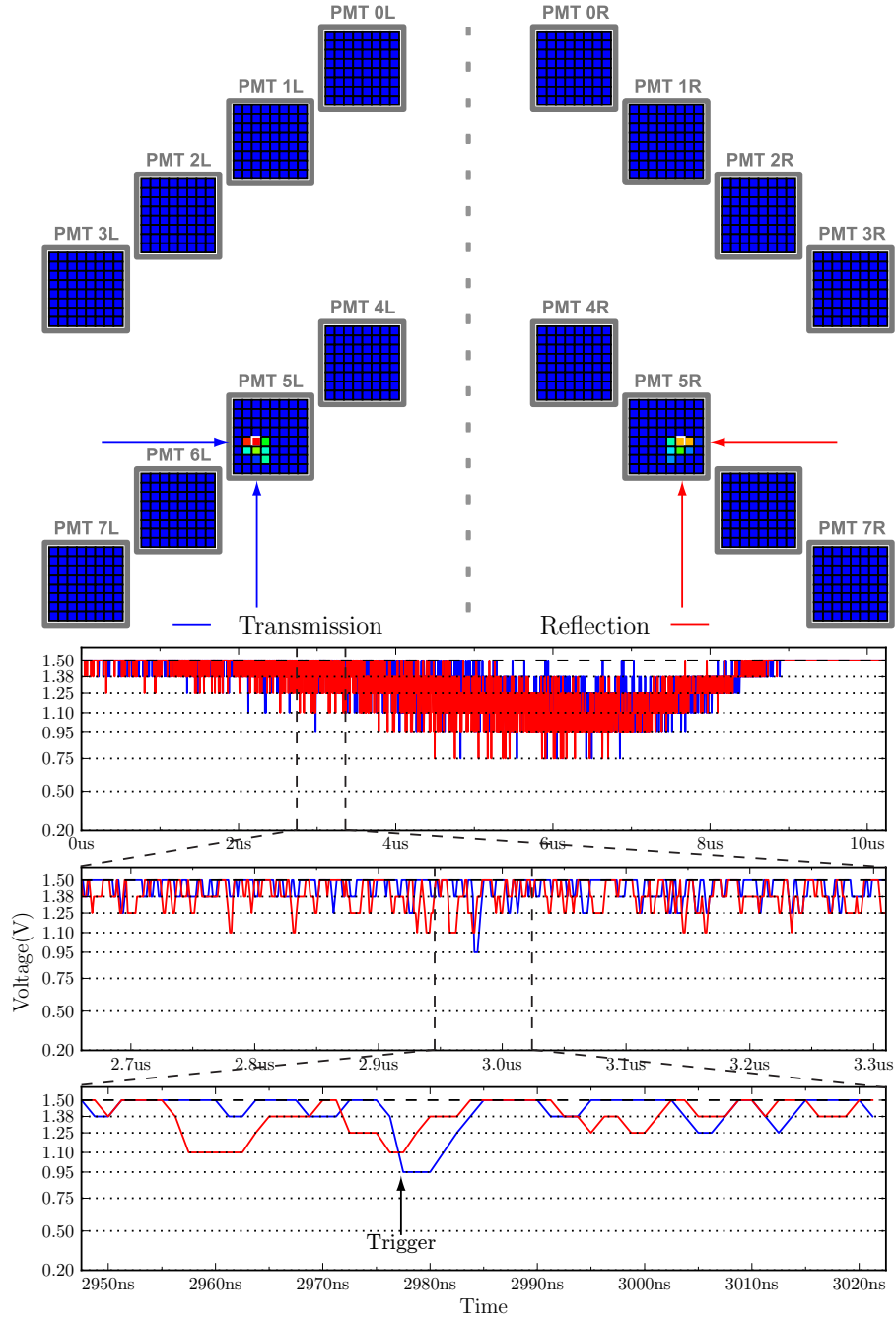


Figure 5.13: This coincidence event triggered one pixel but is seen in a cluster of five pixels. The waveform is a  $\sim 9 \mu\text{s}$  pulse composed of many single-photoelectron bursts that overlap, causing the camera to trigger as the flash of light increases in intensity.

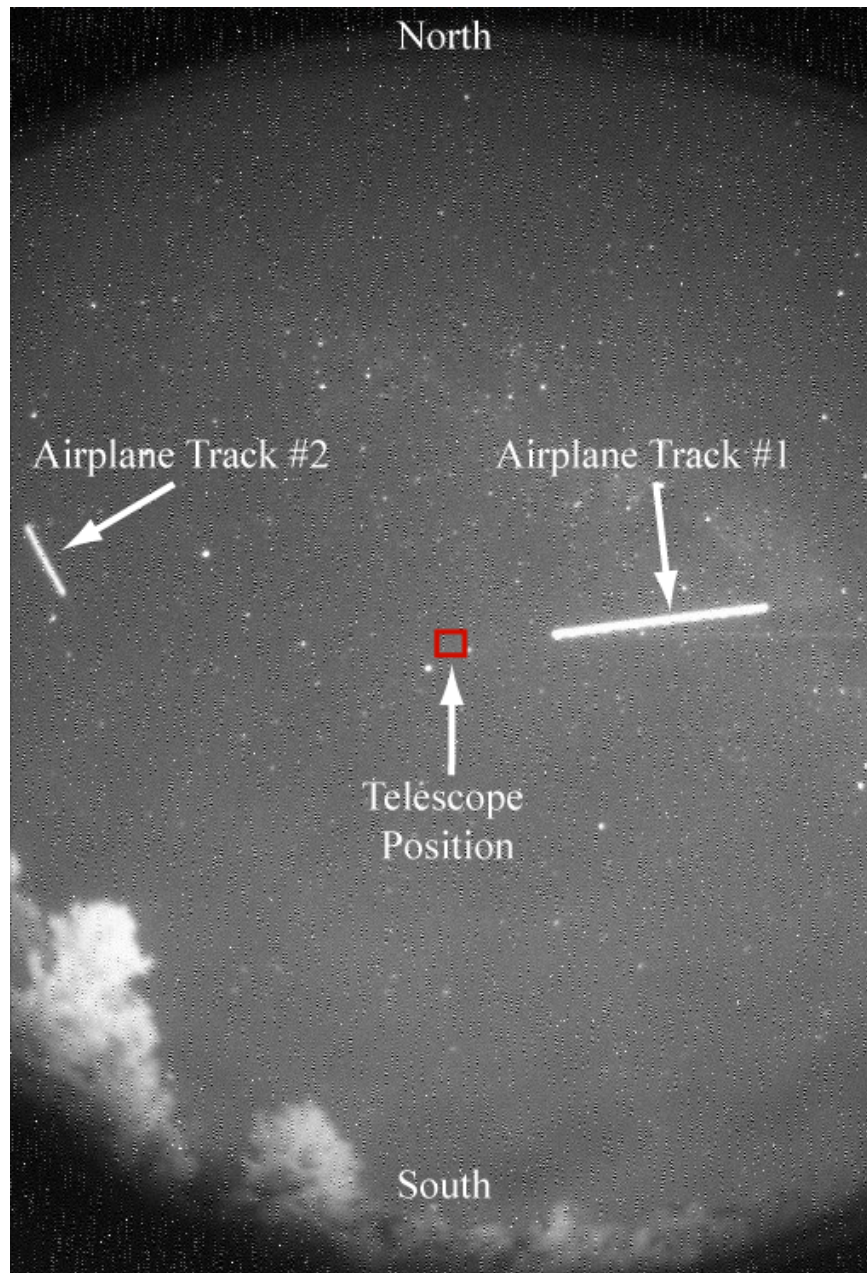


Figure 5.14: The skycam image from the event in [Figure 5.13](#). The line in this skycam photograph is due to an airplane that had a chance crossing with the telescope's field of view (red box) causing the camera to trigger. This image was captured before the trigger event. Unrelated to the camera trigger, there is a second airplane seen to the West, illustrating the common appearance of airplanes in our skies.

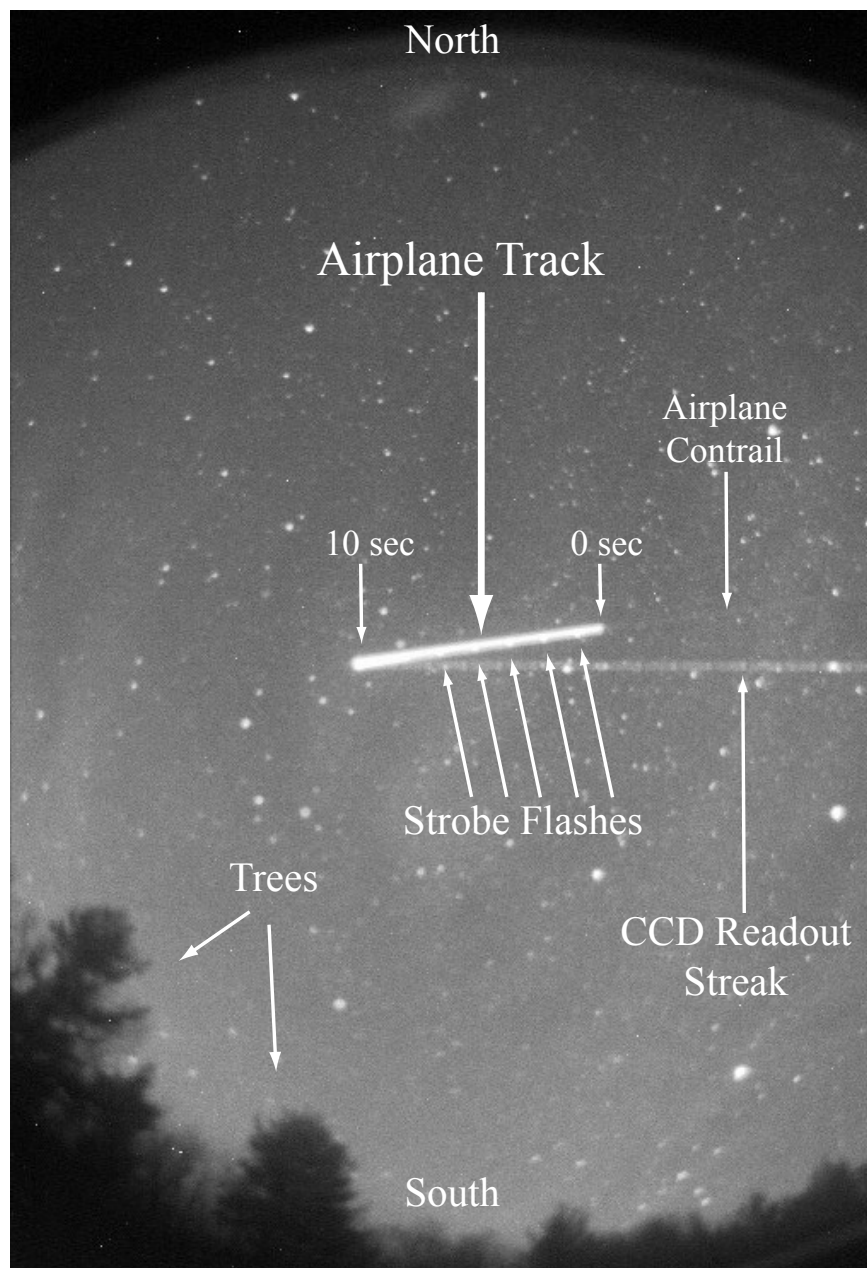


Figure 5.15: A different skycam image, with annotations of the features in the image.

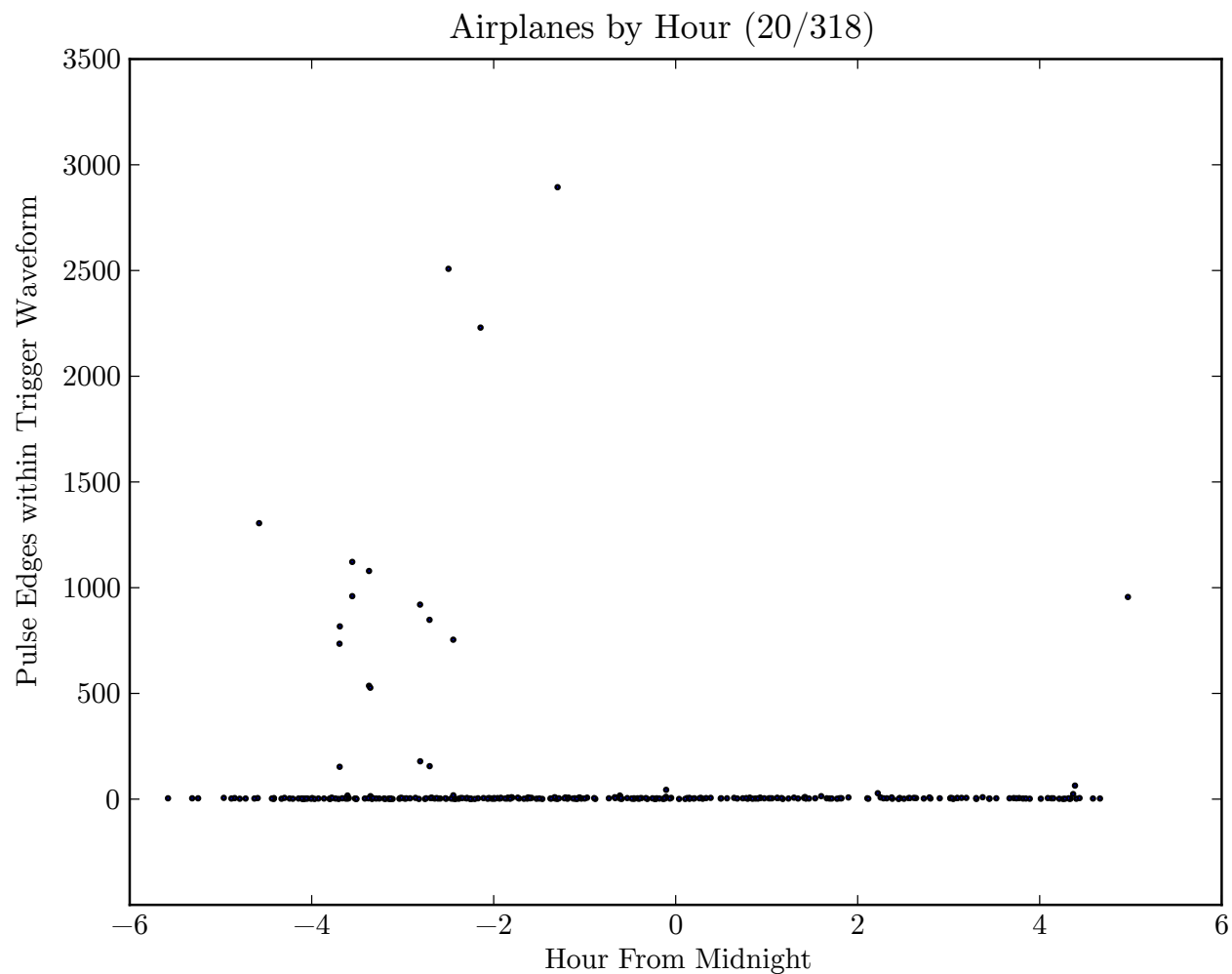


Figure 5.16: The number of pulses within the trigger waveforms can be used to distinguish the airplane induced trigger events from other types. Here we have plotted the trigger time of the 318 trigger events in the AdvCam observing database versus the number of negative-going pulse edges in the triggered pixel's waveform.

### 5.2.5 Cosmic Rays

A typical cosmic ray coincidence trigger image is shown in [Figure 5.17](#) and the corresponding waveforms of four pixels pairs from this event are shown in [Figure 5.18](#). Cosmic ray events are typically characterized by multiple triggered pixel pairs in one PMT. The  $10\mu\text{s}$  digitized waveform from the triggered pixels of these events normally contains only a single 2–10 ns pulse of moderate to high amplitude. The shape and size of the image varies between cosmic ray events. The size typically spans an entire photomultiplier tube but less than the distance between PMTs. The pulse is never seen in two photomultipliers viewing different portions of the sky. Eighteen cosmic ray events have been identified out of the 318 coincidence events recorded by the AdvCam. The event images are shown in [Figure 5.19](#). For compactness, only the PMT pair in which the event was seen is displayed in the figure.

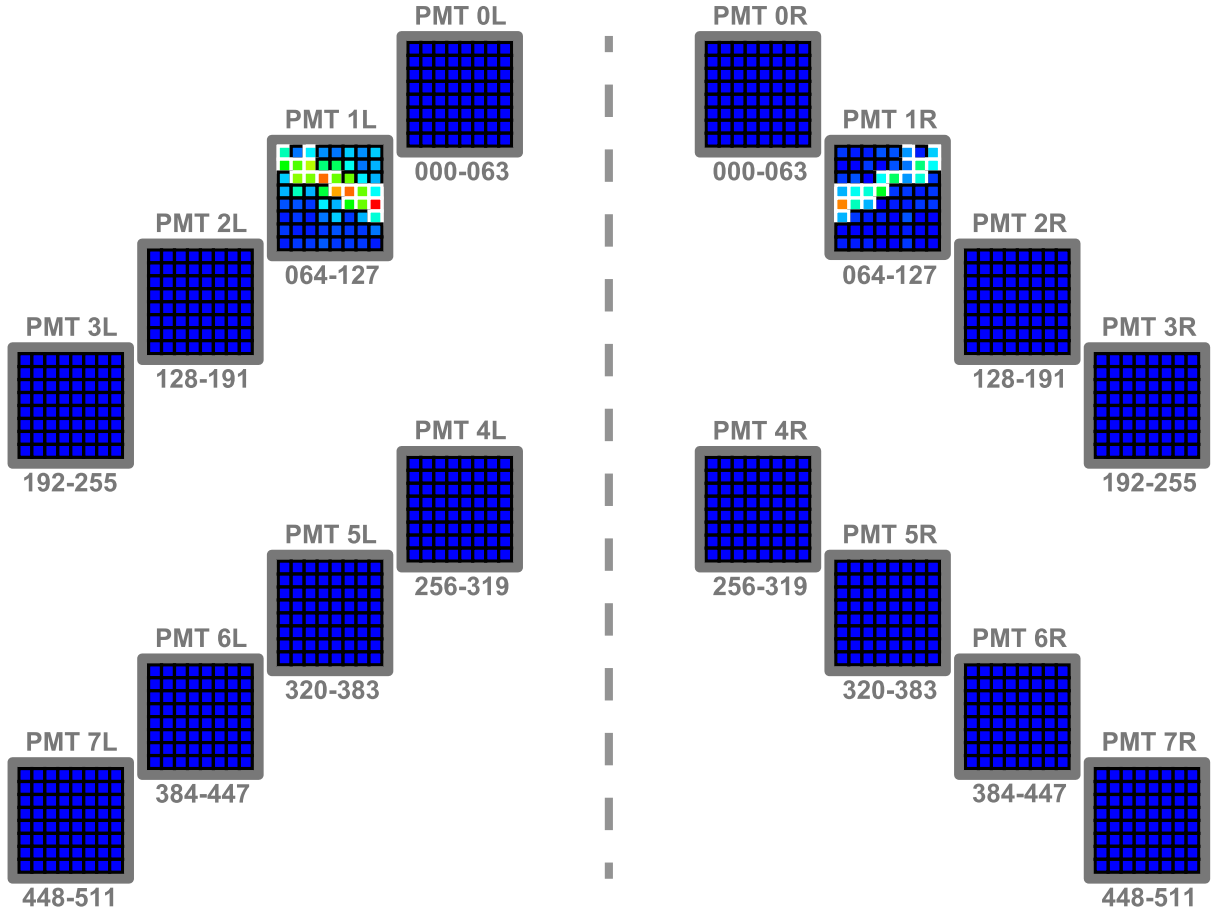


Figure 5.17: Cosmic ray coincidences typically span an entire PMT and have more than one pixel pair triggered. The pulse from the Čerenkov flash is generally a few nanoseconds long and of moderate to high amplitude.



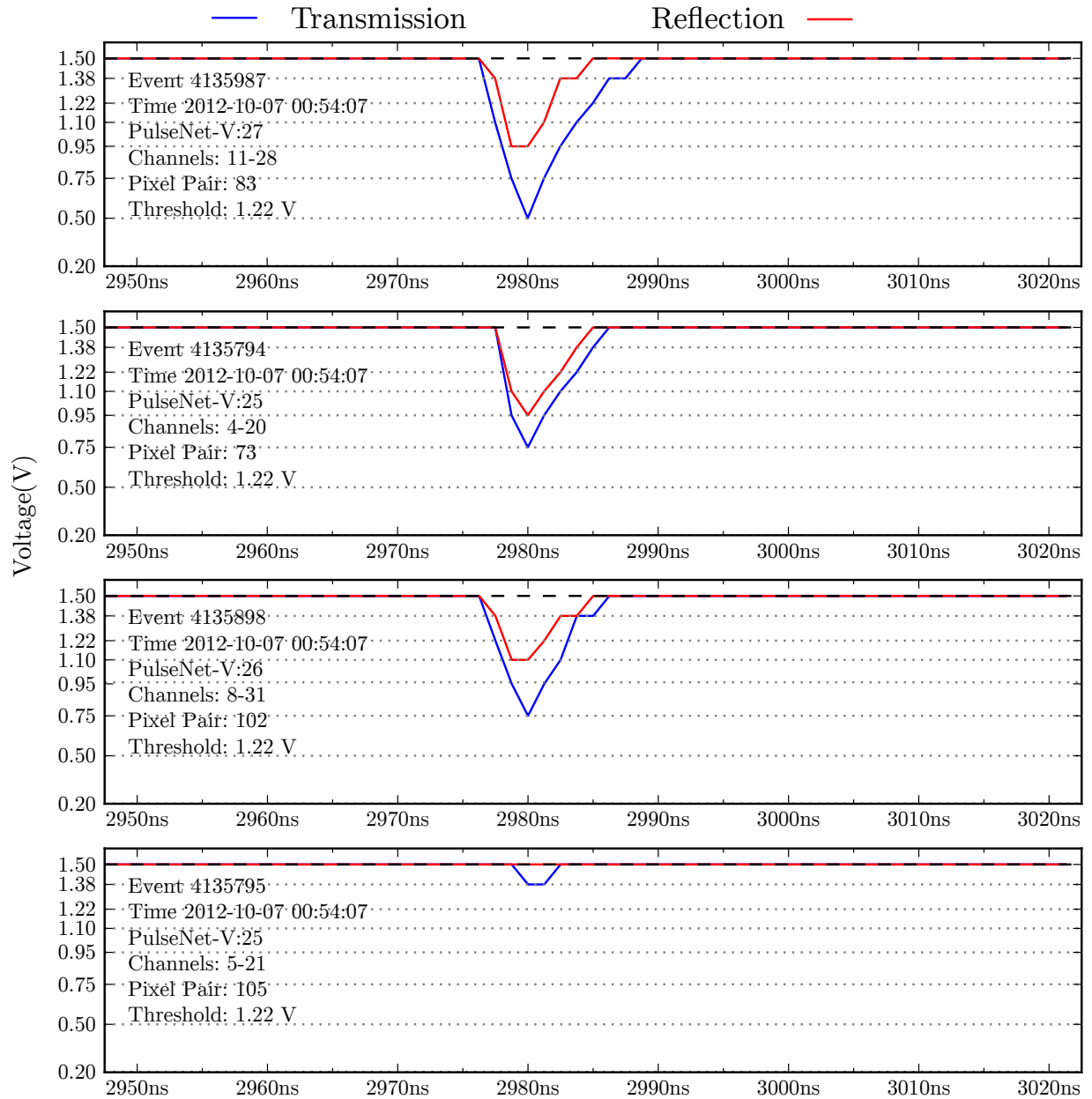


Figure 5.18: The waveforms of four pixels from the event seen in Figure 5.17 are shown above.

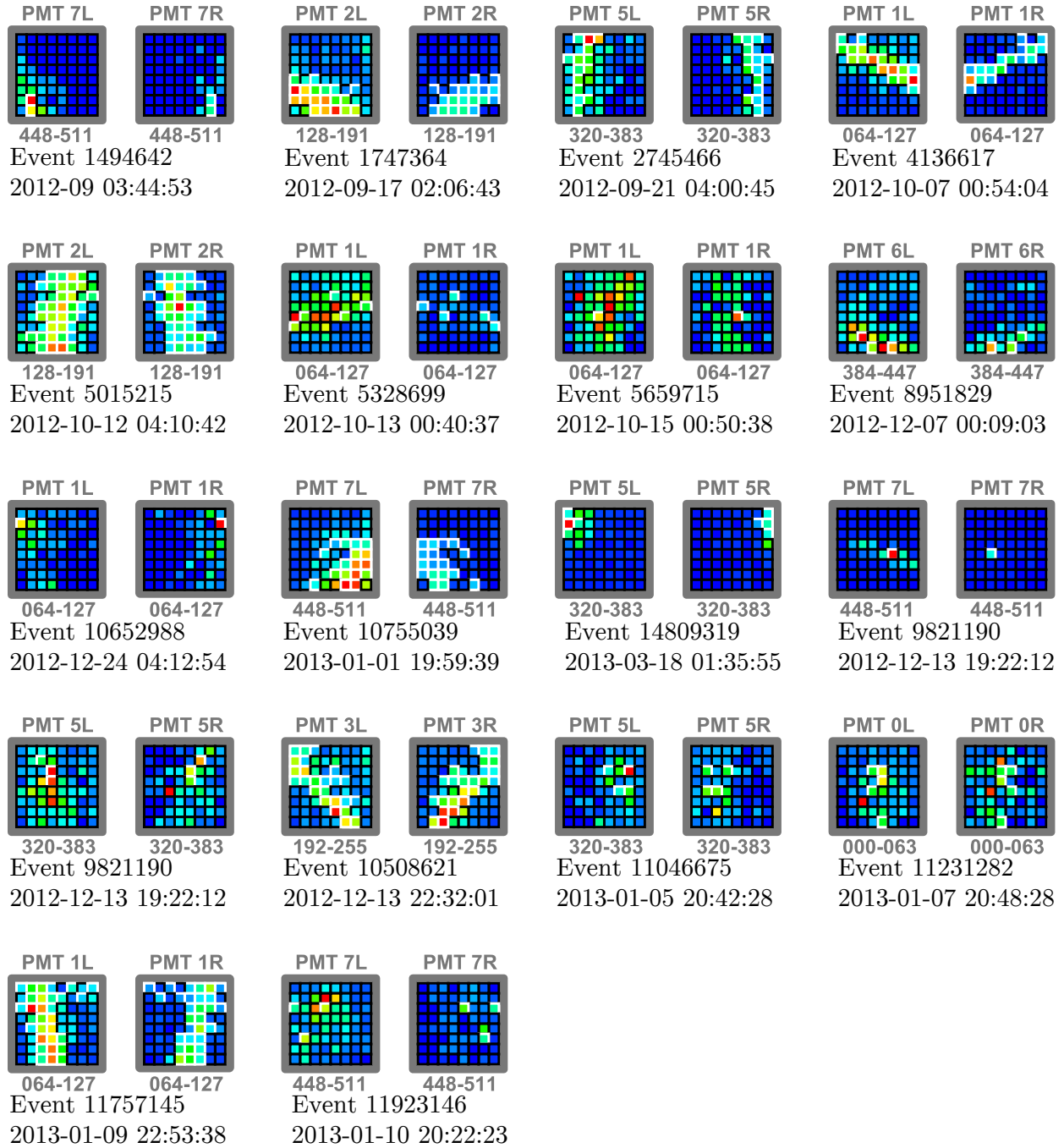


Figure 5.19: Eighteen cosmic ray coincidence images have been recorded by the AdvCam. Only the triggered PMT pair are shown above. The pixel color within the PMT pair corresponds to accumulated charge normalized to a blue (low) to red (high) color map.

## 5.3 Cosmic Ray Simulations

The suspected cosmic ray coincidences deserve some extra attention as they exhibit pulses on the nanosecond scale, similar to what might be expected from a pulsed laser transmitter. A series of simulations were performed to compare the suspected cosmic ray coincidences to the appearance of the imaged Čerenkov light from cosmic ray induced extensive air showers. A natural first question is “How should cosmic rays look as viewed from the telescope’s perspective?” This question was answered by simulating cosmic ray protons (the most common type of cosmic ray primary particle) of a range of energies, incoming angles, and impact distance from telescope and plotting the resulting Čerenkov light. The plots are shown in § 5.3.2. We also asked, more quantitatively, what is the expected cosmic ray trigger rate? Determining the cosmic ray coincidence rate from simulation requires a detailed model of cosmic ray air showers, the telescope, and camera. We used a program called Corsika to simulated the cosmic rays and wrote a python code to simulate the AdvCam and all-sky telescope. The coincidence rate depends on the overall light sensitivity of the telescope and camera, so an indication of the light sensitivity can be obtained by comparing the observed rate to the expected rate.

### 5.3.1 Corsika

Čerenkov photon data was produced using CORSIKA v.7.35[35], a program which performs detailed Monte Carlo simulations of extensive air showers. Protons, electrons, gamma rays, and 47 other elementary primary particles may be simulated using options specifying the primary’s energy, zenith angle, azimuth angle, and starting altitude. The primary particle is tracked as it interacts with the atomic nuclei in the atmosphere and creates new particles and electromagnetic radiation. Multiple models are available for the high energy hadronic interactions, three options exist for lower energy hadronic interactions, and there are two different electromagnetic interaction models. The interaction models have been validated by many high energy experimental groups. Corsika is also used by gamma ray astronomy collaborators to design and understand their imaging atmospheric Čerenkov telescopes.

In the following simulations, Corsika was compiled with the default quark-gluon string model (QGSJET01) for high energy primary interactions and the GHEISHA routines for low energies ( $<80\text{GeV}$ ). Electron and photon interactions are handled by the EGS4 code. The `CERENKOV` option was selected to compel generation of Čerenkov light, as well as the `CERWLEN` option for wavelength dependent Čerenkov light and refraction in the atmosphere. To account for atmospheric absorption, mirror reflectivity, and detector quantum efficiency, the `CEFFIC` option was invoked. Finally, the `THIN` option was specified to reduce simulation times.

### 5.3.2 Telescope Perspective

The Čerenkov image created by cosmic rays varies depending upon the energy of the cosmic ray primary particle, incoming angle, and the distance away from the telescope from which the air shower core impacts the ground (called the impact parameter). [Figure 5.20](#) shows the Čerenkov images of a 500 TeV proton arriving at the telescope with various impact parameters. As the impact parameter increases, the Čerenkov image goes from circular to an elongated streak. A change in incident angle causes a simple translational shift in the image. A more energetic primary results in a brighter Čerenkov image roughly proportional to the primary energy.

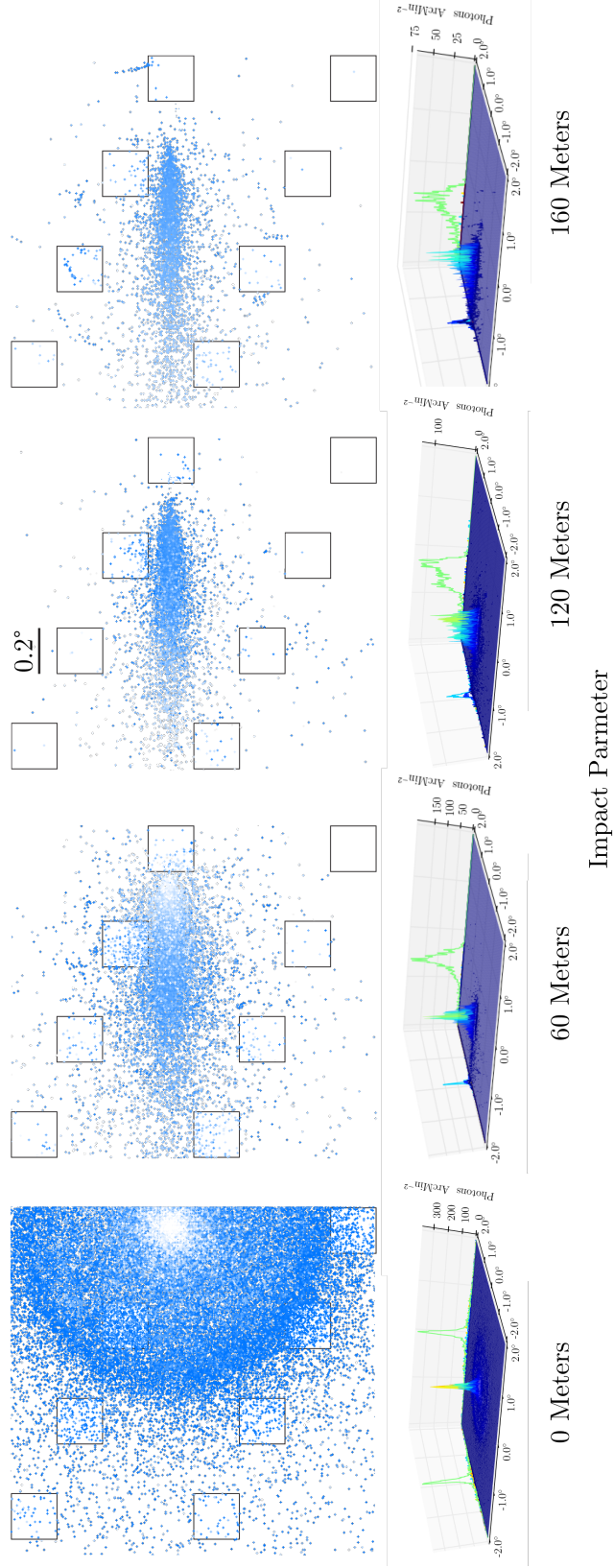


Figure 5.20: Effect of impact parameter: The Čerenkov light from a 500 TeV cosmic ray becomes less intense and more elongated for impact points farther from the telescope. To get a sense of the angular size of the Čerenkov image, the eight boxes in each image represent the AdvCam's photomultiplier tubes.

### 5.3.3 Energy Threshold

Compared to imaging atmospheric Čerenkov telescopes (IACTs), the Advanced All-sky Telescope is much less sensitive to cosmic ray and gamma rays. All-sky has a smaller collector area, 1 m compared to 10-20 m, so photon collection is down by at least a factor of 100. The smaller collector area is not advantageous, of course, because signal photon collection is reduced by the same amount as Čerenkov “noise” photons. However, the solid angle of the all-sky photomultiplier tube pixels are a quarter the size of the most advanced atmospheric Čerenkov telescopes. This spreads the light from the Čerenkov image, reducing the number of Čerenkov photons each pixel receives. An interstellar laser pulse would have an angular extent limited only by the point spread function of the telescope. The point spread function of the all-sky telescope is  $\sim 2$  arcmin, roughly equal to the pixel size of the PMTs. IACTs are generally located at a high elevation. This helps to reduce atmospheric absorption of the Čerenkov light and limits the amount of sky background light. The all-sky system is located at a relatively low elevation, about 100 m. Simulations of the Whipple 10 m atmospheric Čerenkov telescope put its cosmic ray threshold in the low hundreds of GeV<sup>1</sup>. [16] As a point of comparison, the equivalent energy threshold for Advanced All-sky is  $\sim 50$ – $250$  TeV as is explained below.

To determine the cosmic ray energy threshold of the all-sky system using the AdvCam, a Monte Carlo simulation was performed with Corsika and a custom python code that simulates the AdvCam. The Corsika simulations provide the python code with the position and incoming angle of Čerenkov photons from the simulated extensive air shower. For each simulated air shower, ten telescope positions are randomly chosen within a  $200 \text{ m} \times 200 \text{ m}$  area. The python code traces the Čerenkov photons through the telescope optics, entrance window, and beamsplitter and determines if the signal from the photons that land on paired photomultiplier pixel will exceed the trigger threshold. The photon loss of the telescope mirrors and photomultipliers is taken into account by Corsika through the use of data files which specify the mirror reflectivity and photomultiplier quantum efficiency in 5 nm steps from 180 nm to 700 nm. The Corsika simulation code also accounts for the scattering

---

<sup>1</sup>The energy threshold of IACTs is defined as the energy at which the differential gamma ray event rate peaks for a source with a power law spectrum with an index of  $\alpha \approx 1.6$ .

and absorption of the Čerenkov photons in the atmosphere. A US standard atmosphere was specified for all the simulations performed here. Due to processing power and time constraints, only cosmic ray protons were simulated as primary particles. Also to reduce computation time, the optical thinning option was enabled, and only six primary energies were considered: 50 TeV, 75 TeV, 100 TeV, 250 TeV, 500 TeV, and 1000 TeV. For each energy, 100 proton primaries were simulated; with ten telescope positions per air shower, each energy is sampled 1000 times. We will call each of these samples a “pointing”. The primary particle is randomly given an incoming angle relative to the telescope between  $-2^\circ$  and  $+2^\circ$ . The six primary energies were simulated at zenith angles of  $0^\circ$ ,  $15^\circ$ ,  $30^\circ$ , and  $45^\circ$ . For each of the four zenith angles, the fraction of pointings which resulted in a coincidence trigger of the simulated AdvCam is plotted on the left in [Figure 5.21](#). It is clear that at higher zenith angles, a smaller fraction of cosmic rays trigger the camera. This is because at higher zenith angles, the air showers develop farther away from the telescope. This results in less intense Čerenkov light due to  $R^2$  loss and atmospheric absorption. The cosmic ray trigger fraction is multiplied by the cosmic ray flux density (flux data from Zombeck [\[64\]](#)) to produce the differential trigger rate plot seen on the right of [Figure 5.21](#). The majority of the AdvCam’s observations have been conducted at declinations between  $0^\circ$  and  $30^\circ$ , which roughly corresponds to the  $45^\circ$  to  $15^\circ$  zenith angles of the simulation. As seen in the figure, for a  $45^\circ$  zenith angle, the energy threshold is  $\sim 250$  TeV and between 50–100 TeV for a  $15^\circ$  zenith angle.

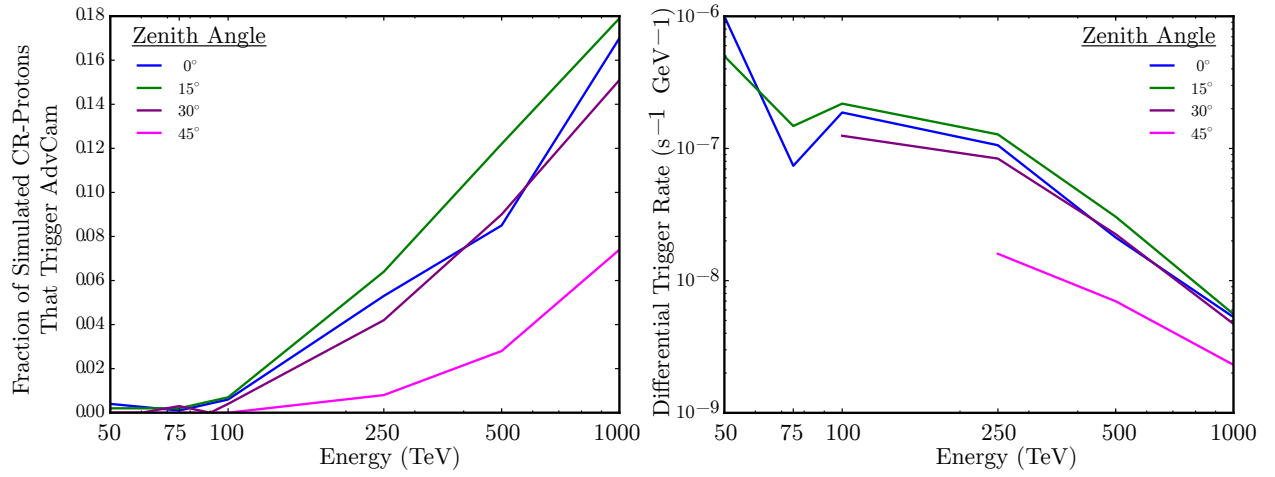


Figure 5.21: Left: The fraction of simulated extensive air showers that trigger the camera is plotted for four zenith angles. For proton primaries of energy  $< 100$  TeV arriving within  $2^\circ$  of the telescope axis, the camera is rarely triggered by the EAS's Čerenkov light. The fraction is greatest ( $\sim 18\%$ ) for 1000 TeV protons when the telescope is pointed  $15^\circ$  from zenith, but cosmic rays of this energy arrive very rarely. Right: Here, the trigger fraction plot on the left is multiplied by the cosmic ray flux rate (data from Zombeck [64]) to get the differential trigger rate.



### 5.3.4 Cosmic Ray Trigger Rate

Does the observed cosmic ray trigger rate comport with that of the simulation? We know from observations that over the course of the 174 hours of observations, at least 18 cosmic ray coincidences have been recorded. This amounts to a cosmic ray trigger rate of  $0.1 \text{ hr}^{-1}$ . If we integrate the plot of the simulated differential trigger rate over the entire range of simulated energies, we get an integrated trigger rate that we can compare to the observed trigger rate. For the  $45^\circ$  and  $30^\circ$  zenith angle the simulated integrated trigger rate is  $0.1$  and  $0.7 \text{ hr}^{-1}$ , respectively. This corresponds fairly well to the observed rate considering the limited number of energies and pointings that were used in the Monte Carlo simulation. This simulated rate was calculated under the assumption of a coincidence threshold corresponding to 8 detected photo-electrons. Working back from this 8 photo-electron threshold and accounting for parameter values of the mirror efficiency, photomultiplier quantum efficiency, beamsplitter efficiency, and entrance window loss in the simulation, the AdvCam's minimum sensitivity according to the simulation is  $\sim 60 \text{ photons}\cdot\text{m}^{-2}$ .

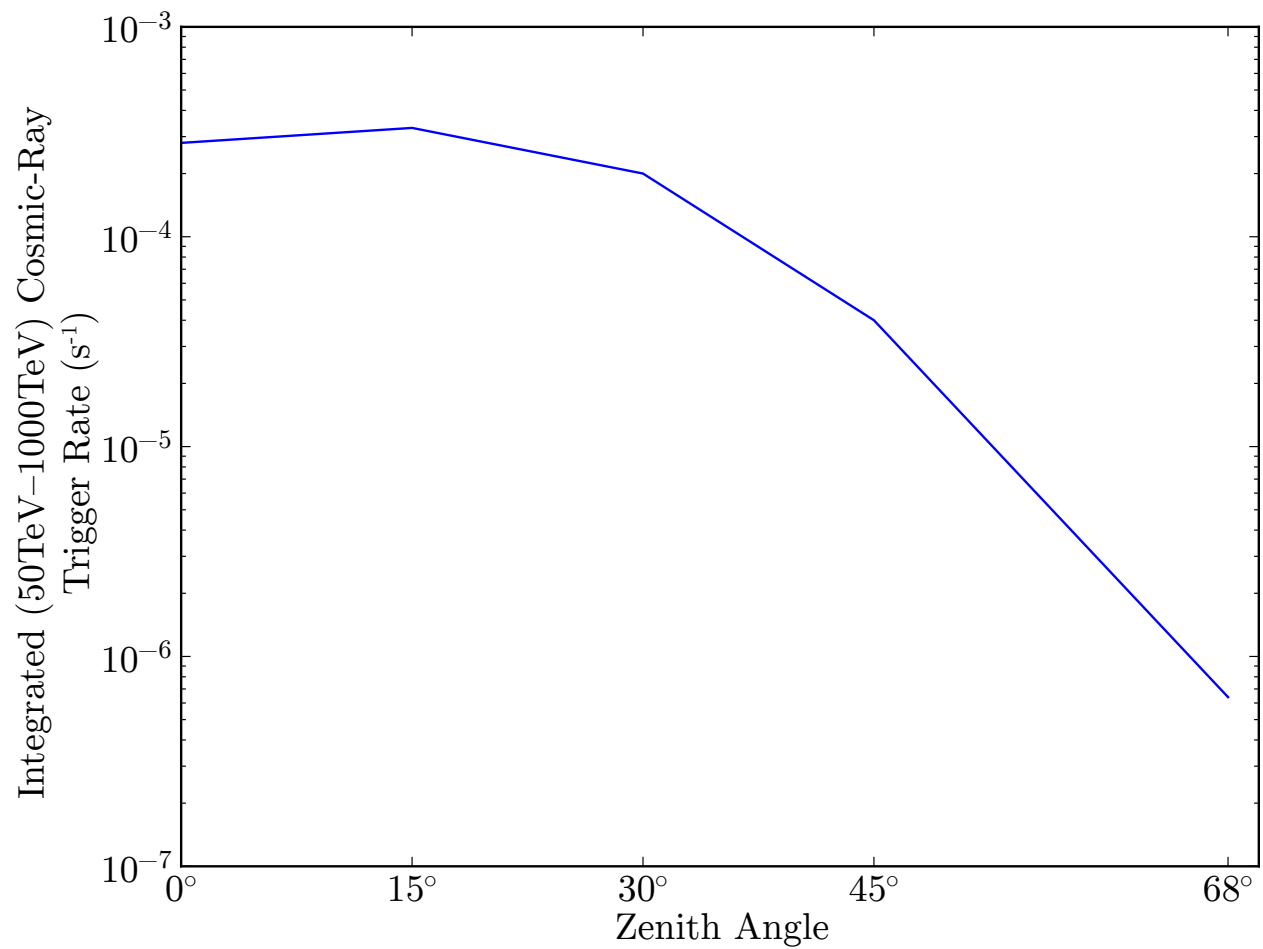


Figure 5.22: The differential trigger rates from [Figure 5.21](#) were integrated over energy to produce the plot above.

## 5.4 Pointing Calibration

A practical application of the astronomy pulse counters is for precise calibration of the telescope's position relative to the sky. Before the Advanced All-Sky Camera, readout of astronomy mode counters of the PulseNet ASIC was too slow to be useful to capture stars transiting across a PMT. The situation has been corrected in PulseNet-V; pulse counter readout of all pixels occurs in parallel and count update rates can be adjusted between 0.75 and 10 seconds. Count rates are periodically requested by `oseti.py` and saved to the experiment database on Costas but are also pushed to the control room server via UDP port 6099. Any internet connected computer can tunnel the UDP port from the server over an SSH connection and receive the count updates. A graphical application called `astro_img` was built in the Processing language to view the count rates. Processing is a java program hence the `astro_img` application can be run on any computer with a java runtime such as Windows, Macintosh OS, or Linux. [Figure 5.23](#) shows a screenshot from `astro_img` showing the star Deneb transiting PMT2. This is not a coincidence triggered image but an image put together based on the astronomy counter values.

During the initial weeks of observations with the Advanced All-Sky Camera, multiple transit events were recorded, along with the sidereal time and telescope encoder value (and index) during the transit events. [Table 5.2](#) lists the stars and corresponding data points used to determine a regression line for converting encoder values to sky declination, as shown in [Figure 5.24](#). The sidereal times at which the stars appeared in the first pixel column as they crossed PMT2 was also recorded. The sidereal time offsets from the stars' right ascensions were averaged and converted into a distance using the camera's plate scale in order to locate the position of the southern meridian. The offset in right ascension is  $1^{\text{m}} 29^{\text{s}}$ , i.e. the meridian is  $\sim 32$  mm from the edge of PMT2 in the direction of PMT3. These offsets are diagramed in [Figure 5.25](#).

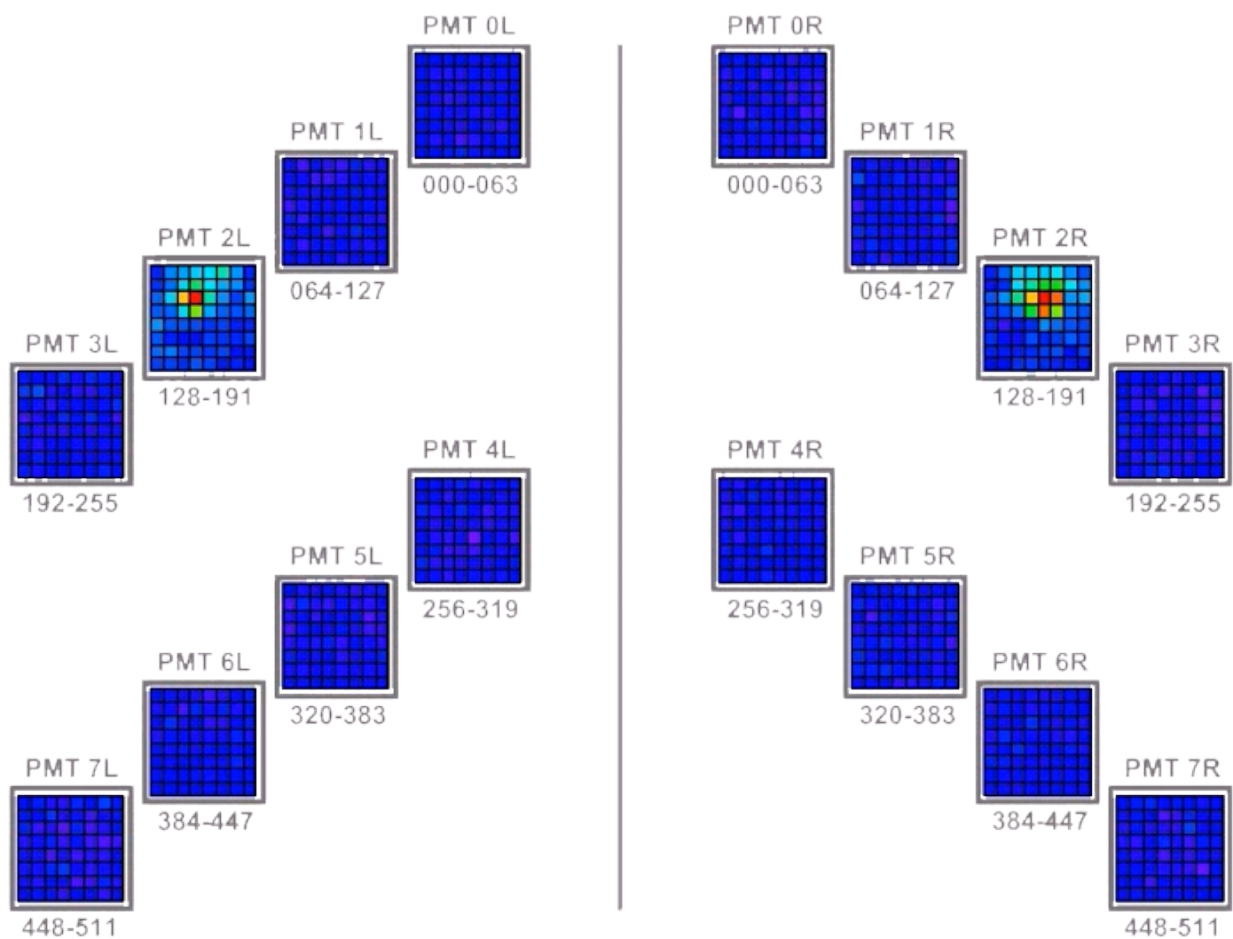


Figure 5.23: Stars can be located using astronomy mode to image the sky by counting single photo-electron pulses from each PMT pixel. The pulse counts are plotted using Processing, a graphical programming language. In the image above, Deneb, a bright star ( $m_v = 1.25$ ) in the constellation Cygnus, is shown crossing PMT2.

Table 5.2: Five star transits were used to determine the encoder-to-declination regression line. An additional seven stars were used to locate the southern meridian.

Star	RA	DEC	Encoder	Sidereal Time@Edge of PMT2
Vega	18 <sup>h</sup> 37 <sup>m</sup> 23 <sup>s</sup>	38° 48' 05"	44174	18 <sup>h</sup> 39 <sup>m</sup> 11 <sup>s</sup>
Altair	19 <sup>h</sup> 51 <sup>m</sup> 26 <sup>s</sup>	8° 54' 24"	17284	
Deneb	20 <sup>h</sup> 41 <sup>m</sup> 54 <sup>s</sup>	45° 19' 50"	50054	20 <sup>h</sup> 44 <sup>m</sup> 03 <sup>s</sup>
$\alpha$ Lacertae	22 <sup>h</sup> 31 <sup>m</sup> 51 <sup>s</sup>	50° 21' 11"	54592	22 <sup>h</sup> 34 <sup>m</sup> 09 <sup>s</sup>
$\alpha$ Andromeda	00 <sup>h</sup> 09 <sup>m</sup> 05 <sup>s</sup>	29° 09' 51"	35530	00 <sup>h</sup> 10 <sup>m</sup> 45 <sup>s</sup>
$\eta$ Pegasi	22 <sup>h</sup> 43 <sup>m</sup> 38 <sup>s</sup>	30° 17' 32"		22 <sup>h</sup> 45 <sup>m</sup> 23 <sup>s</sup>
$\phi$ Pegasi	22 <sup>h</sup> 42 <sup>m</sup> 23 <sup>s</sup>	29° 22' 43"		22 <sup>h</sup> 44 <sup>m</sup> 00 <sup>s</sup>
$\epsilon$ Aquarii	22 <sup>h</sup> 48 <sup>m</sup> 23 <sup>s</sup>	-09° 26' 41"		20 <sup>h</sup> 50 <sup>m</sup> 05 <sup>s</sup>
$\alpha$ Lyrae	18 <sup>h</sup> 37 <sup>m</sup> 23 <sup>s</sup>	38° 48' 05"		18 <sup>h</sup> 39 <sup>m</sup> 10 <sup>s</sup>
$\alpha$ Pegasi	23 <sup>h</sup> 05 <sup>m</sup> 25 <sup>s</sup>	15° 16' 36"		23 <sup>h</sup> 07 <sup>m</sup> 00 <sup>s</sup>
$\gamma$ Pegasi	00 <sup>h</sup> 13 <sup>m</sup> 55 <sup>s</sup>	15° 15' 23"		00 <sup>h</sup> 15 <sup>m</sup> 35 <sup>s</sup>
$\delta$ Andromeda	00 <sup>h</sup> 40 <sup>m</sup> 02 <sup>s</sup>	30° 55' 52"		00 <sup>h</sup> 41 <sup>m</sup> 33 <sup>s</sup>

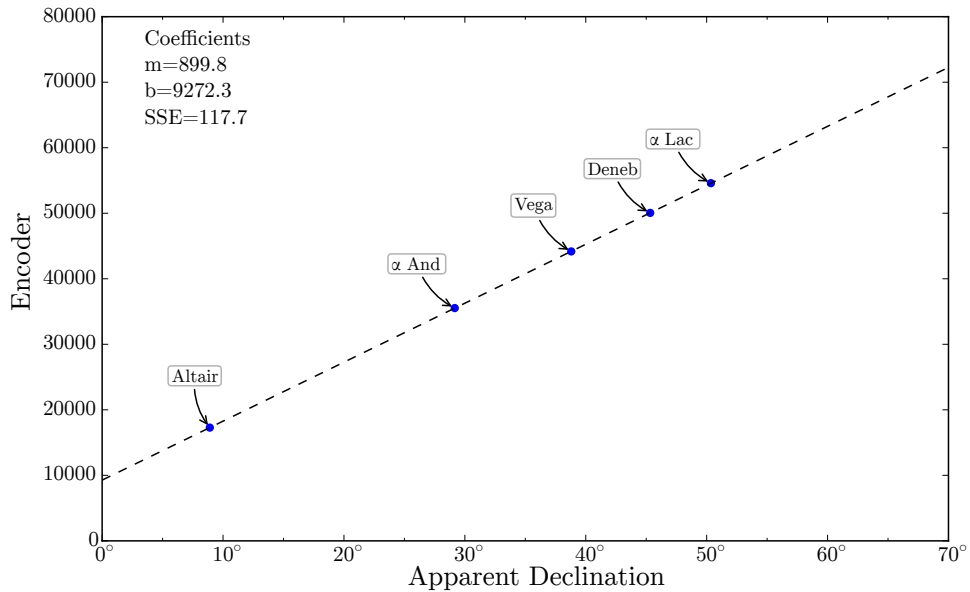


Figure 5.24: Star transit regression line.

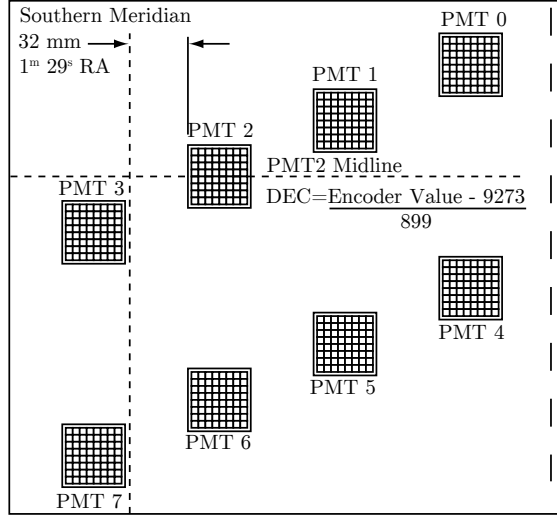


Figure 5.25: The star transits resulted in a calculated offset of  $1^m 29^s$  in RA between the edge of PMT2 and the southern meridian. The equation for calculating the declination position of the midline of PMT2 is shown in the diagram.

## 5.5 Limits on the Prevalence of Transmitting Civilizations

Given that the initial observations of the Advanced All-sky Survey did not encounter any coincidence events that could be attributed to a distant pulsed laser source, what can be learned from this exercise? Assuming no civilizations were detected, we can place limits on the density of civilizations in the nearby galaxy who are attempting pulsed optical communication. Following the analysis of Howard [38], we first develop a model that estimates the number of stars that are concurrently observed by the all-sky camera during an observation. In general, the number of stars viewed when looking at the sky depends on the sky coordinates (right ascension  $\alpha$  and declination  $\delta$ ). There are, of course, more stars in the plane of the galaxy, and extinction will obscure stars along different sightlines. We will use a model that assumes a volume density of stars  $\rho_*(r, \delta, \alpha, \lambda)$  that depends on direction and range. This attempts to account for extinction and the effect of the photomultiplier's spectral sensitivity on the number of stars observed. The total number of stars  $N_*$  integrated

over the sky area observed is

$$\iiint \rho_*(r, \delta, \alpha, \lambda) \cos \delta \, d\delta \, d\alpha \, dr = N_*(\lambda). \quad (5.1)$$

We will use the average model of interstellar absorption  $f_{\text{ext}}(r, \lambda)$  developed in § 1.2.1 and the quantum efficiency  $Q_E(\lambda)$  of the photomultipliers to calculate  $\rho_*(r, \delta, \alpha, \lambda)$ .

$$\rho_*(r, \delta, \alpha, \lambda) = \rho_*^0 \cdot f_{\text{ext}}(r, \delta, \alpha, \lambda) \cdot Q_E(\lambda) \quad (5.2)$$

At a range of  $\sim 1$  kpc, the average interstellar extinction reduces a transmitted light pulse by 20–70%. We will assume that this is the maximum range of the all-sky system. There are  $\sim 10^8$  stars within this volume, so the stellar density  $\rho_*$  will be normalized so that  $N_* = 10^8$  for  $R = 1$  kpc at a wavelength in the middle of the AsCam’s photomultiplier tube sensitivity band (400 nm). This will allow us to make comparisons with previous, more simplified analysis that used a directionally uniform stellar density.

The amount of time spent observing the stars within range depends on the drift time. All-sky is a transit survey, that is, stars drift past the telescope’s field of view at a rate that depends on the declination. The time for a star to drift through a PMT is the lowest when observing the celestial equator ( $\delta = 0^\circ$ ), about 48 seconds. The drift time for observation  $i$  is codified for each sky coordinate by:

$$T_i(\alpha, \delta) = \begin{cases} \frac{48 \text{ sec}}{\cos(\delta)} & \text{for } \alpha \text{ and } \delta \text{ in observation } i \\ 0 & \text{otherwise} \end{cases} \quad (5.3)$$

For a hypothetical transmitter that sent one pulse every  $P$  seconds, the probability of seeing a pulse in the  $i^{\text{th}}$  observation  $p_i$  is just the time spent observing the transmitter’s location divided by repetition time  $P$ . Note that the “min” function is to ensure that the probability is less than one. So the probability density becomes:

$$p_i(\alpha, \delta, P) = \min \left( 1, \frac{T_i(\alpha, \delta)}{P} \right). \quad (5.4)$$

The probability densities for all observations are combined using the following equation:

$$p(\alpha, \delta, P) = 1 - \prod_i \left( 1 - \min \left( 1, \frac{T_i(\alpha, \delta)}{P} \right) \right). \quad (5.5)$$

The product calculates the joint probability density of unsuccessful detections  $(1 - p_i)$  in overlapping observations; the complement of the product  $(1 - \prod_i)$  is interpreted as the probability of a successful detection in at least one of the observations. The total number of successful detections is the detection probability  $p$  (per star) times the number of stars times the fraction of stars  $f_*$  hosting a transmitter with repeat time  $P$ , integrated over the observed sky locations:

$$N_{detect} = f_*(P) \iiint p(\alpha, \delta, P) \rho_*(r, \delta, \alpha, \lambda) dr \cos \delta d\delta d\alpha. \quad (5.6)$$

Even though in our observations there were no successful detections, this could have been a result of observing a transmitter's location, but not during its transmit time. The Poisson probability of observing  $k = 0$  events is

$$\begin{aligned} Pr(k) &= \frac{\lambda^k e^{-\lambda}}{k!} \\ Pr(0) &= e^{-\lambda} \end{aligned} \quad (5.7)$$

where  $\lambda$  is the expected number of events. So with equal chances of a detection ( $e^{-N_{detect}} = 50\%$ ), the fraction of transmitting stars becomes:

$$f_*(P) = \min \left( 1, \frac{\ln 2}{\iiint p(\alpha, \delta, P) \rho_*(r, \delta, \alpha, \lambda) dr \cos \delta d\delta d\alpha} \right) \quad (5.8)$$

where the minimum value of 1 indicates a fraction of stars hosting transmitting civilizations at 100%. The fraction of stars with transmitting civilizations versus repetition time for the two all-sky cameras is shown in [Figure 5.26](#). The first generation, ASIC-based all-sky camera (Gen 1 AsCam), which observed for a total of 7320 hours, is plotted in blue-green and the second generation, FPGA-based camera (AdvCam, discussed in [Chapter 4](#)), which has observed a seventh of the available sky during 174 hours of observations, is plotted in pink-purple. In the model, extinction and the photomultiplier tube's spectral sensitivity is taken into account, so the limit varies with wavelength. Though the AdvCam has observed for a fraction of the time the AsCam has observed, the limits it places on stars with transmitting civilizations is nearly as good at 600 nm and orders of magnitude better at 700 nm and 800 nm. The AsCam limits are much less strict between 600 nm and 800 nm as its photomultipliers have much reduced sensitivity at these longer wavelengths. For both



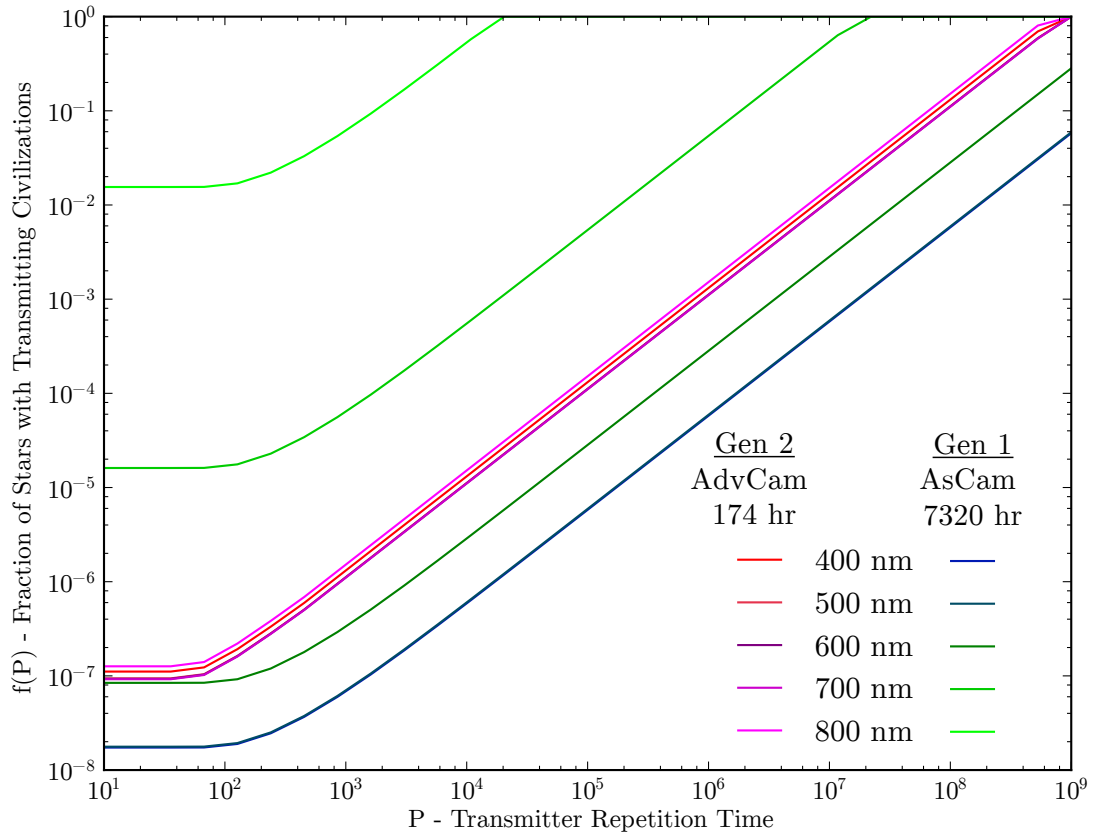


Figure 5.26: The limits placed on the number of stars with transmitting civilizations varies with wavelength according to our model. The Advanced All-sky Camera has observed for only 2% of the time that the first generation all-sky camera has observed but exceeded its between 700–800 nm.

cameras, the tightest constraint is placed on the number of transmitting civilizations for transmit repetition times less than the minimum observation time per star. For one pass over the Northern sky, this is  $\sim 48$  seconds. The AsCam observed the Northern sky from  $-10^\circ$  to  $60^\circ$  nearly four times over the course of seven years, extending this observation time per star to about 250 seconds. With each pass of the full sky, the limit  $f(P)$  does not decrease much but is extended out to longer repeat times. According to our model, the all-sky survey places the limit at  $\sim 10^{-8}$  for the fraction of stars in the galaxy with civilizations operating a transmitter of repeat time  $< 10^2$  and wavelength between 400 nm and 500 nm. The Advanced All-sky Camera places this limit at  $\sim 10^{-7}$  for transmitters of repeat time less than  $\sim 1$  min and wavelength between 600 nm and 800 nm.

## 5.6 Recommendations For Future Work

With PulseNet-V and the Advanced All-sky Camera, our all-sky search for pulsed optical signals from other civilizations has received a well-deserved boost in the quality of the data it collects, but I hope it is not the end of development for Harvard all-sky experiments. The knowledge gained from designing and operating the new camera has led to valuable insights for improvements that could be applied to future instruments. The progression of all-sky surveys should tend towards larger telescope collecting area and more photomultiplier tube pixels. Larger collecting areas increases sensitivity by lowering the number of photons per square meter that are required to detect a distant laser pulse. The increase in sensitivity allows detection of smaller pulse energies and more distant transmitters. Additional photomultiplier tube pixels would increase the amount of sky observed, reducing the time required for a full sky survey and increasing sensitivity to longer pulse repeat times.

Given that we haven't detected any optically transmitting civilizations yet, we may be very distant from our nearest transmitting neighbor. This argues for extending pulsed optical observations to longer wavelengths to avoid undue extinction in the interstellar medium. Above 900 nm, absorption by water vapor complicates the atmospheric transmission window. The J (1.1–1.4  $\mu\text{m}$ ), H (1.5–1.8  $\mu\text{m}$ ), and K (2.0–2.4  $\mu\text{m}$ ) bands still offer low sky brightness at night and high sky transparency, so ground based infrared observations are possible. The

limiting factor, presently, is the quality of red and infrared detectors. Photomultiplier tubes with multi-alkalai photocathodes, as used here, have sensitivities out to 920 nm, however the quantum efficiency is low ( $< 1\%$ ). In the near-infrared, detectors normally must be cryogenically cooled to control the dark current. Thermoelectric cooled InP/InGaAs PMTs exist but the cooling apparatus is bulky and would only be practical for a single-pixel targeted pulsed optical survey. In time, these complications may be obviated by new detector technology. Until that time, the visual band should continue to be preferred for future all-sky pulsed optical surveys. Still, opportunities for searching the infrared spectrum such as piggy-backed observations on telescopes with existing infrared detectors or data-mining infrared surveys for CW spectroscopic lines (à la Reines and Marcy [51]) should be exploited by the broader SETI community if and when those opportunities arise.

One specific opportunity for pulsed optical SETI that has gone unexploited lies in the field of very high energy (VHE) gamma ray astronomy and the technology that community has been advancing. Gamma ray astronomy in the range of 30 GeV to 100 TeV uses imaging air Čerenkov telescopes (IACT) to image the Čerenkov radiation from the electromagnetic cascade of high energy gamma rays entering the atmosphere. It is a burgeoning field with large collaborations such as VERITAS, H.E.S.S., MAGIC, CANGAROO III, and the planned AGIS and CTA. Each collaboration has spent millions of dollars optimizing their own telescopes and cameras. The modern imaging cameras used on these gamma ray telescopes generally consist of hundreds to thousands of light detectors (photomultiplier tubes and avalanche photodiodes), and high-speed electronics to digitize the fast pulses of incoming photons. The requirements of fast photon detection to capture the Čerenkov flashes of gamma rays are quite similar to the needs of pulsed optical SETI surveys. For instance, the VERITAS cameras have pulse waveform-capture abilities by making use a discrete flash ADC (FADC) for every photomultiplier tube output. A schematic of the VERITAS FADC system is shown in [Figure 5.27](#). The elements of the VERITAS system are very similar to the Advanced All-sky Camera. VERITAS uses discrete 500 Msps, 8-bit FADCs, an SRAM for sample storage, a comparator (constant-fraction discriminator) with adjustable threshold for triggering, a backplane for routing triggers and clocks, and a VME bus for communication. The Advanced All-sky Camera has 1.5 Gsps, 3-bit flash ADCs, block RAM for sample storage, LVDS comparators with adjustable thresholds for triggering, a motherboard for

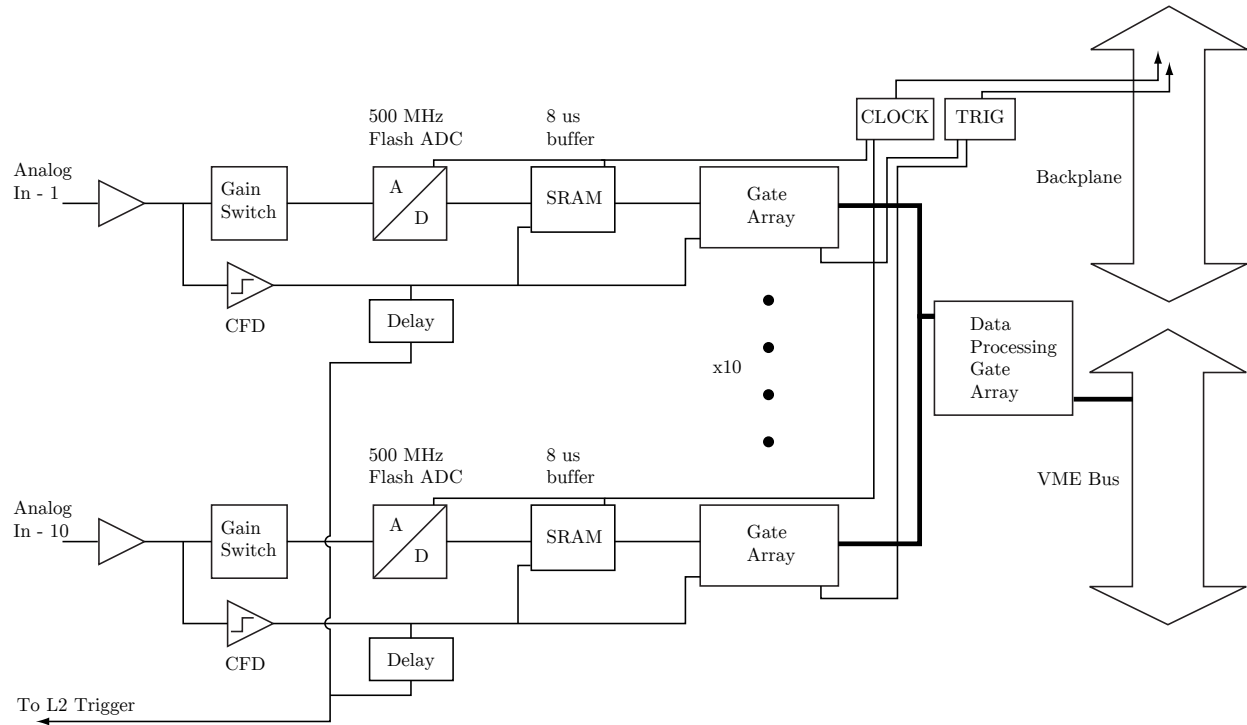


Figure 5.27: The VERITAS cameras have 500 photomultiplier tubes sampled by the flash ADC system. Ten channels are located on a single 9U VME board. Each channel includes a 500 Msp/s ADC that sends samples directly to an SRAM which holds 8  $\mu$ s of sample storage. A constant-fraction discriminator with an adjustable threshold and pulse time is used for triggering the system.

trigger and clock routing, and Ethernet switches for communication. The similarities are so apparent that it may be beneficial to keep abreast of the developments of the next-generation VHE gamma ray telescopes to see if their waveform-capture electronics could be directly used in a pulsed optical SETI survey. A novel addition to the VERITAS system is the autoranging gain switch in front of the FADC. The analog switch normally connects a high-gain amplifier to the FADC. If a strong pulse saturates the high-gain amplifier, the switch connects a delayed, low-gain amplifier to the FADC momentarily. The lower gain pulse follows the truncated, saturated pulse. This extends the dynamic-range of the system from 256 to 1500. This might not be necessary or useful for a pulsed optical SETI system, but it is an example of the kinds of innovations that VHE gamma ray astronomy has produced.

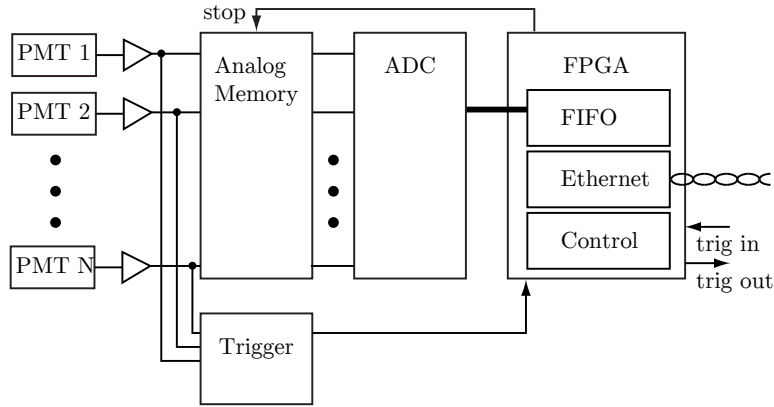


Figure 5.28: H.E.S.S. and MAGIC telescopes use an analog memory based digitization and readout system. The analog memory samples at high-speed (1 Gsps) but is stopped by the trigger system. A slow (40MHz) ADC can then sample the pulse from the analog memory at high resolution (12-bit).

The MAGIC II telescope uses a different readout topology than VERITA but also potentially illuminating [60]. It is an analog memory based system. Instead of a high-speed ADC at the front-end of a readout chain, the MAGIC II sends analog signals from its detectors to an analog memory called the Domino Ring Sampler (DRS). The DRS version 4 can sample nine channels at up to 6 GHz (950 MHz bandwidth) and provides 1024 samples for each channel. When triggered, the DRS stops sampling and an external 40 MHz, 12-bit ADC transfers the digital samples one by one to SRAM storage through an FPGA. This topology lowers the power requirements and increases the sample resolution by using a low speed ADC to do the digital conversion only after the system has triggered (which should be less than 100% duty cycle). The front-end DRS has a high input bandwidth and is much less expensive than ADCs at an equivalent sample speed. The DRS4 costs  $\sim \$1$  per channel while a 1 Gsps ADC currently cost  $\sim \$400$  per channel. While the 1024 samples per channel is smaller than the 8192 samples per channel for the Advanced All-sky Camera, the DRS4 has the ability to cascade its eight channels in series for 8192 samples. The chip specs 69 dB of signal-to-noise, which translates to 12-bit resolution, much better than the 3-bits achieved with Advanced All-sky. This front-end topology should be considered for pulsed optical SETI.

The telescope designs could also be employed in pulsed optical SETI. The imaging air Čerenkov technique necessitates very large collector areas combined with a large field-of-view. The H.E.S.S. II, for example, is a parabolic shaped reflector with 875 90 cm hexagonal mirrors for a total mirror area of 614 m<sup>2</sup>. Its camera has a 3.2° field-of-view comprised of 2048 pixels each subtending 4 arcminutes. This pixel size is about twice that of the Advanced All-sky Camera. Even for a telescope as massive as H.E.S.S. II, the point spread function is well controlled to less than one pixel for the area within 1.6° of the axis [18]. Earlier generation IACTs are of a more manageable size; the 12 m H.E.S.S. (I) telescopes are a spherical design (Davies-Cotton) with 382 round mirrors, 108 m<sup>2</sup> total collecting area, 960 detectors, and a 10 arcminute pixel size. Large engineering efforts went into these telescopes. The designs are well tested and rugged. With small modifications, such as employing a camera with a smaller pixel size, these telescope designs could be employed in high sensitivity pulsed optical SETI surveys. Collaborators planning future VHE gamma ray telescope arrays, such as the Čerenkov Telescope Array (CTA), are considering building large numbers of telescopes with mirror areas of a few m<sup>2</sup> to cover multi-km<sup>2</sup> areas for the detection of gamma rays at energies above 10 TeV [2]. Though small compared to other IACTs, these yet-to-be-designed telescopes will have collecting areas much larger than Harvard’s all-sky telescope. Though the telescopes’ implementation details are yet to be determined, as has been already noted, the important telescope parameters like the field-of-view and PSF of IACTs are generally compatible with the needs for wide-field pulsed optical SETI surveys. Since there will be many of them, the unit cost for the CTA’s smaller telescopes may be low enough to be considered by the value-minded SETI community.

Building a new, large collecting area, IACT-style telescope to increase the sensitivity of pulsed optical SETI surveys might require a budget that is not feasible given that the entire cost of the Harvard all-sky effort has been <\$1 million over a period of 13 years. A dedicated telescope is certainly desirable, however if this is not possible, existing gamma ray telescopes could be retrofitted with a pulsed optical SETI trigger system. In fact, an IAC telescope can very nearly be used in a pulsed optical search with only a few modifications. Holder et al. [36] describes using the Whipple 10 m telescope to search for optical pulses using the image shape as a discriminator. A dedicated SETI trigger system, however, could provide much more reliable optical pulse detection for IACT arrays. Most of the modern

VHE gamma ray systems (H.E.S.S., MAGIC, VERITAS) have trigger pathways that are somewhat independent of the data acquisition and readout electronics. Because of this modularity, additional trigger systems can be added without affecting the primary gamma ray trigger pathway. A SETI trigger system could consist of coincidence circuits for individual pixels or pixel regions in different telescopes of the array that view identical areas of the sky, similar to the matched pairs of the all-sky camera. Two or more array telescopes could be used in the coincidence circuit, as long as the telescopes are pointed at the same sky coordinate. Gamma ray telescopes must be used in pairs or more to function as reliable pulsed optical SETI detectors. The point spread functions of gamma ray telescopes are normally equal to or smaller than their camera's pixel size, so an optical point source tends to be focused into only a single detector. This is a problem because photomultiplier tubes have sources of dark current that cause large-amplitude output pulses to occur frequently. A lone gamma ray telescope has no way to distinguish the dark current pulses from optical point sources. In order to capture actual flashes of light and not be triggered by dark current pulses, gamma ray telescope trigger systems enforce a coincidence of adjacent clusters of photomultiplier tubes. This type of trigger works when the light from an optical pulse covers a broad area of the camera, as is the case for the Čerenkov light of cosmic ray and gamma ray extensive air showers, but it will not work in the case of an optical point source in which the light is only collected by one or two pixels.

The direction of VHE gamma ray astronomy is tending toward using tens of telescopes of 2 or 3 different sizes to maximize sensitivity to a wide range of gamma ray energies: less than 100 GeV, between 100 GeV to 10 TeV, and above 10 TeV. Having many telescopes allows them to be used in groups to observe adjacent and overlapping fields in the sky. In the future, this type of capability will enable, for the first time, full-sky surveys at full sensitivity [2]. Implementing a pulsed optical SETI trigger subsystem for the next-generation of IACTs makes a lot of sense given that future VHE gamma ray observations will finally cover large areas of the sky rather than being limited to the galactic plane and a small number of other point locations. With so much overlap between pulsed optical SETI and VHE gamma ray astronomy camera topologies, the Advanced All-sky Camera (AdvCam) may even provide an example to the next generation imaging air Čerenkov telescopes (IACT). The trigger system used in the AdvCam is integrated into the logic-fabric of an FPGA and works by

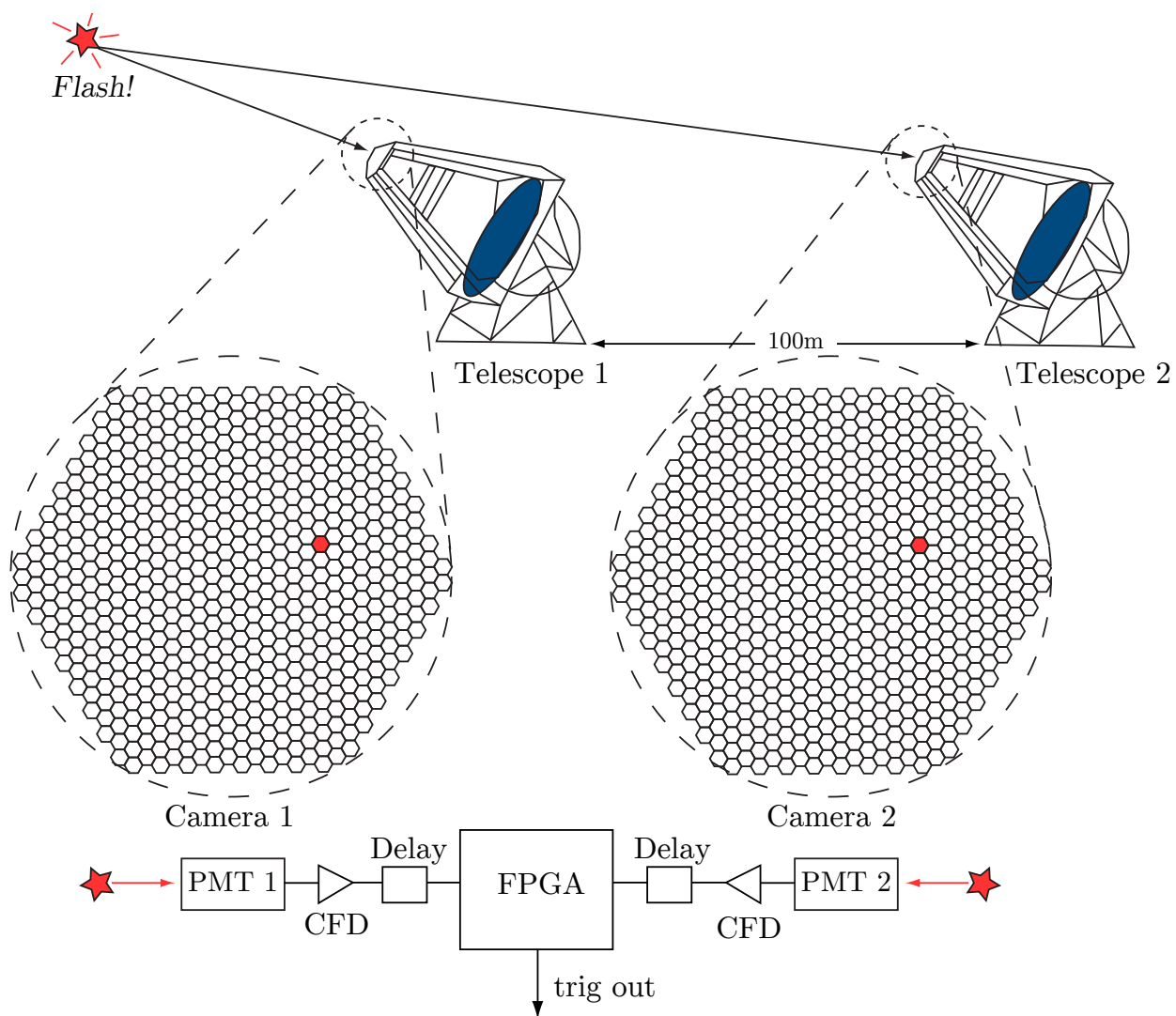


Figure 5.29: An optical SETI trigger could be constructed for imaging air Čerenkov telescopes that responds to coincidences from matched sky pixels from separate telescopes.



processing the digital sampled versions of the analog photomultiplier tube signals. Current FADC-based trigger systems of IACTs, such as used on VERITAS (Figure 5.27) are separate from the FADC data acquisition electronics, adding significant complexity to the electronics design. The integrated AdvCam trigger system has not been used before in any IACT but the increasing power of integrated circuits “may soon make digital trigger processors an attractive and feasible option” [2]. Advanced All-sky has a working implementation of this approach and offers a proof of concept (albeit simplified) design example.

The Advanced All-sky Camera has allowed us to probe the nearby galaxy for pulsed laser transmitters and explore its limits as a configurable nanosecond optical astronomical camera. The all-sky telescope and camera have their limitations, however, so to substantially lower the limits on the prevalence of transmitting civilizations (see Figure 5.26) and perhaps to make a detection, a new all-sky survey may need to be designed. Here is a proposal for a system that could provide a modest boost in capability over the current Harvard all-sky survey.

The proposed system is comprised of two telescopes, each with a camera similar to the Advanced All-sky Camera design. Coincidence timestamps and pixel locations from the individual cameras would be forwarded to a higher level trigger unit that would send an array trigger to the two telescopes. The telescopes should be separated by enough distance to avoid being triggered by the same cosmic ray air showers but close enough so that the detector readout electronics can buffer more time than the signal propagation delay between telescopes. Very high-energy cosmic rays can create a Čerenkov ground pattern over more than a square kilometer, so a baseline of 1000 m would give a reasonable propagation delay of  $\sim 5 \mu\text{s}$ . The Advanced All-sky Camera can already buffer  $10 \mu\text{s}$  at a sampling rate of 800 Msps, a number which will only rise if subsequent versions use the latest FPGA silicon devices. The camera detectors should use individual photomultiplier tubes with extended-red sensitivity and infrared sensitivity if available. Most important for the detectors is to have a very low large-amplitude dark current pulse rate. This is the most difficult background noise source to reduce. Considering other detector technologies, geiger-mode avalanche photodiodes (GAPDs) in multi-pixelated packages with large fill factors and low output capacitance are becoming available; they should be considered as an alternative photodetector as they have the advantages of higher quantum efficiency,

mechanical robustness, little aging even when exposed to bright light, and low voltage operation. They can be especially effective when used with optimal Winston light cone concentrators [9]. While multi-pixelated phototubes may be more economical, the gain between pixels cannot be equalized and individual anodes may receive too much light from a star, requiring a reduction in the tubes' high voltage, reducing the gain for all pixels in the tube.

The two telescopes could be based on one of the IACT-type designs (Davies-Cotton, segmented parabolic, or Schwarzschild-Couder), but with an increased focal length to reduce the plate scale so that pixels subtend  $<2$  arcminutes. This dilutes Čerenkov images and decrease triggers from cosmic ray showers and local muons. The Davies-Cotton (DC) type would be an appropriate choice as they are well documented and widely used. They are composed of many segmented spherical mirrors that make up a single spherical main reflector. The camera is situated at the prime focus in front of the main mirror. Since DC telescopes have no secondary mirror, there is little shadowing of the primary. Alignment is easily accomplished by adjusting the mirror facets. Winston cones can be used to block off-axis background light from entering the detectors, an advantage in areas with skyglow from nearby cities (as is the case in Harvard, MA). Davies-Cotton designs do introduce a time arrival distribution for an instantaneous parallel beam flash. An ideal 4 m f/15 Davies-Cotton reflector has a time spread of  $\sim 1.1$  ns which is adequate for the coincidence overlap (2.5 ns) normally used by the AdvCam. The time spread is mainly dominated by the innermost mirrors. The time spread can be reduced for larger diameters by moving the inner mirrors closer to a parabolic shape [9].

The system should ideally be located in an area with very dark skies to reduce the random coincidence rate and maximize photomultiplier life. The most numerous type of camera coincidences are from pixel pairs that both cross the trigger threshold at the same time, caused mainly by pileup of multiple night sky photons and starlight, but also from ion feedback, after pulsing, or other detector systematic noise source<sup>2</sup>. Experience with the AdvCam has shown that even when using matched detector pairs in coincidence, an

---

<sup>2</sup>Cosmic ray induced Čerenkov light and airplanes do trigger the camera, but these triggers are easily recognizable by their angular size and waveform shape.

extra few orders of magnitude of suppression of coincidences are still needed to lower this “accidental” rate. The accidental rate could be lowered by adding a third bank of detectors and requiring a triple coincidence to trigger the camera. The disadvantage of this approach is that the light collected by the telescope would be further divided to the third bank of detectors, reducing the signal that arrives at the original two detectors. Introduction of a second telescope requires duplication of the camera electronics and photodetectors, but the coincidence rate  $r$  is reduced by

$$r_c = r^2 \tau_{\text{tcw}} \quad (5.9)$$

where  $\tau_{\text{tcw}}$  is the coincidence window time for the coincidences between the two telescopes. If  $\tau_{\text{tcw}}$  is just limited to the GPS time resolution ( $10\mu\text{s}$ ) and the individual camera coincidence rate  $r = 10^{-2}$ , then two telescope coincidences would randomly occur on average three times in a century.

# Bibliography

- [1] D. S. Abbot and E. R. Switzer. The Steppenwolf: A Proposal for a Habitable Planet in Interstellar Space. *ApJ*, 735:L27, July 2011.
- [2] M. Actis et al. Design concepts for the Cherenkov Telescope Array CTA: an advanced facility for ground-based high-energy gamma-ray astronomy. *Experimental Astronomy*, 32:193–316, December 2011.
- [3] J. R. Albertine. History of Navy HEL technology development and systems testing. In S. Basu and J. F. Riker, editors, *Society of Photo-Optical Instrumentation Engineers (SPIE) Conference Series*, volume 4632 of *Society of Photo-Optical Instrumentation Engineers (SPIE) Conference Series*, pages 32–37, June 2002.
- [4] O. C. Allkofer, K. Carstensen, and W. D. Dau. The absolute cosmic ray muon spectrum at sea level. *Physics Letters B*, 36(4):425 – 427, 1971. ISSN 0370-2693. URL <http://www.sciencedirect.com/science/article/pii/0370269371907416>.
- [5] Z. K. Berta et al. The Flat Transmission Spectrum of the Super-Earth GJ1214b from Wide Field Camera 3 on the Hubble Space Telescope. *ApJ*, 747:35, March 2012.
- [6] P. Blasi, R. Dick, and E. W. Kolb. Ultra-high energy cosmic rays from annihilation of superheavy dark matter. *Astroparticle Physics*, 18:57–66, August 2002.
- [7] B. P. Bowler, M. C. Liu, T. J. Dupuy, and M. C. Cushing. Near-infrared Spectroscopy of the Extrasolar Planet HR 8799 b. *ApJ*, 723:850–868, November 2010.
- [8] R. N. Bracewell. *The galactic club: intelligent life in outer space*. W.H. Freeman and Co. Ltd, UK, 1975.
- [9] T. Bretz and M. Ribordy. Design constraints on Cherenkov telescopes with Davies-Cotton reflectors. *ArXiv e-prints*, January 2013.
- [10] J. A. Cardelli, G. C. Clayton, and J. S. Mathis. The relationship between infrared, optical, and ultraviolet extinction. *ApJ*, 345:245–256, October 1989.
- [11] A. Cassan et al. One or more bound planets per Milky Way star from microlensing observations. *Nature*, 481:167–169, January 2012.

- [12] S. Cecchini and M. Spurio. Atmospheric muons: experimental aspects. *Geoscientific Instrumentation, Methods and Data Systems Discussions*, 2:603–641, August 2012.
- [13] B. Chen, J. L. Vergely, B. Valette, and G. Carraro. Comparison of two different extinction laws with HIPPARCOS observations. *A&A*, 336:137–149, August 1998.
- [14] G. Cocconi and P. Morrison. Searching for Interstellar Communications. *Nature*, 184: 844–846, 1959.
- [15] C. Coldwell. *A Search for Interstellar Communications at Optical Wavelengths*. PhD thesis, Harvard University, 2002.
- [16] M. Connolly. Two dimensional analysis of incomplete parameterised archival data from the Whipple 10 metre imaging atmospheric cherenkov telescope centered on AE Aquarii. Masters thesis, Centre for Astronomy, School of Physics, National University of Ireland, Galway, 2010.
- [17] J. M. Cordes and T. J. Lazio. Interstellar Scattering Effects on the Detection of Narrow-band Signals. *ApJ*, 376:123–133, July 1991.
- [18] R. Cornils, K. Bernlohr, G. Heinzelmann, W. Hofmann, and M. Panter. The optical system of the H.E.S.S. II telescope. In *29th International Cosmic Ray Conference Pune*, volume 00, pages 101–106, 2005.
- [19] M. J. Crowe. *The extraterrestrial life debate 1750-1900. The idea of a plurality of worlds from Kant to Lowell*. Cambridge: University Press, 1986.
- [20] R. Diehl et al. Radioactive  $^{26}\text{Al}$  from massive stars in the Galaxy. *Nature*, 439:45–47, January 2006.
- [21] B. T. Draine. Interstellar Dust Grains. *ARA&A*, 41:241–289, 2003.
- [22] D. Dravins, H. O. Hagerbo, L. Lindegren, E. Mezey, and B. Nilsson. Optical astronomy on milli-, micro-, and nanosecond timescales. In D. L. Crawford and E. R. Craine, editors, *Society of Photo-Optical Instrumentation Engineers (SPIE) Conference Series*, volume 2198 of *Society of Photo-Optical Instrumentation Engineers (SPIE) Conference Series*, pages 289–301, June 1994.
- [23] R. D. Ekers. *SETI 2020 : A Roadmap for the Search for Extraterrestrial Intelligence*. SETI Press, Mountain View, Calif., 2002.
- [24] Z. Fodor, S. D. Katz, A. Ringwald, and H. Tu. Strongly Interacting Neutrino as the Highest Energy Cosmic Rays. In H. V. Klapdor-Kleingrothaus, editor, *Particle Physics Beyond the Standard Model*, page 857, 2004.
- [25] J. P. Gardner et al. *The James Webb Space Telescope*, pages 1–4020. Springer, 2009.

- [26] R. Gilmozzi and J. Spyromilio. The European Extremely Large Telescope (E-ELT). *The Messenger*, 127:11, March 2007.
- [27] N. Glade, P. Ballet, and O. Bastien. A stochastic process approach of the drake equation parameters. *International Journal of Astrobiology*, 11:103–108, April 2012.
- [28] E. Goulielmakis et al. Single-Cycle Nonlinear Optics. *Science*, 320:1614–, June 2008.
- [29] R. Greeley, M. Dougherty, R. Pappalardo, and J. Lebreton. Europa jupiter system mission (EJSM) exploring the emergence of habitable worlds around gas giants. Joint Jupiter Science Definition Team Report to NASA JPL D-67959, NASA-ESA, 2010. URL <http://www.lpi.usra.edu/opag/JJSDTNASAReport.pdf>.
- [30] D. Grinspoon. *Lonely Planets: The Natural Philosophy of Alien Lif*. Harper Colling, New York, 2003.
- [31] Guinness World Records. [http://www.guinnessworldrecords.com/content\\_pages/record.asp?recordid=53519](http://www.guinnessworldrecords.com/content_pages/record.asp?recordid=53519), September 5, 2005. Accessed: 2013-03-10.
- [32] J. Hakkila, J. M. Myers, B. J. Stidham, and D. H. Hartmann. A Computerized Model of Large-Scale Visual Interstellar Extinction. *AJ*, 114:2043, November 1997.
- [33] Hamamatsu Multianode Photomultiplier Tube Assembly H7546A, H7546B. (datasheet). [http://www.hamamatsu.com/resources/pdf/etd/H7546A\\_H7546B\\_TPMH1240E12.pdf](http://www.hamamatsu.com/resources/pdf/etd/H7546A_H7546B_TPMH1240E12.pdf), 2007. Retrieved 2013-03-27.
- [34] T. H. Hankins, J. S. Kern, J. C. Weatherall, and J. A. Eilek. Nanosecond radio bursts from strong plasma turbulence in the Crab pulsar. *Nature*, 422:141–143, March 2003.
- [35] D. Heck and T. Pierog. Corsika: A Monte Carlo Code to Simulate Extensive Air Showers. Report FZKA 6019, Forschungszentrum Karlsruhe, 1998. Available from [http://www-ik.fzk.de/corsika/physics\\_description/corsika\\_phys.html](http://www-ik.fzk.de/corsika/physics_description/corsika_phys.html).
- [36] J. Holder, P. Ashworth, S. LeBohec, H. J. Rose, and T. C. Weekes. Optical SETI with Imaging Cherenkov Telescopes. In *International Cosmic Ray Conference*, volume 5 of *International Cosmic Ray Conference*, page 387, 2005.
- [37] D. Horan. *The Discovery of TeV  $\gamma$ -rays from the BL Lacertae, 1H1426+428*. PhD thesis, University College Dublin, Dublin, Ireland, 2001.
- [38] A. W. Howard. *Astronomical Searches for Nanosecond Optical Pulses*. PhD thesis, Harvard University, Cambridge, MA, 2003.
- [39] A. W. Howard et al. Search for Nanosecond Optical Pulses from Nearby Solar-Type Stars. *ApJ*, 613:1270–1284, October 2004.

- [40] A. W. Howard et al. The Occurrence and Mass Distribution of Close-in Super-Earths, Neptunes, and Jupiters. *Science*, 330:653–, October 2010.
- [41] Clemente Ibarra-Castanedo. Infrared Spectrum.gif. [http://commons.wikimedia.org/wiki/File%3AInfrared\\_spectrum.gif](http://commons.wikimedia.org/wiki/File%3AInfrared_spectrum.gif), 2007. Licensed under the Creative Commons Attribution-Share Alike 3.0 Unported license.
- [42] L. Kolokolova and W. Sparks. Circular Polarization for Remote Detection of Chirality of Biological Origin. In *AAS/Division for Planetary Sciences Meeting Abstracts #40*, volume 40 of *Bulletin of the American Astronomical Society*, page 485, September 2008.
- [43] M. Lampton. Optical SETI: The Next Search Frontier. In G. Lemarchand and K. Meech, editors, *Bioastronomy 99*, volume 213 of *Astronomical Society of the Pacific Conference Series*, page 565, 2000.
- [44] M. McCaughrean. ESA’s report to the 39th cospar meeting. ESA Report SP-1323, European Space Agency, 2012. URL <http://sci.esa.int/science-e/www/object/index.cfm?fobjectid=50671#>.
- [45] D. S. McKay et al. Search for Past Life on Mars: Possible Relic Biogenic Activity in Martian Meteorite ALH84001. *Science*, 273:924–930, August 1996.
- [46] E. I. Moses. National Ignition Facility: 1.8-MJ 750-TW ultraviolet laser. In M. A. Lane and C. R. Wuest, editors, *Society of Photo-Optical Instrumentation Engineers (SPIE) Conference Series*, volume 5341 of *Society of Photo-Optical Instrumentation Engineers (SPIE) Conference Series*, pages 13–24, May 2004.
- [47] NASA. NASA exoplanet archive, feb 2013. URL <http://exoplanetarchive.ipac.caltech.edu/index.html>.
- [48] B. M. Oliver and J. Billingham, editors. *Project Cyclops: A Design Study of a System for Detecting Extraterrestrial Intelligent Life*, 1971.
- [49] K. D. Olum and J. J. Blanco-Pillado. Ultra-high-energy cosmic rays from relic topological defects. In J. C. Wheeler and H. Martel, editors, *20th Texas Symposium on relativistic astrophysics*, volume 586 of *American Institute of Physics Conference Series*, pages 844–849, October 2001.
- [50] B. C. Reed. Education notes/rubrique pédagogique - stellar magnitudes and photon fluxes. *Journal of the Royal Astronomical Society of Canada*, 87:123, 1993.
- [51] A. E. Reines and G. W. Marcy. Optical SETI: A Spectroscopic Search for Laser Emission from Nearby Stars. *ArXiv Astrophysics e-prints*, December 2001.

- [52] A. E. Reines and G. W. Marcy. Optical Search for Extraterrestrial Intelligence: A Spectroscopic Search for Laser Emission from Nearby Stars. *PASP*, 114:416–426, April 2002.
- [53] G. H. Rieke and M. J. Lebofsky. The interstellar extinction law from 1 to 13 microns. *ApJ*, 288:618–621, January 1985.
- [54] T. P. Robitaille and B. A. Whitney. The Present-Day Star Formation Rate of the Milky Way Determined from Spitzer-Detected Young Stellar Objects. *ApJ*, 710:L11–L15, February 2010.
- [55] Carl Sagan. “Who Speaks For Earth?”. *Cosmos: A Personal Journey*. DVD. Cosmos Studios, 1990.
- [56] R. Schwartz and C. Townes. Interplanetary and Interstellar Communication by Optical Masers. *Nature*, 190:205–208, 1961.
- [57] S. Seager, E. L. Turner, J. Schafer, and E. B. Ford. Vegetation’s Red Edge: A Possible Spectroscopic Biosignature of Extraterrestrial Plants. *Astrobiology*, 5:372–390, June 2005.
- [58] Secretary of Defense Approves Laser Experiment to Improve Satellite Protection. (press release). <http://www.defense.gov/releases/release.aspx?releaseid=1431>, October 2, 1997. Retrieved 2013-03-09.
- [59] L. E. Strigari, M. Barnabè, P. J. Marshall, and R. D. Blandford. Nomads of the Galaxy. *MNRAS*, 423:1856–1865, June 2012.
- [60] D. Tescaro et al. The readout system of the MAGIC-II Cherenkov Telescope. *ArXiv e-prints*, July 2009.
- [61] C. Townes. At What Wavelengths Should We Search for Signals from Extraterrestrial Intelligence? *Proc. Natl. Acad. Sci.*, 80:1147–1151, 1983.
- [62] P. A. Čerenkov. Visible Radiation Produced by Electrons Moving in a Medium with Velocities Exceeding that of Light. *Physical Review*, 52:378–379, August 1937.
- [63] T. C. Weekes. Very High Energy Gamma-Ray Astronomy. *Physics Reports*, 160:1–121, 1988.
- [64] Martin V. Zombeck. *Handbook of Space Astronomy and Astrophysics*. Cambridge University Press, Cambridge, U.K., 2007.